



Universidad de Oviedo
Universidá d'Uviéu
University of Oviedo

Energy Engineering Department

PhD Thesis

PhD Programme in Energy and Process Control

Design and Modelization of a Vertical-Axis Hydrokinetic Turbine for Low Flow Velocities

Author:

Ahmed Gharib Sayed Yosry

Dissertation submitted in partial fulfillment of the requirements for the
degree of Doctor of Philosophy in Energy Engineering with International
Mention

Advisor: Prof. Eduardo Blanco Marigorta
Full Professor, Department of Energy Engineering, University of Oviedo

Gijón, Spain
SEPTEMBER 2023



Universidad de Oviedo
Universidá d'Uviéu
University of Oviedo

Departamento de Ingeniería Energética

Tesis Doctoral

Programa de Doctorado en Energía y Control de Procesos

Diseño y Modelización de una Turbina Hidrocínética de Eje Vertical para Bajas Velocidades

Autor:

Ahmed Gharib Sayed Yosry

**Tesis presentada en cumplimiento parcial de los requisitos para el grado de
Doctor en Filosofía en Ingeniería Energética con Mención
Internacional**

Tutor: Prof. Edurado Blanco Marigorta
Catedrático, Departamento de Ingeniería Energética, Universidad de Oviedo

Gijón, España
SEPTIEMBRE 2023

*A mi esposa, familia y amigos
y en especial, a mis padres*

*To my wife, family and friends
and especially, to my parents.*

Acknowledgements

First and foremost, I would like to express my heartfelt appreciation and thanks to my thesis advisor, **Prof. Eduardo Blanco Marigorta**, for his unwavering support, valuable guidance, and endless patience throughout the duration of my thesis. His dedication to addressing any technical or personal issues that arose during the thesis has been invaluable.

I would also like to extend my sincere gratitude, appreciation, and thanks to **Prof. Eduardo Álvarez Álvarez**. His guidance, collaboration, and valuable comments were instrumental in shaping the experimental work of my research.

Furthermore, I would like to acknowledge and thank **Prof. Dr.-Ing. Jörg Seume**, the head of the Fluid Dynamic and Turbomachinery Institute (TFD) at the University of Hannover, Germany, and **Dr.-Ing. Lars Wein**, the team leader. Their warm welcome and support during my internship allowed me to participate in the CRC project. I am particularly grateful to **Ing. Dominik Ahrens** for his invaluable support and guidance throughout this period in the project.

I extend my special thanks to all the members of the research team, including **Prof. Joaquín, Ton and Adrián**. I would also like to express my appreciation to my colleagues **Rodolfo, Aitor, and Victor** for their remarkable efforts in this regard. I am also grateful for the support and camaraderie of my office colleagues, namely **Celia, Luis, Aitor, Angie, Eva, Alain, Manuel and Andrés**. Additionally, I would like to extend my gratitude to our technicians **Fran, Germán, and Charo** for their valuable assistance.

My utmost appreciation goes to my partner and beloved wife, **Basma**. I want to thank her for standing by me during the difficult and challenging times before the good ones. Her patience and support, despite my frequent absence due to living abroad, have meant the world to me. As I conclude this chapter in my life, a new one opens in the company of our lovely children, **Omar, Fayroz, and Farida**. Their presence and unconditional love bring me immense joy and fulfillment. Finally, I want to express my deepest thanks to my father, my mother, my sisters, and my brother. Their encouragement and extreme support have been the driving force behind my accomplishments in this chapter of my life. I am eternally grateful for the life values they have instilled in me and for their infinite belief in my abilities.

Abstract

Boosting the production and the direct utilization of renewable energy sources is considered a key solution in the energy transition process to reduce the dependency on fossil fuels and mitigate the impacts of climate change. There are several types of renewable energy sources, each with their unique characteristics and benefits. Hydropower is considered the largest producer of renewable electricity all over the world. The hydropower sector represents around 16 % of the global electricity production, more than all other renewables combined.

The process of harvesting hydrokinetic energy involves capturing energy from various sources such as tides, ocean currents, or river flow. Vertical-axis hydrokinetic turbines (VAHTs) are considered economical and reliable options to harness the flow currents, specifically for distributed electricity generation. The simplicity in the design and the insensitivity to the flow direction, make VAHTs a viable technical and economical choice. However, the straight-bladed VAHTs are often designed for relatively high water velocities.

This dissertation addresses the design and characterization of small vertical-axis hydrokinetic turbine for low flow velocities. The blade profile, solidity and aspect ratio of the turbine model have been selected looking for a self-starting and efficient operation. The turbine model has been fabricated using the additive manufacturing technology precisely at a fraction of the cost offered by traditional machining technologies. Experimental Tests have been performed in an open channel rig, with inlet velocities ranging from 0.33 m/s to 0.69 m/s . The experimental characterization allows to assess the effect of different parameters, including the turbine blockage on the overall performance of the turbine.

A numerical complementary study to the experimental previous one has been carried out. It outlines an intensive three-dimensional multiphase simulation of the turbine model under free-surface variations to investigate the interactions between the turbine rotor and the channel section, including the free-surface. The volume of fluid (VOF) method is applied to simulation air/water interface. In addition, a single-phase three-dimensional simulation, without considering the free-surface, has also been carried out for comparison with the multiphase results, to examine the effect of the free-surface on the turbine output.

Continued with the turbine model assessment, a cost-effective novel method to test the hydrokinetic turbine models under open-field conditions (no blockage effects) has been investigated. experimental tests have been performed in an open-circuit subsonic wind tunnel under open-field conditions. The experimental runs have been carried out using

the same Reynolds number value as in previous water channel experiments, to enable a comparison between the results obtained from both tests. To check the validity of the proposed approach, a theoretical method for correcting the blockage effects -based on the traditional actuator disk theory and adapted for the open channel flow cases- is applied to the water channel tests and compared with the wind tunnel experiments.

Finally, the dissertation has been extended to include the performance enhancement of hydrokinetic turbines, focusing on improving the overall efficiency, by varying the channel geometry. This has been achieved by using an obstacle on the channel bed. By means of experimental and multiphase numerical methodologies, the power output and the flow behaviour have been investigated to evaluate the effectiveness of this approach.

Resumen

Impulsar la producción y la utilización directa de fuentes de energía renovables se considera una solución clave en el proceso de transición energética para reducir la dependencia de los combustibles fósiles y mitigar los efectos del cambio climático. de los combustibles fósiles y mitigar los efectos del cambio climático. Existen varios tipos de fuentes de energía renovables, cada una con sus características y beneficios únicos. La energía hidroeléctrica, incluida la mareomotriz, se considera la mayor productora de electricidad renovable en todo el mundo. electricidad renovable en todo el mundo. El sector hidroeléctrico representa alrededor del 16 % de la producción mundial de electricidad, más que todas las demás energías renovables juntas.

El proceso de aprovechamiento de la energía hidrocínética consiste en captar energía de diversas fuentes, como las mareas, las corrientes oceánicas o el caudal de los ríos. Las turbinas hidrocínéticas de eje vertical se consideran económicas y fiables para ello, concretamente para la generación distribuida de electricidad. La sencillez en el diseño y la insensibilidad a la dirección del flujo, las convierten en una opción viable, técnica y económicamente, incluso en condiciones de baja intensidad mareomotriz o en condiciones de baja velocidad de flujo. Sin embargo, la turbina de eje vertical de álabes rectos suele ser criticada por sus escasas características de autoarranque, especialmente en condiciones de baja velocidad de flujo.

Esta tesis aborda el diseño y caracterización de una pequeña turbina hidrocínética de eje vertical para bajas velocidades de flujo. El perfil del álabe, la solidez y la relación de aspecto del modelo de turbina se han seleccionado buscando un funcionamiento autoarrancable y eficiente. El modelo de turbina se ha fabricado utilizando la tecnología de fabricación aditiva con precisión a una fracción del coste ofrecido por las tecnologías tradicionales de mecanizado. Las pruebas experimentales se han realizado en un equipo de canal abierto, con velocidades de entrada que oscilan entre 0.33 m/s y 0.69 m/s. La caracterización experimental permite evaluar el efecto de diferentes parámetros, incluido el bloqueo de la turbina, sobre el rendimiento global de la misma.

Se ha realizado un estudio numérico complementario al experimental anterior. Se esboza una simulación multifásica tridimensional intensiva del modelo de turbina bajo variaciones de superficie libre para investigar las interacciones entre el rotor de la turbina y la sección del canal, incluida la superficie libre. El método de volumen de fluido (VOF) se aplica a la simulación de la interfaz aire/agua. Además, también se ha realizado una

simulación tridimensional monofásica, sin considerar la superficie libre, para compararla con los resultados multifásicos y examinar el efecto de la superficie libre en el rendimiento de la turbina.

Continuando con la evaluación del modelo de turbina, se han realizado pruebas experimentales en un túnel de viento subsónico de circuito abierto en condiciones de campo abierto (sin bloqueo). Las ejecuciones experimentales se han llevado a cabo utilizando el mismo valor de número de Reynolds que en los experimentos anteriores con canales de agua, para poder comparar los resultados obtenidos en ambas pruebas. Para validar este enfoque, se aplican dos ecuaciones de corrección del bloqueo a los ensayos en canal de agua para estimar el comportamiento operacional en aguas abiertas y compararlo con los resultados de los ensayos en túnel de viento.

Por último, la tesis se ha ampliado para incluir la evaluación de una turbina hidrocínética basada en el arrastre, centrándose en la mejora del rendimiento global en canales de agua, mediante el uso de un obstáculo en el lecho del canal. Mediante metodologías experimentales y numéricas multifásicas, se han investigado la potencia de salida y el comportamiento del flujo para evaluar la eficacia de este enfoque.

Contents

1	Introduction	1
1.1	Background	1
1.2	The kinematics of Lift-type VAHT	7
1.3	Design Parameters for Vertical-axis Turbines	7
1.4	Self-starting Characteristics	11
1.5	Channel Geometry	13
1.6	Blockage Phenomenon	14
1.7	Analytical and Numerical Approaches	15
1.8	Free-surface Effects	15
1.9	Dissertation Aims and Objectives	16
1.10	Dissertation Outlines	17
2	Design, Fabrication and Experimental Testing of the VAHT	19
2.1	Overview	19
2.2	The Turbine Model Design	19
2.3	Fused Deposition Modeling Process	21
2.4	The Experimental Setup	22
2.5	Measurement and Data Accuracy	26
2.6	Linear Momentum Actuator Disc Theory	27
2.7	Objectives	28
2.8	Peer-reviewed Journal Publication	29
2.8.1	Design and Characterization of a Vertical-axis Micro Tidal Turbine for Low Velocity Scenarios	29
2.9	Journal Metrics	42

3	Multiphase Modelling of the VAHT with Free-surface Variations	43
3.1	Overview	43
3.2	CFD Governing Equations	43
3.3	The Turbulence Model	45
3.4	The VOF Multiphase Model	46
3.5	The Grid Conversion Index Method (GCI)	47
3.6	Objectives	49
3.7	Peer-reviewed Journal Publication	50
3.7.1	Experimental and Multiphase Modeling of Small Vertical-axis Hydrokinetic Turbine with Free-surface Variations	50
3.8	Journal Metrics	65
4	Open-field Testing Experiments: Wind Tunnel Case	67
4.1	Overview	67
4.2	The Wind Tunnel Configuration	67
4.3	Blockage Phenomenon and Correction Formulas	71
4.4	Objectives	72
4.5	Peer-reviewed Journal Publication	73
4.5.1	Wind–Water Experimental Analysis of Small SC-Darrieus Turbine: An Approach for Energy Production in Urban Systems	73
4.6	Journal Metrics	89
5	Efficiency Enhancement Varying the Channel Geometry	91
5.1	Overview	91
5.2	The Turbine Model Configuration	91
5.3	The Numerical Model	94
5.4	Objectives	95
5.5	Peer-reviewed Journal Publication	96
5.5.1	Increased Efficiency of Hydrokinetic Turbines Through the Use of an Obstacle on The Channel Bottom	96
5.6	Journal Metrics	111

6	Results and General Discussion	113
6.1	Overview	113
6.2	Experimental Assessment of the Turbine Model	113
6.3	Turbine Modeling with Free-surface Variations	116
6.4	Open-field Testing Approach	121
6.5	Efficiency Enhancement Experiments	123
7	Conclusions and Future Work	125
7.1	Conclusions	125
7.2	Conclusions (Spanish)	127
7.3	Contributions	130
7.3.1	Contributions of the Dissertation Published in International Journals	130
7.3.2	Contributions of the Dissertation Published in International Conferences	132
7.4	Future Work	133
7.5	Dissertation Funding	133
	Bibliography	135
	List of Figures	145
	List of Tables	147
	List of Acronyms	149
	List of Symbols	151
A	Appendix A	153
A.1	3-D Slicing and Printing Parameters	153
A.2	Simulation Setup	154
B	Appendix B	155
B.1	Houlsby's Analytical Model Equations	155

C Appendix C	163
C.1 Complementary Peer-reviewed Journal Publications	163
C.1.1 Power Performance Assessment of Vertical-axis Tidal Turbines Using an Experimental Test Rig	163
C.1.2 Influence of a Simple Baffle Plate on the Efficiency of a Hydrokinetic Turbine	176
C.1.3 Design and Experimental Performance Characterization of a Three-blade Horizontal-axis Hydrokinetic Water Turbine in a Low Velocity Channel	185
C.2 International Conference publications	195
C.2.1 An Approximation of Using Vertical-axis Tidal Turbine for Water Desalination in the SUEZ Canal Waterway	195
C.2.2 Internet of Energy Applied to Water Hydrokinetic Smart-grids: A Test Rig Example	205
C.2.3 Diagnostic Strategies for Microturbines Operating Status Applied to Predictive Maintenance: Experimental Test Case	215

Chapter 1

Introduction

1.1 Background

The recent string of crises highlights the urgency of expediting the shift towards a global energy system that is sustainable and diversified [1]. The world economy is suffering from the consequences of relying heavily on fossil fuels, as seen by the skyrocketing prices of oil and gas and the ongoing instability in Ukraine. The COVID-19 pandemic has only exacerbated the situation, causing economic hardship and concerns about energy affordability for citizens. Meanwhile, the effects of climate change caused by human activities are becoming increasingly visible worldwide.

The energy transition is recognized as a key solution for reducing dependency on fossil fuels and mitigating the impacts of climate change. As described in Fig. 1.1, six crucial technologies that can help attain climate objectives include: 1) Boosting the production and direct utilization of renewable energy sources; 2) Making substantial advancements in energy efficiency; 3) Converting end-use sectors to electricity; 4) Implementing green hydrogen and related products; 5) Integrating bio-energy with carbon capture and storage; and 6) Implementing carbon capture and storage in the final stage of energy use [2].

Actively advancing these technologies can lead to substantial reductions in emissions, helping us reach the target of a net-zero carbon world by mid-century. As by 2050, it is expected to achieve a yearly decrease of 36.9 Gt of CO_2 emissions. Boosting the production and direct utilization of renewable energy sources is considered one of the most effective ways in the energy transition process, which can help to reduce the dependency on fossil fuels, decrease greenhouse gas emissions, and promote energy security.

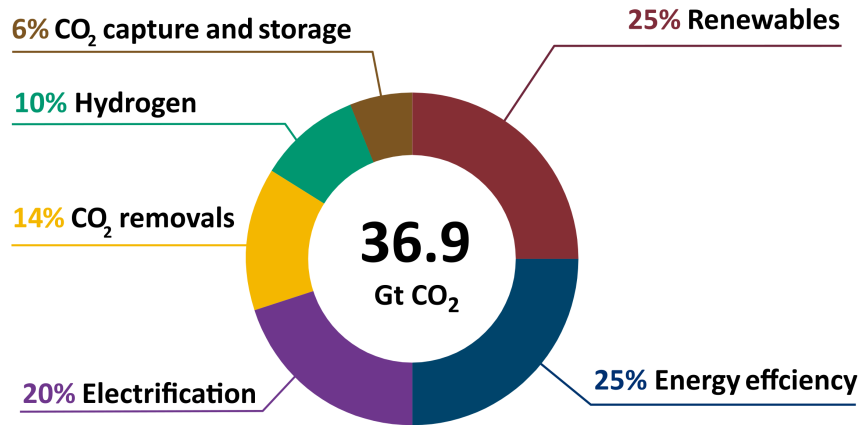


Figure 1.1: The energy transition vision for 2050 [2].

In 2021, China maintained its dominance in boosting the production of renewable energy, accounting for 46 % of global renewable capacity additions as illustrated in Fig. 1.2. The European Union also is one of the largest markets for increased capacity, surpassing its previous record set in 2011 for the first time [3]. Although the growth in renewable energy production is relatively limited in the Middle East and Africa (see Fig. 1.2), it is considered a region with abundant potential for renewable energy sources

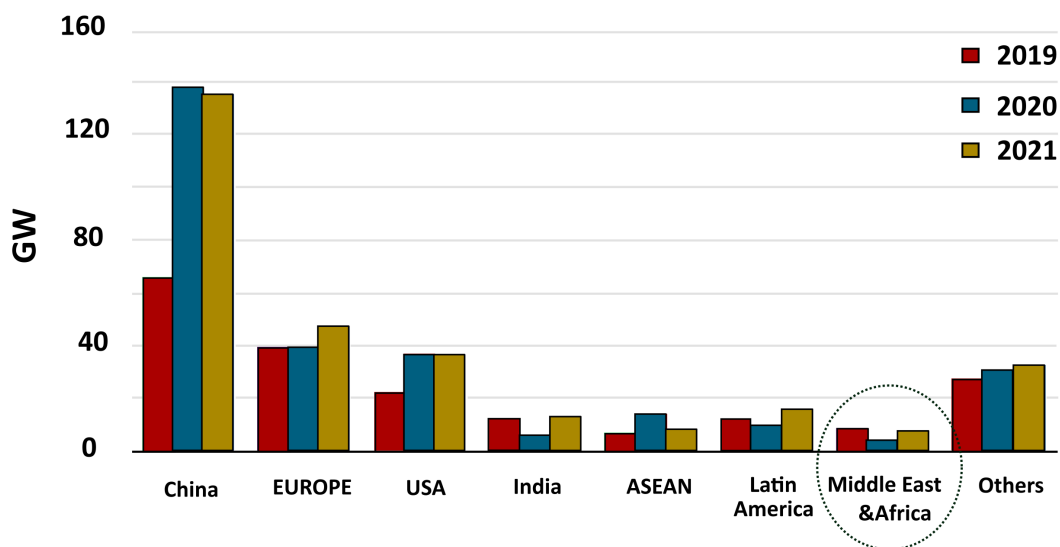


Figure 1.2: Renewable net capacity additions by region, 2019-2021 [3].

The growth of African economies is driving up energy demand and the need for more sustainable and resilient energy systems. Despite having significant potential for renewable energy, the Middle East and Africa currently only account for 3 % of global installed renewable generation capacity. This leaves ample opportunity for growth in the deployment of clean energy in that region. Innovative technologies and solutions should be utilized to speed up the energy transition and attract investment in climate change mitigation and adaptation [4].

Despite its vast potential, the use of renewable energy sources in Egypt remains also limited. Approximately 12% of Egypt’s energy production originates from renewable energy sources, with a combined capacity of 24 *MWh* [5]. As illustrated in Fig. 1.3, most of this renewable power is generated through the hydro/marine sector, boosting a capacity of 15 *MWh*. Solar power follows closely, accounting for 4.5 *MWh* of renewable energy production. Finally, wind power holds the third rank with a production capacity of 4.2 *MWh*. Meanwhile, the remaining energy production in Egypt comes from the utilization of fossil fuels.

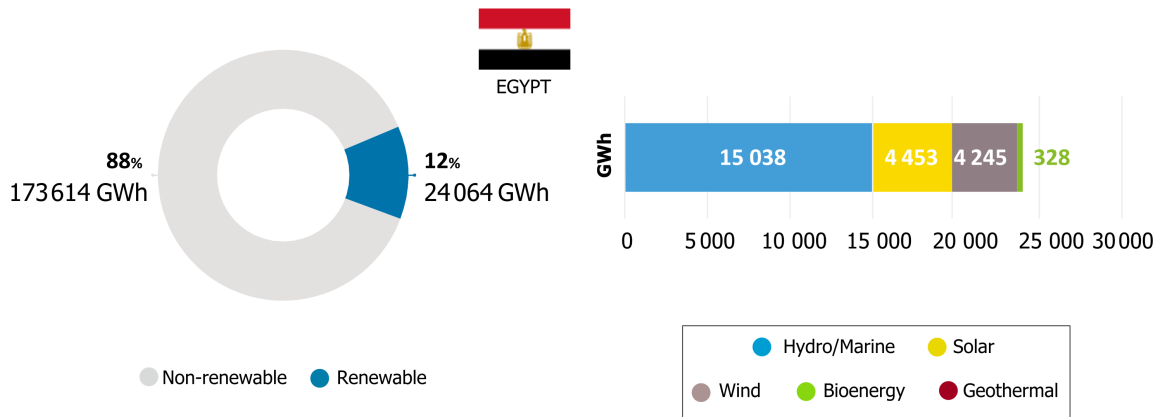


Figure 1.3: Fossil and Renewable electricity generation in Egypt 2022 [5].

One of the main reasons for the limited use of renewable energy sources in Egypt is the lack of investment in this sector. In 2016, Egypt made a commitment to move towards clean energy and has set a goal to derive 42% of its total electricity generation from renewable sources by 2035. This objective is accomplished through multiple strategies. The Egyptian government has allocated significant resources to develop the renewable energy sector, while also providing financial incentives and subsidies to encourage investment in renewable energy. This includes tax breaks, low-interest loans, and grants for research and development. Furthermore, the Egyptian government invests in the development of infrastructure to support the integration of renewable energy into the existing power network. This can involve upgrading the grid system, building new transmission lines, and providing technical assistance to renewable energy project developers [5].

Egypt, with its unique geographical location between two seas, the Mediterranean Sea and the Red Sea, along with the presence of the majestic Nile River, holds immense potential for harnessing hydro power and tidal current energy. The strategic positioning of Egypt allows for the utilization of both marine and riverine resources to generate clean and renewable energy [6]. The powerful flow of the Nile River presents an opportunity for the installation of hydrokinetic power stations, which can efficiently convert the water flow current into electricity. Moreover, the coastal areas of Egypt are blessed with strong tidal currents caused by the regular ebb and flow of the Mediterranean and Red Seas. By harnessing the kinetic energy of these tides, Egypt can tap into a substantial source of renewable energy, contributing to its sustainable development goals and reducing its

reliance on fossil fuels. With careful planning and investment, Egypt has the potential to become a leading hub for hydro power and tidal energy production in the region, fostering a greener and more energy-efficient future [7].

There are several types of renewable energy sources, each with its unique characteristics and benefits. The most common types of renewable energy sources are solar, wind, hydro, biomass, and geothermal energy. Table 1.1 lists the power capacities of these different sources over the world for three consecutive years [8]. Globally, hydropower is considered the world's largest producer of renewable electricity (see Fig. 1.4). This sector represents around 16 % of global electricity production, more than all other renewables combined, which makes it an ideal complement to modern clean energy systems. The total installed capacity has been reached 1308 gigawatts (*GW*) in 2022, with a record of 4306 terawatt hours (*TWh*) generated [9]. This value will need to grow by around 60 % by 2050 according to the target of a net-zero carbon world. This additional capacity will come not only through the building of new hydropower plants, but also from the research and development of new technologies.

Table 1.1: Renewable power capacity over the world three consecutive years [8].

Year / Power source	2019		2020		2021	
	GW	%	GW	%	GW	%
Hydropower	1,150	44.60	1,170	41.21	1,195	37.98
Solar PV	621	24.08	760	26.77	942	29.94
Wind	650	25.21	743	26.17	845	26.86
Biomass	137	5.31	145	5.11	143	4.55
Geothermal	14.0	0.54	14.1	0.50	14.5	0.46
Solar thermal	6.1	0.24	6.2	0.22	6.0	0.19
Ocean power	0.5	0.02	0.5	0.02	0.5	0.02
Total power [GW]	2,579		2,839		3,146	
Investments [billion \$]	298.4		342.7		365.9	

One of the fields in which this research is focused is the upgrading and modernizing the existing hydropower machines to improve the overall performance and increase the rated output. Another field is the distributed production using the smallest possible infrastructure, especially in areas with low energy concentration. The research presented in this dissertation is framed in this context: the use of small hydrokinetic turbines with low flow currents, which represents an important technological challenge but, at the same time, reflects the most realistic operating conditions.

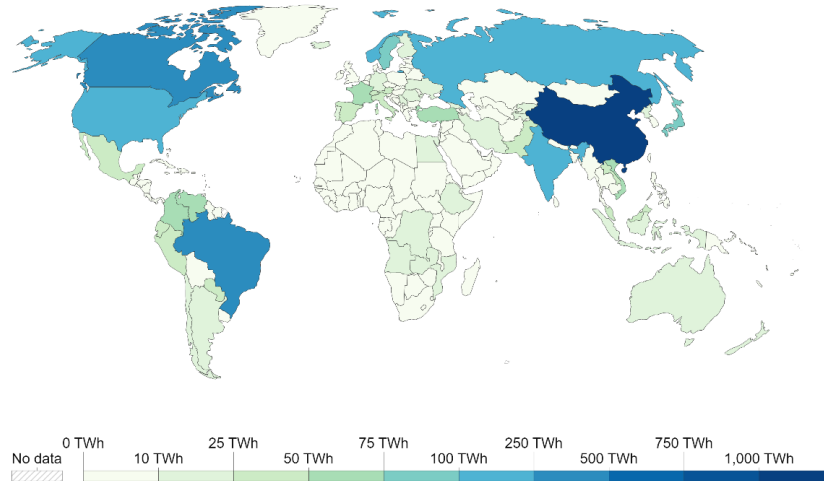


Figure 1.4: Global map of the annual hydropower generation in 2022 [9].

The process of harvesting hydrokinetic or tidal current energy involves capturing energy from various sources such as waves, tides, ocean currents, or river flow. Conceptually, a hydrokinetic turbine machine converts the available kinetic energy of water currents (seawater, rivers, or channels) to useful mechanical power [10]. As presented in Fig. 1.5, hydrokinetic turbines can be divided into two main categories according to the relative position of the axis of rotation and the incoming stream: axial-flow and cross-flow [11]. The axial-flow turbines have a parallel axis and flow, while the cross-flow turbines have a perpendicular axis and flow (see Fig. 1.6).

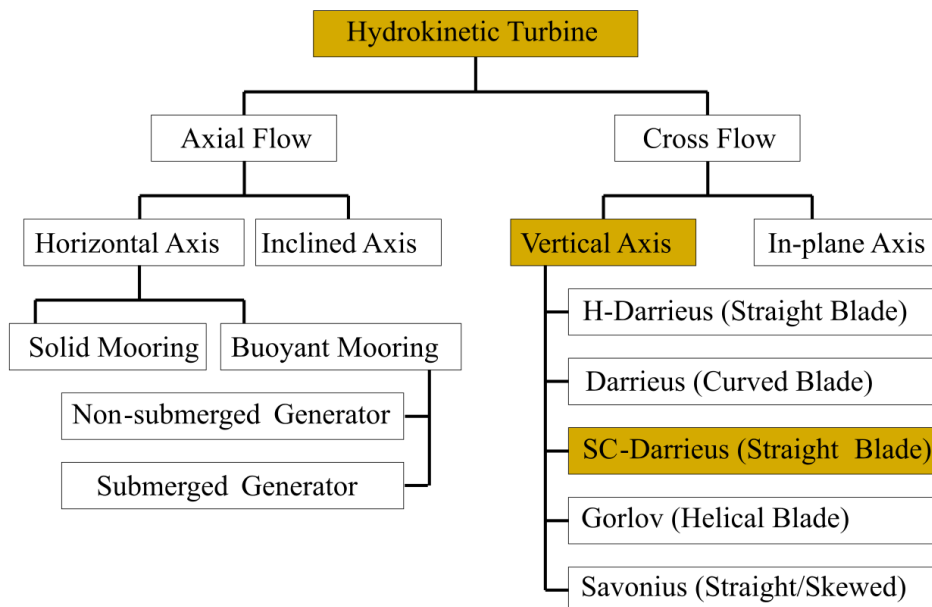


Figure 1.5: Hydrokinetic turbine classifications [11].

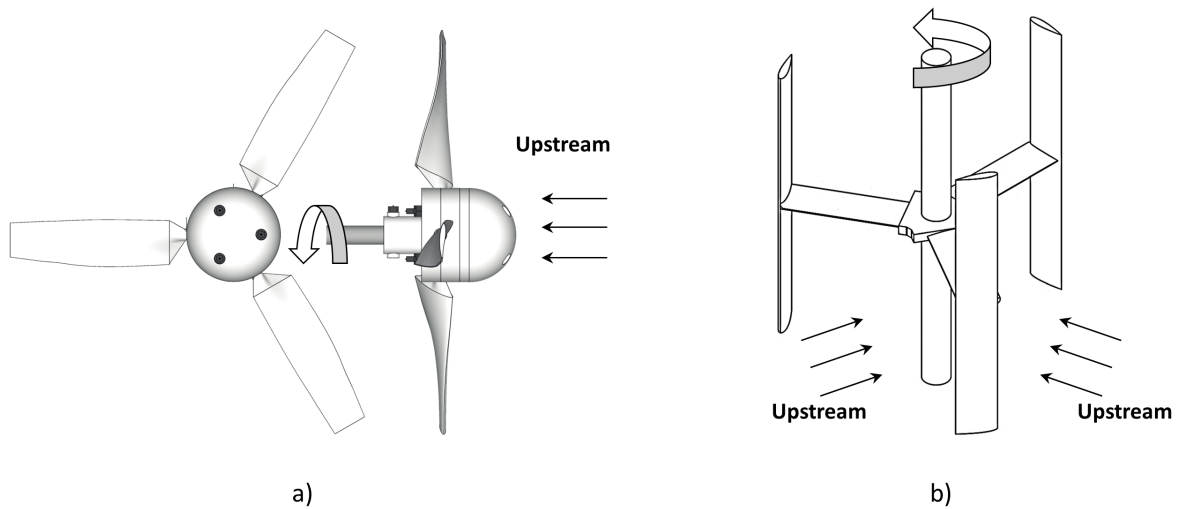


Figure 1.6: Hydrokinetic turbine examples: a) Axial-flow model and b) Cross-flow model.

It is still not evident that the horizontal-axis hydrokinetic turbines outperform the vertical-axis hydrokinetic ones in terms of performance when evaluated fairly. Nevertheless, VAHT has become the subject of research interest in recent years, due to its benefits over HAHT, especially when used in small-scale applications [12]. One of the key benefits of VAHTs compared to HAHT ones is the simplified and cost-efficient blade production process. VAHT blades, being symmetrical and without taper, are simple and inexpensive to manufacture. On the other hand, HAHT blades, being twisted and tapered and often several meters in length, are more complex to produce and transport, resulting in higher costs. Also, there is no need for a yaw mechanism for the VAHTs because the blades are mounted on the rotor in an evenly spaced manner so that the rotor can see the flow current in all directions [13].

Cross-flow turbines are categorized into three categories based on their power generation capability: small, mini, and micro [14]. This study focuses on micro cross-flow turbines with a power capacity of up to 100 kW. These turbines are still in the development phase and various pre-commercial prototypes are being tested with varying capacities, such as the 20 kW "LucidPipe" by Lucid Energy in the US, the 10 kW "En-Current" by New Energy in Canada, and the 1 kW "Sub-merged" by Energy Alliance in Russia [15, 16].

Based on the driving force, the vertical axis turbines can be divided into two categories, lift and drag-based, mainly due to the shape of the blades. Darrieus and Gorlov turbines are widely recognized as lift-based, while the Savonius type is purely drag-based [17]. The category of lift-force based configurations features different types of rotors, with the Darrieus rotor being a common example [18]. This type of rotor has been utilized for wind energy generation for many years [19–21] and can also be applied to harness the kinetic energy of water in rivers [22, 23], oceans [24], canals, and tidal systems [25, 26].

1.2 The kinematics of Lift-type VAHT

The left-based VAHT's working principle is shown in Fig. 1.7, in which the turbine is assumed to turn at a constant rotational velocity (ω). The relative velocity (V_R) is found by combining the upstream water velocity (u_∞) and the blade velocity (u). An interaction occurs once the water approaches the hydrofoil of the rotor blades, resulting in hydrodynamic forces from the pressure and shear distributions on the hydrofoil [27]. These forces are resolved into two components: the drag (F_D) and the lift force (F_L). The lift force of the hydrofoil is primarily due to the pressure difference on its surface and is considered the key force in generating torque and power of these kinds of turbines. However, the drag force generated is relatively small and generally depends on the hydrofoil type.

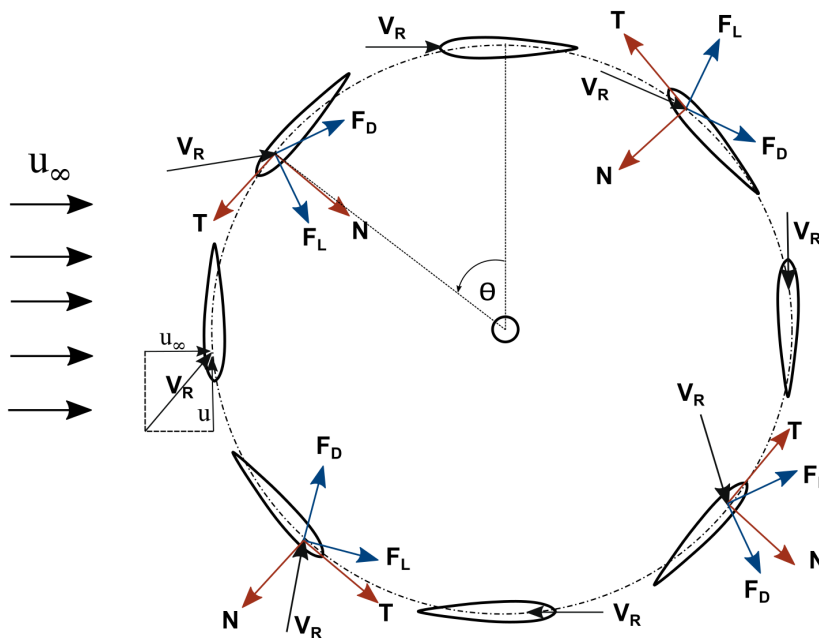


Figure 1.7: The working concept of lift-based vertical axis turbine.

1.3 Design Parameters for Vertical-axis Turbines

Investigating the impact of various geometrical parameters on the VAHTs performance is a topic of interest. Many factors, such as number of blades, blade profile, aspect ratio, and blade solidity, can greatly influence the overall performance and the output of the turbine. The following sections provide a detailed examination of these parameters, with the goal of shedding light on their influence on turbine efficiency. By delving into these parameters in depth, a more nuanced understanding of their impact can be gained, allowing for a more informed approach to turbine design and operation.

- **Turbine Solidity**

The turbine solidity is a dimensionless parameter that represents the ratio of the blade area to the flow passage area through the turbine. It is a measure of the degree to which the turbine blades occupy the flow passage. It is defined as the ratio of the total blade area to the total annulus area through which the working fluid flows. For vertical axis turbines, is calculated as:

$$\sigma = \frac{n \cdot C}{R} \quad (1.1)$$

Where, n is the number of blades, C is the chord length and R is the radius of the turbine rotor. Experimentally, the power coefficient C_p of the vertical-axis turbine (the ratio between the power output and the power available from the flow) is found to rise as the solidity increases, this is valid up to a certain limit, and after that the C_p decrease [28]. However, high-solidity turbines have a better starting capabilities [29]. Specifically, at low tip speed ratios (λ is the ratio between the tangential velocity of the blade tip and the upstream flow velocity) [30]. Additionally, Experiments and numerical simulations [31] have shown that increasing the turbine solidity leads to significant increases in both the static torque and dynamic torque at low flow velocities. The rotor can start easily and operate over a wider range of tip speed ratios, resulting in the ability to harness energy from a broader spectrum of water speeds.

One of the ways to increase the blade solidity is increasing the number of blades, which adds more cost and total weight of the turbine, without a proportional increase in power. So, for low velocity applications increasing the solidity by boosting the blade chord (Fig. 1.8) is much better than increasing the number of blades [32].

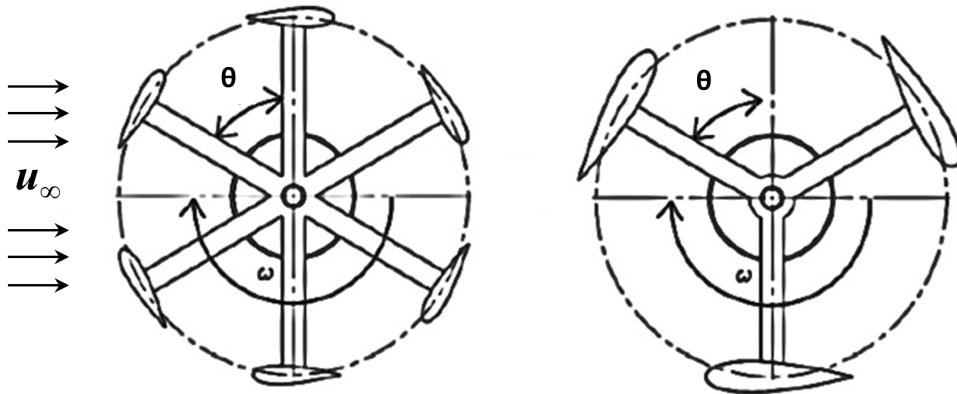


Figure 1.8: Schematic of boosting the solidity through number of blades and chord length [32].

The hydrodynamic performance of VAHTs with a NACA-0015 blade profile has been examined through experimental studies for various solidity values. The maximum power coefficient has been obtained at a high solidity value of 2.0 [33]. The same concept has been applied to the S-1210 non-symmetric blade profile for a range of high solidity values between 1.6 and 2.4 [34]. It has been demonstrated that a high blade solidity leads to enhancing the starting characteristics and increase the power performance of the turbine. The optimal rotor solidity that yields the highest power coefficient and that has been considered in the current study is found to be 2.0.

- **Number of Blades**

It is important to consider the trade-off between performance, efficiency, stability and cost when selecting the number of blades for vertical-axis turbines. The number of blades has a significant effect on both the performance and the stability of the rotor. Usually, increasing the number of blades can rise the power output of VAHTs by capturing more of the kinetic energy in the fluid flow. However, increasing the number of blades results in a decrease in overall performance. This is returned to the interference between the blades and an increase in the produced drag [27].

A one-bladed vertical axis turbine has a simple design, but it is not commonly used because it has low efficiency and is less stable compared to other types of vertical axis turbines [35]. The two-bladed rotors are easier to be manufactured, but produce a higher torque fluctuation and are more susceptible to vibrations. On the other hand, the three-bladed ones have a more balanced distribution of load and are less likely to vibrate [36]. Hence, the three-blade configurations usually are more efficient than other designs with more blades. However, increasing the number of blades decrease the vibrations issues [37].

- **Blade Profile**

The blade profile and thickness determine the flow nature over the blade surface which affects the turbine performance. A well-designed blade profile can increase the lift-to-drag ratio, leading to more efficient energy conversion and higher power output. An optimal blade profile should balance between maximizing lift and minimizing drag, even at higher angles of attack, while also considering the mechanical constraints of the blade.

Numerically, the features of a wide range of symmetrical and non-symmetrical profiles (see Fig. 1.9) have been investigated [38,39]. Increasing the blade thickness broadens the range of tip speed ratios, in which the turbine operates efficiently and effectively extracts more energy [40]. However, if the thickness is excessively increased, the drag becomes unreasonably high, and the power coefficient values drop significantly [41]. hence it is recommended an intermediate profile which combines both advantages. The NACA 4-digit series is commonly used for vertical axis turbines, demonstrating good performance in air and water [42, 43]. Under low Reynolds number conditions, a comparison of three symmetrical airfoils of 12%, 15%, and 18% thickness finds that the NACA-0015 airfoil

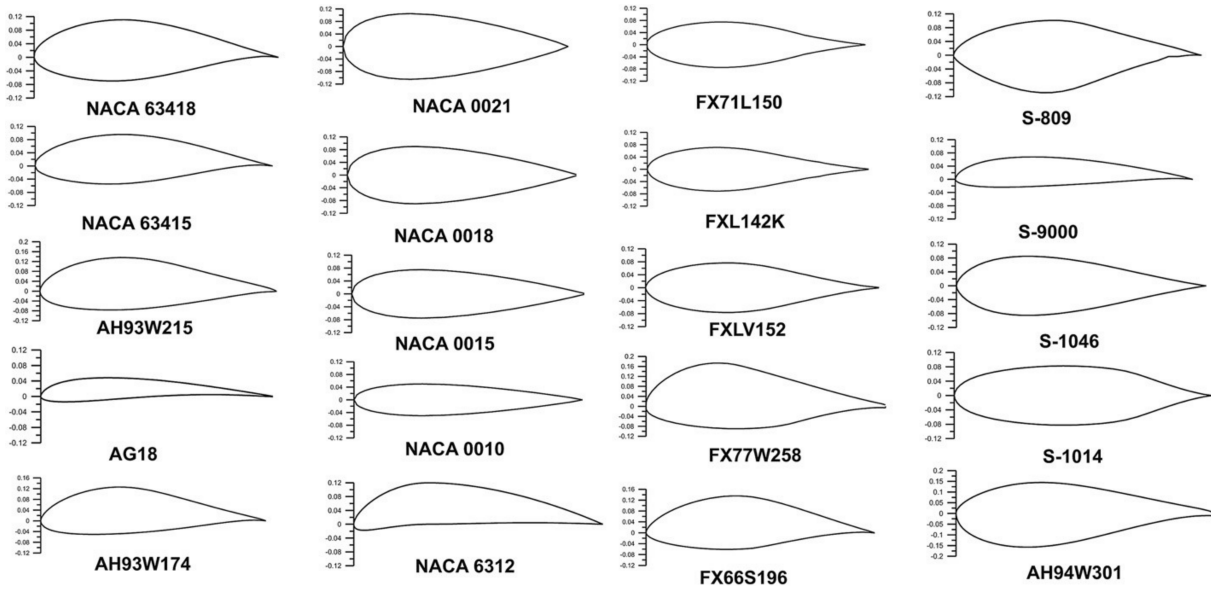


Figure 1.9: Different configurations of symmetric and non-symmetric airfoils. [39].

produces the highest performance [44]. Additionally, a comparison between the non-symmetrical profiles DU-06-W-200 and S1046, and the symmetrical ones of NACA-0012 and NACA-0015 has been carried out [45]. The symmetric with zero camber NACA-0015 profile is found to be the optimal selection for the low flow velocity applications.

For high solidity turbines, increasing the thickness of the hydrofoil proves to be advantageous, not just for reducing dynamic separation effects, but also for enhancing the starting and the overall performance. This has been proved based on testing seven different blade profiles from the symmetrical NACA series with a thickness ranging between 8% and 40% [46]. Based on optimization processes, the NACA-0015 has been found to give the best performance with VAHTs, especially for low Reynolds number conditions [47].

• Aspect Ratio

Another parameter to be defined for the vertical-axis turbines is the aspect ratio. It is the ratio between the turbine height to the diameter. This parameter significantly affects the turbine performance, including power and starting characteristics, especially under confined and low flow velocity conditions.

Many investigations have been carried out to determine the optimum value of this ratio for vertical-axis turbines. For instance, an experimental analysis for three symmetrical-bladed rotor, with high solidity value, has been performed with various rotor aspect ratios ranging from 0.8 to 1.2 under different flow velocities. This rotor is found to give the highest power coefficient of 0.32 for aspect ratio value 1.0. Also, for this value, the turbine exhibits self-starting under all the velocity conditions [34]. The same conclusion for the aspect ratio value has been obtained for another turbine rotor, with different design aspects [20, 48].

Investigations have been extended also to include the unsymmetrical-bladed rotors, namely S815 and EN0005, and one conventional symmetrical of NACA-0018 blade. All the rotors exhibit positive static torque coefficients (indicate that the rotors possess self-starting) and reach higher C_p values at the aspect ratio value of 1.0 [49]. Based on the previous literature, the aspect ratio for the designed model in the current study has been set to 1.0, as it gives the best performance and starting characteristics for low flow velocities.

1.4 Self-starting Characteristics

The straight-bladed vertical axis turbine is often criticized for its poor self-starting features, specifically under low flow velocity conditions, which is considered a significant disadvantage. In order to address this concern, various studies have been carried out and numerous suggestions have been put forward.

Hybridization between the drag-based (Savonius) and the lift-based (Darrieus) turbines is one of the proposed solutions to overcome the self-starting issue. This approach merges the advantages of both types to improve overall performance. By combining these two turbines, the hybrid system can start more easily and operate efficiently in a wider range of flow conditions.

This combined system has two potential configurations. In the first one, the Savonius rotor is positioned outside the Darrieus turbine. For the second configuration, the Darrieus blades encompass the Savonius ones. Despite having several benefits such as a simple design, self-starting and easy installation, the hybrid turbine faces the challenge of not having a design that provides the highest efficiency, as the drag resistance is observed for the low velocity conditions [50].

Experimentally, this hybrid system has been tested in a circulating water channel. For a better starting performance, the results conclude that the arm radius of the Darrieus and the Savonius should not be co-axial. Additionally, a reduction of 30 % in the power coefficient is observed in the hybrid system compared to the standalone Darrieus rotor. However, the self-starting abilities of the hybrid system have been improved compared to the standalone Darrieus rotor [51]. The same conclusion regarding the starting characteristics improvements also has been confirmed numerically [52].

The hybridization concept has been also studied experimentally in a towing tank as presented in Fig. 1.10, in which both rotors are assembled to a single axis. To ensure optimal start-up performance regardless of the flow direction of the water, the Savonius rotor is divided into two sections, an upper and a lower stage, with each part having a 90 degree twist angle. This system guarantees the self-start of the system for a flow velocity of 0.5 m/s upwards [53]. A field evaluation of the same configuration, featuring two semi-elliptical Savonius rotor blades and three NACA0015 Darrieus blades, has been also evaluated [54, 55].

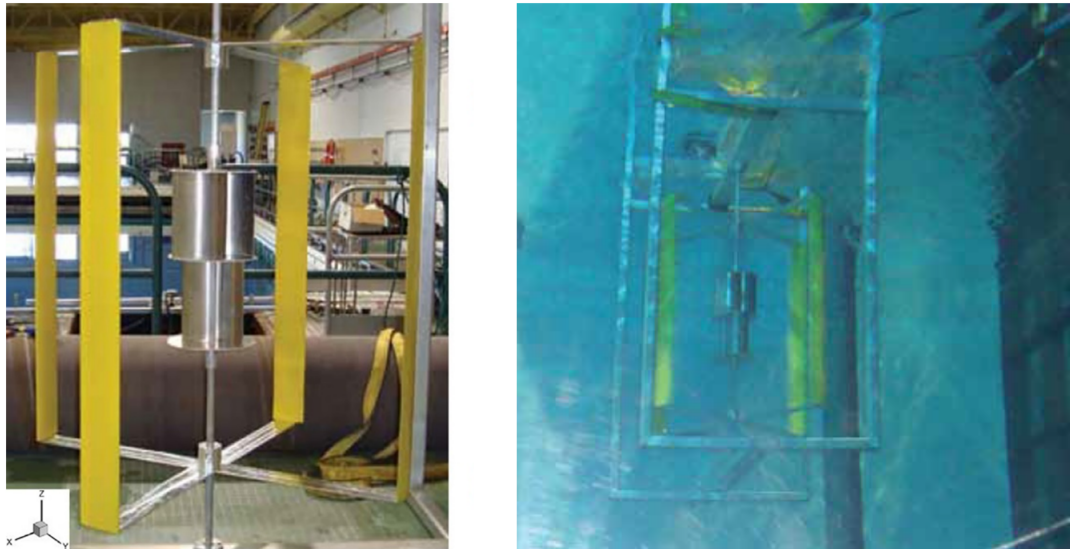


Figure 1.10: The hybrid system configuration and tests inside the towing tank [53].

The hybrid system, in its conventional form, has a low performance due to the additional drag effect on the left-based turbine. The concept of the asynchronous hybrid turbine has been developed to enhance the performance of this hybrid system [56]. In which, each turbine rotates at a unique angular velocity that aligns with its optimal speed for the maximum efficiency. This concept is achieved through the implementation of a planetary gear train in the system as illustrated in Fig. 1.11. Both of the turbines are connected to the outer gears of an epicyclic gear train, and each rotates at a distinct speed based on the gear ratio of the epicyclic gear to which it is linked. The central gear of the epicyclic gear system is connected to the main shaft.

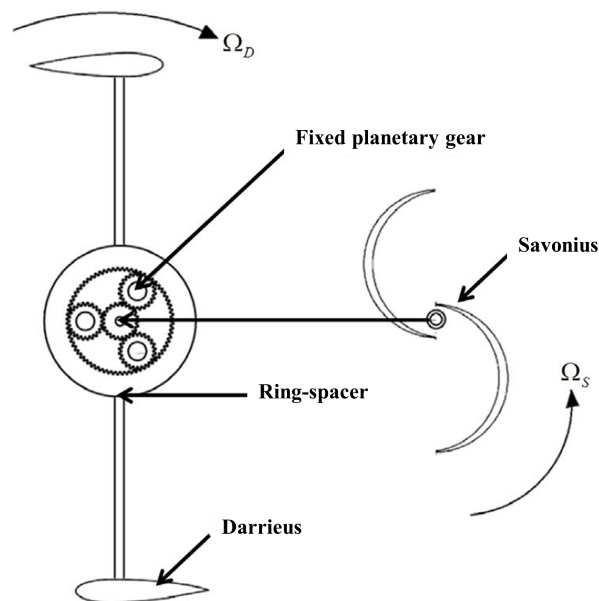


Figure 1.11: Diagrammatic representation of the asynchronous hybrid system [56].

The blade pitching control methodology is one of the offered solutions to overcome the self-starting issue in the VAHTs. It permits the modification of the blade angle of attack in relation to the flow direction (see Fig. 1.12), enabling the generation of adequate torque for the turbine starting. Numerous approaches have been implemented to improve the blade pitching, including both numerical [57] and analytical models [58, 59]. These methodologies have been applied to optimize the turbine overall performance.

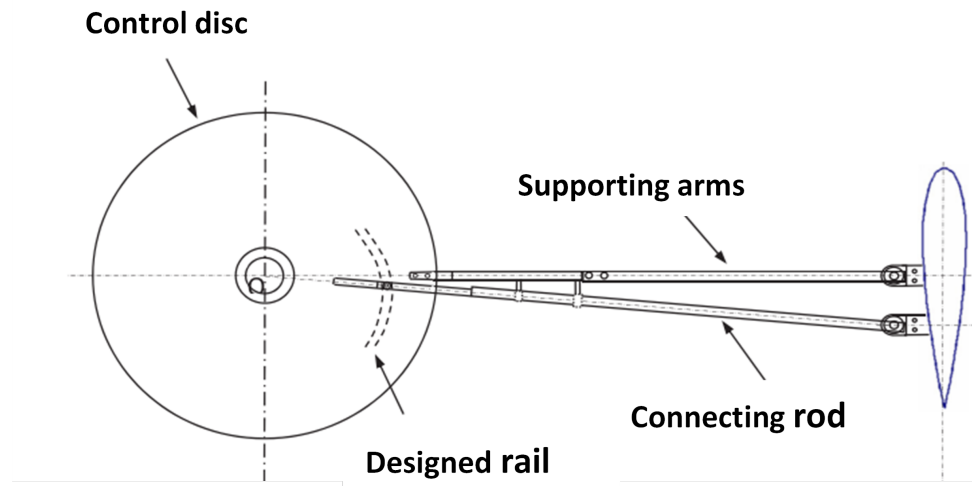


Figure 1.12: Sketch of the pitch control system [60].

The blade sinusoidal pitching is one of the blade pitch control methodologies which aims to enhance the starting performance and the overall output of the VAHTs [60]. In a comparison between a fixed-blade turbine and a variable-pitch one with actively pitched blades, the sinusoidal pitching significantly improves more the turbine starting performance. Selecting the appropriate amplitude for blade pitching enhance the turbine efficiency and at the same time, minimize fluctuations in the power output, the rotational speed, and the torque produced [61]. This approach has been effectively utilized on a 7 kW prototype of significant size, resulting a notable enhancement in the starting characteristics compared to the conventional design [62]

1.5 Channel Geometry

The configuration of the hydrodynamic channel is an important factor in determining the velocity and pressure of the fluid around and inside the turbine rotor, which affecting its overall efficiency. The impact of incorporating an augmentation channel on the straight-blade VAHTs is explored through a comparison between a standalone turbine operating under open-field conditions and another one situated within an augmentation channel (see Fig. 1.13). The study focuses on examining the variations in hydrodynamic forces impacting the blade and the rotor, the power and torque generated by the shaft, and the rotational speed of the turbine. The augmentation channel significantly reduces

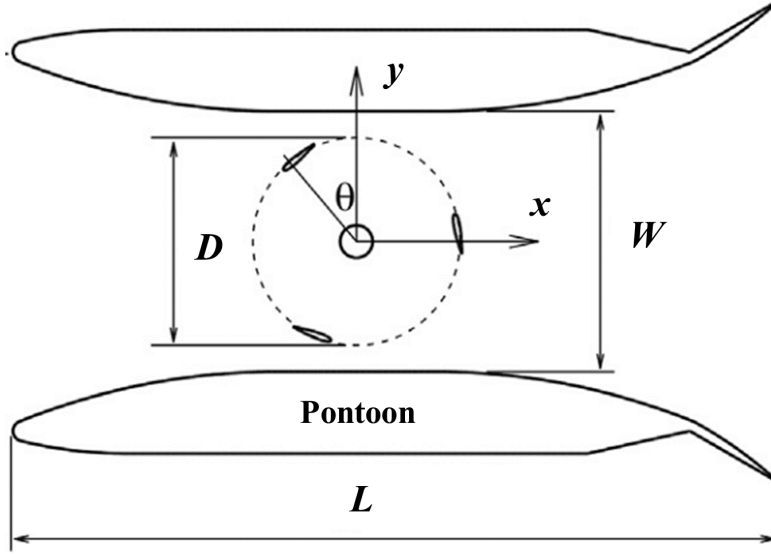


Figure 1.13: Layout of the augmentation channel and the pontoon profile details [61].

the fluctuations of hydrodynamic torques and rotational speed, leading to a more stable and efficient operation of the turbine. In addition, the power output is found to be 30 % greater than a standalone turbine operating in open-field conditions [61]. The same conclusion has been confirmed numerically and experimentally using the bare and shrouded configurations [63]. An extended study of the channel effects has been carried out [64], which considers seven different shapes of the water channels. The velocity and the pressure coefficients have been assessed for each channel shape, which emphasize the importance of considering the shape of the hydrodynamic channel in the design and optimization of hydrokinetic turbines.

1.6 Blockage Phenomenon

Hydrokinetic turbines and their wind-based counterparts are fundamentally different in several key ways. Most notably, hydrokinetic turbines operate in the presence of a free surface with the impact of flow blockage. Usually, wind turbines operate within the atmospheric boundary layer, while the hydrokinetic ones consider the effects of the wall boundary layers. These differences have important implications on the design and the operation of these two types of turbines. The Blockage is a fundamental aspect that affects the operation of hydrokinetic turbines, specifically in narrow channels. This phenomenon has a direct impact on the energy production from the rotor, affecting the turbine efficiency. The flow in a confined channel experiences changes in three main parameters; the velocity of the fluid around the rotor, the pressure changes in the wake, and the longitudinal pressure gradients associated with the boundary layer of the channel. As a result of these changes, an increase in the power and the thrust is obtained compared to the operation in open-field conditions (without any blockage effects) [65].

In order to optimize the performance of hydrokinetic turbines, it is essential to consider the blockage ratio (B), which is the ratio between the total area of the turbine (A_T) and the cross-sectional area of the channel (A) [66]. Several investigations have been carried out to quantify the effects of blockage on the turbine performance through experimental and numerical methods [67, 68]. Their findings suggest that the impact of blockage is insignificant when values are below 10%. However, an increase in blockage leads to a significant improvement in performance [69].

1.7 Analytical and Numerical Approaches

To improve and optimize the performance of the VAHTs, efficient analytical and numerical calculation tools are essential. On a basic level, various theoretical approaches have been developed to define the actuator disc model in an open channel flow, taking into account the Froude number and the free-surface drop behind the turbine [70] and also the mixing zone downstream [71]. Moreover, the models have been extended to include these effects on the power output from a turbine array [72]. The analytical tools have been developed and extended to be applied as a sub-correction model to evaluate the power available to a turbine array through Depth-averaged simulations [73], as an alternative to the expensive three-dimensional simulations of turbine farms.

On the numerical level, investigations based on the single-phase flow analysis and without considering the free-surface effects, have been carried out to study the flow field around the VAHTs. Typically, these studies solve the Navier-Stokes equations in a domain where the free surface is fixed, using sliding mesh to simulate the turbine rotation, and Reynolds Averaged Navier-Stokes (RANS) turbulence models. It is unusual to find a research using the Large Eddy Simulation (LES) methodology, however it is sometimes employed for specific purposes. For instance, it is used for studying in more detail the turbine wake [74, 75], and to look for the effect of the solidity related to the flow separation at the blades [76]. Regarding the simulation of the turbine, as mentioned above, the method that often gives the best results is the sliding mesh technique. The moving reference frame (MRF) is not usually enough due to the important interaction between the blades and the walls. Although other systems have been applied, such as the immersed boundary [77]. One of the most interesting issues in this type of simulations is the effect of the blockage that results from placing the turbine in a channel of limited dimensions, either as an isolated turbine [78, 79], as a turbine farm [80, 81] or even using flow acceleration elements [61].

1.8 Free-surface Effects

Most of the single-Phase based models are not entirely realistic for precisely evaluating the performance and describing the flow pattern of hydrokinetic turbines in open channels.

This inadequacy stems from their failure to incorporate the variations in free-surface level in their analysis. For instance, Nishi et al. [82] have found that the single-phase simulation of an axial-flow turbine, in a shallow water channel, over-predicts the turbine output by a factor of 2.0 with respect to the multiphase and the experimental results. The multiphase investigations can be grouped basically depending on the topology of the turbines studied. With respect to horizontal axis turbines, it has been studied, among other things, the effect of the closeness to the walls and the free surface on the turbine performance [63, 83], the wake recovery [84], the drop of the free surface behind the rotor [85] or the influence of the proximity to the critical Froude number [86]. There are also studies related to collection devices aimed at increasing the power output [87]. Regarding non horizontal-axis turbines, multiphase investigations of Savonius type turbines [88] and cross-flow ones [69] have focused on exploiting the free-surface simulation to obtain the optimal depth position. Although sometimes, as in the last mentioned article, there is also an in-deep study on the velocity and the pressure fields. Also, in relation to the Darrieus type turbines, the topology with the horizontal-axis (perpendicular to the current), has been the most studied. As before, the influence of the depth and the submersion has been particularly investigated. Some researches have been carried out on the Darrieus turbines inside open channels and their interaction with the free-surface, however this investigations address only the turbine in its horizontal position [89, 90].

1.9 Dissertation Aims and Objectives

Small vertical-axis hydrokinetic turbines are considered economical and reliable for distributed electricity generation. Low initial cost, reliability and ease of installation make them cover all sides of the economic viability triangle in the energy market. The implementation of hydrokinetic turbines in Egypt, specifically in the Nile River, offers tremendous potential for harnessing renewable energy. Moreover, the utilization of these turbines to capture tidal streams in both the Mediterranean and Red Sea presents compelling opportunities for sustainable power generation. As it is evident from ongoing investigations, the hydrokinetic turbines are usually designed for relatively high water velocities. The main challenge addressed by this research is to design and assess a small vertical-axis hydrokinetic turbine that able to rotate and produce energy under low flow velocity scenarios. Also, to present a detailed analysis of the turbine model with a particular emphasis on their performance in open water channels with free-surface variations. The research aims to examine, experimentally and numerically, the impact of various factors such as flow rate, upstream velocity and blockage, on the turbine efficiency. Additionally, tends to explore and evaluate a novel method for enhancing the efficiency of hydrokinetic turbines by varying the channel geometry. The remarkable relevance and significance of this research are evident in the practical applications it enables, paving the way for a greener and more efficient energy landscape in Egypt and beyond.

1.10 Dissertation Outlines

This thesis is organized in seven chapters and three appendices:

- **Chapter 1** introduces the research line of this dissertation, including an overview of the renewable energy resources and recent challenges in the energy sectors. Furthermore, the classification of hydrokinetic turbines is presented, focusing on the vertical-axis one and its design aspects from the literature. Moreover, the objectives and outlines of the dissertation are presented.
- **Chapter 2** presents the turbine model design criteria, fabrication methodology, experimental test rig, and instrumentation. Also, the influence of different parameters, such as flow rate, upstream velocity, and blockage, on turbine performance is presented and discussed. The obtained experimental results in this chapter are compared with the theoretical ones obtained from the selected analytical model. The relation between slope and performance in an inclined channel is also assessed.
- **Chapter 3** characterizes experimentally and numerically the performance of the turbine model under different flow and free-surface conditions. An intensive three-dimensional multiphase model is developed to understand the complex free-surface flow field around the rotor and to clarify its influence on the turbine output. The volume of fluid model is used to track the free-surface air-water interface. Also, the velocity field and the pressure coefficient distribution, around the turbine rotor, are studied and correlated with the free-surface variations from upstream to downstream of the turbine.
- **Chapter 4** discusses a cost-effective novel method to test the hydrokinetic turbine model under open-field conditions (no blockage effects). The experimental runs have been carried out inside an open-jet wind tunnel using the same Reynolds number value as in previous water channel tests. Two blockage correction equations are applied to the water channel tests to confirm the validity of this approach.
- **Chapter 5** focuses on improving the performance of the hydrokinetic turbine through the use of an obstacle on the channel bottom. Experiments have been carried out using two obstacles with different heights. Also, a multiphase model is developed to investigate the impact of the obstacle height on the flow rate passing through the turbine rotor.
- **Chapter 6** highlights the key findings of the study and provides a broad discussion on the extent to which the research objectives are fulfilled.
- **Chapter 7** summarizes the main findings obtained throughout this dissertation and future research lines aimed to improve the addressed methods.

- **Appendix B** includes the detailed explanation and equations of the linear actuator disc theory adapted for open-channel flow (Houlsby's model).
- **Appendix A** presents the additive manufacturing and the CFD parameters used in this dissertation as well as the simulation setup.
- **Appendix C** includes complementary peer-reviewed journal and conference publications conducted during this dissertation.

Chapter 2

Design and Experimental Characterization of The Turbine Model

2.1 Overview

As mentioned previously, operating small-scale vertical axis hydrokinetic turbines under realistic flow velocities remains a challenge. This chapter presents the design aspects of a small-scale VAHT for low flow velocity conditions. Also, the experimental characterization process of the model inside an open-surface water channel and the effect of different operating parameters are presented and discussed.

2.2 The Turbine Model Design

The vertical-axis hydrokinetic model is basically formed by three straight blades, two ending plates, a collet-chuck holding system, and a ball-bearing support as illustrated in Fig. 2.1. The geometrical parameters of the turbine model are provided in table 2.1. These parameters have been carefully selected in order to obtain a self-starting and an efficient operation. Specifically, the NACA-0015 symmetrical airfoil has been chosen due to its good hydrodynamic performance at low Reynolds number [91]. The thickness has been selected based on a comparison between different symmetrical airfoils under low flow velocity conditions [41]. Additionally, the ratio between the turbine height to the diameter (aspect ratio) has been set to 1.0, which has been found to enhance the performance of small turbines under confined conditions [92].

The introduction section of the current study lists several investigations that offer many recommendations to overcome the starting issue. However, most of the proposed

solutions add complexity to the turbine design. Increasing the blade chord is considered the most practical and effective solution for low starting torque. Thus, a blade chord of 0.05 m has been chosen, resulting in a solidity value of 2.0 [34].

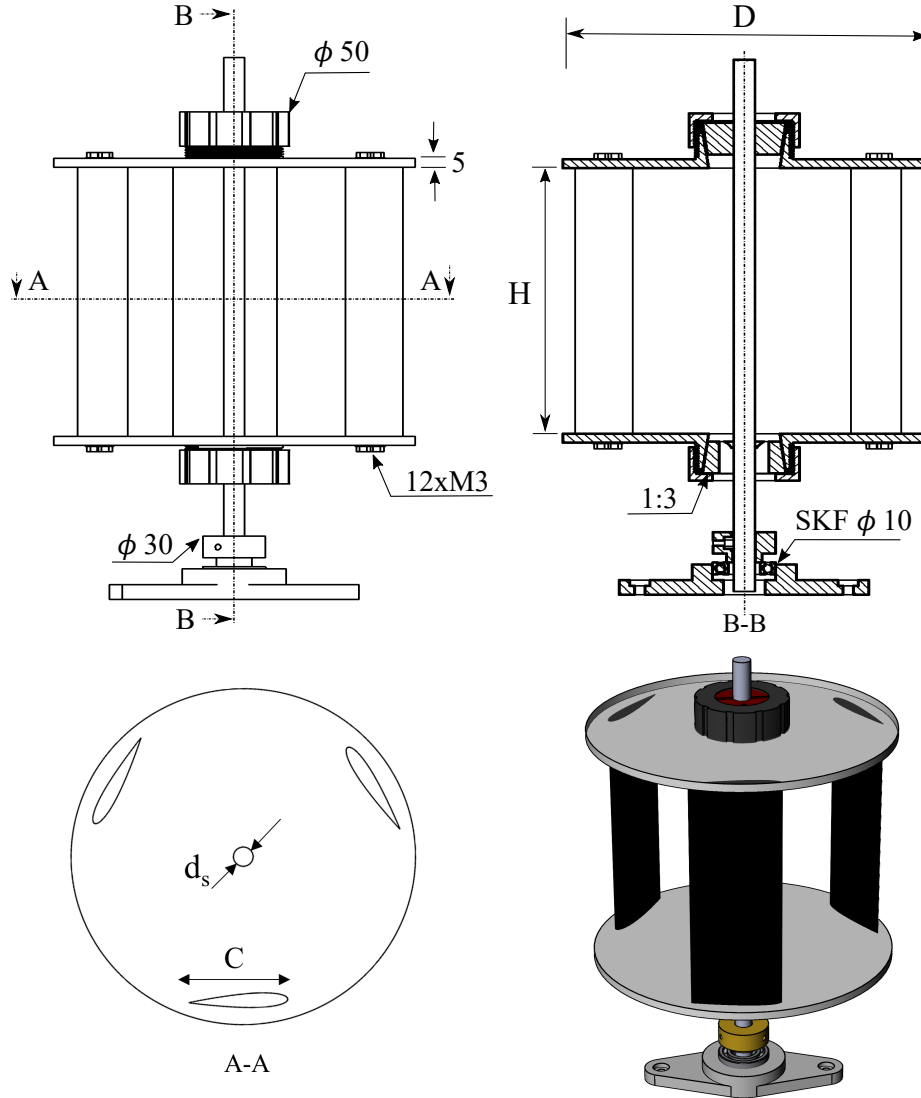


Figure 2.1: A detailed schematic of the turbine model.

Table 2.1: General specifications of the turbine rotor.

Parameter	Specification
Rotor diameter (D)	0.15 m
Blade profile	NACA-0015
Chord length (C)	0.05 m
Solidity (σ)	2
Number of blades (n)	3
Shaft diameter (d_s)	0.01 m

2.3 Fused Deposition Modeling Process

The turbine model has been designed using 3D-CAD software and fabricated through the additive manufacturing technology using Poly-lactic Acid (PLA) material for its high strength and flexibility. The model can be precisely fabricated using the 3D printing methodology at a fraction of the cost offered by traditional machining technologies, as it produces highly accurate models with no need for post-processing or surface finishing. The final quality and surface roughness of the printed parts are controlled by the number and height of the additive layers. To obtain a smooth blade surface, a layer height of 0.1 mm and a printing velocity of 45 mm/s are applied for the current turbine model. More information about the slicing parameters and the printing configurations are provided in appendix A. Snapshots from the slicing software (Ultimaker cura V5.3) and the printing process are shown in Fig. 2.2.

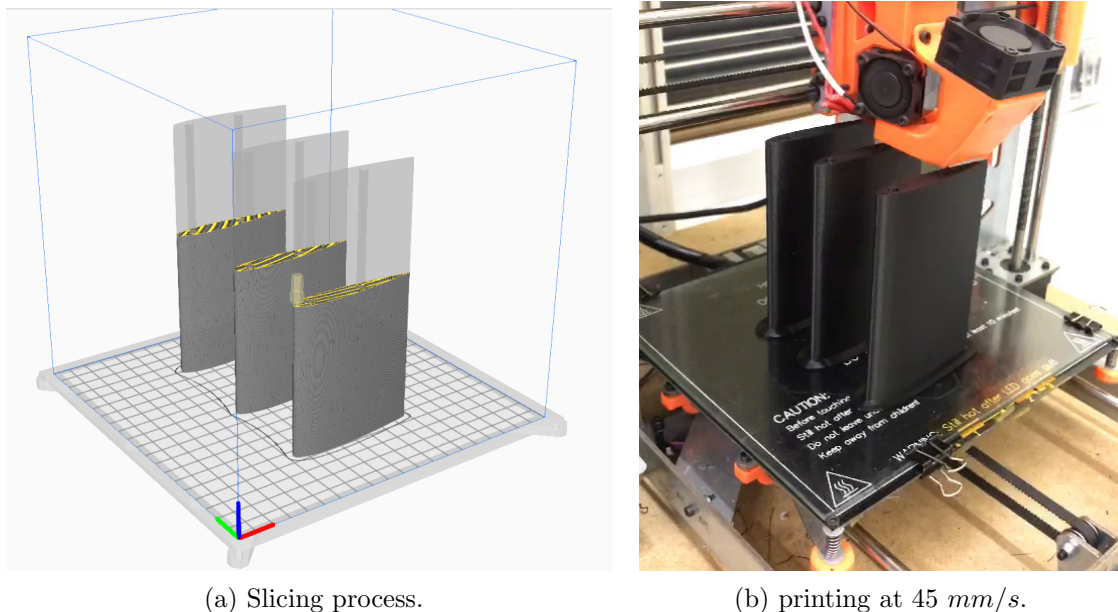


Figure 2.2: Snapshots of the blade profile slicing and printing processes.

The turbine blades have been printed in a vertical position to obtain a uniform blade surface and to reduce the fabrication time for each blade (about 5 hours per blade). Additionally, all the auxiliary components for the turbine and the measuring system (see Fig. 2.3) have been fabricated with the same process using the in-house 3D printers at the university of Oviedo. These components include the bearing holders (Fig. 2.3a), the ending plates (Fig. 2.3b) and the torque sensor (including the brake and the torque transducer) supporting structure (Fig. 2.3c).

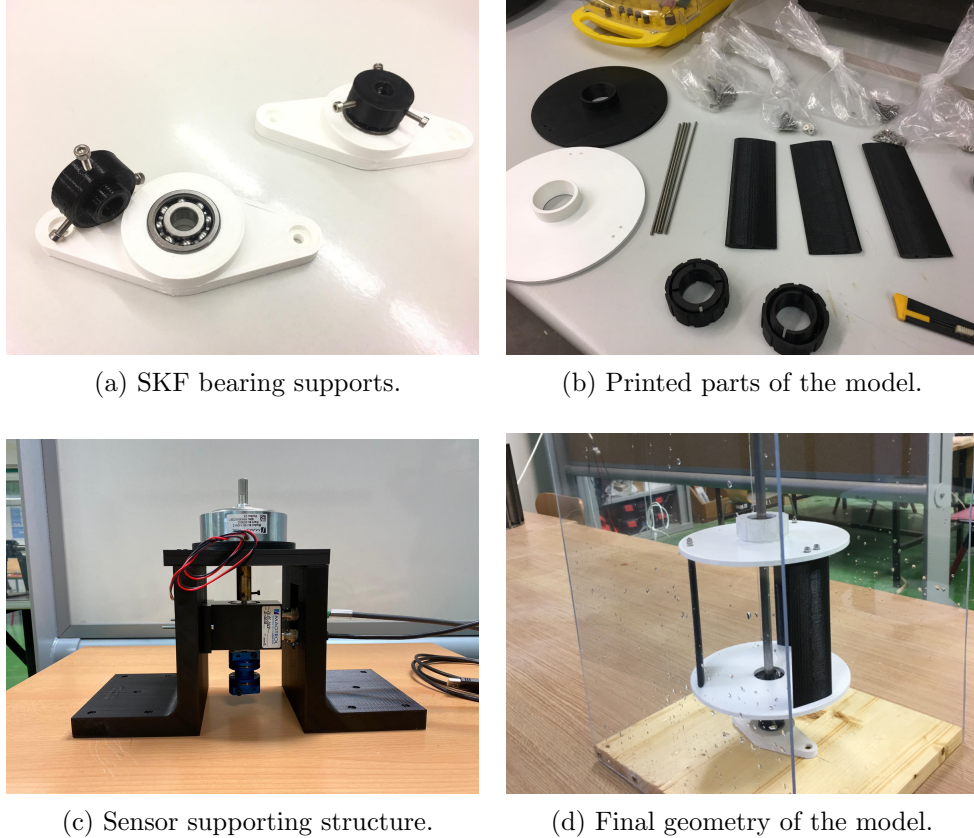


Figure 2.3: Snapshots of the different components of the turbine model.

2.4 The Experimental Setup

Experimental tests have been carried out in an open water channel facility to evaluate the performance of the small VAHT under low flow velocity conditions. As illustrated in Fig. 2.4, the water channel system consists of a rectangular-section glassed channel, with recirculation tanks, pumps and control gate. Also, it contains a brake-torque measuring system governed by a control and data acquisition (SCADA) set-up. This system not only displays but also records both measured and calculated variables. The measured variables include the rotational speed, the water flow rate, the upstream water height, and the mechanical torque. By measuring these values, the calculated variables are obtained including the upstream velocity (obtained by combining the flow rate and water height), the tip speed ratio, the turbine power output and the power coefficient.

The channel is 1.5 *m* long (can be extended to 3.0 *m*) and has a rectangular section of 0.3 x 0.5 *m* with water velocity in the test section ranging between 0.14 *m/s* and 0.9 *m/s*, and with a height regulated by a control gate at the discharge of the channel. The flow is achieved by two 15 *kW* centrifugal pumps, with a combined nominal flow rate of 600 *m*³/*hr*, with a variable velocity frequency regulation. Figure 2.5 shows a photo of the water channel test rig with the measuring instruments.

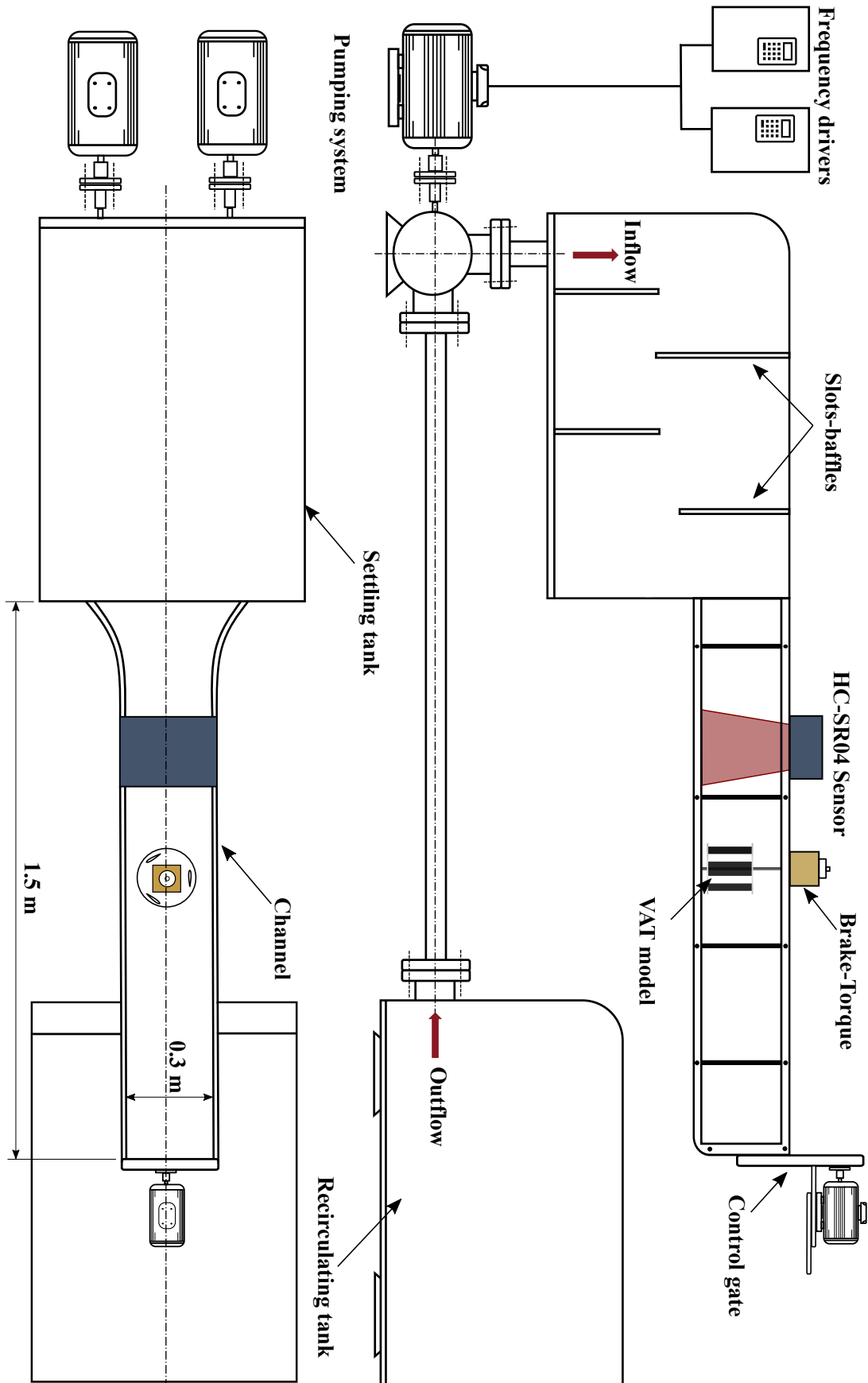


Figure 2.4: A detailed schematic of the experimental test rig.



Figure 2.5: A photo of the water channel with the measuring instruments.

To measure the upstream velocity during the experiment, two techniques have been used in parallel to avoid possible confusions. The first one is by measuring the water depth, considering the possible fluctuations, using an ultrasonic measuring system (see Fig. 2.6) to obtain an average value. It consists of three sensor boards (PIC16F1823 MCU), each board with an ultrasonic sensor (HC-SR04). The water height has been measured several times in different points along the channel and an average value is calculated. Due to the surface fluctuations, the uncertainty of the water average height measurements has been estimated between 0.7% and 1.1%. The second measuring method is by recording channel flow videos using a high-speed camera (1000 fps) and analysing them through a video player that allows to see frame by frame.

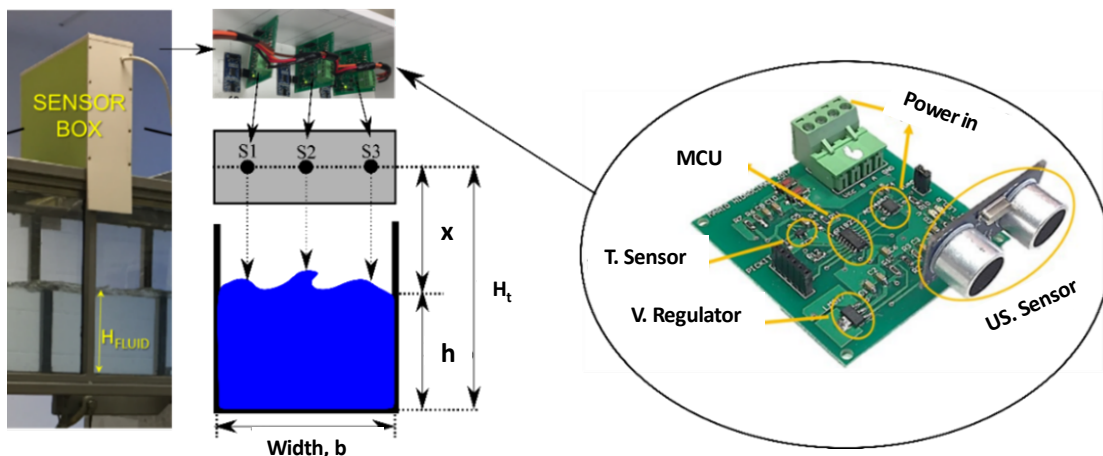


Figure 2.6: The water height measuring sensors.

The brake-torque measuring system as shown in Fig. 2.7 includes the torque transducer with a nominal rate of 0.5 N/m and a maximum measuring value of 1 N/m . It is equipped with two flexible couplings that connect the sensor with the turbine shaft and the brake device. The torque sensor is connected to a voltage source of 24 V and the brake device is controlled through an electrical current load unit. The torque transducer has a high precision torque and rotational speed sensors, combined with a hysteresis brake (Magtrol TS103 and Magtrol HB-140M-2 respectively, with a precision of 0.1% in the torque and 0.015% in the rotating speed). Also, an oscilloscope device is connected to the torque sensor to show the torque wave output by the turbine blades during the power loading process in real-time.

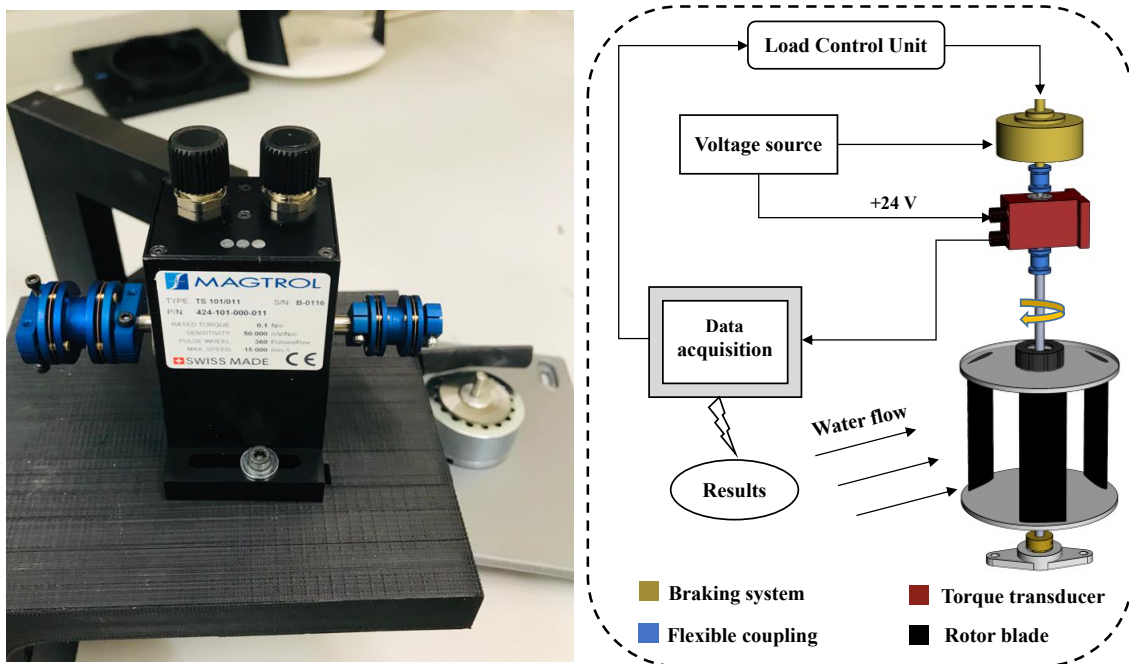


Figure 2.7: The torque sensor measuring and control configurations.

The experimental characterization tests have been carried out using three different flow rates of $0.05 \text{ m}^3/\text{s}$, $0.06 \text{ m}^3/\text{s}$, and $0.065 \text{ m}^3/\text{s}$. For each value, the control gate is employed to obtain different velocities and flow conditions. In this way, for each flow rate, five upstream velocities are selected within the range of 0.33 m/s to 0.69 m/s . Each of these values involves a specific upstream water height and turbine blockage. The experimental measurements allow obtaining the Power and the non-dimensional curves (tip speed ratio and power coefficient) for each operating condition. Also, these experiments allow assessing the effect of different parameters, including the turbine blockage on the overall performance of the turbine.

2.5 Measurement and Data Accuracy

Measurement uncertainty is an essential component in the current experimental work, as it provides an indication of the reliability and accuracy of both the measured and calculated values. The measurement from the torque transducer has been adapted for a sampling frequency of 5,000 samples per second. For each measuring point, the data is stored continuously for a time period of 200 seconds. This has been applied to the measurements of rotational speed, torque, and power output. Then, the average value is determined for each of the measured quantities, and the uncertainty is calculated. Several methods can be used to estimate the uncertainties. In the current experimental study, the standard deviation method has been applied to focus primarily on quantifying the random uncertainties and to characterize the dispersion of the measurements. It provides an indication of the random fluctuations in the measured data, which is calculated as follow:

$$\sigma = \sqrt{\frac{\sum_{i=1}^n (x_i - \bar{x})^2}{n - 1}} \quad (2.1)$$

Where σ is the standard deviation, and n is the number of repeated measurements. The mean value of the measured data is calculated as: $\bar{x} = (x_1 + x_2 + \dots + x_n)/n$. Then, the relative standard deviation σ_r is calculated as follow:

$$\sigma_r = \left(\frac{\sigma}{\bar{x}}\right) \times 100\% \quad (2.2)$$

To consider the surface fluctuations in the upstream height measurements, the experimental runs are repeated 25 times at different points along the channel, and an average value is calculated along with its uncertainty. For the water height measurements, 19 of the 25 repeated runs have a percent difference less than 0.85 % in magnitude from their respective mean value, while the remaining values have a percent difference between 0.94 and 1.15 %. Table. 2.2 lists the different uncertainties in the experimental measurements.

Table 2.2: Measurement uncertainties for the experimental tests.

Parameter	Measuring range	Accuracy	Uncertainty
Upstream height	0.05 : 2 m	0.3 %	±1 %
Rotational speed	1 : 15000 rpm	0.015%	±0.4 %
Torque	0.0001 : 2 N.m	0.05%	±0.6 %
Angle	0°: 360°	0.01 %	±0.25 %

For the calculated variables, the uncertainty is about 1.15 % for the upstream velocity and λ , around 0.12 % for the power measurements and 3.5 % for the power coefficient.

2.6 Linear Momentum Actuator Disc Theory

To further explore the phenomena in the present study, the experimental results are compared with the calculations of the Linear Momentum Actuator Disc Theory (LMADT) adjusted for open channel flow [71] (see Fig. 2.8).

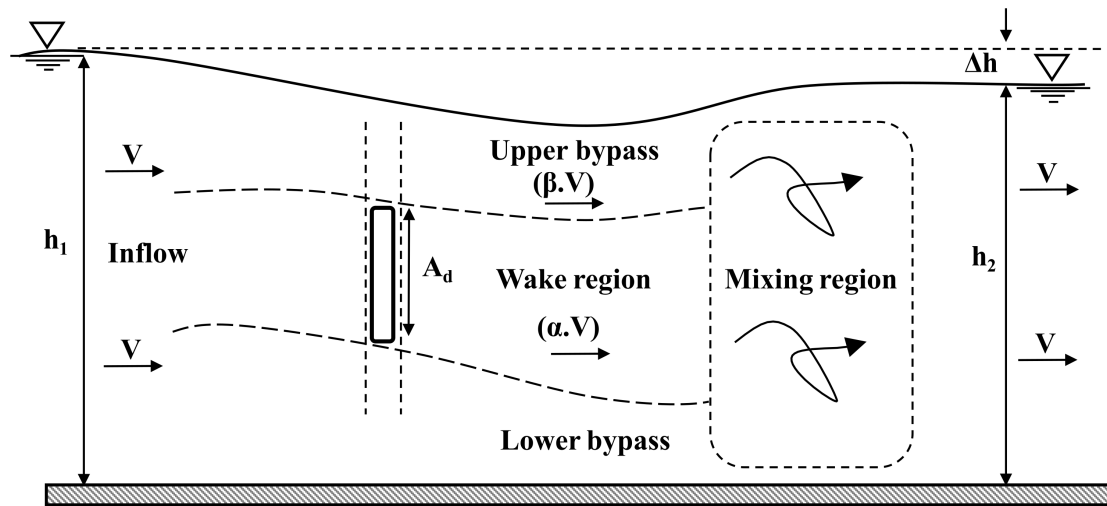


Figure 2.8: One-dimensional LMADT in an open channel flow.

This model avoids the previous limitations [70], as it considers the free-surface drop and the mixing zone downstream the turbine rotor. It uses the following assumptions:

- The actuator disc is inside a frictionless open channel with a flat seabed.
- Subcritical flow at the inlet.
- The flow is divided into two stream tubes: core flow and bypass flow around the actuator disc.
- Uniform flow and hydrostatic pressure at upstream and far- downstream zones.
- Mixing zone of the wake and bypass flow downstream the disc.

The detailed derivations of the analytical model are presented in the appendix B.1. The calculation sequences are started by specifying both the non-dimensional upstream Froud number ($F_r = u_1/\sqrt{gh_1}$) and the blocking ratio ($B = A_T/A$), where u_1 and h_1 are the upstream velocity and height, and A_T and A are the turbine and the channel cross-section areas. Also, the turbine wake flow velocity coefficient (α_4) is specified with a positive value and lower than one. The model dimensionless quantities are then calculated through the following equations:

$$\begin{aligned} \frac{F_r^2}{2} \beta_4^4 + 2\alpha_4 F_r^2 \beta_4^3 - (2 - 2B + F_r^2) \beta_4^2 - (4\alpha_4 + 2\alpha_4 F_r^2 - 4) \beta_4 \\ + \left(\frac{F_r^2}{2} + 4\alpha_4 - 2B\alpha_4^2 - 2 \right) = 0 \end{aligned} \quad (2.3)$$

Once the value of the bypass flow velocity coefficient (β_4) is determined, the turbine flow velocity coefficient (α_2) is computed from the subsequent equation:

$$\alpha_2 = \left(2(\beta_4 + \alpha_4) - \frac{(\beta_4 - 1)^3}{B\beta_4(\beta_4 - \alpha_4)} \right) / \left(4 + \frac{(\beta_4^2 - 1)}{\alpha_4\beta_4} \right) \quad (2.4)$$

Henc, the dimensionless thrust coefficient (C_T) and the free-surface drop (Δh) are calculated as follows:

$$C_T = (\beta_4^2 - \alpha_4^2) \quad (2.5)$$

$$\frac{1}{2} \left(\frac{\Delta h}{h} \right)^3 - \frac{3}{2} \left(\frac{\Delta h}{h} \right)^2 + \left(1 - F_r^2 + \frac{C_T B F_r^2}{2} \right) \frac{\Delta h}{h} - \frac{C_T B F_r^2}{2} = 0 \quad (2.6)$$

Therefore, the power coefficient including the losses in the mixing zone ($C_P + C_{PW}$) is calculated:

$$C_P + C_{PW} = \frac{1}{B} \left(1 - \left(\frac{1}{1 - \Delta h/h} \right)^2 + \frac{2\Delta h/h}{F_r^2} \right) \quad (2.7)$$

Finally, the efficiency of the turbine (η) is determined:

$$\eta = \frac{C_P}{C_P + C_{PW}} \quad (2.8)$$

2.7 Objectives

The ongoing investigations reveal that hydrokinetic turbines are typically designed for water velocities that are relatively high. This chapter presents the design criteria, the fabrication methodology and the experimental characterization of a small-scale vertical axis hydrokinetic turbine for low flow velocities. The influence of different parameters including the water flow rate, the upstream velocity, and the blockage on the turbine performance is to be discussed. The non-dimensional tip speed ratio and power coefficient curves are used to compare the performance of these different parameters. The obtained results are compared with the theoretical ones from the analytical model. Finally, the relation between slope and performance in an inclined channel is to be assessed.

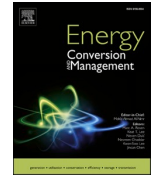
2.8 Peer-reviewed Journal Publication

2.8.1 Design and Characterization of a Vertical-axis Micro Tidal Turbine for Low Velocity Scenarios



Contents lists available at ScienceDirect

Energy Conversion and Management

journal homepage: www.elsevier.com/locate/enconman

Design and characterization of a vertical-axis micro tidal turbine for low velocity scenarios

Ahmed Gharib Yosry^{a,c}, Aitor Fernández-Jiménez^b, Eduardo Álvarez-Álvarez^{b,*},
Eduardo Blanco Marigorta^a

^a GIFD Group, Energy Department, University of Oviedo, C/ Wifredo Ricart s/n, Gijón, Spain

^b Hydraulic R&D Group, EP Mieres, University of Oviedo, Mieres, Spain

^c Mechanical Power Department, Faculty of Engineering, Port Said University, Egypt

ARTICLE INFO

Keywords:

Micro tidal turbine
Cross-flow hydrokinetic turbine
Low flow velocity
Turbine blockage

ABSTRACT

Small tidal turbines are considered economical and reliable for distributed electricity generation. Low initial cost and ease of installation make them cover all sides of the economic viability triangle in the energy market. However, operating these turbines under realistic tidal velocities remains a great challenge. The work presented herein involves the design and assessment of a micro vertical axis hydrokinetic turbine, operating at low water velocities. The blade profile, solidity and aspect ratio of the turbine model have been selected looking for a self-starting and efficient operation. Thanks to the continuous development in the additive manufacturing technology, the model can be precisely fabricated at a fraction of the cost offered by traditional machining technologies. Experiments have been performed at three flow rates with a range of inlet velocities from 0.3 to 0.7 m/s. Power curves have been obtained for each operating condition, from zero load up to the point of maximum power. Additionally, the non-dimensional tip speed ratio and power coefficient have been used to compare the performance of the different parameters. It has been found that the upstream velocity has the most obvious effect on the turbine performance, and that the peak power coefficient is linked to the intensification in the blockage ratio. Furthermore, the actuator disc theory adjusted for open channel flow has been compared and found in consonance with the experimental results. This theory has also been employed to define the turbine efficiency which, from 0.45 m/s upwards, is over 70%, and as high as 81%. Finally, the performance in an inclined channel has been analysed, finding the correlations of the maximum power points and their corresponding tip speed ratios as a function of the slope.

1. Introduction

The Covid-19 pandemic caused a drop in global electricity production. Despite this, generation based on renewable energy increased, in some countries by more than 45% [1]. Specifically, the hydropower energy sector demonstrated reliability, resilience, and flexibility at the time of global crisis. In this sector, the total installed capacity reached 1308 gigawatts (GW) in 2019, and there was a record of 4306 terawatt hours (TWh) generated [2]. Also, according to the International Renewable Energy Agency (IRENA) 2020 [3], this value will need to grow by around 60% by 2050 to help limit the rise in global temperature. In addition, such growth would help to generate about 600,000 skilled jobs during the next 10 years.

This additional capacity will come not only through the building of

new hydropower plants, but also from the research and development of new technologies. One of the fields in which this research is focused is the upgrading and modernizing the existing hydropower machines to improve the overall performance and increase the rated output. Another field is the distributed production using the smallest possible infrastructure, especially in areas with low energy concentration. The research presented in this article is framed in this context: the use of tidal turbines with low current speeds, which represents an important technological challenge but, at the same time, reflects the most realistic operating conditions.

The exact prediction of energy cost, energy potential and economic viability of tidal turbines depend on four main factors: tidal intensity, channel properties, rotor design and energy market [4]. According to data obtained from prototype installations, the cost of electricity generation with hydrokinetic turbines is between 80 and 125\$/MWh [5].

* Corresponding author.

E-mail addresses: ahmed.gharib@eng.psu.edu.eg (A. Gharib Yosry), edualvarez@uniovi.es (E. Álvarez-Álvarez).

<https://doi.org/10.1016/j.enconman.2021.114144>

Received 15 January 2021; Accepted 6 April 2021

Available online 17 April 2021

0196-8904/© 2021 Elsevier Ltd. All rights reserved.

Nomenclature	
<i>Acronym</i>	
<i>LMADT</i>	Linear momentum actuator disc theory
<i>MPP</i>	Maximum power point
<i>MVATT</i>	Micro vertical axis tidal turbine
<i>PLA</i>	Polylactic acid
<i>TSR</i>	Tip Speed ratio
<i>Symbols</i>	
<i>A</i>	Turbine rotor cross-sectional area, m ²
<i>A_c</i>	Channel cross-sectional area, m ²
<i>A_d</i>	Disc area, m ²
<i>B</i>	Blockage ratio
<i>C</i>	Blade chord length, m
<i>C_p</i>	Power coefficient
<i>D</i>	Turbine diameter, m
<i>d_s</i>	Shaft diameter, m
<i>f</i>	Manning friction coefficient
<i>Fr</i>	Froude number
<i>g</i>	Gravitational acceleration, m/s ²
<i>H</i>	Blade height, m
<i>h₁</i>	Upstream water height, m
<i>h₂</i>	Downstream water height, m
<i>N</i>	Number of blades
<i>n</i>	Rotational speed, rpm
<i>P</i>	Power output, W
<i>Q</i>	Water flow rate, m ³ /s
<i>R</i>	Radius of rotor, m
<i>R_h</i>	Hydraulic radius, m
<i>S</i>	Equivalent slope
<i>T</i>	Torque, N.m
<i>V</i>	Flow velocity, m/s
<i>ρ</i>	Water density, Kg/m ³
<i>α</i>	Wake flow velocity coefficient
<i>β</i>	Bypass flow velocity coefficient
<i>η</i>	Turbine efficiency
<i>Ω</i>	Angular velocity, rad/s
<i>σ</i>	Solidity

This is comparable to the cost of photovoltaic energy in urban areas (63–227\$/MWh), but is still some way from that of wind energy (26–54 \$/MWh) or utility scale photovoltaic energy (29–42\$/MWh) [6]. One of the main advantages of the tidal energy is its predictability, much higher than any other renewable sources. On the other hand, the intensity of the tides is quite variable and depends on the geographical location, lunar cycle, etc. In addition, during the tidal sequence, the velocity oscillates between zero and the maximum in a sinusoidal pattern. Therefore, it is preferable for tidal turbines to start up and perform efficiently at low speeds.

Conceptually, a hydrokinetic turbine machine converts the available kinetic energy of water currents (sea water, rivers or channels) to useful mechanical power. According to the relative position of the axis of rotation and the incoming stream, hydrokinetic turbines can be classified in two main groups, axial-flow turbines (axis and flow are parallel) and cross-flow turbines (axis and flow are perpendicular). In fact, axial hydrokinetic turbines have a design similar to horizontal axis wind turbines. “SeaGen” turbine with 1.2 MW capacity is the world’s first commercial-scale turbine which installed by Marine Current Turbines in Northern Ireland coast in (2008) [7]. It opened the door for more pre-commercial tests, for instance the 1 MW “HS1000” prototype by the European Center of Marine Energy (EMEC) in Orkney, UK in (2011) [8], and the 110 kW “Voith Hydro turbine” prototype that was tested near the South Korean island of Jindo by Voith Company in (2011) [9]. Typically axial turbines are installed in deep water looking for high flow velocities but this require high investments as well as operation, and maintenance costs. [10].

Cross-flow turbines are also based on the vertical axis rotor designs of the wind industry. Despite not being as efficient as axial turbines, the simplicity of the rotor-generator coupling system allows to reduce the construction and maintenance costs which makes cross-flow turbines a favorable option for tidal electricity production. According to their axis position, cross-flow turbines are divided in vertical and horizontal axis turbines [11]. Although, horizontal axis turbines are used for medium and large-scale projects [12], they are not considered as a feasible choice to harness energy in low water velocity conditions [13]. The simplicity in the design and insensitivity to the flow direction, make vertical axis turbines a viable option -technically and economically- even in low intensity tidal conditions [4]. Moreover, their ease of installation and the possibility of grouping them in arrays -maximizing the water flow cross sectional area occupied-make them more suitable for both farm and stand-alone isolated applications [14] compared to axial flow and

horizontal axis turbines [15]. All of the above has encouraged the research to enhance their performance [16] and to optimize numerically and experimentally various characteristic parameters [17].

According to their power capacity, cross-flow turbines are classified into three types: small, mini and micro cross-flow turbines [18]. This investigation focuses on the micro type, which includes those turbines with a power capacity up to 100 kW. These turbines are currently under development and many pre-commercial prototypes are being evaluated with different capacities. For instance, the 20 kW “LucidPipe” turbine manufactured by Lucid Energy in USA [19], the 10 kW “EnCurrent” by New Energy in Canada and the 1 kW “Sub-merged” by Energy Alliance in Russia [20].

One of the major drawbacks of the straight-blade vertical axis turbine is the poor self-starting features. To overcome this issue, several investigations have been carried out offering many recommendations: using Savonius and Darrieus rotors together for making the Darrieus fully self-starting [21], application of directed guide-vane [22] and controlling blade pitch mechanically [23]. Experimentally, the combination between Savonius and Darrieus rotors was widely investigated by Bhuyan et al. [24] for three bladed simple H-Darrieus rotor and a hybrid system with Savonius rotor connected at its center. Also, this methodology was checked numerically by Fertahi et al. [25]. A novel vertical axis turbine with three rotatable auxiliary blades was designed and fabricated by Su et al. [26] used the technique of two turbine combination but with three rotatable auxiliary blades, thus building a cup-shaped cross-section like Savonius rotors. Furthermore, Gundersen [27] tested a vertical axis hydrokinetic turbine in a river with flexible foils allowing the turbine to self-start at low water velocities (more than 0.4 m/s) and reached higher peak power coefficients from 0.2 to 0.37 at low tip speed ratio values ranging from 1.4 to 2.2. In general, it can be said that the combination of Darrieus and Savonius obtains a better self-starting characteristic but reducing the peak performance.

One of the offered solutions to overcome starting issue is increasing the turbine solidity which is calculated as $\sigma = N \cdot C / R$, where N is the number of blades, C is the chord length and R is the radius of the turbine rotor. Singh et al. [28] performed an experimental analysis for high solidity (from 0.8 to 1.2) three-bladed H-Darrieus rotor to evaluate its self-starting characteristics. It was noticed that high solidity gave better starting torque and power coefficient, where the maximum power coefficient of 0.32 was obtained for rotor solidity 1.0. Mohamed et al. [29] also investigated the effect of solidity together with hybrid systems to improve the self-starting ability of two-bladed H-Darrieus rotor. It was

found that the solidity increment (as high as 0.43) improves the self-starting ability of H-Darrieus rotor as it increases the static torque coefficient. Eboibi et al. [30] showed experimentally the effect of solidity at low Reynolds numbers on the performance of a vertical axis turbine, concluding that the higher solidity attained better overall power coefficient and self-starting capability than the lower solidity turbine at low flow velocities. Numerically, Guillaud et al. [31] performed a Large Eddy Simulations (LES) on vertical axis hydrokinetic turbines emphasizing the previous experimental findings about the effect of increasing the turbine solidity on the starting ability.

The operation of vertical axis turbines inside confined tidal channels is attracting more attention than open field conditions as most emplacements have, to some extent, those characteristics. For confined flow conditions there are many influential factors that cannot be ignored, for instance the blockage ratio which represents the turbine occupation of the channel cross-section. Many investigations have studied the blockage effect both experimentally and numerically [32,33]. It was concluded that the blockage influence is negligible for values lower than 10%, but increasing this value showed a noticeable enhancement of the performance. In wide channels, the performance is also boosted by the use of channelling devices [34] which can increase the power coefficient by about 50%. The same influence was recorded for horizontal axis turbines [35]. Additionally, the free-surface position strongly affects the turbine performance inside channels. The maximum value of the power coefficient has been found with the free-surface was just above the turbine level [36]. Furthermore, this coefficient can be multiplied with the blocking of a specific flow region [37].

As it is evident from ongoing investigations, the hydrokinetic turbines are usually designed for relatively high water velocities. Usually, for the most efficient vertical axis hydrokinetic turbines, the minimum self-starting velocity is about 1 m/s. However, many tidal currents do not have a great intensity and, anyhow, during the tidal oscillation, the turbine should work even at the lowest possible velocities. Thus, the challenge addressed by this research is the design and manufacture of a small-scale turbine able to rotate and produce energy under very low flow velocity scenarios. In the following sections the turbine model design criteria and fabrication methodology are presented together with the description of the experimental test rig and instrumentation. The influence of different parameters including flow rate, upstream velocity and blockage on the turbine performance is presented and discussed. Also, the results obtained are compared with the theoretical ones. However, as the actuator disc theory has to be adapted for an open channel flow, the modified theory is described first.

2. Linear momentum actuator disc theory

The available kinetic energy of water currents than can be converted to useful mechanical power (P) is defined as $P = 0.5 \cdot \rho \cdot A \cdot C_p \cdot V^3$ where ρ is the water density, V is the flow velocity (upstream the turbine), A is the area swept by the turbine blades (in front of the incoming stream) and C_p is the non-dimensional power coefficient which represents the fraction of the power extracted by the turbine from the water current. Linear Momentum Actuator Disc Theory (LMADT) was introduced firstly by Betz [38] obtaining the well-known Betz limit for wind turbines that restricts the maximum power coefficient to 59%. However, the adoption of Betz calculations in its standard form were found to be inaccurate for hydrokinetic turbines, as the open-air flow is not constrained by the channel boundaries nor the free-surface.

Different approaches had been carried out to define actuator disc theory models in an open channel flow. The model developed by Garrett & Cummins [39] considered the channel boundaries but it didn't take into account the free-surface drop downstream the turbine. Whelan et al. model [40] corrected the previous model but it didn't consider the mixing zone that occurs in the downstream, which definitely affects the total energy removed from the flow. Finally, Houlsby et al. [41] developed an extension of the LMDAT model that, although more complex,

avoids the previous limitations (Fig. 1).

Houlsby et al. [41] model uses the following assumptions:

- The actuator disc is inside a frictionless open channel with flat seabed.
- Subcritical flow at the inlet.
- The flow is divided into two stream tubes: core flow and bypass flow around the disc.
- Uniform flow and hydrostatic pressure at upstream and far-downstream zones.
- Mixing zone of the wake and bypass flow downstream the disc.

They employ the momentum equation through the actuator disc and mixing zone, and the Bernoulli equation outside them. With these assumptions and relations, they obtain an analytical form of the turbine power output as a function of the upstream velocity V_1 , the turbine area A and several flow dimensionless parameters:

$$P = \frac{\rho V_1^3 A \alpha (\beta + \alpha) [2B\beta(\beta^2 - \alpha^2) - (\beta - 1)^3]}{2B[4\alpha\beta + (\beta^2 - 1)]} \quad (1)$$

where B is the blockage ratio defined as $B = A/A_c$, being A_c the channel cross-sectional area, α is the turbine wake velocity coefficient which represents the velocity reduction in the wake region, and β is the bypass velocity coefficient. These three parameters must fulfil the following quartic polynomial equation:

$$\left(\frac{1}{2}Fr^2\right)\beta^4 + (2\alpha Fr^2)\beta^3 - (2 - 2B + Fr^2)\beta^2 - (4\alpha + 2\alpha Fr^2 - 4)\beta + \left(\frac{1}{2}Fr^2 + 4\alpha - 2B\alpha^2 - 2\right) = 0 \quad (2)$$

where $Fr = V/(gh)^{0.5}$ is the upstream Froude number.

3. Micro turbine model design and fabrication

A Micro Vertical Axis Tidal Turbine (MVATT) model with fixed pitch and straight blades has been designed and manufactured to be tested and characterized in an open surface water channel. A 3D schematic and images of the turbine model are shown in (Fig. 2), with its dimensions given in Table 1. The model consists of two ending plates (i), three untwisted NACA 0015 straight blades (ii), slotted collet holding system (iii) and ball bearing support (iv).

Frequently, the NACA 4-digit series is employed for vertical axis turbines with good performance in air [42] and water [43]. It is also known that, increasing the blade thickness is preferable from the separation point of view, which is one of the most critical phenomena in low velocity scenarios [44]. However, the added drag caused by this thickness will negatively affect the turbine performance, hence an intermediate profile which combine both advantages will be preferable. In a comparison between three different symmetrical airfoils of 12%, 15% and 18% thickness under low Reynolds number conditions, the better results were obtained with NACA-0015 [45]. Also, Kanyako et al. [46] numerically simulated NACA-0015, DU-06-W-200, S1046, and NACA-0018 airfoils and they concluded that NACA-0015 was the optimal sectional profile for low flow velocities. Accordingly, the symmetric NACA-0015 which has zero camber and intermediate thickness, was selected for the designed model.

Another parameter to be defined is the turbine aspect ratio (ratio between the turbine height to the diameter), which significantly affects the turbine performance especially in confined conditions and low flow velocity. In the designed model, the aspect ratio has been set to 1.0, as it was found to give the best performance and the highest tip speed ratio for small turbines [47]. The height and diameter have been selected as 0.15 m in accordance with the dimensions of the test rig utilized in this study.

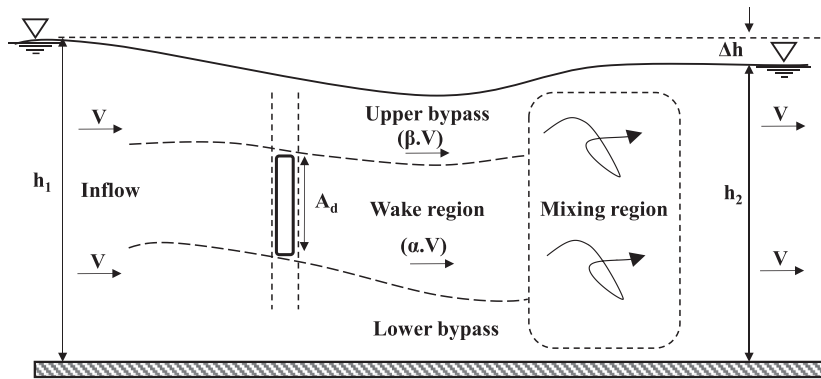


Fig. 1. One-dimensional LMADT in an open channel flow.

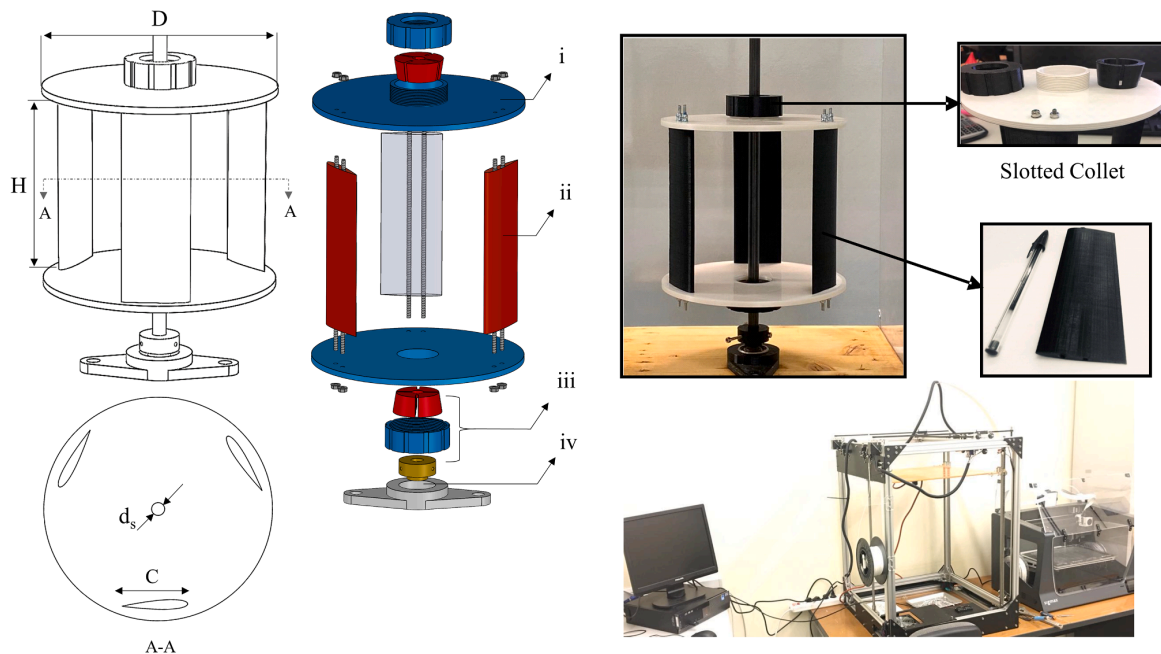


Fig. 2. Schematic and manufacturing details of the turbine model.

Table 1
Geometric parameters of MVATT model.

Parameter	Specification
Rotor diameter (D)	0.15 m
Rotor height (H)	0.15 m
Blade profile	NACA-0015
Chord length (C)	0.05 m
Solidity (σ)	2
Number of blades (N)	3
Shaft diameter (d_s)	0.01 m
Model mass	0.3 kg
Moment of Inertia	0.0052 kg.m ²

Several investigations have been listed in the introduction offering many recommendations to overcome the starting issue. However, most of the proposed solutions add more complexity to the turbine design. Among the simplest ones, increasing the blade chord is considered the most practical and effective solution for the low starting torque.

Especially important for small-scale models where the power to friction ratio is often not enough to start the turbine automatically. Hence, a chord of 0.05 m is considered in the design, resulting a high solidity value of ($\sigma = 2$). Furthermore, two ending plates of 0.15 m in diameter support the turbine blades and improve the hydrodynamic performance. These plates improve the flow in the region close to the blade tip, preventing the leakage from the pressure to the suction side of the blade, and reducing both the tip vortices and the flow in the spanwise direction [48].

The proposed model was designed using 3D-CAD software and manufactured through 3D printing technology using Polylactic acid (PLA) material for its high strength and flexibility. Using the 3D printing technology, time and cost are estimated to be ten times less than using aluminium [49]. It also offers high accuracy and no need for post processing and surface finishing, as the number and height of the additive layers determine the final quality and surface roughness of the printed parts. To increase the blades rigidity, each one has two embedded stainless-steel rods, 3 mm in diameter. Furthermore, the turbine is coupled with the shaft using a slotted-chuck, allowing the turbine to be

positioned at different vertical distances from the channel bed.

4. Experimental test rig and instrumentation

The performance evaluation of the MVATT model under low water velocity conditions has been carried out in a recirculating hydraulic channel at the Polytechnic Engineering School of Mieres (University of Oviedo). This channel (Fig. 3.) includes: pumping system, recirculation tanks, control gate, a rectangular section channel, and a brake-torque arrangement coupled with a control and data acquisition (SCADA) system.

Water recirculation is provided by two 15 kW centrifugal pumps (1), each with a nominal flow rate of 300 m³/h, controlled by two drive converters (2). The water flows from the settling tank (3) through the glass channel and falls into the recirculating tank (4) at the end. The channel (5) has a rectangular section (0.5 m high, 0.3 m wide and 1.5 m long) obtaining flow velocities varying from 0.14 m/s to 0.9 m/s at maximum flow rate. The control gate (6) located at the channel discharge regulates the different operating conditions.

The brake-torque arrangement consists of an integrated high precision torque and rotational speed sensor (7) Magtrol TS103 (0.5 Nm of rated torque, accuracy <0.1% and 1,5000 rpm max. speed, accuracy <0.015%) and a hysteresis brake Magtrol HB-140M-2 controlled by DC current. They are mechanically connected to the turbine shaft through flexible couplings (Fig. 4). To obtain the water height, three ultrasonic sensor (HC-SR04) are used, covering the width of the channel. They have a testing range from 0.05 to 2 m and a precision of 0.001 m. To take into account the surface fluctuations, the water height is measured several times in different points along the channel and an average value is calculated. This value is contrasted with the one found from the analysis of the high-speed camera videos (1000 fps). The uncertainty of the water height measurement, including the fluctuations is between 0.7% and 1.1%. A dedicated controller, connected to the sensors and drivers, is used to run the SCADA software managing the experiments. The SCADA also visualizes and stores measured and calculated variables. The measured ones are: rotational speed n , water flow rate Q (through the calibration of the pumps rotating speed), upstream water height h and mechanical torque T . The calculated ones are: the upstream velocity (obtained from the flow rate and the water height), tip speed ratio $TSR = \Omega.R/V$ (ratio between the tangential velocity of the blade tip and the upstream flow velocity), turbine power output P , and power coefficient $C_p = P/(0.5 \cdot \rho \cdot A \cdot V^3)$. For the calculated variables, the uncertainty is about 1.15% for the upstream velocity and TSR, around

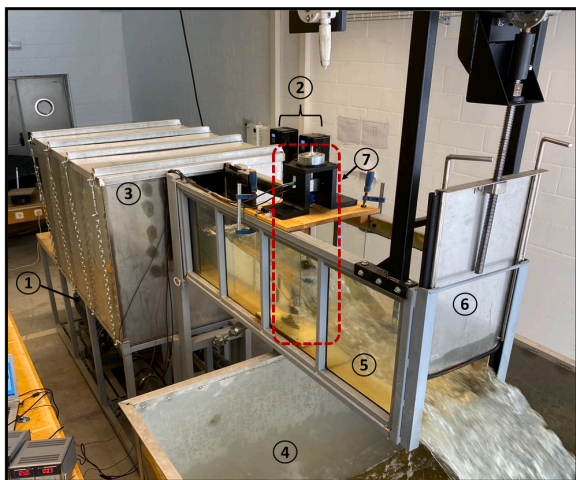


Fig. 3. Experimental set-up configuration.

0.12% for the power measurements and 3.5% for the power coefficient.

The rotor is positioned in the middle of the channel length, with a vertical clearance of 0.05 m between the bed and the bottom plate (10% of the channel height), so that the rotor is outside of the bed boundary layer.

5. Methodology

Tests were realized using three flow rates: $Q_1 = 0.05 \text{ m}^3/\text{s}$, $Q_2 = 0.06 \text{ m}^3/\text{s}$ and $Q_3 = 0.065 \text{ m}^3/\text{s}$. For each flow rate, the control gate was employed to obtain different flow conditions ranging from the lowest applicable velocity up to the maximum possible velocity (critical flow condition at channel outlet). In this way, five upstream flow velocities were selected for each flow rate within the range from 0.33 m/s to 0.69 m/s. Each upstream velocity involves also a specific upstream water height and turbine blockage.

The experimental procedure is handled through four successive steps:

- Firstly, the turbine is positioned into the channel, and the flow conditions are set using the pumping system and the control gate.
- Secondly, the turbine is allowed to rotate freely without any external load. The rotational speed increases up to its maximum value ($n = n_{max}$) where the torque produced is just enough to compensate the mechanical losses ($T = T_{min}$).
- Thirdly, the turbine is gradually loaded by increasing the current supplied to the brake. For each operating point the rotational speed, mechanical torque, and upstream water height are registered. Depending on the flow condition, between 7 and 16 different operating points can be usually measured (Fig. 5).
- Finally, as the load increases, the rotational speed slows down, and the torque produced rises until reaching the maximum power point (MPP). Above that point, if the load is increased, the turbine arrives at a condition where it cannot produce enough torque and stops abruptly.

The measured data is post processed to obtain P , C_p and TSR . With those values the turbine characteristic curves are plotted.

6. Results and discussion

The experimental measurements are used to assess the effect of different parameters, including the upstream flow velocity and the turbine blockage, on the overall performance of the MVATT. Also, the MPP and peak power coefficient are compared with one-dimensional actuator disc theory. Finally, an analysis is carried out to study the effect of the slope in an inclined channel.

6.1. Power output measurements

As it was mentioned before, for each flow rate value, the power produced from the turbine model was obtained for different flow conditions. For instance, Fig. 6 shows the power curves for the highest flow rate Q_3 where the power values are plotted against the rotational speeds. Each curve corresponds to one upstream velocity value from 0.43 m/s to 0.69 m/s. At the lowest velocity value, the channel is nearly overflowing (Fig. 7a) and at the highest one, the control gate is fully opened (Fig. 7c).

It can be noted that, for increasing upstream velocity values, the power produced increases and the rotational speeds are shifted to higher values. For the lowest upstream velocity (0.43 m/s), the rotational speeds range from 115 rpm to 150 rpm with a maximum power of 0.5 W. For the highest upstream velocity (0.69 m/s), the range extends from 180 rpm to 270 rpm, and the power reaches 3.5 W. The power increase is higher than the cube of the upstream velocity which would match the change in kinetic energy. This is a consequence of the intensification of the blockage as the velocity increases.

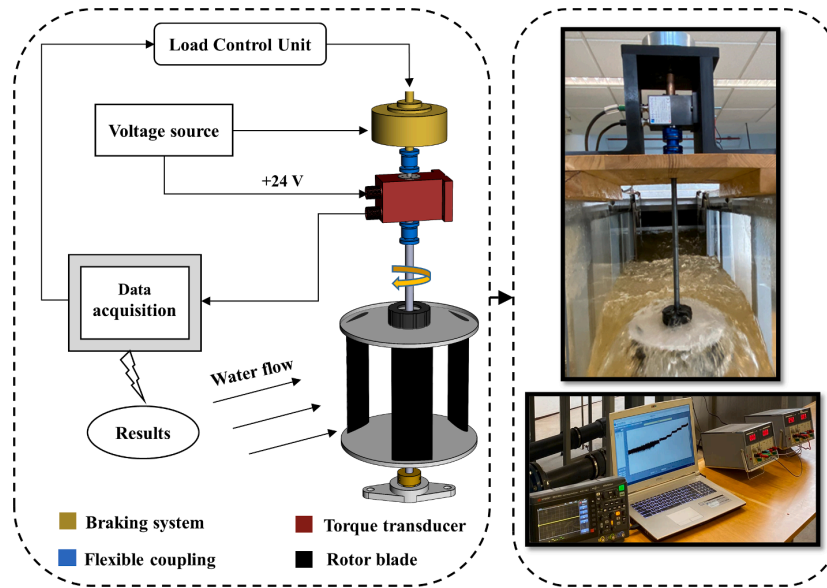


Fig. 4. Turbine model with control and measuring system.

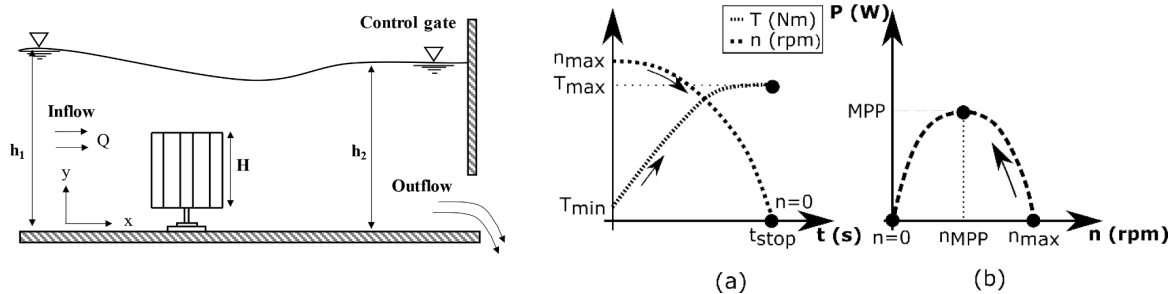


Fig. 5. Sequential test procedure.

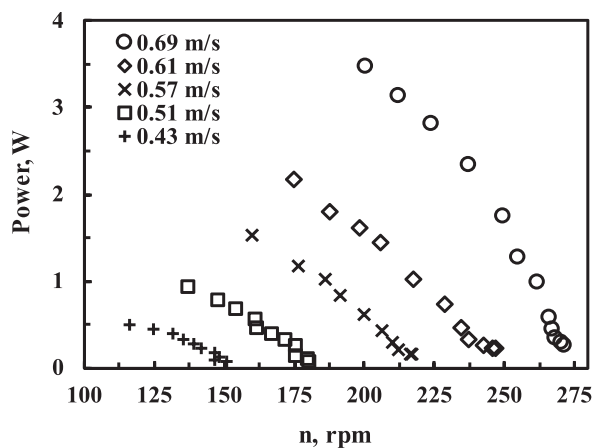


Fig. 6. Power output versus rotational speed with Q_3 .

For each upstream velocity, the maximum rotational speed corresponds to the zero-load condition. Increasing the turbine load decreases the rotational speed, which also rises the average angle of attack between the flow and the blades. This higher angle of attack produces more lift and consequently a higher torque and power. However, when the angle of attack reaches the stall conditions, the lift falls and the drag grows, which cause a sudden drop in the torque. From that point onwards, the power output from the turbine decreases with the decline of the rotational speed, which makes this part of the curve unstable. Operation and measurement on this zone would require an active control system.

6.2. Upstream velocity effect on performance characteristics

The variation of power output with upstream flow velocities for the three flow rates is shown in the 3D curves in Fig. 8. Traditionally, the characteristics of the MVATT are expressed in terms of non-dimensional parameters TSR and C_p to better compare the performance of different flow rates and upstream velocities. For an ideal turbine operating in an open field (no blockage effect), those curves should be identical, but for a non-ideal turbine operating in a confined channel, the characteristic

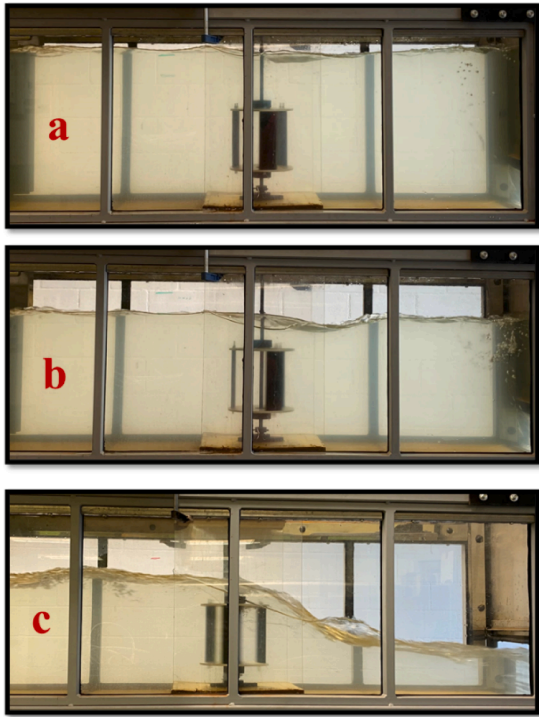


Fig. 7. Turbine model at Q_3 with different upstream velocities: (a) 0.43 m/s, (b) 0.57 m/s and (c) 0.69 m/s.

curves have substantial differences. These non-dimensional curves are also plotted in Fig. 8.

In practice, the maximum and minimum values of the upstream velocities differ slightly for each flow rate, as the limits correspond to the respective overflow and fully opened gate conditions. Since the maximum upstream velocities are higher when the flow rate increases, the power achieved with greater flow rates is also higher. However, comparing similar values of upstream velocity, the curves are remarkably close to each other. It can be said that the upstream velocity has the most obvious effect on the turbine performance.

About the specific values, starting with the highest flow rate Q_3 , the lowest upstream velocity (0.43 m/s) has a maximum C_p of 0.55 for a TSR of 2.1; this case corresponds to the fully filled channel where the blockage ratio is minimal ($B = 0.15$). Higher upstream velocity values have higher power coefficients, and the curve shifts to higher TSR values. The peak power coefficient increases by 22%, 34%, 55% and 81.6% while the corresponding TSR increases by 2.4%, 4.8%, 7.1% and 10.5% for upstream velocities of 0.51 m/s, 0.57 m/s, 0.61 m/s and 0.69 m/s, respectively. The peak power coefficient reaches its maximum value of 0.99 at a TSR of 2.3 for the highest velocity (0.69 m/s). In this case the channel gate is fully opened with a critical outlet flow condition, and a blockage of $B = 0.238$.

For a constant flow rate, the increase in the peak power coefficient with the upstream velocity is linked to the increase in the blockage ratio. The turbine model occupies 15% of the channel cross-section when the flow fills the whole channel. That value corresponds to the smallest practical velocity for all flow rates. For a fixed flow rate, the upstream water velocity increases by reducing the upstream water height, which implies an increase in the blockage ratio. In the performed experiments, the blockage ranges from a minimum value of 15% to maximum values of 23.8%, 24.3% and 27.7% for flow rates Q_3 , Q_2 and Q_1 , respectively.

As it was mentioned before, the Betz limit ($C_{p_{max}} = 0.59$) is not

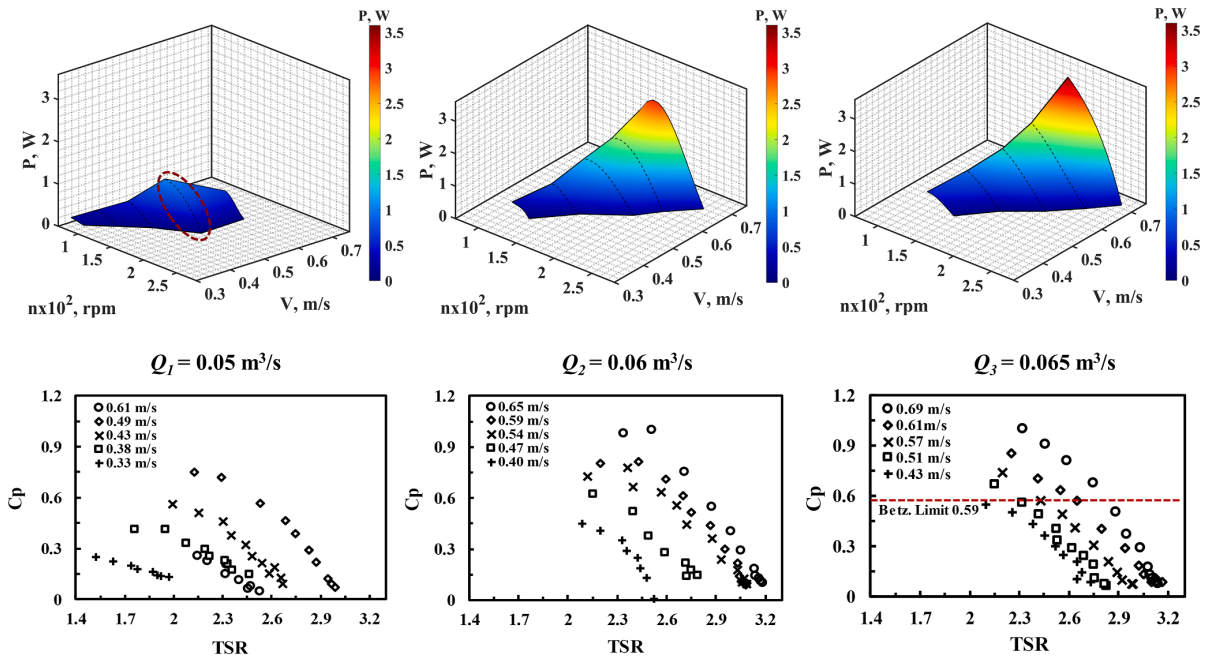


Fig. 8. Turbine power and characteristic curves for different upstream velocities with Q_1 , Q_2 and Q_3 .

applicable to a channel turbine, and this hypothesis is confirmed experimentally. For instance, at the highest flow rate, the peak power coefficient corresponding to the lowest upstream velocity is already 0.55. And, with higher upstream velocities, the peak power coefficient exceeds the Betz limit up to a 68%. The blockage accelerates the flow around the turbine rotor, resulting in a higher power output compared with an unrestricted flow. Furthermore, for a sub-critical flow, the water height goes down as the energy is extracted, increasing the blockage effect. In fact, the difference in static head around the turbine rotor makes the total available energy greater than the kinetic one.

With respect to the other tested flow rates, the intermediate one (Q_2) has the same tendencies, but the lowest flow rate (Q_1) behaves slightly different. For Q_2 , by increasing the upstream velocity from 0.4 m/s to 0.65 m/s, the peak power coefficient and the TSR increased by 116% and 12% respectively. For Q_1 , they also increase from 0.33 m/s to 0.49 m/s by 196% and 42% respectively. However, at that point, an inflection is observed when the upstream velocity goes from 0.49 m/s to 0.61 m/s, as the peak C_p value drops by 65% and the TSR remains constant at 2.15.

For this flow condition, the water level at the upstream side is nearly at the same elevation as the turbine top plate and, due to the water surface drop in the downstream side, the backside of the rotor is exposed to the air as shown in Fig. 9. The drop in the power coefficient is due to two reasons: first, the turbine rotor is not covered completely with water, reducing the effective area; and secondly, a partial flow separation occurs as the air enters the suction side of the blade, as reported by Birjandi et al. [50] for partially submerged turbines. The flow separation affects the lift force and, as a result, negative torque values are obtained at the top of the blades, reducing the power produced from the turbine and causing the power coefficient to drop suddenly.

6.3. Comparison between analytical model and experimental data

To further explore the phenomena in the present study, the experimental results are compared with the calculations of the LMADT theory developed by Hously et al. [41]. In the analytical model, the wake velocity coefficient (α) represents how physically the turbine stops the flowing water and determines the maximum available power output from the turbine. Being a simplified theory, the equations do not consider the rotational speed of the turbine. However, this effect is incorporated in the wake velocity coefficient. The rotational speed at which the maximum power is obtained corresponds to the α value that gives the maximum power in the calculations.

The optimum value of this coefficient has been calculated by solving numerically the quartic polynomial equation (Eq. (2)) for the three flow rates in the experimental tests and determining the whole range of the upstream velocities that give a valid solution for the model equations. For all the calculated conditions, the MPP is achieved analytically when the turbine rotor reduces the far-wake flow velocity to 1/3 of current upstream flow ($\alpha = 0.33$). Fig. 10 shows the comparison between results obtained in the experiments and the analytical model for the maximum power point versus the upstream velocity for the three flow rates.

A reasonably good match between experimental and analytical results was found for the whole ranges of upstream velocities from 0.33 m/s to nearly 0.69 m/s. However, the experimental results are somewhat



Fig. 9. Fully opened gate condition at Q_1 .

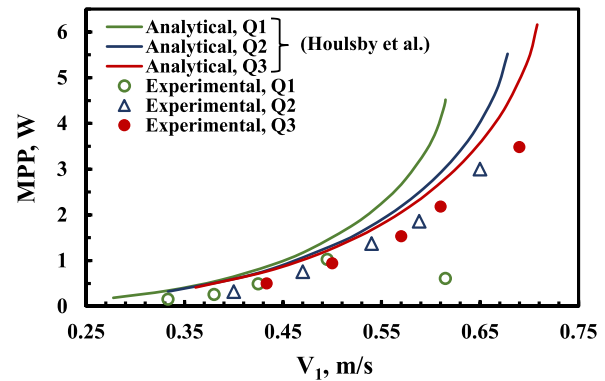


Fig. 10. Experimental results and analytical model predictions.

lower than the analytical ones because the model does not consider friction losses from the channel walls. The only point that deviates from the trend is the one corresponding to the highest upstream velocity of the lowest flow rate, due to the partial immersion of the turbine as explained before. In the analytical results, the lines corresponding to different flow rates diverge for high upstream velocities, due to the different increase in the blockage ratio (for the same velocity, the lower the flow rate, the higher the blockage). However, in the experimental results, this separation is not so evident. This could be due to the higher losses produced by the greater increase in velocity caused by the blockage, or by the differences of the flow conditions between the experimental turbine and the Hously's model. Nevertheless, the maximum upstream velocity (fully opened gate condition) for each flow rate is basically the same for both experimental and analytical results.

To some extent, the Froude number combines the effect of velocity and blockage, but the flow rate and the upstream velocity have been chosen as parameters because they have a simpler physical significance. The Froude number calculations prove that all points along the channel are subcritical -dominance of gravitational forces- in accordance with the analytical assumptions.

To examine the blockage effect, it is very useful to employ the power coefficient which divides the turbine power output by the flow kinetic energy flux. This eliminates the effect of the cubic value of the upstream velocity. The expression obtained by the analytical model for the peak power coefficient value is:

$$C_{p,max} = \frac{[2B\beta(9\beta^2 - 1) - 9(\beta - 1)^3](3\beta + 1)}{27B[4\beta + 3(\beta^2 - 1)]} \quad (3)$$

As it can be observed, the power coefficient is a function of two dimensionless parameters: blockage (B), and bypass coefficient (β). For an unrestricted flow, these two parameters would be constants and the peak power coefficient would be equal to the Betz limit. However, in the case of a channel, the values still vary with the operating conditions (flow rate and upstream velocity).

The variation of peak power coefficient with upstream inlet velocity for both analytical and experimental results is shown in Fig. 11 (a), while the variation of blockage ratio with upstream velocity is shown in Fig. 11 (b). For the analytical results, at low upstream velocities – and low blockage – there is a little difference between the three flow rates. The peak power coefficient tends to the Betz limit when the upstream velocity approaches zero (zero blockage). However, when the upstream velocity increases and the blockage effect rises, the curves diverge and the difference between the flow rates grows. This is more evident from a blockage value about 0.2 upwards. For the experimental results, the difference is much less noticeable between the three flow rates along the whole range of the upstream velocities. Even so, a variation in the trendlines can be observed, which is somehow related to the analytical

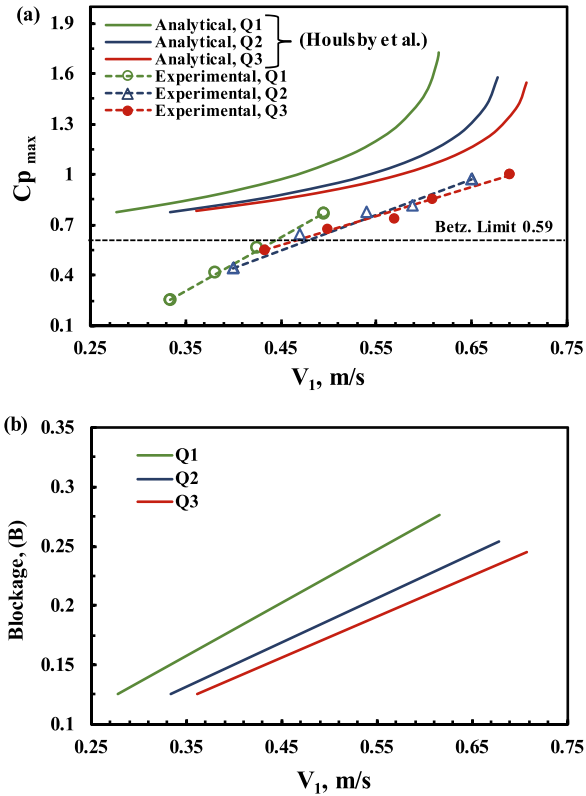


Fig. 11. Influence of blockage on turbine performance. (a) Variation of peak power coefficient with upstream velocity at various flow rates: Experimental and Analytical data; (b) variation of blockage with upstream inlet velocity at various flow rates.

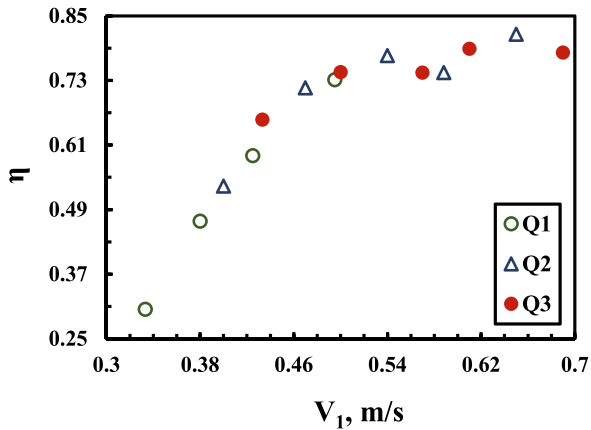


Fig. 12. Experimental turbine efficiency with respect to the analytical model.

pattern.

Since the analytical value of the peak power coefficient is the maximum that can theoretically be obtained, the ratio between the experimental and analytical values can be employed as a measure of the turbine efficiency. This relationship has been displayed in Fig. 12. Efficiency values are low for small upstream velocities. However, from 0.45 m/s and above, the efficiency is over 70%, and as high as 81%. As the upstream velocity range is different for each flow rate, this has a direct

impact on the efficiency obtained: the higher efficiencies can only be achieved with the higher flow rates.

6.4. Turbine performance in an inclined channel

The turbine model that has been developed in this investigation to harness tidal currents can also be used in other open flows such as channels and rivers. In these cases, the flow conditions are linked to the slope and friction. The analytical theory has been developed for an ideal channel flow and the operating conditions are input data. Also, the channel test rig has characteristics quite similar to an ideal one, externally regulated with the pumps and the control gate. A relation between the operating conditions of the horizontal and inclined channel (Fig. 13) can be obtained using the Manning equation:

$$S = \left(\frac{Qf}{A_c R_h^{2/3}} \right)^2 \quad (4)$$

where S is the channel slope, f is the manning friction coefficient and R_h is the hydraulic radius that corresponds to the water height downstream of the turbine. For the following calculations, a friction coefficient of 0.01 has been selected which represents a smooth channel, although this value would vary according to the nature of the channel.

The variation of the maximum power point with the slope is shown in Fig. 14(a). The experimental values of the three flows fit quite well to the equation: $MPP = 0.038 \cdot S^2$, implying that the maximum power point is proportional to the square value of the channel slope. Another interesting point is the tip speed ratios that obtain the maximum power output TSR_{MPP} , because the knowledge of these values is necessary for the electrical control of the turbine. Their variation with the slope is shown in Fig. 14(b). In this case there is a higher dispersion but the values are fairly well adjusted to the equation: $TSR_{MPP} = 1.4 \cdot S^{0.25}$ indicating that, the tip speed ratio corresponding to the maximum power point is proportional to the fourth root of the slope.

6.5. Scale considerations

The turbine developed in this work has a dimension conditioned by the size of the test rig. The model is small compared to those used to generate electricity and a bigger one will have to be built for field testing. Larger models usually work better than smaller ones, among other things, because the ratio of mechanical losses to power output decreases as the size increases. In this case, the similarity conditions are more complex than for wind turbines where the kinematic similarity is given by the Strouhal number and the power coefficient is a function exclusively of the tip speed ratio [51]. For low velocities, the Reynolds number is also an important factor. For small Reynolds numbers, the performance of lift-based turbines is usually reduced due to the poorer performance of the blade profile. Therefore, larger turbines have usually better self-start and efficiency characteristics for low flow velocities because, for the same tip speed ratio, the Reynolds number is proportional to the turbine size.

In hydrokinetic turbines, the Froude number also influence the kinematic similarity. Typically, it cannot be maintained if the turbine size changes. In fact, in this research, the tests performed at different flow velocities correspond to different Froude numbers and that is the reason for the multiple C_p - TSR curves, and this also allows to analyse qualitatively the performance of larger turbines. At the same upstream velocity, a larger turbine will have a smaller Froude number and will produce a proportionally larger blockage (Eq. (2)). As has been experimentally proven, a larger blockage generates a higher power coefficient so that larger turbines will start at least at the same velocity and perform better than the studied model.

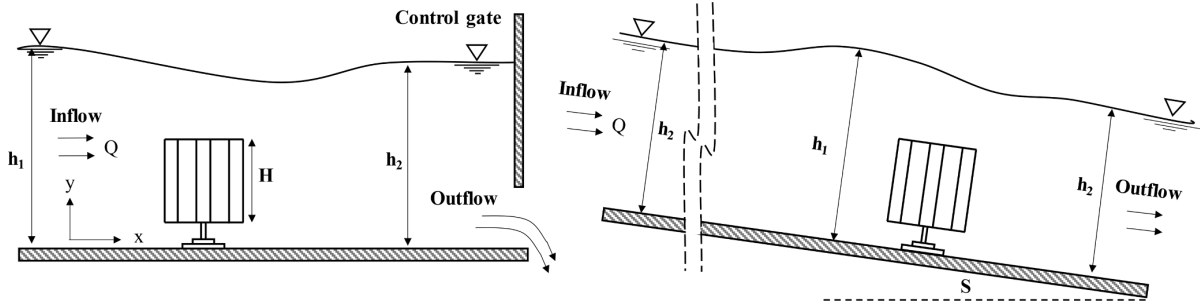


Fig. 13. Conceptual schematic of the channel inclination.

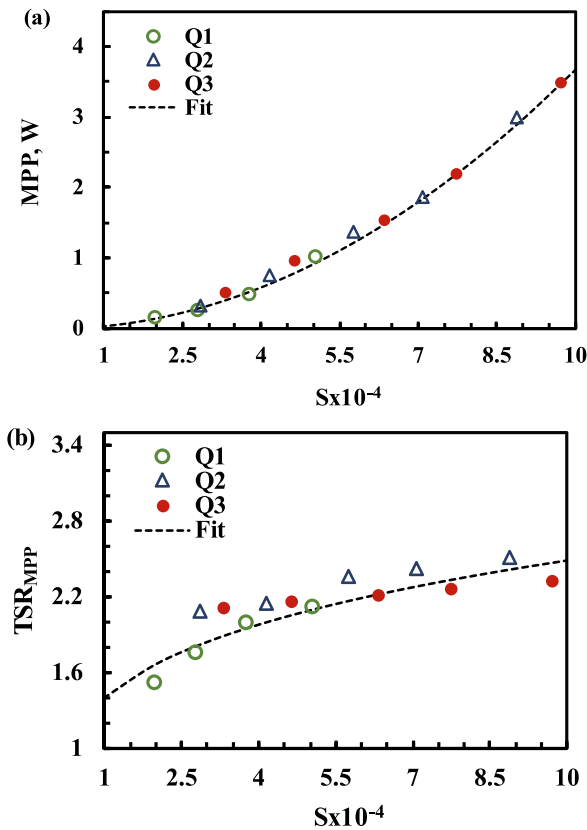


Fig. 14. Variation of peak power coefficient (a), and tip speed ratio corresponding to the maximum power point (b) in function of channel slope for different flow rates.

7. Conclusions

A vertical axis micro tidal turbine has been designed and manufactured. The turbine model has three straight blades with fixed pitch and a NACA-0015 profile. A solidity of 2.0 together with an aspect ratio of 1.0 has been selected, looking for self-starting and efficient operation with low flow velocities. It has been fabricated using additive manufacturing technology.

Tests have been performed in an open channel rig at three flow rates of 0.05 m³/s, 0.06 m³/s and 0.065 m³/s, with inlet velocities ranging from 0.33 m/s to 0.69 m/s. Power and non-dimensional curves have been obtained for each operating condition. The experimental measurements allow to assess the effect of different parameters, including the turbine blockage on the overall performance of the turbine.

- With higher upstream velocity, the power rises, and the rotational speeds shift to higher values. The power increase is higher than the cube of the upstream velocity as a consequence of the intensification of the blockage.
- Increasing the load beyond the maximum power point, decreases the output from the turbine with a decline of the rotational speed. Operation and measurement on this unstable zone would require an active control system.
- The non-dimensional parameters TSR and Cp have been used to compare the performance of different flow rates and upstream velocities. The power coefficient achieved with greater flow rates is higher. However, the upstream velocity has the most obvious effect on the turbine performance. With the lowest upstream velocity tested (0.33 m/s), the peak power coefficient is 0.25 with TSR 1.52, with the highest upstream velocity (0.69 m/s), the peak power coefficient reaches 0.99 with TSR 2.32.
- It has been observed, for one of the flow conditions, that if the turbine is partially submerged, the power output drops sharply (more than 40%).
- For a constant flow rate, the increase in the peak power coefficient with the upstream velocity is linked to the increase in the blockage ratio. The blockage accelerates the flow around the turbine rotor, resulting in a higher power output compared with an unrestricted flow. Furthermore, for a sub-critical flow, the water height goes down as the energy is extracted, increasing the blockage effect. In fact, the difference in static head around the turbine rotor makes the total available energy greater than the kinetic one.

Also, the experimental results have been compared with the calculations of the actuator disc theory adjusted for open channel flow.

- Betz limit is not applicable to channel turbines, and this hypothesis has been confirmed experimentally.
- A reasonably good match between experimental and analytical results was found for the whole ranges of upstream velocities. However, the experimental results are somewhat lower than the analytical ones because the model does not consider friction losses from the channel walls.

- In the analytical results, the lines corresponding to different flow rates diverge for high upstream velocities, due to the different increase in the blockage ratio. In the experimental results, this separation is not so evident, most likely due to the higher losses caused by the blockage.
- The turbine efficiency has been defined in relation to the maximum theoretical power obtainable. Small upstream velocities have only marginal efficiencies but, from 0.45 m/s upwards, the efficiency is over 70%, and as high as 81%.

Finally, the relation between slope and performance in an inclined channel has been assessed.

- The variation of the maximum power point is proportional to the square value of the channel slope.
- The tip speed ratios that obtain the maximum power output have a slight dispersion, but they fit an equation proportional to the fourth root of the slope.

CRediT authorship contribution statement

Ahmed Gharib Yosry: Investigation, Writing - original draft. **Aitor Fernández-Jiménez:** Software, Methodology. **Eduardo Álvarez-Álvarez:** Investigation, Data curation. **Eduardo Blanco Marigorta:** Writing - review & editing.

Declaration of Competing Interest

The authors declare that they have no known competing financial interests or personal relationships that could have appeared to influence the work reported in this paper.

Acknowledgments

The author would like to express his gratitude to the Egyptian Cultural Affairs and Missions Sector (the Egyptian Ministry of Higher Education and Scientific Research) along with Port Said University for their financial support.

References

- [1] Renewable energy market update. Renew energy mark up; 2020. <https://doi.org/10.1787/afbc8c1d-en>.
- [2] IHA. In: Hydropower status report 2020. Int Hydropower Assoc; 2019. p. 1–83. <https://doi.org/10.1103/PhysRevLett.111.027403>.
- [3] IRENA. In: Renewable capacity statistics. Int Renew Energy Agency; 2020. p. 1–66.
- [4] Li Y, Lence BJ, Calisal SM. An integrated model for estimating energy cost of a tidal current turbine farm. *Energy Convers Manage* 2011;52:1677–87. <https://doi.org/10.1016/j.enconman.2010.10.031>.
- [5] dos Santos IFS, Camacho RGR, Tiago Filho GL, Botan ACB, Vinent BA. Energy potential and economic analysis of hydrokinetic turbines implementation in rivers: an approach using numerical predictions (CFD) and experimental data. *Renew Energy* 2019;143:648–62. <https://doi.org/10.1016/j.renene.2019.05.018>.
- [6] Lazard Ltd. Levelised cost of energy analysis – version 14.0 2020;14:1–21.
- [7] Lago LI, Ponta FL, Chen L. Advances and trends in hydrokinetic turbine systems. *Energy Sustain Dev* 2010;14:287–96. <https://doi.org/10.1016/j.esd.2010.09.004>.
- [8] Rourke FO, Boyle F, Reynolds A. Tidal energy update 2009. *Appl Energy* 2010;87:398–409. <https://doi.org/10.1016/j.apenergy.2009.08.014>.
- [9] IT Power. Development, installation and testing of a large scale tidal current turbine 2005;72. <https://doi.org/T/06/00210/00/REP URN 05/1698>.
- [10] Zomers A. The challenge of rural electrification. *Energy Sustain Dev* 2003;7:69–76. [https://doi.org/10.1016/S0973-0826\(08\)60349-X](https://doi.org/10.1016/S0973-0826(08)60349-X).
- [11] Yuce MI, Muratoglu A. Hydrokinetic energy conversion systems: a technology status review. *Renew Sustain Energy Rev* 2015;43:72–82. <https://doi.org/10.1016/j.rser.2014.10.037>.
- [12] Barbarelli S, Amelio M, Castiglione T, Florio G, Scornaienchi NM, Cutrupi A, et al. Analysis of the equilibrium conditions of a double rotor turbine prototype designed for the exploitation of the tidal currents. *Energy Convers Manage* 2014;87:1124–33. <https://doi.org/10.1016/j.enconman.2014.03.046>.
- [13] Kumar R, Raahemifar K, Fung AS. A critical review of vertical axis wind turbines for urban applications. *Renew Sustain Energy Rev* 2018;89:281–91. <https://doi.org/10.1016/j.rser.2018.03.033>.
- [14] Zhang D, Liu X, Tan M, Qian P, Si Y. Flow field impact assessment of a tidal farm in the Putuo-Hulu Channel. *Ocean Eng* 2020;208:107359. <https://doi.org/10.1016/j.oceaneng.2020.107359>.
- [15] Okulov VL, Naumov IV, Kabardin IK, Litvinov IV, Markovich DM, Mikkelsen RF, et al. Experiments on line arrays of horizontal-axis hydroturbines. *Renew Energy* 2021;163:15–21. <https://doi.org/10.1016/j.renene.2020.08.148>.
- [16] Mosbahi M, Ayadi A, Chouaibi Y, Driss Z, Tucciarelli T. Performance improvement of a novel combined water turbine. *Energy Convers Manage* 2020;205:112473. <https://doi.org/10.1016/j.enconman.2020.112473>.
- [17] Talukdar PK, Sardar A, Kulkarni V, Saha UK. Parametric analysis of model Savonius hydrokinetic turbines through experimental and computational investigations. *Energy Convers Manage* 2018;158:36–49. <https://doi.org/10.1016/j.enconman.2017.12.011>.
- [18] Boccaletti C, Fabbri G, Marco J, Santini E. An overview on renewable energy technologies for developing countries: the case of Guinea Bissau. *Renew Energy Power Qual J* 2008;1:343–8. <https://doi.org/10.24084/repqj06.295>.
- [19] Sornes K. Small-scale water current turbines for river applications. *Zero Emiss Resour Organ* 2010:1–19.
- [20] Vermaak HJ, Kusakana K, Koko SP. Status of micro-hydrokinetic river technology in rural applications: a review of literature. *Renew Sustain Energy Rev* 2014;29:625–33. <https://doi.org/10.1016/j.rser.2013.08.066>.
- [21] Gupta R, Biswas A, Sharma KK. Comparative study of a three-bucket Savonius rotor with a combined three-bucket Savonius-three-bladed Darrieus rotor. *Renew Energy* 2008;33:1974–81. <https://doi.org/10.1016/j.renene.2007.12.008>.
- [22] Takao M, Takita H, Maeda T, Kamada Y. A straight-bladed vertical axis wind turbine with a directed guide vane row – effect of guide vane solidity on the performance. *Proc Int Offshore Polar Eng Conf* 2009;18:414–8. <https://doi.org/10.1299/jsmkyushu.2008.199>.
- [23] Parashchivou I, Trifu O, Saeed F. H-Darrieus wind turbine with blade pitch control. *Int J Rotating Mach* 2009;2009. <https://doi.org/10.1155/2009/505343>.
- [24] Bhuyan S, Biswas A. Investigations on self-starting and performance characteristics of simple H and hybrid H-Savonius vertical axis wind rotors. *Energy Convers Manage* 2014;87:859–67. <https://doi.org/10.1016/j.enconman.2014.07.056>.
- [25] ed-Din Fertahi S, Bouhal T, Rajad O, Kouksou T, Arid A, El Rhafiki T, et al. CFD performance enhancement of a low cut-in speed current Vertical Turbine through the nested hybridization of Savonius and Darrieus. *Energy Convers Manage* 2018;169:266–78. <https://doi.org/10.1016/j.enconman.2018.05.027>.
- [26] Su H, Dou B, Qu T, Zeng P, Lei L. Experimental investigation of a novel vertical axis wind turbine with pitching and self-starting function. *Energy Convers Manage* 2020;217:113012. <https://doi.org/10.1016/j.enconman.2020.113012>.
- [27] Zeiner-Gundersen DH. A novel flexible foil vertical axis turbine for river, ocean, and tidal applications. *Appl Energy* 2015;151:60–6. <https://doi.org/10.1016/j.apenergy.2015.04.005>.
- [28] Singh MA, Biswas A, Misra RD. Investigation of self-starting and high rotor solidity on the performance of a three S1210 blade H-type Darrieus rotor. *Renew Energy* 2015;76:381–7. <https://doi.org/10.1016/j.renene.2014.11.027>.
- [29] Mohamed MH. Impacts of solidity and hybrid system in small wind turbines performance. *Energy* 2013;57:495–504. <https://doi.org/10.1016/j.energy.2013.06.004>.
- [30] Eboibi O, Danoa LAM, Howell RJ. Experimental investigation of the influence of solidity on the performance and flow field aerodynamics of vertical axis wind turbines at low Reynolds numbers. *Renew Energy* 2016;92:474–83. <https://doi.org/10.1016/j.renene.2016.02.028>.
- [31] Guillaud N, Balarac G, Goncalves E, Zanetti J. Large Eddy simulations on vertical axis hydrokinetic turbines – power coefficient analysis for various solidities. *Renew Energy* 2020;147:473–86. <https://doi.org/10.1016/j.renene.2019.08.039>.
- [32] Kolekar N, Banerjee A. Performance characterization and placement of a marine hydrokinetic turbine in a tidal channel under boundary proximity and blockage effects. *Appl Energy* 2015;148:121–33. <https://doi.org/10.1016/j.apenergy.2015.03.052>.
- [33] Espina-Valdés R, Fernández-Jiménez A, Fernández Francos J, Blanco Marigorta E, Álvarez-Álvarez E. Small cross-flow turbine: design and testing in high blockage conditions. *Energy Convers Manage* 2020;213:112863. <https://doi.org/10.1016/j.enconman.2020.112863>.
- [34] Roa AM, Aumelas V, Maître T, Pellone C. Numerical and experimental analysis of a darrieus-type cross flow water turbine in bare and shrouded configurations. *IOP Conf Ser Earth Environ Sci* 2010;12:012113. <https://doi.org/10.1088/1755-1315/12/1/012113>.
- [35] Myers L, Bahaj AS. Wake studies of a 1/30th scale horizontal axis marine current turbine. *Ocean Eng* 2007;34:758–62. <https://doi.org/10.1016/j.oceaneng.2006.04.013>.
- [36] Talukdar PK, Kulkarni V, Saha UK. Field-testing of model helical-bladed hydrokinetic turbines for small-scale power generation. *Renew Energy* 2018;127:158–67. <https://doi.org/10.1016/j.renene.2018.04.052>.
- [37] Patel V, Eldho TI, Prabhu SV. Performance enhancement of a Darrieus hydrokinetic turbine with the blocking of a specific flow region for optimum use of hydropower. *Renew Energy* 2019;135:1144–56. <https://doi.org/10.1016/j.renene.2018.12.074>.
- [38] Betz A. Das Maximum der theoretisch möglichen Ausnutzung des Windes durch Windmotoren. *le. Gesamte Turbinenwes* 1920;17:307.
- [39] Garrett C, Cummins P. The efficiency of a turbine in a tidal channel. *J Fluid Mech* 2007;588:243–51. <https://doi.org/10.1017/S0022112007007781>.
- [40] Whelan JJ, Graham JMR, Peiró J. A free-surface and blockage correction for tidal turbines. *J Fluid Mech* 2009;624:281–91. <https://doi.org/10.1017/S0022112009005916>.

- [41] Houlby GT, Vogel CR. The power available to tidal turbines in an open channel flow. *Proc Inst Civ Eng Energy* 2017;170:12–21. <https://doi.org/10.1680/jener.15.00035>.
- [42] Elsakka MM, Ingham DB, Ma L, Pourkashanian M. CFD analysis of the angle of attack for a vertical axis wind turbine blade. *Energy Convers Manage* 2019;182: 154–65. <https://doi.org/10.1016/j.enconman.2018.12.054>.
- [43] Khanjanpour MH, Javadi AA. Optimization of the hydrodynamic performance of a vertical Axis tidal (VAT) turbine using CFD-Taguchi approach. *Energy Convers Manage* 2020;222:113235. <https://doi.org/10.1016/j.enconman.2020.113235>.
- [44] Jain S, Saha UK. On the influence of blade thickness-to-chord ratio on dynamic stall phenomenon in H-type Darrieus wind rotors. *Energy Convers Manage* 2020;218: 113024. <https://doi.org/10.1016/j.enconman.2020.113024>.
- [45] Claessens MC. The design and testing of airfoils for application in small vertical axis wind turbines [Masters Thesis] 2006:1–137.
- [46] Kanyako F, Janajreh I. Numerical investigation of four commonly used airfoils for vertical axis wind turbine. In: Hamdan MO, Hejase HAN, Noura HM, Fardoun AA, editors. *ICREGA'14 – Renew. energy gener. appl.*, Cham: Springer International Publishing; 2014, p. 443–54.
- [47] Sengupta AR, Biswas A, Gupta R. Studies of some high solidity symmetrical and unsymmetrical blade H-Darrieus rotors with respect to starting characteristics, dynamic performances and flow physics in low wind streams. *Renew Energy* 2016; 93:536–47. <https://doi.org/10.1016/j.renene.2016.03.029>.
- [48] Gosselin R, Dumas G, Boudreau M. Parametric study of H-Darrieus vertical-axis turbines using CFD simulations. *J Renew Sustain Energy* 2016;8:053301. <https://doi.org/10.1063/1.4963240>.
- [49] Liu P, Bose N, Frost R, Macfarlane G, Lillenthal T, Penesis I. Model testing and performance comparison of plastic and metal tidal turbine rotors. *Appl Ocean Res* 2015;53:116–24. <https://doi.org/10.1016/j.apor.2015.08.002>.
- [50] Birjandi AH, Bibeau EL, Chatoorgoon V, Kumar A. Power measurement of hydrokinetic turbines with free-surface and blockage effect. *Ocean Eng* 2013;69: 9–17. <https://doi.org/10.1016/j.oceaneng.2013.05.023>.
- [51] Li B, Zhou DL, Wang Y, Shuai Y, Liu QZ, Cai WH. The design of a small lab-scale wind turbine model with high performance similarity to its utility-scale prototype. *Renew Energy* 2020;149:435–44. <https://doi.org/10.1016/j.renene.2019.12.060>.

2.9 Journal Metrics

The following data are based on the last updated one from the Web of Science database for the year of 2023.

Article No. 1	
Journal	ENERGY CONVERSION AND MANAGEMENT
Title	Design and characterization of a vertical-axis micro tidal turbine for low velocity scenarios
Category Quartile	Q1
Impact Factor	11.533
Impact Factor (5 years)	10.818
CiteScore	18
No. of Citations [Apr 2021 - May 2023]	23

Chapter 3

Multiphase Modelling of the VAHT with Free-surface Variations

3.1 Overview

limited investigations have been carried out considering the interactions between the turbine rotor and the channel section, including the free-surface. The following chapter presents a complementary study to the experimental previous one. It outlines an experimental and a three-dimensional multiphase simulation of the vertical-axis turbine model under free-surface variations. The volume of fluid (VOF) method is applied in the present simulation to model the free-surface (air/water interface). This model has been selected for its capability of reproducing and capturing the free-surface deformation accurately under different flow conditions. From the experimental results, three different cases have been selected for the simulation. The first case (C_1) in which the channel is fully-filled with water and the control gate is slightly opened, with an upstream velocity value of 0.43 m/s ; the second case (C_2) with an intermediate opening and an upstream velocity value of 0.57 m/s ; finally, the third case (C_3), where the control gate is fully opened and the upstream velocity value reaches 0.69 m/s . In addition, for the first case configuration, a single-phase three-dimensional simulation, without considering the free-surface, has also been carried out for comparison with the multiphase results, to examine the effect of the free-surface on the turbine output.

3.2 CFD Governing Equations

The main equations that govern the incompressible flow is the continuity equation ($\nabla \cdot \vec{u} = 0$, where $\vec{v} = (u, v, w)$) and the momentum Navier-Stokes equations. These equations that define the velocity and pressure of a fluid at any point in the space had been discovered almost two centuries ago by the French engineer Claude Navier and the

Irish mathematician George Stokes [93]. These partial differential equations are directly derived from Newton's laws of motion, which are the same for any situation involving fluid flow. The specific application to concrete cases is defined by the initial values and the boundary conditions. Therefore, for the case of incompressible flow, the momentum Reynolds Average Navier Stokes (RANS) equations are as follows:

$$\begin{aligned}
 \rho \frac{\partial u}{\partial t} + \rho \operatorname{div}(\vec{v}u) + \frac{\partial P}{\partial x} - \operatorname{div}(\mu \operatorname{grad}(u)) - S_{Mx} &= 0 \\
 \rho \frac{\partial v}{\partial t} + \rho \operatorname{div}(\vec{v}v) + \frac{\partial P}{\partial y} - \operatorname{div}(\mu \operatorname{grad}(v)) - S_{My} &= 0 \\
 \rho \frac{\partial w}{\partial t} + \rho \operatorname{div}(\vec{v}w) - \rho g + \frac{\partial P}{\partial z} - \operatorname{div}(\mu \operatorname{grad}(w)) - S_{Mz} &= 0
 \end{aligned} \tag{3.1}$$

Where (ρ) and (P) are the fluid density and pressure respectively, (μ) is the dynamic viscosity, (g) is the gravity, (div) is the divergence operator, (grad) is the gradient operator, and (S_{Mx}, S_{My}, S_{Mz}) is the source term that includes contributions due to the mass forces (gravitational, centrifugal and electromagnetic).

Turbulence is defined as an intrinsic instability phenomenon of the flow that causes it to behave in an apparently chaotic manner. Descriptively, it could be said that turbulent flow consists of the formation of more or less random vortices around the main direction of motion, which arise when the fluid velocity exceeds a specific threshold. Below this limit, viscous forces predominate over inertial forces, damping the chaotic behavior of the flow.

Since turbulent fluctuations are essentially irregular, the deterministic analysis is not possible, and it is more useful to do so through their statistical properties. In general, turbulent flow is characterized by the mean values of its properties $(\bar{u}, \bar{v}, \bar{w}, \bar{P})$ and their fluctuations (u', v', w', P') .

$$\begin{aligned}
 u &= \bar{u} + u' \\
 v &= \bar{v} + v' \\
 w &= \bar{w} + w' \\
 P &= \bar{P} + P'
 \end{aligned} \tag{3.2}$$

Turbulence is considered as the incorporation of all fluctuations with frequencies higher than the variation of the mean velocity value $(\bar{u}, \bar{v}, \bar{w})$, and can be regarded as the deviation of the instantaneous value from the mean value. The temporal average (\bar{h}) of a turbulent function (h) is defined as:

$$\bar{h} = \frac{1}{\Delta t} \int_0^{\Delta t} h dt \tag{3.3}$$

Where the time interval (Δt) must be greater than the time scale of the slowest variations of the turbulent function which occurs in the large eddies. This turbulent agitation produces additional stresses (Reynolds stresses) that lead to the Reynolds-Average Navier-Stokes equations (RANS) [94].

$$\begin{aligned}
 \rho \frac{\partial \bar{u}}{\partial t} + \rho \operatorname{div}(\vec{v} \bar{u}) + \frac{\partial \bar{P}}{\partial x} - \operatorname{div}(\mu \operatorname{grad}(\bar{u})) + \left[\frac{\partial (\overline{\rho u'^2})}{\partial x} + \frac{\partial (\overline{\rho u'v'})}{\partial y} + \frac{\partial (\overline{\rho u'w'})}{\partial z} \right] - S_{M_x} &= 0 \\
 \rho \frac{\partial \bar{v}}{\partial t} + \rho \operatorname{div}(\vec{v} \bar{v}) + \frac{\partial \bar{P}}{\partial y} - \operatorname{div}(\mu \operatorname{grad}(\bar{v})) + \left[\frac{\partial (\overline{\rho u'v'})}{\partial x} + \frac{\partial (\overline{\rho v'^2})}{\partial y} + \frac{\partial (\overline{\rho v'w'})}{\partial z} \right] - S_{M_y} &= 0 \\
 \rho \frac{\partial \bar{w}}{\partial t} + \rho \operatorname{div}(\vec{v} \bar{w}) - \rho g + \frac{\partial \bar{P}}{\partial z} - \operatorname{div}(\mu \operatorname{grad}(\bar{w})) + \left[\frac{\partial (\overline{\rho u'w'})}{\partial x} + \frac{\partial (\overline{\rho v'w'})}{\partial y} + \frac{\partial (\overline{\rho w'^2})}{\partial z} \right] - S_{M_z} &= 0
 \end{aligned} \tag{3.4}$$

3.3 The Turbulence Model

A turbulent model is a numerical procedure that solves the system of RANS equations. Due to the small-scale and the high frequency value of the velocity fluctuations, direct simulation is almost not applicable as it requires a great computational effort. The RANS equations can be time-averaged, ensemble-averaged, or any other technique can be used to eliminate small-scale fluctuations. The result is a set of equations that can easily solved.

The ($k - \omega$) model, developed by Wilcox [95], is the most widely used and tested of all turbulent models for solving large-scale problems with low computational cost. It works well in a wide range of thin layers and recirculating flows, without the need to adjust model constants on a case-by-case basis, as well as in confined flows where Reynolds shear stresses are most important. It is a two-equation model, where the first equation describes the transport of turbulent kinetic energy (k) and the second represents the specific rate of dissipation (ω). The Reynolds stress term ($\rho \cdot \nabla \vec{u} \cdot \vec{u}$) in the RANS equation is solved using the shear stress transport ($k-\omega$ SST) turbulence model developed by Menter [96]. This model combines robust formulations of the near wall ($k-\omega$) Wilcox model and the ($k-\varepsilon$) far wall one through a blending function that ensures a smooth transition between the two models without user interaction. The transport equations of the ($k-\omega$ SST) turbulence model are as follow:

$$\rho \frac{\partial (K)}{\partial t} + \rho \nabla(\vec{u} \cdot k) = \nabla \left[\left(\mu + \frac{\mu_t}{\sigma_k} \right) \nabla K \right] + G_k - \rho \epsilon \tag{3.5}$$

$$\rho \frac{\partial (\omega)}{\partial t} + \rho \nabla(\vec{u} \cdot \omega) = \nabla \left[\left(\mu + \frac{\mu_t}{\sigma_k} \right) \nabla \omega \right] + \beta \rho \omega^2 + S_\omega \tag{3.6}$$

Where (k) is the turbulent kinetic energy term, G_k represents the generation of turbulence kinetic energy due to mean velocity gradients, (ω) is the specific dissipation rate, (μ_t) is the turbulent eddy viscosity, (β) is empirical coefficient and (S_ω) is the blending function.

3.4 The VOF Multiphase Model

Usually, numerical investigations are based on the single-phase flow analysis, without considering the free-surface effects, are carried out to study the flow field around the hydrokinetic turbines. Typically, these studies solve the Navier-Stokes equations in a domain where the free surface is fixed, using the sliding mesh technique to simulate the turbine rotation, and (k- ω SST) turbulence models.

Nevertheless, such models are not sufficiently realistic, to accurately assess the performance and characterize the flow field of hydrokinetic turbines in open channels, because they do not consider the change of the free-surface in their analysis.

The volume of fluid (VOF) method, developed by Hirt and Nichols [97], is applied in the present simulation to model the free-surface (air/water interface). It has the capability of reproducing and capturing the free-surface deformation accurately under different flow conditions. For this method, the water volume fraction is defined as $\alpha = V_w/V$, where (V_w) is the water volume in the cell and (V) is the total volume of the mixture. The physical properties of the air-water multiphase fluid can be calculated as:

$$\rho_m = \alpha \cdot \rho_w + (1 - \alpha)\rho_a \quad (3.7)$$

$$\mu_m = \alpha \cdot \mu_w + (1 - \alpha)\mu_a \quad (3.8)$$

where ρ_m and μ_m are the mixture density and dynamic viscosity respectively. A value of $\alpha = 0.5$ represents the free-surface location. The VOF governing equations are the mass, momentum and volume conservation equations. The VOF model assumes that the pressure and velocity fields are the same for both phases and solves a single momentum equation. The volume fraction for each q-th phase, denoted as α_q , is defined as the space occupied by each phase (as a fraction of total space), satisfying:

$$V_q = \int_V \alpha_q \cdot dV \quad \sum_{q=1}^N \alpha_q = 1 \quad (3.9)$$

Thus, for each phase, a continuity equation and three momentum equations are defined:

$$\frac{\partial (\alpha_q \rho_q)}{\partial t} + \nabla \cdot (\alpha_q \rho_q \vec{v}_q) = 0 \quad (3.10)$$

$$\begin{aligned} \alpha_q \rho_q \frac{\partial \bar{u}}{\partial t} + \alpha_q \rho_q \text{div} (\vec{v} \bar{u}) + \frac{\partial \alpha_q \bar{P}}{\partial x} - \text{div} (\alpha_q \mu_q \text{grad} (\bar{u})) + \\ + \left[\frac{\partial (\alpha_q \rho_q \overline{u'^2})}{\partial x} + \frac{\partial (\alpha_q \rho_q \overline{u'v'})}{\partial y} + \frac{\partial (\alpha_q \rho_q \overline{u'w'})}{\partial z} \right] - S_{Mx} = 0 \end{aligned}$$

$$\begin{aligned}
& \alpha_q \rho_q \frac{\partial \bar{v}}{\partial t} + \alpha_q \rho_q \operatorname{div}(\vec{v} \bar{v}) + \frac{\partial \alpha_q \bar{P}}{\partial y} - \operatorname{div}(\alpha_q \mu_q \operatorname{grad}(\bar{v})) + \\
& \quad + \left[\frac{\partial (\alpha_q \rho_q \overline{u'v'})}{\partial x} + \frac{\partial (\alpha_q \rho_q \overline{v'^2})}{\partial y} + \frac{\partial (\alpha_q \rho_q \overline{v'w'})}{\partial z} \right] - S_{My} = 0 \\
& \alpha_q \rho_q \frac{\partial \bar{w}}{\partial t} + \alpha_q \rho_q \operatorname{div}(\vec{v} \bar{w}) - \alpha_q \rho_q g + \frac{\partial \alpha_q \bar{P}}{\partial z} - \operatorname{div}(\alpha_q \mu_q \operatorname{grad}(\bar{w})) + \\
& \quad + \left[\frac{\partial (\alpha_q \rho_q \overline{w'u'})}{\partial x} + \frac{\partial (\alpha_q \rho_q \overline{w'v'})}{\partial y} + \frac{\partial (\alpha_q \rho_q \overline{w'^2})}{\partial z} \right] - S_{Mz} = 0
\end{aligned} \tag{3.11}$$

3.5 The Grid Conversion Index Method (GCI)

The whole domain in the current study has been discretized using a fully structured mesh with hexahedral shaped cell. The size and mesh shape are provided in the following sections. The Grid Conversion Index (GCI) method, developed by Roache [98], has been applied to test the mesh refinement in the current study. It is based on the generalized Richardson extrapolation, involving comparison of discrete solutions in two different spacing meshes. The discrete solutions f are assumed to have a series representation in the grid spacing h of:

$$f = f[exact] + g_1 h + g_2 h^2 + g_3 h^3 + \dots \tag{3.12}$$

The functions g_1 , g_2 , and so on are defined in the continuum and do not depend on any discretization. For infinitely differentiable solutions, these functions are related to all orders to the solution derivatives through the elementary Taylor series expansions, but this is not a necessary assumption for Richardson Extrapolation, nor is the infinite series indicated in equation

For a second-order method, $g_1 = 0$. To eliminate the leading-order error terms in the assumed error expansion, the two separate discrete solutions, f_1 and f_2 , are combined on two different grids with uniform discrete spacing of h_1 (fine grid) and h_2 (coarse grid). Then, the equation 3.12 is solved for g_2 to obtain a more accurate estimate of $f[exact]$. For h^2 extrapolation:

$$f = f[exact] + (h_2^2 f_1 - h_1^2 f_2) / (h_2^2 - h_1^2) + H.O.T \tag{3.13}$$

where $H.O.T$ are higher-order terms. Using the grid refinement ratio ($r = h_2/h_1$), this result can be conveniently expressed in terms of a correction to the fine-grid solution f_1 , dropping $H.O.T$:

$$f[exact] \cong f_1 + (f_1 - f_2)/(r^2 - 1) \quad (3.14)$$

The most common use of this method is with a grid doubling, or halving, With $r = 2$, equation (3.14) becomes:

$$f[exact] \cong 4/3f_1 - 1/3f_2 \quad (3.15)$$

It is often stated that equation (3.15) is fourth-order accurate if f_1 and f_2 are second-order accurate. Typically, the use of simple second-order interpolation avoids complexities with nonuniform grids and near-boundary points. A fine-grid Richardson error estimator approximates the error in a fine-grid solution f_1 by comparing this solution to that of a coarse grid, f_2 , and is defined as:

$$E_1^{fine} = \frac{\epsilon}{1 - r^p} \quad (3.16)$$

while a coarse-grid Richardson error estimator approximates the error in a coarse-grid solution, f_2 , by comparing the solution to that of a fine grid, f_1 , and is defined as:

$$E_2^{coarse} = \frac{r^p \epsilon}{1 - r^p} \quad (3.17)$$

where $\epsilon = f_2 - f_1$, in which f_1 and f_2 are the fine and the coarse-grid numerical solutions obtained with grid spacing of h_1 and h_2 respectively at the order of accuracy p .

The uncertainty in the generalized Richardson-based error estimators are taken into account due to various factors and to put all grid-convergence studies on the same basis as grid doubling with a second-order method. A safety factor F_s is incorporated into these estimators and the *GCI* is defined for fine and coarse grids as:

$$GCI_1^{fine} = F_s |E_1| \quad (3.18)$$

$$GCI_2^{coarse} = F_s |E_2| \quad (3.19)$$

The *GCI*'s are not the error estimators but are the F_s times the error estimators. In the current study, a safety factor of 1.25 has been selected [98] based on the balance between the accuracy and the computational cost.

3.6 Objectives

The main objective of the current chapter is to characterize experimentally and numerically the performance of a small vertical-axis turbine under different flow and free-surface conditions. An intensive three-dimensional multiphase simulation has been carried out to understand the complex flow field around the turbine rotor and to clarify the influence of the free-surface variations on the turbine output. The volume of fluid (VOF) model is used to track the free-surface air-water interface. Also, the sliding mesh technique is employed for the rotation of the turbine. The numerical model is validated against the experimental findings. The velocity field and the pressure coefficient distribution, around the turbine rotor, have been studied and correlated with the free-surface variations from upstream to downstream of the turbine. Finally, the vortex street generated by the blade-plate interaction has been analyzed.

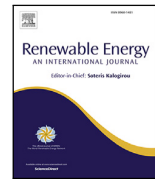
3.7 Peer-reviewed Journal Publication

3.7.1 Experimental and Multiphase Modeling of Small Vertical-axis Hydrokinetic Turbine with Free-surface Variations



Contents lists available at ScienceDirect

Renewable Energy

journal homepage: www.elsevier.com/locate/renene

Experimental and multiphase modeling of small vertical-axis hydrokinetic turbine with free-surface variations

Ahmed Gharib Yosry^{a,b,*}, Eduardo Álvarez Álvarez^c, Rodolfo Espina Valdés^c, Adrián Pandal^a, Eduardo Blanco Marigorta^{a,**}

^a GIFD Group, Energy Department, University of Oviedo, C/ Wifredo Ricart s/n, Gijón, Spain

^b Mechanical Power Department, Faculty of Engineering, Port Said University, Egypt

^c Hydraulic R&D Group, EP Mieres, University of Oviedo, Mieres, Spain

ARTICLE INFO

Keywords:

Vertical-axis turbine
VOF
Multiphase CFD
Froude number
Water channel
Free surface

ABSTRACT

Vertical-axis hydrokinetic turbines are promising option to harness the low velocity currents. However, limited investigations have been carried out considering the interactions between the turbine rotor and the channel section, including the free-surface. Thus, a vertical-axis turbine model has been designed and manufactured, to be tested in an open channel. Also, a three-dimensional multiphase simulation has been carried out, using the volume of fluid (VOF) model, to capture the air–water interface and to investigate the free-surface variations effects on the turbine output. Experimentally, the turbine model has been characterized under different flow conditions and free-surface levels. The peak power coefficients are found to increase with the upstream velocity. This effect is directly linked to the blockage ratio and the Froude number. A reasonably good match has been found between the experimental and the numerical results. The VOF model is able to simulate the free-surface longitudinal variations, and the effect of the turbine blockage of the channel. The velocity field and the pressure coefficient distribution, around the turbine rotor, have been studied and correlated with the free-surface variations from upstream to downstream of the turbine. Finally, the vortex street generated by the blade–plate interaction has been analyzed.

1. Introduction

Hydrokinetic turbines transform the kinetic energy available in water currents into a useful mechanical work [1]. Based on the alignment of the rotor axis with respect to the water flow, three generic categories can be defined; the first one is the horizontal-axis turbines, alternately called axial-flow turbines, which have the axes parallel to the fluid flow and employ propeller type rotors. The second category is the cross flow turbines, known as “floating waterwheels”, in which the rotor axis is orthogonal to the water flow but parallel to the water surface, and are based on the hydrodynamic drag. Finally, the Darrieus type or vertical-axis turbines, whose axes are also perpendicular to the fluid flow, but working on the hydrodynamic lift, and are usually derived from the rotor designs of the wind industry [2].

Among these types, vertical-axis turbines are considered a viable choice to harness the energy in the water current, particularly for low flow velocities, due to its simple design and insensitivity to the flow direction [3]. However, within the blue economy, as a more restricted

markets are exploited, continued innovation of these kind of turbines is necessary to ensure their competitiveness with other types [4].

Many investigations have been carried out to optimize and enhance the design parameters of the vertical-axis turbine, including the number of blades [5], the profile type [6] and the aspect ratio value [7]. Of the vertical-axis turbine types, the lift-based ones give the highest peak performance, specifically the straight bladed turbines. However, one of the handicaps of this turbine category is the limited self-starting capability. Increasing the turbine solidity (which is calculated as $\sigma = n \cdot C/R$, where n is the number of blades, C is the chord length and R is the radius of the turbine rotor) is the simplest solution offered to overcome this issue [8]. However, high solidity profiles cause a low power efficiency, specifically at low Reynolds number condition. To overcome this issue, the blade pitch control is applied and tested for high solidity straight-bladed turbines [9], in which the maximum power coefficient increases by 78%. Another variable pitch techniques based on the double-disk multiple stream-tube are also applied [10,11]. The flexible-high solidity foil offers a self-starting capability at water

* Corresponding author at: GIFD Group, Energy Department, University of Oviedo, C/ Wifredo Ricart s/n, Gijón, Spain.

** Corresponding author.

E-mail addresses: ahmed.gharib@eng.psu.edu.eg (A.G. Yosry), eblanco@uniovi.es (E.B. Marigorta).

<https://doi.org/10.1016/j.renene.2022.12.114>

Received 18 August 2022; Received in revised form 30 September 2022; Accepted 28 December 2022

Available online 2 January 2023

0960-1481/© 2022 The Author(s). Published by Elsevier Ltd. This is an open access article under the CC BY-NC-ND license (<http://creativecommons.org/licenses/by-nc-nd/4.0/>).

Nomenclature

B	Blockage ratio
C	Blade chord length, m
C_p	Power coefficient
D	Turbine diameter, m
d_s	Shaft diameter, m
Fr	Froude number, $Fr = U / \sqrt{gh}$
H	Blade height, m
h	Upstream water height, m
N	Rotational speed, rpm
n	Number of blades
P	Power output, W
Q	Water flow rate, m^3/s
R	Radius of rotor, m
T	Torque, N m
σ	Solidity
A	Turbine cross-sectional area, m^2
λ	Tip speed ratio, $\lambda = \Omega \cdot R / U$
Ω	Angular velocity, rad/s
U	Upstream velocity, m/s
ρ	Water density, kg/m^3
α	Water volume fraction
V_w	Water volume, m^3
V	Mixture volume, m^3
μ	Dynamic viscosity, pa.s
g	Gravitational acceleration, m/s^2
Γ_σ	Surface tension, N/m
C_T	Instantaneous torque coefficient
y^+	Non-dimensional wall distance
Z^*	Normalized water height
L	Channel maximum depth, m
ζ^*	Normalized vorticity, $\zeta^* = \nabla \bar{u} / [u \cdot c]$
θ	Azimuth angle, degree

velocity of 0.5 m/s and above with a power coefficient value reaches to 0.37 for vertical-axis tidal turbines [12]. Hybridization between two different turbines [13] is also one of the effective solutions, Govind [14] proposes a novel strategy to combine 12 kW NREL horizontal-axis turbine with 10 kW H-type vertical axis rotor on the same tower. The excess torque from the horizontal rotor is transferred to the vertical rotor through a continuously variable transmission.

The optimization studies of vertical-axis turbines are very diverse. For instance, with respect to improving the efficiency, Villeneuve et al. [15] predict and assess the efficiency and the power output of a vertical axis turbine using a novel three-dimensional numerical model, which evaluates the potential of the detached end plates. The turbine with circular plates is 31% more efficient than the one without ending plates. With respect to the blade profile and size, among the many researches in this field, it is worth mentioning the one by Saeidi et al. [16] which applies the double-multiple stream tube modeling along with the blade element momentum theory to optimize the design of the same turbine. Otherwise, the performance of a V-shaped blades rotor has been studied numerically to improve the power output at moderate tip speed ratios, obtaining a noticeable delay of the flow separation [17]. In another instance [18], the power output from a two-blades vertical-axis turbine is analytically studied by applying the Taguchi method, in which the incoming flow angle along with the tip speed ratio are found to be the most significant parameters affecting the turbine power output. Investigations have even been extended to

consider wind and waves effects on the power output and efficiency of the tidal turbines [19].

However, one of the fundamental needs for improving and optimizing these turbines is the availability of effective analytical and numerical calculation tools. On a basic level, different theoretical approaches have been developed to define the actuator disc model in an open channel flow, taking into account the Froude number and the free-surface drop behind the turbine [20] and also the mixing zone downstream [21]. Additionally, the models have been extended to include these effects on the power output from a turbine array [22]. Moreover, the analytical tools have been applied as a sub-correction model to evaluate the power available to a turbine array through Depth-averaged simulations [23], as an alternative to the expensive three-dimensional simulations of turbine farms.

On the numerical level, investigations based on the single-phase flow analysis and without considering the free-surface effects, have been carried out to study the flow field around the hydrokinetic turbines. Typically, these studies solve the Navier–Stokes equations in a domain where the free surface is fixed, using sliding mesh to simulate the turbine rotation, and RANS turbulence models. It is unusual to find research using LES methodology, however it is sometimes employed for specific purposes. For instance, [24,25] use this model to study in more detail the turbine wake, and [26] to look for the effect of the solidity related to the flow separation at the blades. Regarding the simulation of the turbine, as mentioned above, the method that often gives the best results is the sliding mesh technique. The moving reference frame (MRF) is not usually enough due to the important interaction between the blades and the walls. Although other systems have been applied, such as the immersed boundary [27]. One of the most interesting issues in this type of simulations is the effect of the blockage that results from placing the turbine in a channel of limited dimensions, either as an isolated turbine [28,29], as a turbine farm [30,31] or even using flow acceleration elements [32]. In general, the blockage and associated procedures show a remarkable increase in turbine performance.

Nevertheless, such models are not sufficiently realistic, to accurately assess the performance and characterize the flow field of hydrokinetic turbines in open channels, because they do not consider the change of the free-surface in their analysis. For instance, Nishi et al. [33] have found that the single-phase simulation of an axial-flow turbine, in a shallow water channel, over-predicts the turbine output by a factor of 2.0 with respect to the multiphase and the experimental results. The multiphase investigations can be grouped basically depending on the topology of the turbines studied. With respect to horizontal axis turbines, it has been studied, among other things, the effect of the closeness to the walls and the free surface on the turbine performance [34, 35], the wake recovery [36], the drop of the free surface behind the rotor [37] or the influence of the proximity to the critical Froude number [38]. There are also studies related to collection devices aimed at increasing the power output [39]. Regarding non horizontal-axis turbines, multiphase investigations of Savonius type turbines [40] and cross-flow ones [41] have focused on exploiting the free-surface simulation to obtain the optimal depth position. Although sometimes, as in the last mentioned article, there is also an in-deep study on the velocity and the pressure fields. Also, in relation to the Darrieus type turbines, the topology with the horizontal-axis (perpendicular to the current), has been the most studied. As before, the influence of the depth [42] and the submersion [43] has been particularly investigated. Some researches have been carried out on the Darrieus turbines inside open channels and their interaction with the free-surface, however this investigations address only the turbine in its horizontal position [42,43].

The main objective of the present study is to characterize experimentally and numerically the performance of a small vertical-axis turbine under different flow and free-surface conditions. Also, an intensive three-dimensional multiphase simulation has been carried out to understand the complex free-surface flow field around the turbine rotor and to clarify its influence on the turbine output. Experimentally, the

Table 1

Turbine rotor specifications.

Parameter	Specification
Rotor diameter (D)	0.15 m
Rotor height (H)	0.15 m
Blade profile	NACA-0015
Chord length (C)	0.05 m
Solidity (σ)	2
Number of blades (n)	3
Shaft diameter (d_s)	0.01 m

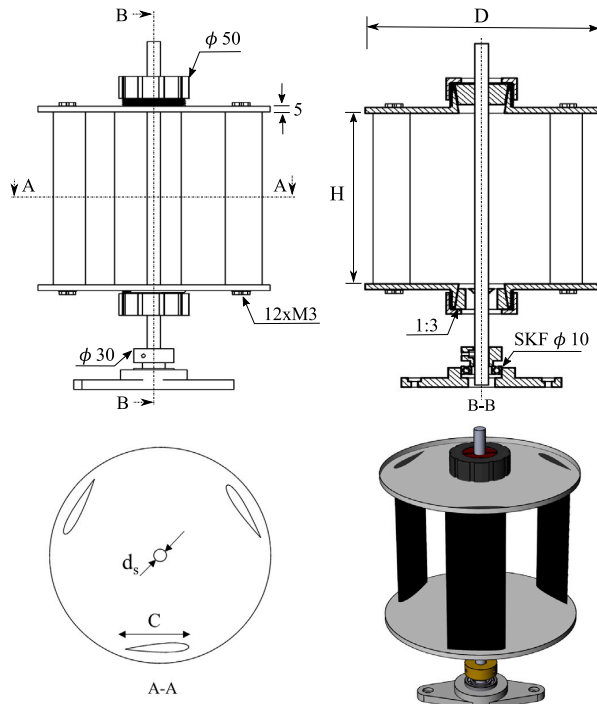


Fig. 1. A detailed schematic of the turbine model.

turbine model design and fabrication aspects are presented. In addition, the experimental test rig including the instrumentation is explained in detail. Numerically, the volume of fluid (VOF) model is used to track the free-surface air–water interface, and the sliding mesh technique is employed for the rotation of the turbine. The numerical model is validated against the experimental findings.

2. Model design and fabrication

A vertical-axis turbine model has been designed and fabricated. It is basically formed by three straight blades with NACA-0015 profile. The detailed schematic in Fig. 1 shows also the two ending plates, shaft-gripping system and ball bearing support. The geometrical parameters of the turbine model are provided in Table 1. These parameters have been carefully selected in order to obtain a self-starting and efficient operation. Specifically, the NACA-0015 symmetrical airfoil has been chosen due to its good hydrodynamic performance at low Reynolds number [6] and under different free-surface effects [44]. The thickness has been selected based on a comparison between different symmetrical airfoils under low flow velocity conditions [45]. Additionally, the ratio between the turbine height to the diameter (aspect ratio) has been set to 1.0, which has been found to enhance the performance of small turbines under confined conditions [46].

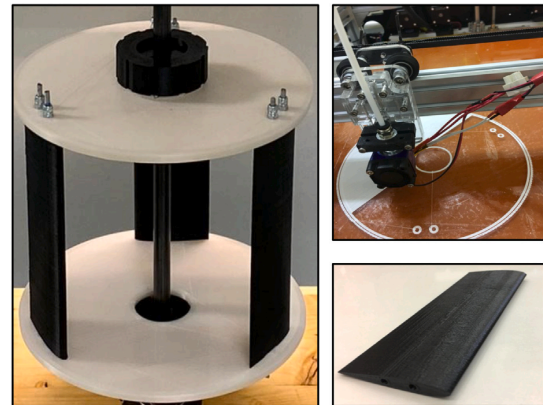


Fig. 2. Turbine model and fabrication process.

Regarding the self-starting issue, a high blade solidity has been selected as the most practical and effective solution for the low starting torque. A blade chord of 0.05 m has been chosen, resulting in a solidity value of 2.0 [7]. The experimental and numerical tests have been carried out at a Reynolds number (based on the upstream velocity and the blade chord) value around 2.5×10^4 . This value is somewhat small compared with those in real applications. However, for large scale prototypes, the performance of lift-based turbines is usually enhanced due to the better characteristics of the NACA-0015 blade profile at higher Reynolds values [47,48]. So, larger turbines will have usually better self-start and efficiency characteristics than the studied model at the same upstream velocity. Finally, the proposed model has two ending plates of 0.15 m in diameter and 0.05 m in thickness to support the turbine blades and improve the hydrodynamic performance through reducing the blade tip vortices and the flow in the span-wise direction [5].

The model is designed using 3D-CAD software and manufactured with the FDM (Fused Deposition Modeling) printing technology using Polylactic acid (PLA) material for its flexibility and high strength. The turbine components have been mounted on a steel shaft of diameter ($d_s = 10$ mm) using a slotted-chuck mechanism, allowing the turbine to be positioned at different heights. Fig. 2 shows a photo of the turbine model and its fabrication process using the additive technology.

3. Methodology

3.1. Experimental methodology

Experimental tests have been carried out in an open water channel facility to evaluate the performance of the small vertical-axis turbine under low flow velocity conditions, and to validate the multiphase flow analysis. The water channel system (Fig. 3) consists of: a rectangular-section glassed channel, with recirculation tanks, pumps and control gate. Also, it contains a brake-torque measuring system governed by a control and data acquisition (SCADA) set-up.

The channel is 1.5 m long and has a rectangular section of 0.3 x 0.5 m with water velocity in the test section ranging between 0.14 m/s and 0.9 m/s, and with a height regulated by a control gate at the discharge of the channel. The flow is achieved by two 15 kW centrifugal pumps, with a combined nominal flow rate of 600 m³/hr, with a variable velocity frequency regulation. The brake-torque measuring system has a high precision torque and rotational speed sensor, combined with a hysteresis brake (Magtrol TS103 and Magtrol HB-140M-2 respectively, with a precision of 0.1% in the torque and 0.015% in the rotating speed). The turbine is connected to the measuring system

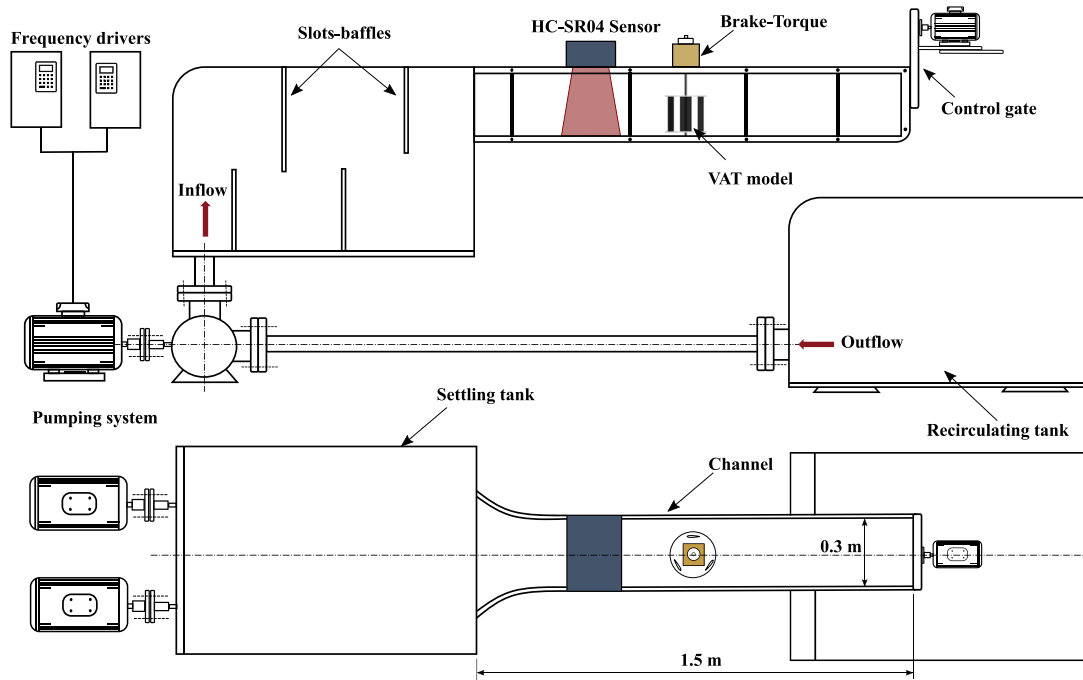


Fig. 3. The experimental test rig.

mechanically through two flexible couplings. The water height of the channel is measured with three ultrasonic sensors (HC-SR04, precision of 0.001 m) through the width of the channel. The water height is also measured in the high speed (1000 fps) videos recorded to monitor the rotation of the turbine. Due to the surface fluctuations, the uncertainty of the water average height measurements has been estimated between 0.7% and 1.1%.

In the experiments, the mechanical torque is measured together with the rotational speed N , the water flow rate Q , and the upstream water height h . From these values, the turbine power output and power coefficient $C_p = P/(0.5 \cdot \rho \cdot A \cdot U^3)$ are calculated in function of the tip speed ratio $\lambda = \Omega \cdot R/U$ (ratio between the tangential velocity of the blade tip and the upstream flow velocity). Three flow rates are used in the experiments: $Q_1 = 0.05 \text{ m}^3/\text{s}$, $Q_2 = 0.06 \text{ m}^3/\text{s}$ and $Q_3 = 0.065 \text{ m}^3/\text{s}$. For each flow rate, different flow conditions are obtained using the control gate, ranging from the lowest applicable velocity up to the maximum possible velocity (critical flow condition at channel outlet). From these values, five upstream flow velocities are selected for each flow rate within the range from 0.33 m/s to 0.69 m/s.

3.2. Numerical methodology

3.2.1. The model

A three-dimensional multiphase analysis – considering the water free-surface – has been performed using ANSYS FLUENT software to simulate the turbine model. From the experimental results, three different cases have been selected for the simulation. The first case (C_1) in which the channel is fully-filled with water and the control gate is slightly opened, with an upstream velocity value of 0.43 m/s; the second case (C_2) with an intermediate opening and an upstream velocity value of 0.57 m/s; finally, the third case (C_3), where the control gate is fully opened and the upstream velocity value reaches 0.69 m/s. In addition, for the first case configuration, a single-phase three-dimensional simulation, without considering the free-surface, has also been carried out for comparison with the multiphase results, to examine the effect of the free-surface on the turbine output.

The volume of fluid (VOF) method developed by Hirt and Nichols [49] is applied in the present simulation to model the free-surface (air/water interface). It has been selected for its capability of reproducing and capturing the free-surface deformation accurately under different flow conditions. For this method, the water volume fraction is defined as $\alpha = V_w/V$, where V_w is the water volume in the cell and V is the total volume of the mixture. The physical properties of the air–water multiphase fluid can be calculated as:

$$\rho = \alpha \cdot \rho_w + (1 - \alpha)\rho_a \quad (1)$$

$$\mu = \alpha \cdot \mu_w + (1 - \alpha)\mu_a \quad (2)$$

where ρ and μ are the mixture density and dynamic viscosity respectively. A value of $\alpha = 0.5$ represents the free-surface location. The VOF governing equations are the mass, momentum and volume conservation equations. The VOF model assumes that the pressure and velocity fields are the same for both phases and solves a single momentum equation [Eq. (3)].

$$\rho \frac{\partial \vec{u}}{\partial t} + \rho \cdot \nabla(\vec{u} \cdot \vec{u}) = -\nabla p + \mu \cdot \nabla^2 \vec{u} + \rho \cdot \vec{g} + \Gamma_\sigma \quad (3)$$

where u and p are velocity and pressure field respectively, \vec{g} is the gravitational acceleration vector and Γ_σ is the surface tension term. In this approach, the tracking of the interface between the fluids is accomplished by solving the volume fraction continuity equation for each of the phases excluding the reference one [Eq. (4)].

$$\frac{\partial}{\partial t}(\alpha \rho_w) + \nabla(\alpha \rho_w \vec{v}) = \sum_{w=1}^{k-1} \gamma_{w \rightarrow a} \quad (4)$$

where a and w refer to the reference phase (air) and the secondary phases (in this case is only one, water), k is the total number of phases, and $\gamma_{w \rightarrow a}$ is the mass flow rate per unit volume from each secondary phase to the reference one.

3.2.2. Computational domain

The computational domain is divided into two main regions: the inner domain, which includes the turbine model and corresponds to

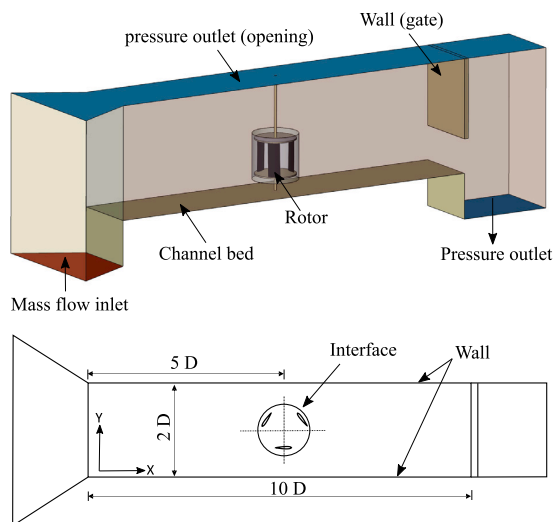


Fig. 4. Computational domain.

the rotating region, and an outer domain for the rest of the channel corresponding to the stationary region. A sketch of the computational domain including the boundary conditions is shown in Fig. 4.

The domain dimensions are based on the hydrodynamic channel size used in the experimental tests, which covers 10 times the turbine diameter in length and a double diameter in width. A mass-flow inlet boundary condition has been applied to the upstream side of the channel domain, while a zero pressure-outlet boundary condition has been selected for the downstream exit. The interface region includes the simulated turbine which is located at the center of the channel region. A sliding-mesh technique has been used between these two zones, keeping the meshes connected during the different angular positions for each time-step. The turbine blade surfaces and the channel walls have no-slip wall boundary conditions. The upper surface has a pressure outlet boundary condition in the multiphase simulation cases and a zero-shear stress boundary condition in the single-phase simulation. Also, the control gate in the multiphase simulations has no-slip wall boundary and its position is changed for each simulated case.

The whole domain has been discretized using a fully structured mesh with hexahedral shaped cells. Fig. 5 illustrates the details of the computational grid for both of the turbine rotor and the channel. Three mesh sizes (*L*, *XL* and *XXL*) have been used to check the mesh quality as listed in Table 2. A refinement factor (*RF*) has been applied around the turbine blades, keeping the first layer height around the blades constant at 1.2×10^{-5} m from the wall surface, resulting in a maximum non-dimensional wall distance (y^+) of 0.7. This value is acceptable to resolve the viscous sub-layer as recommended by the transition turbulence models.

3.2.3. Grid quality evaluation

The Grid Conversion Index (*GCI*) method developed by Roache [50] has been applied to test the mesh refinement. It is based on the generalized Richardson extrapolation, involving comparison of discrete solutions in two different spacing meshes. In the current study, the *GCI* method has been performed for the three meshes in Table 2, using the torque coefficient as the reference value, with a recommended safety factor of 1.25 [50], and a calculated order of convergence value of 3.0. The results of the static torque coefficients and the convergence rates for the three simulated meshes are also presented in the table. The GCI_{12} has been found to be 0.172%, while the GCI_{23} has a value of 0.018% with the asymptotic convergence value of 0.935. This

Table 2
Mesh quality analysis.

Size	Rotor volumes	Total volumes	C_T	Error %	GCI %	RF
Coarse, <i>L</i>	503,622	1,005,3727	0.247	–	–	0.5
Baseline, <i>XL</i>	889,800	1,391,550	0.2581	0.1719%	4.2%	1
Fine, <i>XXL</i>	1,720,200	2,221,950	0.2593	0.0187%	0.4%	2

corresponds to 0.4% change in the torque coefficient value when the mesh is refined from *XL* to *XXL*, indicating that further refinement of the baseline mesh has small influence on the output results.

The Reynolds Averaged Navier–Stokes equations (RANS) is solved using the shear stress transport (*k- ω SST*) turbulence model developed by Menter [51]. This model combines a robust formulations of the near-wall taken from the *k- ω Wilcox* model [52] with the far-wall *k- ϵ* model, through a blending function that ensures a smooth transition between both.

To initiate the simulation, a steady flow calculation is performed to fill the water channel using the same parameters corresponding to the experimental test case (mass flow inlet and control gate height). After the steady simulation process stabilizes and converges, the reference water height obtained from this preliminary simulation is verified with the experimental one. Subsequently, a transient simulation is carried out, in which the time step size corresponds to the time required to move the rotor one small fraction of a turn. Fig. 6, compares results obtained with different degrees/time-step values. It has been found that decreasing the degrees/time-step below $1^\circ/\text{step}$ has a negligible influence, (only 0.38% for $0.5^\circ/\text{step}$). Thus, that value has been applied as a good trade-off between accuracy and computational cost.

The time step convergence criterion has been set for all parameters at 10^{-6} . The overall convergence criterion is based on the variation of the averaged torque coefficient value over a complete revolution between two successive cycles. At the beginning of the solution, starting instabilities have been observed followed by a transient phase (Fig. 7). To achieve a periodical solution with a variation of less than 1% between two subsequent cycles, 28 numerical revolutions have been calculated, even if the solution usually stabilizes earlier.

4. Results and discussion

In this section, the results from the experimental testing and multiphase numerical simulations are used to assess the performance of a small vertical-axis hydrokinetic turbine in an open water channel. The parameters analyzed include the upstream velocity, the Froude number and the free-surface variations.

4.1. Experimental performance characteristics

Experimental tests have been carried out for three flow rates, with several flow conditions (upstream velocities) for each one. The power produced by the turbine has been plotted in Fig. 8. At the top, the power is presented as a function of the rotational speed, while the bottom shows the dimensionless power coefficient as a function of the tip speed ratio. Results have been obtained corresponding to five upstream velocities per flow rate.

For each upstream velocity, the maximum rotational speed corresponds to the zero-load condition. By increasing the turbine load, the rotational speed decreases until it reaches the maximum power point (MPP). From that point on wards, the power output from the turbine decreases with the decline of the rotational speed, which makes this part of the curve unstable. It can also be observed that, by increasing the upstream velocity values, the power output increases and the rotational speeds are shifted to higher values. Similarly, the same trend has been obtained for all upstream velocities, except for the flow rate Q_1 at a velocity of 0.61 m/s. For this flow condition, the water level at the upstream side is nearly at the same elevation as the turbine top

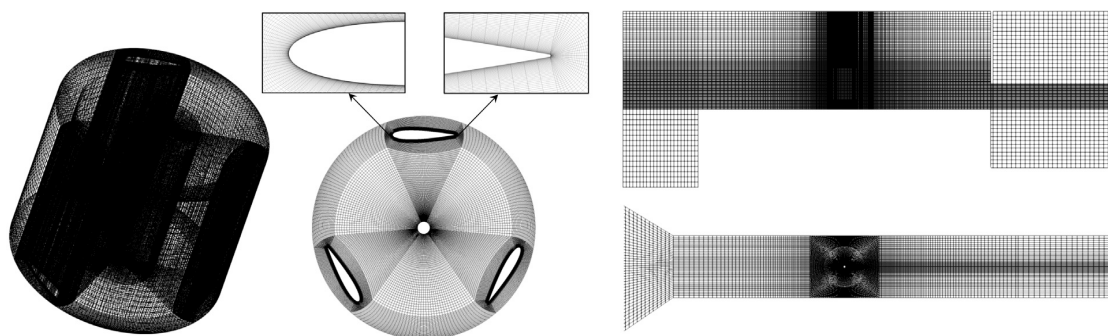


Fig. 5. Computational grid.

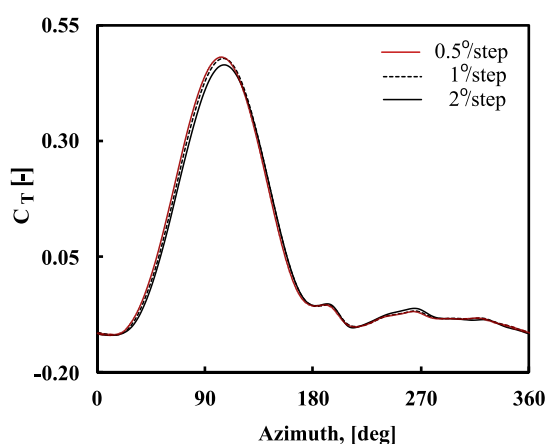
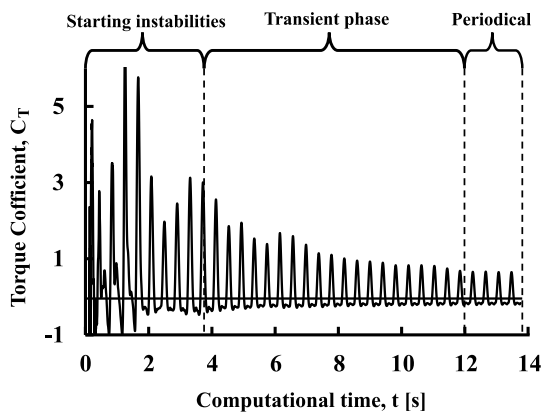
Fig. 6. Torque coefficient for different time-step values at $\lambda = 2.6$.

Fig. 7. Numerical calculations of the torque coefficient of a single blade over 28 cycles.

plate and, due to the water surface drop in the downstream side, the backside of the rotor is exposed to the air.

The characteristics of the vertical-axis turbine are traditionally expressed in terms of the non-dimensional parameters tip speed ratio λ and power coefficient C_p , to better compare the performance at different flow rates and upstream velocities. For an ideal turbine operating in an open field (with no blockage effect), those curves should be identical, but for a non-ideal turbine operating in a confined channel,

the characteristic curves have significant differences (Fig. 8). For each flow rate, the peak power coefficient increases with the upstream velocity. This effect is related to the blockage ratio. When the channel is fully filled with the flow, the turbine model occupies 15% of the channel cross-section. This condition is achieved at the smallest practical velocity for all flow rates. To increase the upstream water velocity, for a fixed flow rate, the water height has to go down, increasing the blockage ratio up to a maximum value of 23.8%.

In fact, the Froude number (ratio between characteristic flow velocity to gravitational wave velocity) plays an important role on the power obtained because it combines the effect of upstream velocity and blockage. It is calculated from $Fr = U/(gh)^{0.5}$ where g is the gravitational acceleration and h is the water height. The effect of the upstream Froude number on the maximum power output MPP for different flow rates is shown in Fig. 9. The Froude number has been varied over a subcritical range of [0.15–0.38] by changing the gate height for different flow rates, giving the aforementioned blockage ratio range of [15%–23.8%]. By increasing the Froude number, which implies an increase in the upstream velocity and a decrease in the upstream water height, the maximum power output from the turbine rotor increases. In the figure it can be seen that, for the higher flow rates (Q_2 and Q_3), the influence of the Froude number on the power is practically linear. However, the lower flow rate Q_1 shows a quite different behavior even with a drop of the maximum value. As mentioned above, this is mainly due to the interference of the free-surface with the turbine.

4.2. Numerical model validation

In the present study, the numerical model has been validated with the experimental data in two steps; the first one is by comparing the turbine characteristic curve, that is obtained experimentally, with the multiphase and single-phase simulations for the first case (C_1) as shown in Fig. 10. The second validation method compares the free-surface from the experimental tests with those obtained from the multiphase simulation of the three cases C_1 , C_2 and C_3 as illustrated in Fig. 11 and in Fig. 12.

With respect to the turbine characteristic curve, the comparison case C_1 corresponds to the maximum flow rate Q_3 and an upstream velocity of 0.43 m/s, with the channel nearly overflowing. A reasonably good match has been found between the experimental and the numerical results for the whole range of tip speed ratios (Fig. 10). Single-phase and multiphase simulations show the same tendencies as the experiments, confirming that the main flow physics are correct in both of them. However, the single-phase model values are somewhat higher than the experimental ones. Most likely because this numerical model does not consider the free-surface deformations found in actual reality, specifically the change in the free-surface level around the rotor when the power is extracted from the turbine. In fact, the difference between the single-phase model and the experiments tends to increase with the

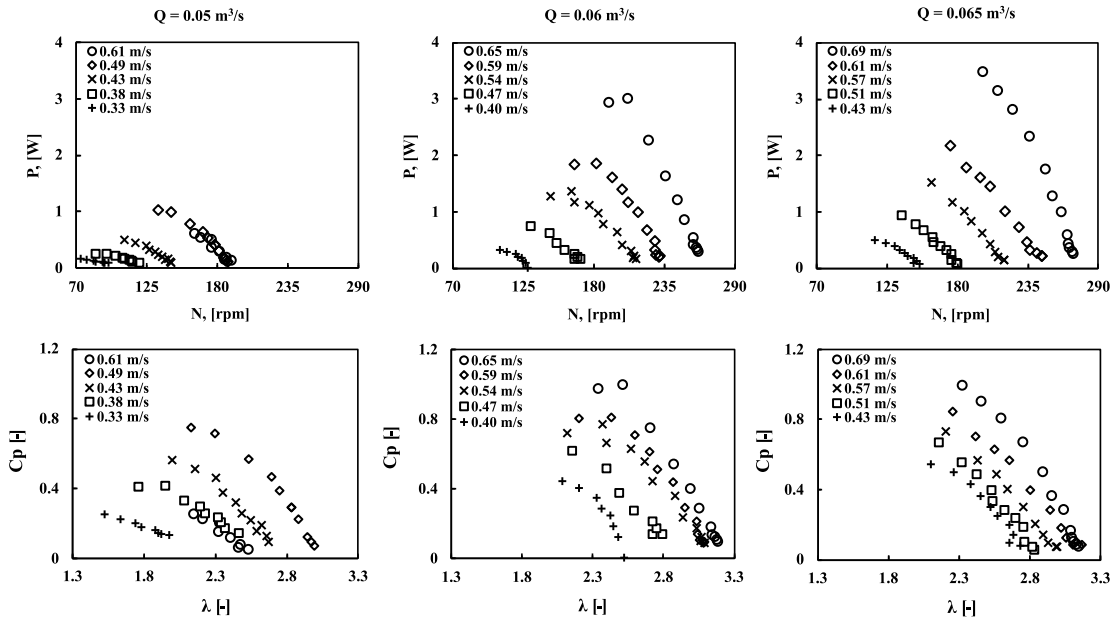


Fig. 8. Power and characteristic curves for different upstream velocities.

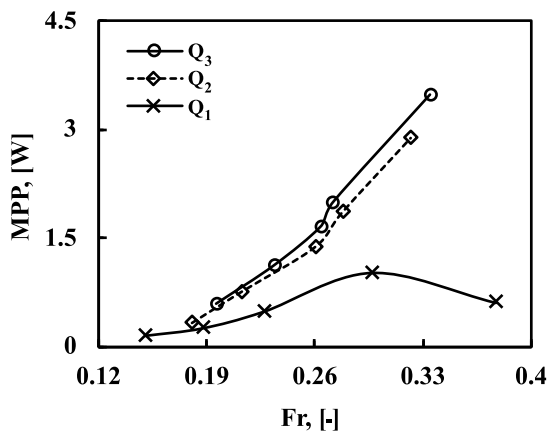


Fig. 9. Variation of MPP with the upstream Froude number for different flow rates.

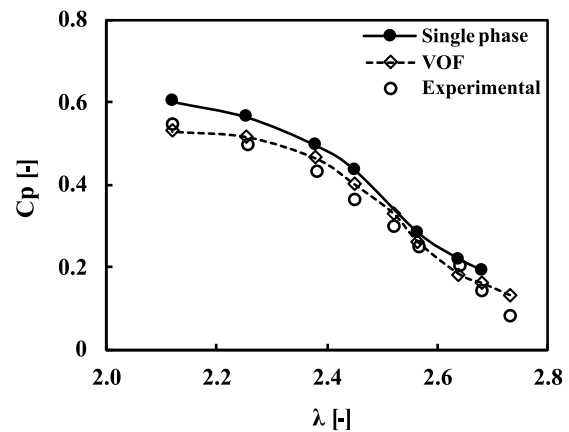


Fig. 10. Characteristic curve validation for (C_1).

power extracted (as the tip speed ratio decreases). By considering the free-surface variations, the VOF model obtains power coefficients much closer to the experimental measured ones for the whole range of the tip speed ratios.

Regarding the free-surface comparison between the experiments and the VOF model, three cases have been selected, corresponding to the highest flow rate Q_3 and the tip speed ratio of $\lambda = 2.3$, but with different upstream velocities. Fig. 11 shows the comparison of the free-surface levels at the middle of the channel for the three cases C_1 , C_2 and C_3 . The results are quite consistent in all of them, following the free-surface variations even when the flow becomes supercritical as in the C_3 case.

Although in a more qualitative mode, Fig. 12 shows the three-dimensional shape adopted by the free-surfaces, comparing the results of the VOF model with the experiments. The VOF model is able to simulate not only the longitudinal variations, but also the interactions with the channel wall boundaries. In C_1 case, it can be observed that

there is a slight decrease of the free-surface just after the turbine, which recovers quickly. In the C_2 case, the drop after the turbine is deeper, corresponding to a higher energy extraction. The subsequent recovery is also more abrupt and turbulent, although the original level is also recovered. In both cases, the free-surface drop is quite smooth covering the whole width of the channel, while the recovery shows more disturbances and wave reflections from the channel walls. In the C_3 case, corresponding to the maximum inlet velocity, the energy extraction is also the highest, which requires the flow to go from a subcritical regimen before the turbine to a supercritical one after the turbine.

4.3. Performance and flow field analysis

The torque produced by the turbine is the sum of each blade contribution. The numerical model enables to easily visualize the variations

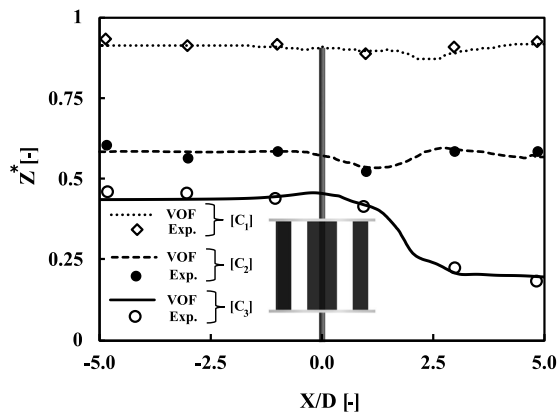


Fig. 11. Free-surface validation with the experimental normalized heights ($Z^* = h/L$) at $\lambda = 2.3$.

produced during each revolution of the rotor and even the effect corresponding to each blade. For instance, Fig. 13 shows the polar distributions of the instantaneous torque coefficient C_T as a three lobed rosette, corresponding to the current three-blades turbine model. The figure compares the results for the case C_1 with the single phase model against the VOF model, for two different tip speed ratios. It also shows the results for the cases C_2 and C_3 with the VOF model.

The three lobes are very clearly defined, which implicitly means that the positive effect of each blade is limited to a relatively small angular range. The peaks coincide in all cases indicating that the angular zone of maximum effect does not change with the upstream flow velocity nor the tip speed ratio, but is geometrically defined. Similar polar trend for a Darrieus horizontal axis water turbine has been reported by Le Hocine et al. [43]. The comparison between the single-phase and VOF simulation shows that the variations are more pronounced in the former, especially when increasing the tip speed ratio. For the cases of the VOF model, the three lobes are also more defined at the higher tip speed ratio, although not as much as in the single phase model.

In this kind of polar figure, the total torque coefficient of the turbine is equivalent to the area enclosed by each curve. The variation in the total torque coefficient between the two tip speed ratios is clearly seen, for instance, the total torque coefficient for the C_1 case is 0.225 for $\lambda = 2.3$ and 0.083 for $\lambda = 2.7$. The average difference between both tip speed ratios is about 52%, as the lower tip speed ratio ($\lambda = 2.3$) always producing more power. The difference in area is also evident between the three cases for each tip speed ratio ($C_3 > C_2 > C_1$). For instance, at $\lambda = 2.3$, the torque coefficient of C_2 case is 38% higher than C_1 one, while the C_3 case is 49% higher. Also the lobes are less defined as the power increases, denoting an increase in the positive angular range.

The change in the turbine output and its performance is directly related to the flow around the turbine rotor and its blades, also with the deviation caused by the deformation of the free-surface. To further explore the phenomena, the velocity vectors at the middle of two different planes for the three VOF simulated cases are shown in Fig. 14. An horizontal plane passing through the mid-height of the turbine on the left (Fig. 14a) and a vertical longitudinal plane passing through the axis of the turbine on the right (Fig. 14b).

In this figure, the wake is clearly visualized. It has different extensions in each case and it is slightly deviated towards the rotational direction of the turbine (upward in Fig. 14a). There are also zones of low velocity in front of the turbine and in the center of the rotor, where the flow slows down. Around the turbine –laterals, top and bottom– the velocities increase, more so the higher blockage (for C_1 , C_2 and C_3 cases the blockage ratios are 15%, 19% and 24% respectively). Inside the

turbine and specifically in the influence zone of the blades, the velocity has also an important circumferential component due to the drag of the blades. The low velocity field around the turbine shaft is most likely due to this circumferential flow. The increase in the velocity around the turbine as a consequence of the blockage is much higher when the turbine is in a channel than in an open field condition. Moreover, the blockage and corresponding velocities increase as the height of the upstream free-surface decreases from C_1 to C_3 case. However, a feature that contrasts with the situation in the open field is the reduction of the flow cross-section downstream of the rotor. In the open field condition, the turbine blockage forces the flow around the turbine to expand until the wake is absorbed. But, as the turbine is inside a channel condition, the free-surface area in the wake zone decreases in elevation.

This has been explained, for instance, by the analytical model offered by Housby et al. [21], which is an extension of the Linear Momentum Actuator Disc Theory (LMDAT). In this model, the flow is decomposed into two main streams; the first one passes through the turbine rotor, loses a part of the energy, and expands behind the turbine in the wake region. The second one is the bypass zone which is formed around the turbine rotor, where no energy is extracted and a higher velocity field is developed due to the turbine blockage. The flow is accelerated in the bypass zone to conserve the mass flux in the wake region causing a reduction in the static head and consequently reducing the free-surface level. Usually, the free-surface elevation is partially recovered when the bypass zone is mixed with the wake and the velocity is equalized. However, in certain cases (if the Froude number is sufficiently high) the flow become supercritical as in C_3 . Paradoxically, the wake extension is reduced as the blockage increases. The drop of the free surface is responsible for this faster wake recovery, because it can be regarded as a contraction of the flow in a nozzle. The difference in levels or more correctly in total head between the upstream and downstream zones is the energy extracted from the flow, although the energy obtained by the turbine is somewhat lower because of the losses produced in the wake. This energy extraction is directly linked to the magnitude of the velocity in the turbine, specifically around the blades. Therefore, the greater the blockage –and the deeper the free surface drop– the more power is obtained.

The wake recovery process can be analyzed in more detail as shown in Fig. 15, which presents the velocity vectors with the normalized vorticity contours (normalized with the upstream velocity and blade chord ratio $\zeta^* = \nabla \vec{u} / [u \cdot c]$) in two sectional plane views: one in the mixing zone, about one diameter behind the turbine rotor (Fig. 15a), and another one in the far-wake region, about two diameters downstream (Fig. 15b). For the three cases, in the mixing zone a low velocity wake region can be appreciated and how the flow in the bypasses around the rotor shifts to fill this area, developing two distinctive main vortices located in the wake of the turbine plates. With the wake evolution from the mixing zone to the far-wake region, these vortices coalesce in one main vortex, leaving a wake which is swirling in a clockwise direction. With the colors of the vorticity contours, it can be noticed that in the mixing zone the vortices have a high intensity and a reduced extension, while in the far-wake the main vortex has a much larger distribution but it is somewhat mitigated.

To further explore the effect of the free-surface on the blade hydrodynamics, the relative streamlines around the turbine blade at various azimuth angular positions from $\theta = 60^\circ$ to $\theta = 300^\circ$ are illustrated in Fig. 16. The angles of 60° and 120° correspond to the zone where positive torque is obtained, while those of 240° and 300° are in the resistance zone. The incidence angle of the relative streamline velocity at the leading edge increases from C_1 to C_3 , especially in the positive production zone, where the lift force direction increases the torque values and the hydrodynamic efficiency. In the C_1 case, the incidence angles are the lowest –very close– to zero but still enough to obtain a positive torque at 60° degrees– and there is no separation at any point. This is favorable in the positive production zone but not in the rest where a noticeable resistant torque is attained. In the cases of

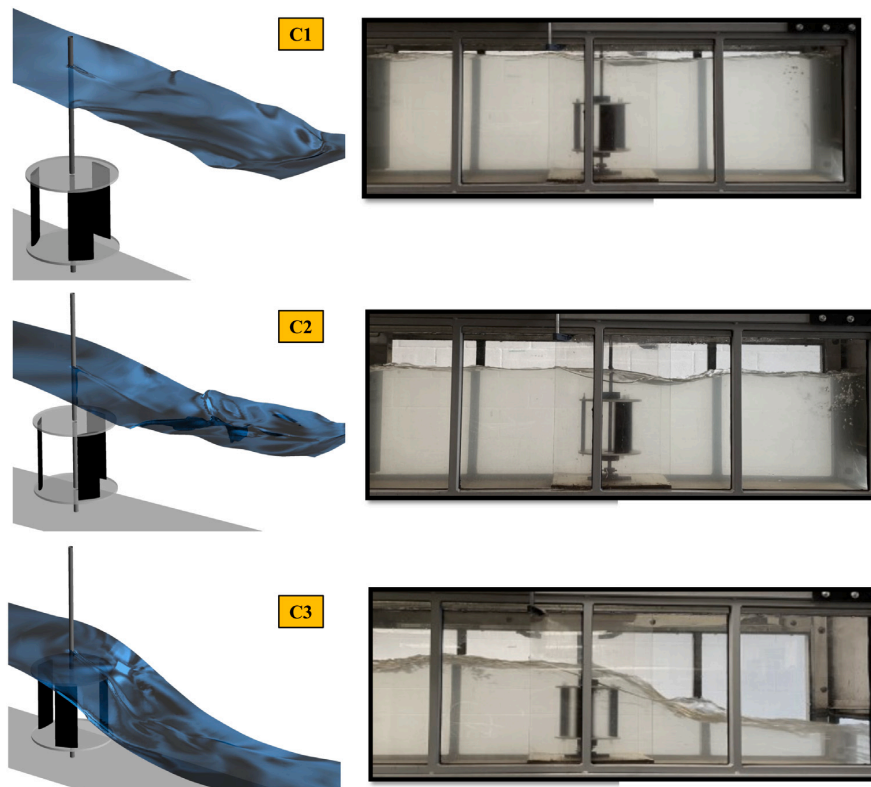


Fig. 12. Free-surface shape around the turbine rotor (isosurface water fraction of 0.5) at $\lambda = 2.3$.

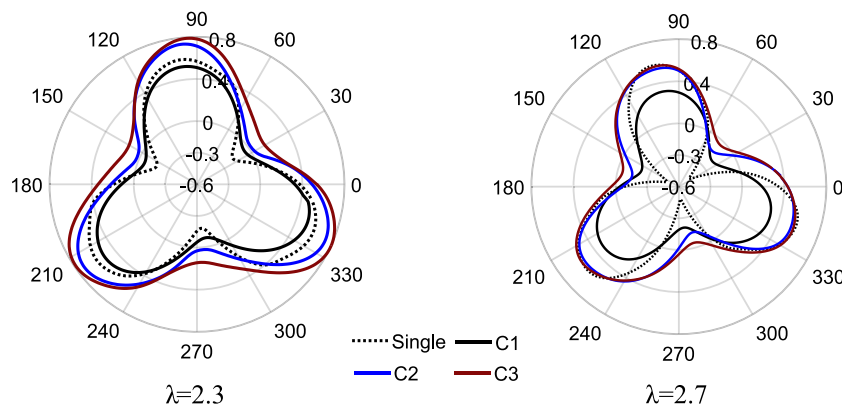


Fig. 13. The polar distributions of the instantaneous torque coefficient (single phase and VOF model cases).

C_2 and C_3 , the free-surface is nearer to the turbine and the relative flow angles have a larger variation range which even leads to the flow separation. Specifically, for the C_3 case, it can be seen how the separation is quite strong with clear separation bubbles. The detachment of the flow at the angle range between 240° and 300° , reduces the forces that generate the rotation resistance, so that the torque does not even become negative in spite of the increased drag. This type of hydrodynamic stall is very specific for these cross-flow turbines but does not exist in axial ones. In the latter it has been found that the primary mechanism of the performance change is linked to the free surface deformation [34]. However, for the model in the current study, the C_3 case has extreme free-surface deformation, but the separation

is already detected in the C_2 case where the shape change of the free surface is not so pronounced. Although further study is needed, it seems that the increase of the incidence angle that generates the positive torque is quite gradual, but the separation of the flow in the resistance zone produces a sudden increase of the power obtained. This indicates that the change in performance is more related to the depth of the free surface than the change in shape.

Fig. 17 shows the pressure coefficient distribution on a single blade for different angular positions and corresponding to the three cases analyzed. A detail of the position and the pressure distribution contours for the C_2 case has been superimposed as a reference at the lower right corner. In these figures, the area between the pressure and suction sides

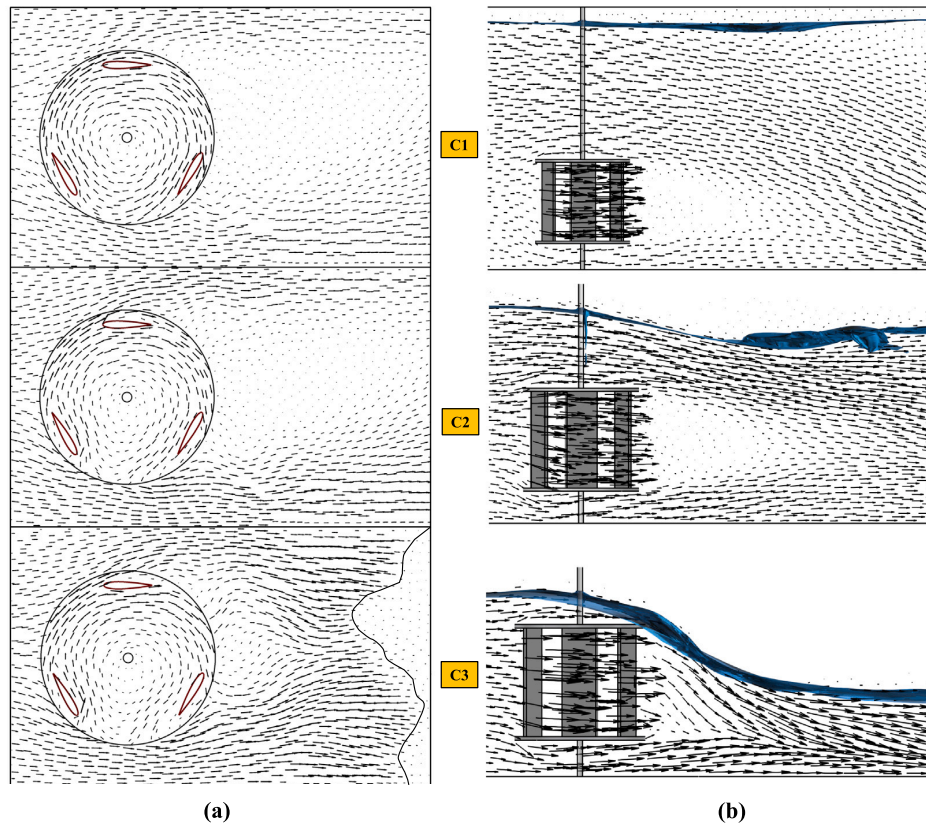


Fig. 14. Velocity vectors with Iso-surface shape ($\alpha = 0.5$) at two different planes: (a) $Z/H = 0.5$ and (b) $Y/D = 0$, at $\lambda = 2.3$.

is proportional to the lift. Normally, this area is desired to be as large as possible, but in cross-flow turbines, the scenario is complicated: the direction of the relative velocity changes substantially around the rotor, so that the velocity component contributing to the driving torque can become even negative for certain angles and flow rates.

In fact, of the angles shown in the figure, only the 60° and 120° ones are in the positive torque zone for this turbine, while the rest are in –what can be called– the resistance zone. For the former ones, the behavior is typical of an airfoil, with over-pressure on one side and under-pressure on the other. The area (lift) grows with the upstream velocity, from the C_1 to the C_3 case. For the 60° , the distribution is very smooth in all three cases as it corresponds to a smooth flow along the profile. For the 120° , in the C_2 and the C_3 cases, a separation bubble is observed near the leading edge although the flow reattaches and there is no stall. This partial separation is due to the increase of the blockage and the lowering of the free-surface from the C_1 to the C_3 case. These effects not only raise the velocity magnitude but also increase the angle of attack, which becomes very close to the limit for the 120° angle.

For the 180° , the pressure coefficient on both sides of the profile practically coincides, thanks to the similarity in the direction between the tangential velocity of the blade and the flow velocity at this position. For the rest of the angles (0° , 240° and 300°), located in the resistance zone, the pressure coefficient behavior is very different from a typical aerodynamic profile. On the face that would correspond to the pressure side, the coefficient begins with an over-pressure peak –which is expected– but then the pressure drops even below the value on the suction side. The same happens, inverted, on the other face: it starts with an under-pressure peak but then rises to even positive values. This line crossover causes a positive lift near the leading edge and a

negative one in the middle and the rear part of the blade. This abnormal behavior is due to the high blade solidity which causes a significant low pressure at the inner zone of the turbine. This effect, along with the blockage discussed above, results in a large change in the direction of the relative velocity. So large that there are areas where the torque force is effectively opposite to the motion, reducing power generation. The C_2 and C_3 cases are further complicated by the separation that causes a second crossing of the pressure coefficient lines. Normally this separation is undesirable because it decreases lift and torque but, in this case, since the torque is negative, the separation is favorable because it minimizes this negative effect.

The normalized vorticity fields around the turbine rotor are shown in (Fig. 18), at a longitudinal vertical plane on the left side (a), and at an horizontal plane passing through the mid-height of the turbine on the right side (b). In both cases, the value represented is the vorticity component perpendicular to each plane, normalized with the upstream velocity and blade chord ratio.

In the vertical plane, the vortices generated by the lower and upper turbine plates can be observed, straddling the wake behind the turbine. The intensity of these vortices and their downstream extension increase with the free-surface lowering (from C_1 to C_2), consistent with the increase in the longitudinal velocity generated by the blockage. However, in the C_3 case, the free-surface drop and the flow convergence behind the turbine produce a much faster mixing of the vortices with the central part of the wake. In the horizontal plane (Fig. 18b), the velocity component corresponds to the blades circulation and has higher values than the transverse directions. It can be clearly visualized the opposing vortices generated on the suction and the pressure sides of the profiles. In the absence of separation, these vortices extend far behind the blade in a smooth and continuous manner, until they interact with

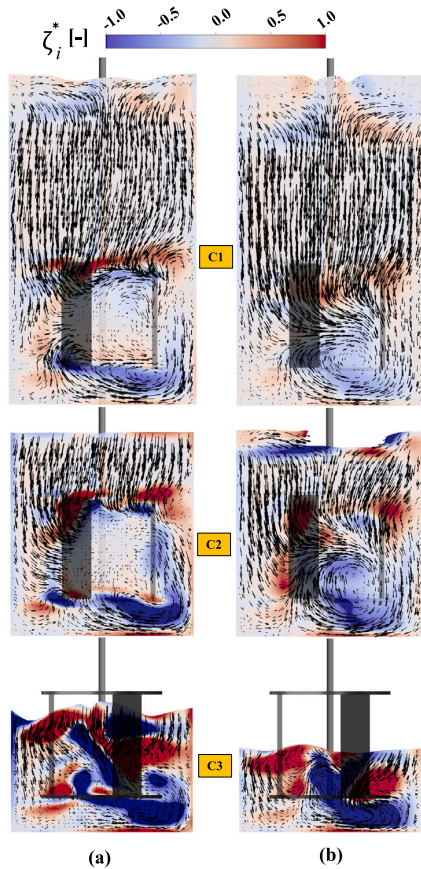


Fig. 15. Velocity vectors with normalized vorticity contours ($\zeta^* = \nabla \bar{u} / (u \cdot c)$) at two downstream planes: (a) $X/D = 1$ and (b) $X/D = 2$, at $\lambda = 2.3$.

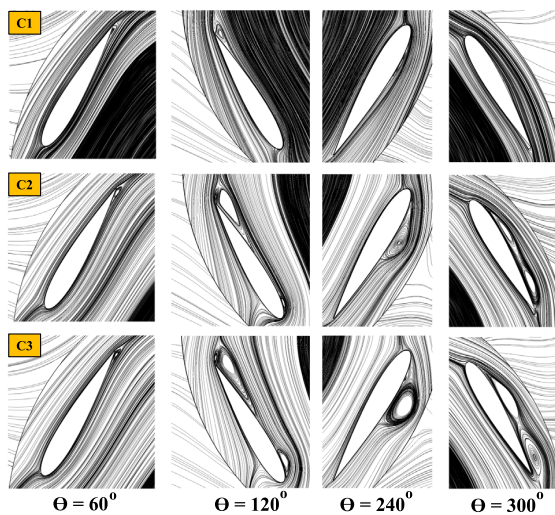


Fig. 16. Instantaneous streamlines around the blade profile at various azimuth angular positions.

the following blades. These vortices separate on each side of the wake, forming a kind of von-Karman street. In the C_1 case, these vortex zones

are smooth lines that take time to disappear. As the upstream velocity increases (C_2), discrete separations of the vortices begin to develop while still maintaining a certain order. For the extreme case (C_3), these separations are much more chaotic, with interaction between the vortices rotating in opposite directions.

The two ending plates cause the flow to be more bi-dimensional between them reducing the vertical drift. In fact, the flow field is quite similar in any section inside the turbine except near the plates. Fig. 19 shows the normalized vorticity fields –corresponding to the C_1 case– around the turbine blades at two different horizontal planes; the upper one at mid-height of the turbine (a), and the lower one near the turbine plate (b). At mid-height, there is no flow separation as the blades rotate, the vortices distribution is very smooth and gradual. The clockwise vortices (negative vorticity values, blue color) separates quite continuously on the left side of the turbine wake (at the top of the figure). However, the counter-clockwise vortices (positive vorticity values, red color) have a discrete pattern with larger vortices separating each time a blade crosses the wake. Close to the plate, the interaction between the vortices of the blades with the plate boundary layer increases the instability. In fact, this interaction generates asymmetric horseshoe-shaped vortices that, on separation, form the main structures of the wake. This can be visualized more clearly in Fig. 20, in which the value of the helicity (the vorticity along the velocity vector) is used to create a three-dimensional image of the horseshoe vortex cloud that forms in the wake of the turbine plates. Although, the vortices generated from the two ending plates seem to increase the complexity and the losses in the wake zone, the plates are very useful from the mechanical point of view to support the turbine blades, and actually improve the hydrodynamic performance. Apart from reducing the blade-tip effects, the plates prevent air from entering the turbine when the surface drops significantly.

5. Conclusions

The performance and the flow field characteristics of a small vertical -axis hydrokinetic turbine inside an open channel have been investigated, through a series of experiments and a free-surface flow analysis, under various operation conditions.

Experimental tests have been carried out for three flow rates with different upstream velocities. It has been found that the peak power coefficients increase with the upstream velocity, and the corresponding tip speed ratios shift to higher values. This effect is directly linked to the blockage ratio and the Froude number. For the higher flow rates (without interference of the free-surface with the turbine), the influence of the Froude number on the power is practically linear.

An intensive three-dimensional multiphase simulation has been carried out to understand the complex free-surface flow around the turbine and its relevance on the overall performance. A reasonably good match has been found between the experimental and the numerical results. The single-phase model values are somewhat higher, as it does not consider the free-surface deformations around the rotor. The VOF model is able to simulate not only the free-surface longitudinal variations, but also the interactions with the channel wall boundaries. The power coefficients obtained are much closer to the experimental ones for the whole range of tip speed ratios. Polar plot diagrams have been used to represent and compare the contribution of each blade on the output torque.

The velocity field around and inside the turbine rotor has been analyzed and correlated with the free-surface variations from upstream to downstream of the turbine. The energy extraction is found to be directly linked to the magnitude of the velocity in the turbine, specifically around the blades, and increasing with the free-surface drop. The surface change is also responsible for the wake recovery behavior.

The relative velocity and the pressure coefficient distribution around the blades have been analyzed with different azimuth angles

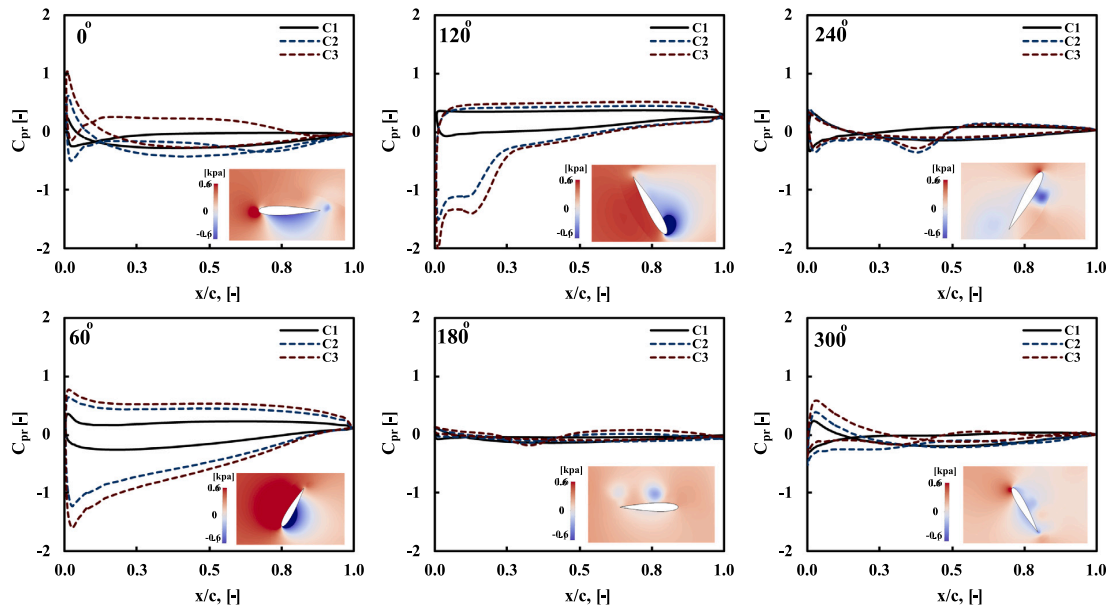


Fig. 17. Pressure coefficient for all cases and pressure contour samples of C_2 on a single blade at $\lambda = 2.3$.

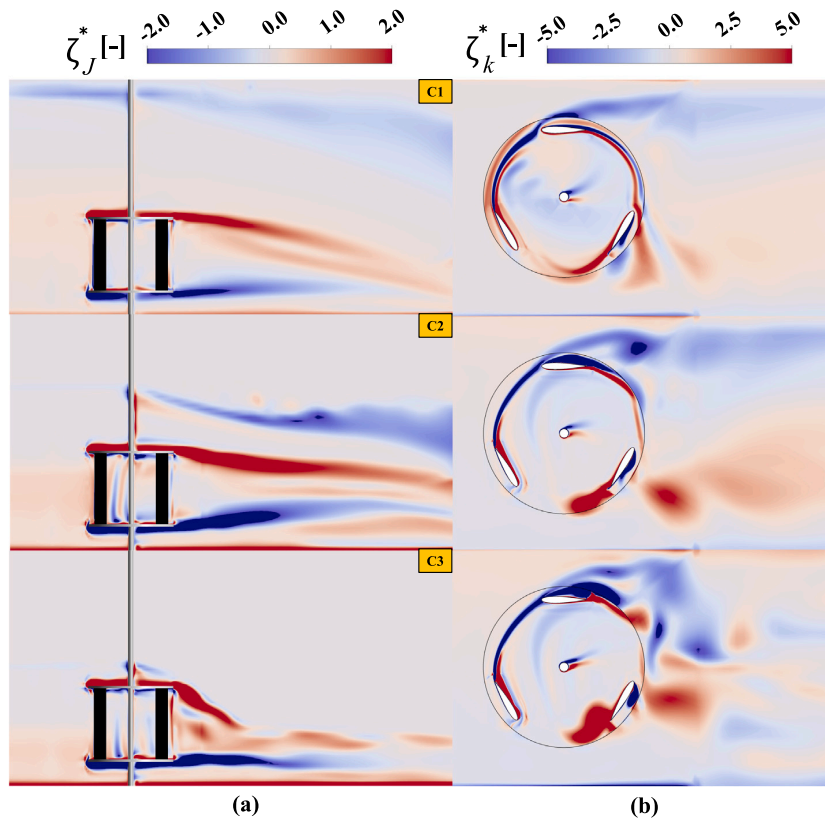


Fig. 18. Normalized vorticity fields ($J - K$) at the middle sections for all cases.

and have provided a better insight into the positive torque production zones and their relation with the flow separation. An abnormal behavior of the pressure coefficient -a crossover from the pressure to

the suction side- have been detected for some cases at specific angular positions. This has been caused by the low pressure zone inside the rotor, due to the high solidity of the blades. The vorticity generated

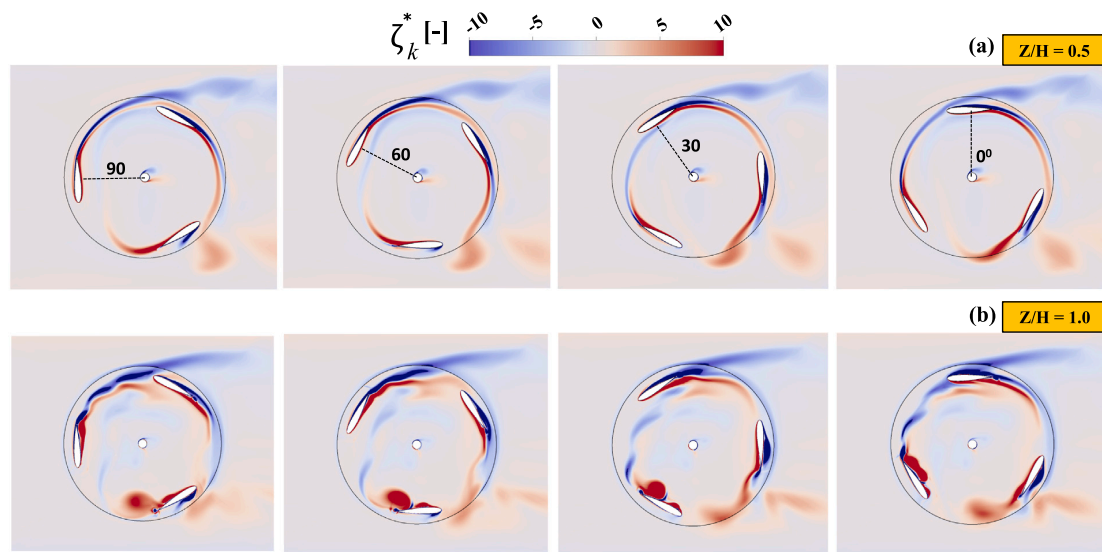


Fig. 19. Normalized vorticity-K contours for four angular positions at two different plans at $\lambda = 2.3$.

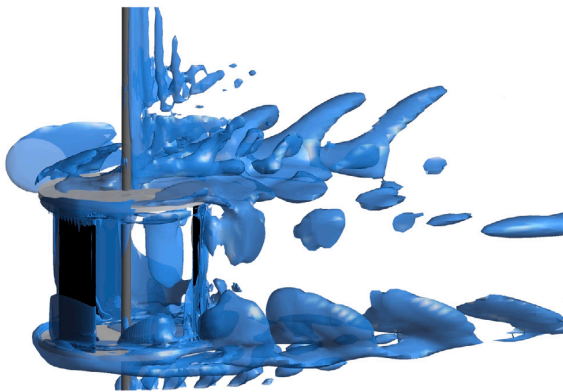


Fig. 20. Absolute helicity showing the horseshoe cloud.

by the blades and the ending plates has been clearly analyzed. The interaction between both of them develops horseshoe vortices that separate from the rotor forming a vortex street.

CRediT authorship contribution statement

Ahmed Gharib Yosry: Conceptualization, Software, Methodology, Writing – original draft. **Eduardo Álvarez Álvarez:** Investigation, Data curation, Review & editing. **Rodolfo Espina Valdés:** Software, Methodology. **Adrián Pandal:** Methodology, Data curation. **Eduardo Blanco Marigorta:** Data curation, Writing – review & editing.

Declaration of competing interest

The authors declare that they have no known competing financial interests or personal relationships that could have appeared to influence the work reported in this paper.

Data availability

Data will be made available on request.

Acknowledgments

The author would like to express his gratitude to the Egyptian Cultural Affairs and Missions Sector (the Egyptian Ministry of Higher Education and Scientific Research) along with Port Said University for their financial support.

References

- [1] J. Gao, H. Liu, J. Lee, Y. Zheng, M. Guala, L. Shen, Large-eddy simulation and Co-Design strategy for a drag-type vertical axis hydrokinetic turbine in open channel flows, *Renew. Energy* 181 (2022) 1305–1316.
- [2] M. Khan, G. Bhuyan, M. Iqbal, J. Quaioco, Hydrokinetic energy conversion systems and assessment of horizontal and vertical axis turbines for river and tidal applications: A technology status review, *Appl. Energy* 86 (10) (2009) 1823–1835.
- [3] B. Kirke, L. Lazauskas, Limitations of fixed pitch Darrieus hydrokinetic turbines and the challenge of variable pitch, *Renew. Energy* 36 (3) (2011) 893–897.
- [4] M.B. Topper, S.S. Olson, J.D. Roberts, On the benefits of negative hydrodynamic interactions in small tidal energy arrays, *Appl. Energy* 297 (2021) 117091.
- [5] R. Gosselin, G. Dumas, M. Boudreau, Parametric study of H-Darrieus vertical-axis turbines using CFD simulations, *J. Renew. Sustain. Energy* 8 (5) (2016) 053301.
- [6] S.-C. Roh, S.-H. Kang, Effects of a blade profile, the Reynolds number, and the solidity on the performance of a straight bladed vertical axis wind turbine, *J. Mech. Sci. Technol.* 27 (11) (2013) 3299–3307.
- [7] M. Singh, A. Biswas, R. Misra, Investigation of self-starting and high rotor solidity on the performance of a three S1210 blade H-type Darrieus rotor, *Renew. Energy* 76 (2015) 381–387.
- [8] O. Eboibi, L.A.M. Danao, R.J. Howell, Experimental investigation of the influence of solidity on the performance and flow field aerodynamics of vertical axis wind turbines at low Reynolds numbers, *Renew. Energy* 92 (2016) 474–483.
- [9] Y.-L. Xu, Y.-X. Peng, S. Zhan, Optimal blade pitch function and control device for high-solidity straight-bladed vertical axis wind turbines, *Appl. Energy* 242 (2019) 1613–1625.
- [10] F. Jing, Q. Sheng, L. Zhang, Experimental research on tidal current vertical axis turbine with variable-pitch blades, *Ocean Eng.* 88 (2014) 228–241.
- [11] S.M. Camporeale, V. Magi, Streamtube model for analysis of vertical axis variable pitch turbine for marine currents energy conversion, *Energy Convers. Manage.* 41 (16) (2000) 1811–1827.
- [12] D.H. Zeiner-Gundersen, A vertical axis hydrodynamic turbine with flexible foils, passive pitching, and low tip speed ratio achieves near constant RPM, *Energy* 77 (2014) 297–304.
- [13] R. Gupta, A. Biswas, K. Sharma, Comparative study of a three-bucket Savonius rotor with a combined three-bucket Savonius–three-bladed Darrieus rotor, *Renew. Energy* 33 (9) (2008) 1974–1981.
- [14] B. Govind, Increasing the operational capability of a horizontal axis wind turbine by its integration with a vertical axis wind turbine, *Appl. Energy* 199 (2017) 479–494.

- [15] T. Villeneuve, M. Boudreau, G. Dumas, Improving the efficiency and the wake recovery rate of vertical-axis turbines using detached end-plates, *Renew. Energy* 150 (2020) 31–45.
- [16] D. Saeidi, A. Sedaghat, P. Alamdari, A.A. Alemrajabi, Aerodynamic design and economical evaluation of site specific small vertical axis wind turbines, *Appl. Energy* 101 (2013) 765–775.
- [17] C. Shashikumar, V. Madav, Numerical and experimental investigation of modified V-shaped turbine blades for hydrokinetic energy generation, *Renew. Energy* 177 (2021) 1170–1197.
- [18] W.-H. Chen, C.-Y. Chen, C.-Y. Huang, C.-J. Hwang, Power output analysis and optimization of two straight-bladed vertical-axis wind turbines, *Appl. Energy* 185 (2017) 223–232.
- [19] J. Gao, D.T. Griffith, M.S. Sakib, S.Y. Boo, A semi-coupled aero-servo-hydro numerical model for floating vertical axis wind turbines operating on TLPs, *Renew. Energy* 181 (2022) 692–713.
- [20] J.I. Whelan, J. Graham, J. Peiro, A free-surface and blockage correction for tidal turbines, *J. Fluid Mech.* 624 (2009) 281–291.
- [21] G.T. Houlshby, C.R. Vogel, The power available to tidal turbines in an open channel flow, *Proc. Inst. Civ. Eng. Energy* 170 (1) (2017) 12–21, <http://dx.doi.org/10.1680/jener.15.00035>.
- [22] C. Vogel, G. Houlshby, R. Willden, Effect of free surface deformation on the extractable power of a finite width turbine array, *Renew. Energy* 88 (2016) 317–324.
- [23] C. Vogel, R. Willden, G. Houlshby, Power available from a depth-averaged simulation of a tidal turbine array, *Renew. Energy* 114 (2017) 513–524.
- [24] S. Yagmur, F. Kose, S. Dogan, A study on performance and flow characteristics of single and double H-type Darrieus turbine for a hydro farm application, *Energy Convers. Manage.* 245 (2021) 114599.
- [25] P. Ouro, S. Runge, Q. Luo, T. Stoesser, Three-dimensionality of the wake recovery behind a vertical axis turbine, *Renew. Energy* 133 (2019) 1066–1077.
- [26] N. Guillaud, G. Balarac, E. Goncalves, J. Zanette, Large eddy simulations on vertical axis hydrokinetic turbines-power coefficient analysis for various solidities, *Renew. Energy* 147 (2020) 473–486.
- [27] P. Ouro, T. Stoesser, An immersed boundary-based large-eddy simulation approach to predict the performance of vertical axis tidal turbines, *Comput. & Fluids* 152 (2017) 74–87.
- [28] T. Kinsey, G. Dumas, Impact of channel blockage on the performance of axial and cross-flow hydrokinetic turbines, *Renew. Energy* 103 (2017) 239–254.
- [29] I.A. Tunio, M.A. Shah, T. Hussain, K. Harijan, N.H. Mirjat, A.H. Memon, Investigation of duct augmented system effect on the overall performance of straight blade Darrieus hydrokinetic turbine, *Renew. Energy* 153 (2020) 143–154.
- [30] K. Sun, R. Ji, J. Zhang, Y. Li, B. Wang, Investigations on the hydrodynamic interference of the multi-rotor vertical axis tidal current turbine, *Renew. Energy* 169 (2021) 752–764.
- [31] S. Zanforlin, Advantages of vertical axis tidal turbines set in close proximity: A comparative CFD investigation in the English channel, *Ocean Eng.* 156 (2018) 358–372.
- [32] B. Chen, S. Cheng, T.-c. Su, H. Zhang, Numerical investigation of channel effects on a vertical-axis tidal turbine rotating at variable speed, *Ocean Eng.* 163 (2018) 358–368.
- [33] Y. Nishi, G. Sato, D. Shiohara, T. Inagaki, N. Kikuchi, Performance characteristics of axial flow hydraulic turbine with a collection device in free surface flow field, *Renew. Energy* 112 (2017) 53–62.
- [34] N. Kolekar, A. Banerjee, Performance characterization and placement of a marine hydrokinetic turbine in a tidal channel under boundary proximity and blockage effects, *Appl. Energy* 148 (2015) 121–133.
- [35] J. Yan, X. Deng, A. Korobenko, Y. Bazilevs, Free-surface flow modeling and simulation of horizontal-axis tidal-stream turbines, *Comput. & Fluids* 158 (2017) 157–166.
- [36] A. Benavides-Morán, L. Rodríguez-Jaime, S. Lain, Numerical investigation of the performance, hydrodynamics, and free-surface effects in unsteady flow of a horizontal axis hydrokinetic turbine, *Processes* 10 (1) (2021) 69.
- [37] X. Sun, J. Chick, I. Bryden, Laboratory-scale simulation of energy extraction from tidal currents, *Renew. Energy* 33 (6) (2008) 1267–1274.
- [38] J. Riglin, W.C. Schleicher, L.-H. Liu, A. Oztekin, Characterization of a micro-hydrokinetic turbine in close proximity to the free surface, *Ocean Eng.* 110 (2015) 270–280.
- [39] Y. Nishi, G. Sato, D. Shiohara, T. Inagaki, N. Kikuchi, A study of the flow field of an axial flow hydraulic turbine with a collection device in an open channel, *Renew. Energy* 130 (2019) 1036–1048.
- [40] M. Nakajima, S. Iio, T. Ikeda, Performance of Savonius rotor for environmentally friendly hydraulic turbine, *J. Fluid Sci. Technol.* 3 (3) (2008) 420–429.
- [41] R. Espina-Valdés, A. Fernández-Jiménez, J.F. Franco, E.B. Marigorta, E. Álvarez-Álvarez, Small cross-flow turbine: Design and testing in high blockage conditions, *Energy Convers. Manage.* 213 (2020) 112863.
- [42] Z. Yin, M. Esmailpour, The hydrodynamic performance of a turbine in shallow free surface flow, *J. Hydrodyn.* 33 (4) (2021) 804–820.
- [43] A.E.B. Le Hocine, R.J. Lacey, S. Poncet, Multiphase modeling of the free surface flow through a Darrieus horizontal axis shallow-water turbine, *Renew. Energy* 143 (2019) 1890–1901.
- [44] J. Deng, S. Wang, P. Kandel, L. Teng, Effects of free surface on a flapping-foil based ocean current energy extractor, *Renew. Energy* 181 (2022) 933–944.
- [45] M. Claessens, The Design and Testing of Airfoils for Application in Small Vertical Axis Wind Turbines (Master of Science thesis), 2006, Aerospace Engineering.
- [46] A. Sengupta, A. Biswas, R. Gupta, Studies of some high solidity symmetrical and unsymmetrical blade H-Darrieus rotors with respect to starting characteristics, dynamic performances and flow physics in low wind streams, *Renew. Energy* 93 (2016) 536–547, <http://dx.doi.org/10.1016/j.renene.2016.03.029>, URL <https://www.sciencedirect.com/science/article/pii/S0960148116302130>.
- [47] K.W. Lewis, The Cumulative Effects of Roughness and Reynolds Number on NACA 0015 Airfoil Section Characteristics (Ph.D. thesis), Texas Tech University, 1984.
- [48] E. Jacobs, A. Sherman, Airfoil Section Characteristics as Affected by Variations of the Reynolds Number, Report-National Advisory Committee for Aeronautics, (227) US Government Printing Office, 1937, pp. 577–611.
- [49] C. Hirt, B. Nichols, Volume of fluid (VOF) method for the dynamics of free boundaries, *J. Comput. Phys.* 39 (1) (1981) 201–225, [http://dx.doi.org/10.1016/0021-9991\(81\)90145-5](http://dx.doi.org/10.1016/0021-9991(81)90145-5), URL <https://www.sciencedirect.com/science/article/pii/0021999181901455>.
- [50] P.J. Roache, Perspective: A method for uniform reporting of grid refinement studies, *J. Fluids Eng.* 116 (3) (1994) 405–413.
- [51] F.R. Menter, Two-equation eddy-viscosity turbulence models for engineering applications, *AIAA J.* 32 (8) (1994) 1598–1605.
- [52] D.C. Wilcox, Reassessment of the scale-determining equation for advanced turbulence models, *AIAA J.* 26 (11) (1988) 1299–1310.

3.8 Journal Metrics

The following data are based on the last updated one from the Web of Science database for the year of 2023.

Article No. 2	
Journal	RENEWABLE ENERGY
Title	Experimental and multiphase modeling of small vertical-axis hydrokinetic turbine with free-surface variations
Category Quartile	Q1
Impact Factor	8.634
Impact Factor (5 years)	8.394
CiteScore	13.6
No. of Citations [Jan 2023 - May 2023]	2

Chapter 4

Open-field Testing Experiments

4.1 Overview

Testing hydrokinetic turbines under open-field conditions (no blockage effects) can be expensive due to the requirement for wider channels. A more cost-effective alternative is to use an open-jet wind tunnel to obtain the same behaviour in the open-field conditions. This approach is governed by ensuring a constant Reynolds number value in both wind tunnel and water flume experiments. Thus, this chapter provides a series of wind tunnel experiments for the turbine model, in an open-field conditions, at the same Reynolds value of the previous water flume experiments. To check the validity of the proposed approach, a theoretical method for correcting the blockage effects is applied to the water channel tests and compared with the wind tunnel experiments. These theoretical correlations are based on the traditional actuator disk theory and adapted for the open channel flow cases. Also, both of the theoretical expectations and the wind tunnel outputs are validated with previous experimental work from the literature.

4.2 The Wind Tunnel Configuration

Experimental tests have been carried out in an open-circuit subsonic wind tunnel. As presented in Fig. 4.1, the wind is discharged through a 30 kW axial fan which is controlled by a variable frequency driver, reaching a maximum wind speed of 36 m/s. In order to decrease the turbulence intensity and prevent vortices from growing and moving toward the measuring test section, the wind crosses a honeycomb net to the settling chamber after the diffuser section, and finally is discharged to the test section. The discharge section is a nozzle shaped with a 1:12 area ratio and $0.75 \times 0.75 \text{ m}^2$ test section.

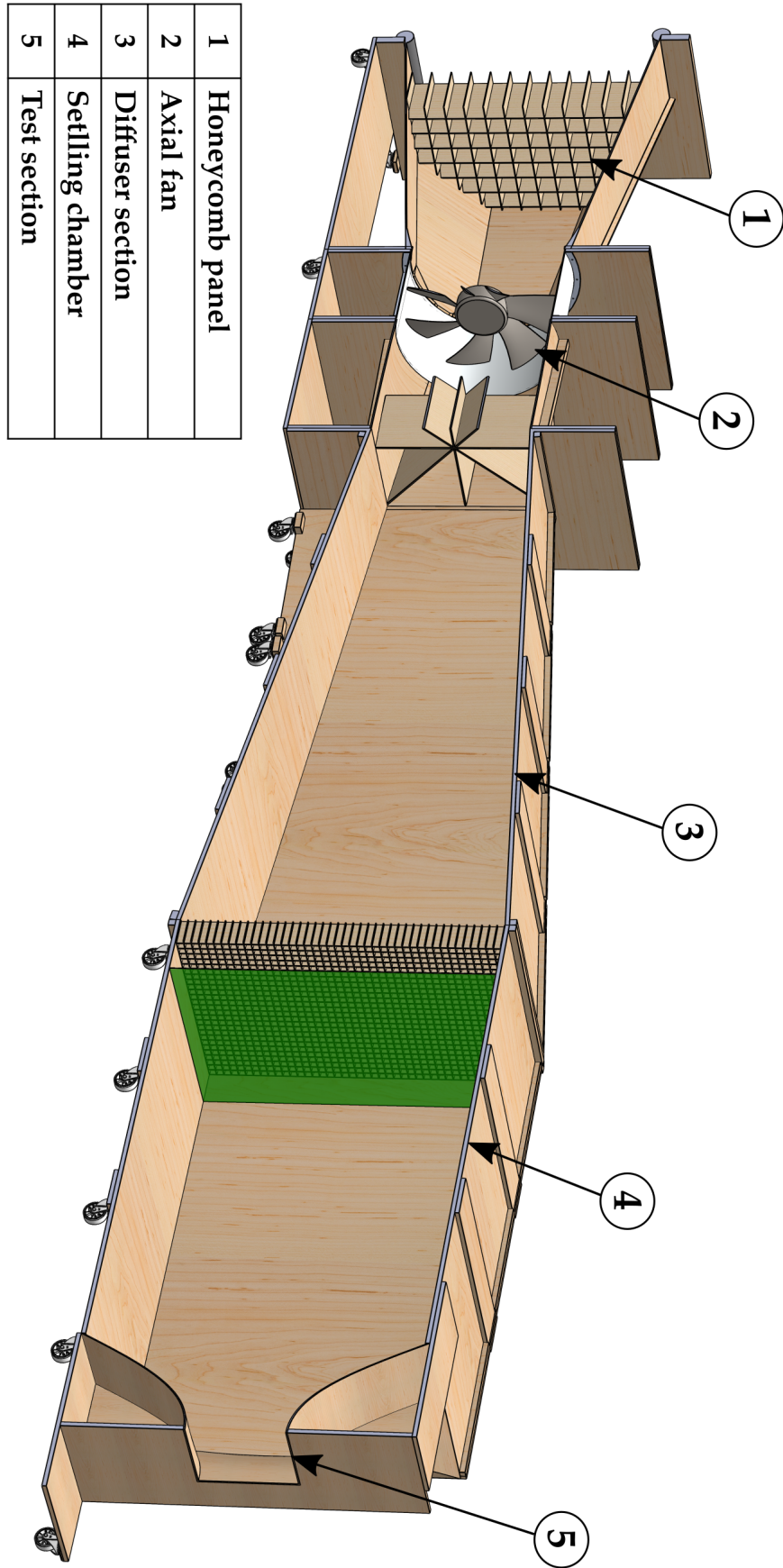


Figure 4.1: A detailed schematic of the open-jet wind tunnel.

As illustrated in Fig. 4.2, the rotor is supported using a portable aluminium structure, allowing the turbine to be centered in front of the test section at a distance equal to 6 times of the turbine diameter. Also, the rotational axis is supported, above and below, by two radial bearings. The brake-torque measuring system is placed at the top of the aluminium structure and connected to the turbine mechanically through two flexible couplings.

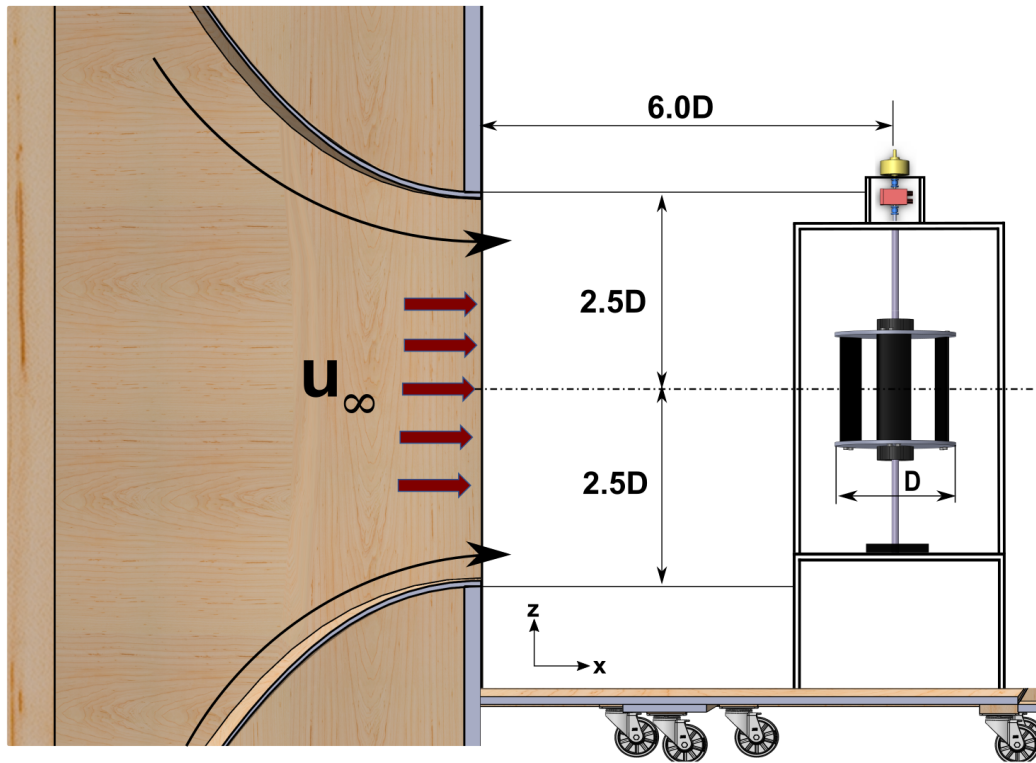


Figure 4.2: The turbine model position in the tunnel.

In the experimental runs, the turbine rotates freely without any loading until reaching the steady state condition where the rotational speed is nearly constant. Thereafter, the turbine is gradually loaded by changing the input current to the brake. Subsequently, the rotational speed decreases and the torque produced rises till reaching the maximum power point. From that point onwards, the power output from the turbine decreases with the decline of the rotational speed until the turbine reaches an unstable condition and stops. As shown in Fig. 4.3, the wind tunnel is equipped with a Pitot tube, differential and digital manometers to characterize the wind flow at different sections. Also, the SCADA system along with different voltage sources are equipped to provide the required power for the measuring instruments. For each test, the rotational speed (N), the wind velocity (U_∞) and the mechanical torque (T) are measured. These registered parameters are post-processed to calculate the power output (P) and the dimensionless parameters: the power coefficient ($C_p = P/(0.5 \cdot \rho \cdot A \cdot U^3)$) and the tip speed ratio ($\lambda = \omega \cdot R/U$).

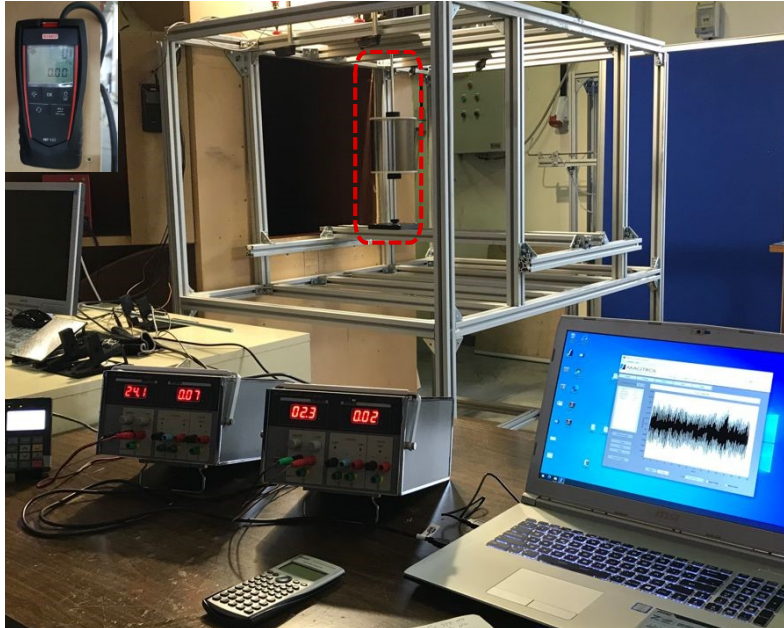


Figure 4.3: A photo of the test rig with different instrumentation.

In the preliminary tests of the turbine model, the model was completely destroyed (as shown in Fig. 4.4). It could not withstand the centrifugal forces resulting from the high rotational velocity during the wind tunnel tests. A new strategy has been implemented in fabricating the model, particularly the turbine blades, by altering the printing position (layer orientations) of the blades from vertical to horizontal. This modification significantly enhances the blade resistance to bending stresses. Also, the two ending plates have been strengthened at the contact area with the blades by increasing the infill density in the fabrication process.

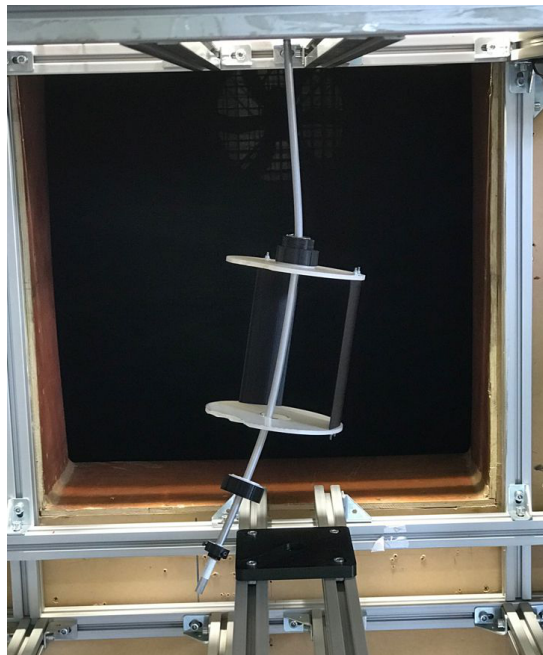


Figure 4.4: The model failure test inside the wind tunnel.

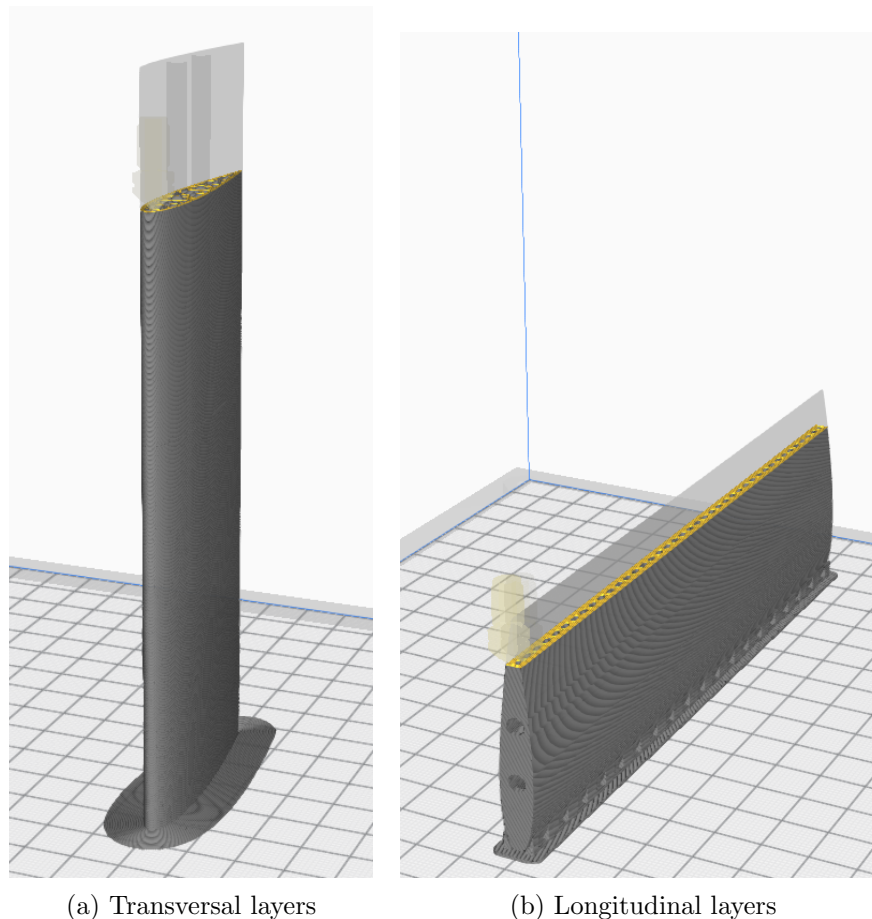


Figure 4.5: Snapshots of the blade profile slicing (layers orientation).

4.3 Blockage Phenomenon and Correction Formulas

Blockage is a fundamental aspect that affects the operation of hydrokinetic turbines in narrow channels. This phenomenon has a direct impact on the energy production from the rotor, affecting the turbine efficiency. The flow in a confined channel experiences changes in three main parameters: the velocity of the fluid around the rotor, pressure changes in the wake, and longitudinal pressure gradients associated with the boundary layer of the channel. As a result of these changes, an increase in power and thrust occurs compared to the flow in open-field conditions.

The impact of blockage on hydrokinetic turbines is often evaluated using the blockage ratio factor (B). Several empirical coefficients have been proposed -based on laboratory experiments or mathematical expressions- to correct for the blockage phenomenon, with the main idea of establish a relationship between the velocity in the confined condition (u_c) and the velocity in the open-field (u_f). These corrections enable the calculation of accurate power parameters. In the current study, two correction methods, proposed by Gauvin (equation (4.1) and (4.2)) and Werle (equation (4.3)), have been applied to the water channel experiments. The confined and open-field velocity ratio is a function of

the blockage ratio and empirical correction factor, which is calculated using the following equations:

$$\left(\frac{u_f}{u_c}\right)^2 = 1 - m \cdot B \quad (4.1)$$

$$\left(\frac{u_c}{u_f}\right) = 1 - B \quad (4.2)$$

Where, m is an empirical correction factor calculated as:

$$m = 8.14 \cdot B^2 - 7.309 \cdot B + 3.23 \quad (4.3)$$

After determining the velocity ratio, the tip speed ratio and the power coefficient can be corrected as follow:

$$\lambda_f = \lambda_c \cdot \left(\frac{u_c}{u_f}\right) \quad (4.4)$$

$$Cp_f = Cp_c \cdot \left(\frac{u_c}{u_f}\right) \quad (4.5)$$

Where, λ_f and Cp_f are the corrected values of the tip speed ratio and the power coefficient, which represent the open-field conditions.

4.4 Objectives





The main objective is to investigate a cost-effective novel method to test hydrokinetic turbine models under open-field conditions (no blockage effects). This is achieved by a series of experiments on the turbine model inside an open-jet wind tunnel. This approach is governed by ensuring a constant Reynolds number value in both wind tunnel and water flume experiments. To check the validity of the proposed approach, two blockage correction equations are applied to the water channel tests to estimate the theoretical behaviour in the open-field tests. Both of the theoretical and the wind tunnel outputs are validated with previous experimental work from the literature.

4.5 Peer-reviewed Journal Publication

4.5.1 Wind–Water Experimental Analysis of Small SC-Darrieus Turbine: An Approach for Energy Production in Urban Systems

Article

Wind–Water Experimental Analysis of Small SC-Darrieus Turbine: An Approach for Energy Production in Urban Systems

Ahmed Gharib-Yosry ¹, Eduardo Blanco-Marigorta ², Aitor Fernández-Jiménez ³, Rodolfo Espina-Valdés ³
and Eduardo Álvarez-Álvarez ^{3,*}

¹ Mechanical Power Department, Faculty of Engineering, Port Said University, Port-Said 42526, Egypt; ahmed.gharib@eng.psu.edu.eg

² Energy Department, University of Oviedo, C/Wifredo Ricart s/n, 33204 Gijón, Spain; eblanco@uniovi.es

³ Hydraulic R&D Group, EP Mieres, University of Oviedo, Gonzalo Gutiérrez Quirós, 33600 Mieres, Spain; fernandezaitor.fuo@uniovi.es (A.F.-J.); espinarodolfo@uniovi.es (R.E.-V.)

* Correspondence: edualvarez@uniovi.es

Abstract: Smart cities have a significant impact on the future of renewable energies as terms such as sustainability and energy saving steadily become more common. In this regard, both wind and hydrokinetic compact-size turbines can play important roles in urban communities by providing energy to nearby consumption points in an environmentally suitable manner. To evaluate the operation of a Darrieus turbine rotor as a wind or hydro microgenerator, a series of wind tunnel and water current flume tests were performed. Power and characteristic curves were obtained for all test conditions. In the wind tests, all curves seemed to be identical, which means that the turbine rotor works properly under open-field conditions. Two blockage correction equations were applied to the water channel tests that were performed under blockage values ranging from 0.2 to 0.35 to estimate the operational behavior in open water. Finally, it has been demonstrated that, with the condition of maintaining the Reynolds number between experiments in the wind tunnel and water flume, the turbine wind characteristics represents the its operation in open-water conditions.

Keywords: sustainability; urban energy systems; wind turbine; hydrokinetic turbine; blockage



Citation: Gharib-Yosry, A.; Blanco-Marigorta, E.; Fernández-Jiménez, A.; Espina-Valdés, R.; Álvarez-Álvarez, E. Wind–Water Experimental Analysis of Small SC-Darrieus Turbine: An Approach for Energy Production in Urban Systems. *Sustainability* **2021**, *13*, 5256. <https://doi.org/10.3390/su13095256>

Academic Editor: Amparo López Jiménez

Received: 30 March 2021

Accepted: 4 May 2021

Published: 8 May 2021

Publisher's Note: MDPI stays neutral with regard to jurisdictional claims in published maps and institutional affiliations.



Copyright: © 2021 by the authors. Licensee MDPI, Basel, Switzerland. This article is an open access article distributed under the terms and conditions of the Creative Commons Attribution (CC BY) license (<https://creativecommons.org/licenses/by/4.0/>).

1. Introduction

Significant progress has been made in generating electricity from sustainable renewable resources, such as the improvement in solar panels performance [1] or the installation of offshore wind arrays [2]. In 2020, the outbreak of the COVID-19 pandemic tested the strength of the world's electricity system. During the first semester and coinciding with the hardest months of the disease and with confinements, the demand for world energy suffered a notable setback with a decrease of 5%, mainly due to the interruption of industrial activity [3]. However, the demand of renewable energy increased by 1%, showing great resilience despite the reduction in overall demand. Thus, the renewable energy sector has shown an extraordinary ability to adapt to this new situation, contributing more than 18% of that which was envisaged in 2019. A variety of factors, such as their independence from the transport of resources (they are located where the resource is available) or their installation at isolated locations, are the main reasons of this extraordinary resilience [4].

In this way, recent studies have estimated that green energy will increase by 10% in 2021, 3% more than expected, because of the resumption of projects that had previously been blocked due to the effects of the pandemic. As a consequence, more than a hundred million dollars, mainly in Europe, United States, China, and India, will be invested to build these facilities so that the ultimate target of zero emissions can be reached by 2030 [5].

A portion of this investment is allocated to research and development of hydrokinetic turbines at ocean currents. These systems harness the great potential that exists in those locations, which in the case of marine currents, is estimated at 800 TWh/year

worldwide [3]. This hydrokinetic power is also predictable over time, and its energetic use can be compatible with other needs such as water supply [6].

With regard to smart cities, there have been inroads in the development of microgeneration using turbines [7]. In this work, the proposed rotor is designed to be used in water and wind, giving competitive advantages by reducing its cost and facilitating its manufacture, since it does not require specific changes (in the design) to adapt to the working fluid. This is possible due to the use of lift-based rotors, the installation of permanent magnet generators, and the development of much more efficient electronic control systems [8]. The system is simple, so that the visual impact and cost are minimized, making it very attractive to be installed in urban environments [9]. Figure 1 shows the dual proposal composed by water and wind turbines using the same rotor design to harness both resources. In this case, the energy is used to supply electricity and other services to a city.

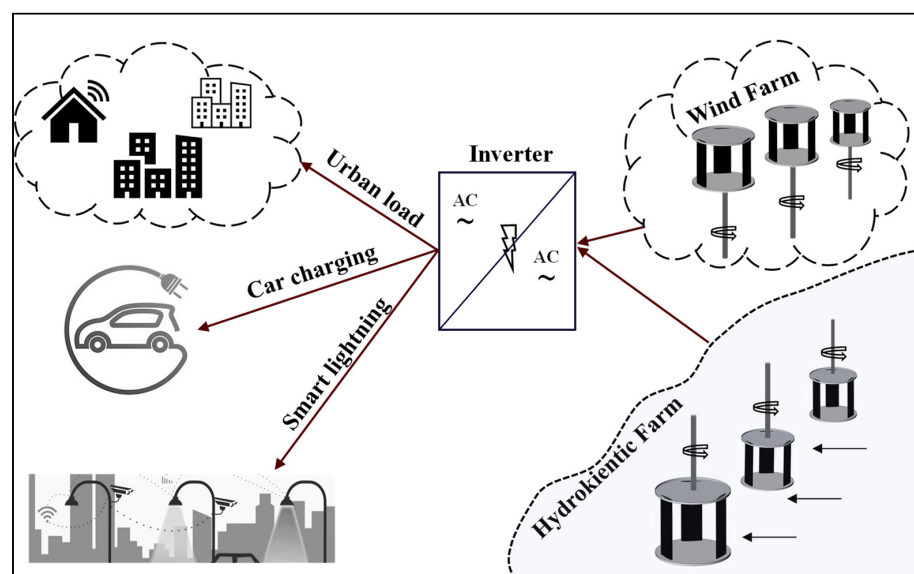


Figure 1. Integration of hydrokinetic and wind turbines for urban systems.

Hydrokinetic turbines use the kinetic term of the current, not requiring the creation of potential elevations, so not only the installation requires less initial investment but also the environmental impact is minimized [10]. Thus, the power obtained by these turbines will mainly depend on the water velocity, together with the area swept by their blades, the fluid density, and the conversion efficiency of the equipment.

Hydrokinetic turbines can be classified into two large groups depending on the direction of the flow and the axis of rotation: axial turbines (flow and axis are parallel) and crossflow turbines (flow and axis are perpendicular). Nowadays, crossflow turbines are those that generate more interest [11]. This is mainly because these rotors, although not as efficient as axial ones, have a much simpler mechanical coupling system that reduces the construction costs and facilitates installation and maintenance activities [12]. One of the most frequently used crossflow rotor designs is Darrieus type with different configurations: Squirrel Cage (SC), H, and curved [13] (Figure 2). These designs are based on aerodynamical profiles used in the wind industry [14].

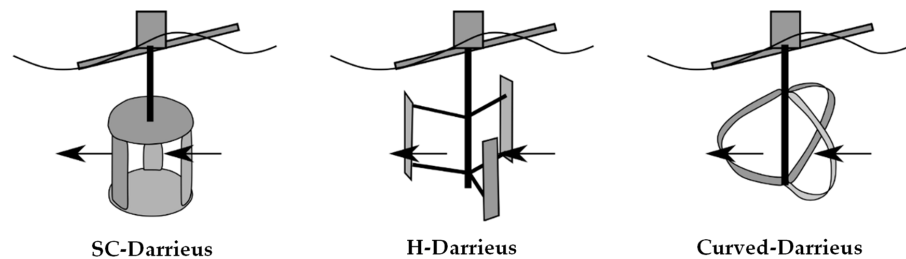


Figure 2. Different designs of Darrieus rotors [15].

Crossflow rotors can be divided in accordance with the axis position in horizontal and vertical axis turbines. Although horizontal turbines have been used mainly for shallow-water conditions [16], vertical rotors allow for greater use of the cross-sectional area of the water current when they are arranged in farms or arrays, allowing for the production of energy under low-velocity conditions [17]. Additionally, because their dimensions rarely exceed 2 m in height and diameter, they have a reduced effect on the environment or river-maritime traffic [18].

The use of vertical axis water turbines under low-velocity and shallow-water conditions is possible due to the appearance of the blockage phenomenon [19]. Under these circumstances, three simultaneous phenomena appear: an increase in the fluid velocity around the rotor, high pressure changes across the rotor, and the appearance of longitudinal pressure gradients associated with boundary layer conditions [20].

Until now, blockage has been studied from two different points of view: the energetic use of the blockage effect and the development of mathematical corrections to extrapolate results (with blockage existence) to open-field conditions. In the first case, the design of the devices is studied, such as the accelerator or the deflectors used to induce blockage conditions into the water stream current [10]. In the second instance, different numerical methodologies are developed to eliminate the effects of blockage that inherently appear in experimental tests and to extrapolate that behavior to open-field conditions [21].

More specifically, most accelerators studies have tested different designs, observing the increases in the extracted power for the same hydrodynamic conditions. Some examples are the results presented by [22,23]. In the case of blocking corrections, the development of numerical expressions to correct these effects are mainly based on the application of the simple actuator disc theory and the use of empirical coefficients. The results presented by [20,24,25] show the value of the corrected open-field velocity from a theoretical study of energy, while [21,26] provide empirical correction coefficients based on laboratory tests.

The study of blockage in crossflow turbines under confined and open-field conditions have been approached. These studies have been carried out using wind and water tunnels, sometimes even simultaneously. On the one hand, some confined flow studies such as the one carried out by Hossein et al. [27], analyzed the effects of blockage and the position of the water free surface on the energy extracted by the rotor. It concludes that there is a clear relationship between both aspects since there is a change in the hydrodynamic operation of the acting forces. This study was approached using a high-speed camera and a torque meter. Additionally, of interest is the work presented by Bachant et al. [28] in which a comparison was made between Gorlov and Savonius rotors under blockage conditions. In this case, the study concludes that Gorlov turbines are more recommended when blockage coefficient is low (<20%).

On the other hand, open-field studies, such as those carried out by Banerjee et al. [29] and Consul et al. [30], have analyzed how certain parameters such as solidity or wake appearance affect the power extraction. Finally, some studies have been made using both wind and water tunnels. For example, the studies presented by [31,32] carried out tests with wind turbines, obtaining power measurements and analyzing the flow characteristics around the blades in a wind tunnel using PIV (Particle Image Velocimetry) techniques. It was then possible to quantify the detachment effect so the blade design could be adjusted.

Other studies such as the one carried by [33,34] tested axial turbines in wind and water tunnels to study in which fluid the chosen designs were more suitable. Furthermore, in the work presented by [35], a Darrieus tidal turbine was studied in similar infrastructure. Wind experiments were used to study the starting and dynamic torque, and the suitability of different blade geometries. After that, the water tunnel was used to verify the dynamic torque values and to obtain the maximum tip speed ratio of the turbine under low flow conditions. Finally, in the studies carried out by [36,37], an accurate study of blockage effects was carried out considering those produced by the wake phenomenon. Thus, it was possible to quantify the effect that the presence of the rotor produces on other turbines specially when they are arranged in arrays. However, none of these publications address the study of blockage conditions by testing the turbine under different fluids and by focusing only on differences in power parameters.

This article presents an analysis of the power stage of a vertical axis turbine (squirrel cage-Darrieus type) with straight blades manufactured with the help of additive manufacturing technology (3D printing). Wind tests are used to obtain the behavior of the turbine at open-field conditions, while water experiments represent blockage conditions. Finally, both situations are analyzed separately so the results are contrasted.

The article is structured as five main sections: introduction, theoretical bases of the experiments (in both wind and water), materials and methods (including descriptions of the rotor, wind tunnel, water flume, and testing procedure), results and discussion, and finally the conclusions.

2. Theoretical Bases

There is a marked difference between the theoretical bases that describe the experimental tests at the wind tunnel and the water flume since the turbine is subjected to the influence of two different fluids (air and water). However, the operation of the turbine is analogous in both cases, meaning that the results are comparable when the Reynolds numbers are equal in wind and water scenarios, which implies that the wind speed should be ten times greater than the water velocity.

2.1. Wind Bases

The experimentation of the turbine in the wind tunnel is based on the application of the actuator disk theory. In these circumstances, the flow is incompressible, and homogeneous, stationary and the rotor has an infinite number of blades, inducing a uniform thrust in all of them. The upstream velocity is progressively reduced as it approaches the disc, reaching its minimum value once the fluid has passed through it due to wake effects [38]. Additionally, far away from the disk (upstream and downstream), the static pressure of the air is equal to the atmospheric pressure (P_{atm}) (Figure 3).

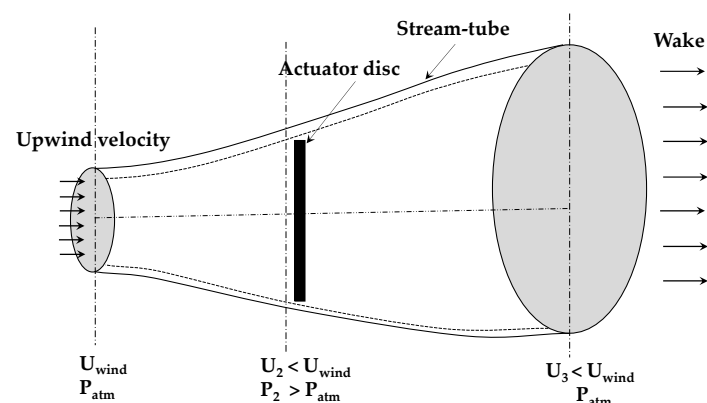


Figure 3. Actuator disk theory at a wind tunnel [39].

Thus, as the wind approaches the rotor, there is a decrease in its speed since energy is driven out by the turbine. By applying the linear momentum conservation equation, the power produced by the turbine depends on the wind density, the area swept by blades, the cubic value of wind velocity, and the power coefficient of the rotor. At maximum power conditions (MPP_{wind}), the power coefficient is limited to 0.59, which corresponds to the Betz limit [40].

2.2. Water Bases

The turbine testing conditions inside the water flume follows the one-dimensional actuator disc model that was put forward by Hously et al. [41]. The rotor acts as a hydrokinetic turbine in conditions of uniform and subcritical flow. More specifically, the following are considered:

- The disc is submerged in water and under blockage conditions.
- Two different zones with uniform flow are distinguished upstream and downstream of the disc.
- A mixing zone also appears due to turbulence phenomena, being located just after the disc.

These conditions are produced in the hydrodynamic water flume using a water gate that is situated downstream from the rotor. Furthermore, since the channel is made of glass (low roughness) and the slope is practically horizontal, a constant velocity profile can be assumed (Figure 4).

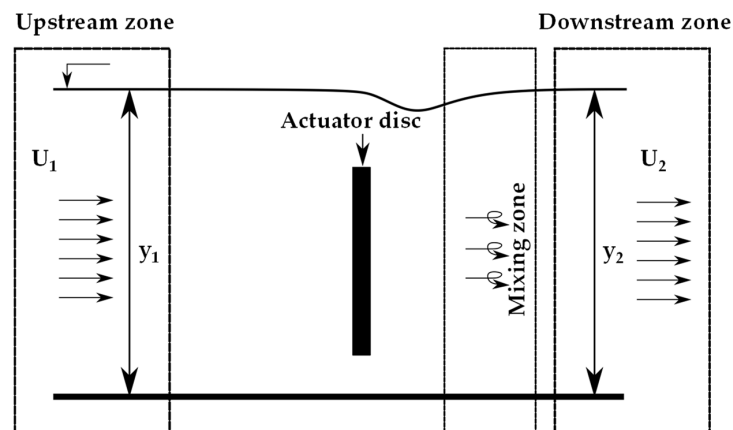


Figure 4. Actuator disk scheme at a water channel [42].

It should be noted that the calculation of power in water turbines is executed by applying the same expression as wind turbines but that, due to the appearance of blockage conditions, the power coefficient is not limited by the Betz law [43].

2.3. Testing Parameters

In both installations, the characterization of the power stage is performed by applying two dimensionless coefficients: tip speed ratio and power coefficient. Other parameters including the hydraulic and mechanical power are also calculated. The following equations are used:

$$\lambda = \frac{\omega \cdot R}{U} \quad (1)$$

$$Cp = \frac{P_m}{P_t} \quad (2)$$

$$P_t = \frac{1}{2} \cdot \rho \cdot A_t \cdot U^3 \quad (3)$$

$$P_m = T \cdot \omega \quad (4)$$

where λ is the relation between the velocity at the tip of the blade and the fluid speed (dimensionless), ω is the rotational speed of the turbine (rad/s), R is the radius of the rotor (m), U is the fluid velocity (m/s), C_p is the power coefficient (dimensionless), P_m is the mechanical power (W), ρ is the fluid density (kg/m³), A_t is the area swept by blades (m²), P_t is the hydraulic power (W), and T is the torque measured by the torque meter (N). The blockage coefficient is defined as the ratio between the turbine area and the channel section:

$$BR = \frac{A_t}{A_c} = \frac{2 \cdot R \cdot h}{b \cdot y} \quad (5)$$

where BR is the blockage ratio (dimensionless), A_c is the channel section (m²), h is the height of the rotor (m), b is the width of the channel (m) and y is the height of the water free surface (m).

Clearly, the wind and water tests differ, not only because two different fluids have been used. In this case, the tests conducted at the water flume are influenced by the blockage so it is necessary to extrapolate the confined results to the open-field conditions. With that in mind, mathematical expressions must be applied to obtain the velocity in open-field conditions. Although, there are many different formulations, in this case, the corrections proposed by Gauvin et al. [21] (Equations (6) and (7)) and Werle [25] (Equation (8)) have been applied because they are suitable for low blockage coefficients [44].

$$\left(\frac{U_F}{U_C}\right)^2 = 1 - m \cdot BR \quad (6)$$

$$m = 8.14 \cdot BR^2 - 7.309 \cdot BR + 3.23 \quad (7)$$

$$\frac{U_C}{U_F} = 1 - BR \quad (8)$$

$$TSR_F = TSR \cdot \left(\frac{U_C}{U_F}\right) \quad (9)$$

$$C_{pF} = C_p \left(\frac{U_C}{U_F}\right)^3 \quad (10)$$

where U_F is the water velocity at open-field conditions (m/s), m is an empirical factor (dimensionless), TSR_F is the tip speed ratio at open-field conditions (dimensionless), and C_{pF} is the power coefficient at open-field conditions (dimensionless). TSR , C_p , and U are the experimental measured values in the water flume (confined conditions).

3. Materials and Methods

3.1. Rotor Description

The designed rotor has a height and radius of $h = 0.15$ m and $R = 0.075$ m, respectively, with three blades spaced at 120 degrees. A NACA-0015 standard profile with a chord of $c = 0.05$ m was used, so its solidity was that of 2. This blade profile was selected for its good behavior under low flow velocity conditions, far superior to asymmetric profiles [45]. Moreover, a decision was taken to use a three-bladed rotor because there are more advantageous in terms of cost and efficiency [46]. Figure 5 shows the characteristics and fabrication process of the turbine.

The turbine and its coupling system were built using 3D additive manufacturing technology, with the Polylactic Acid (PLA) being the selected material. The behavior of PLA under conditions of dynamic stress has been exemplary. Its endurance when working with water is unquestionable, whilst it is readily pliable so that pieces can be adjusted to complex profiles such as NACA-0015 [47]. For both experiments, the shaft diameter was set at 10 mm.

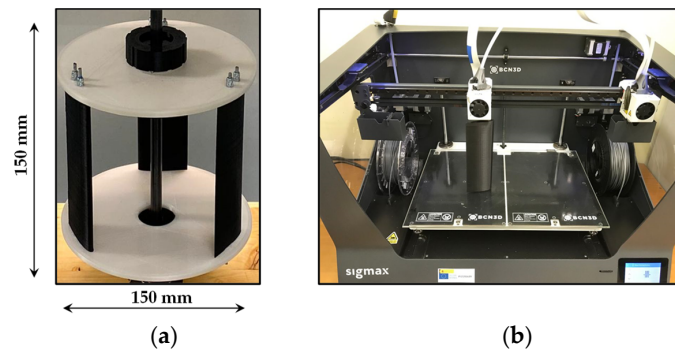


Figure 5. (a) Geometric characteristics of the turbine. (b) Blade fabrication process using a 3D printer.

3.2. Wind Tunnel Description

The wind tunnel has a total length of 13.75 m and a discharge section of $0.68 \times 0.68 \text{ m}^2$, working as an open-air admission circuit and under subsonic conditions. In addition, the discharge section where the turbine was tested is fully open and does not imply blockage. The air movement was produced by an axial fan with a diameter of 1.2 m and a power of 30 kW, controlled by an electronic power inverter that allows maximum wind speeds of up to 35.5 m/s.

The characteristics of the wind tunnel are shown in Figure 6, where (1) is the honeycomb panels controlling admission, (2) is the axial fan, (3) is the diffuser section, (4) is the stilling chamber, and (5) is the testing section.

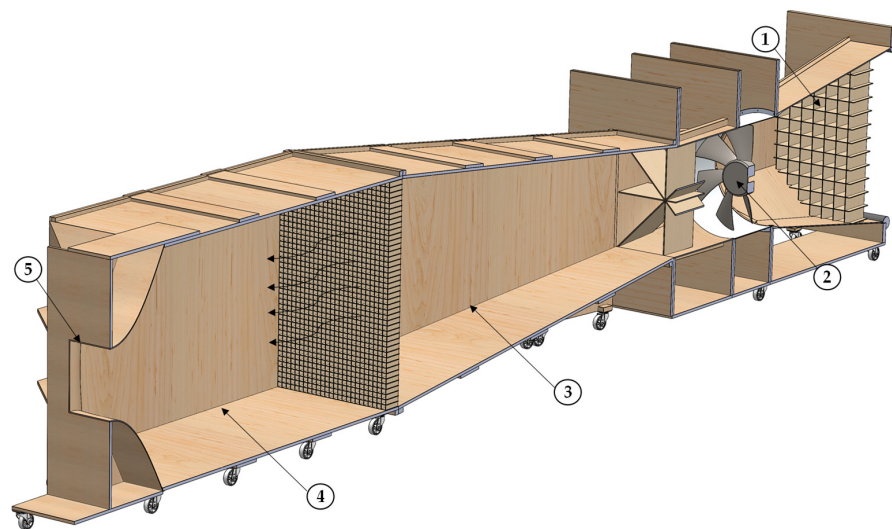


Figure 6. Wind tunnel configuration (sectional-view).

To reduce turbulent phenomena, the wind tunnel has a stilling chamber and length-wise honeycomb panels throughout the facility. Additionally, the installation has different sensors that allow for the parametrization of test conditions. More specifically, Pitot tubes, and differential and digital manometers are available, so wind speed and pressure are known.

The rotor was tested in the tunnel using a portable aluminum structure where the rotor and measurement instruments were included. The rotational axis was joined above and below by two high-performance radial bearings, and the rotor was placed between them. Both the torque meter and electric brake were placed in the upper part. Figure 7 shows the rotor placed at the wind tunnel, where (1) is the power supply devices, (2) is the

tested turbine, (3) is the data acquisition system, (4) is the aluminum structure, and (5) is the digital manometer.

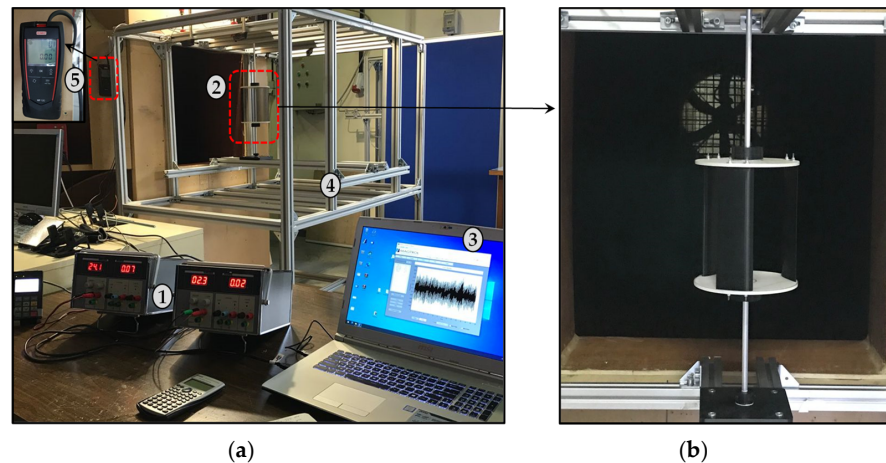


Figure 7. (a) Different devices used during a wind test. (b) The turbine at the testing section.

3.3. Water Flume Description

The water current flume has a rectangular section with a length of 1.5 m, a height of 0.55 m, and a width of 0.3 m, with the floor and walls being made of laminated glass, thus allowing the tests to be recorded. The flow movement was generated by a hydraulic pumping system with a total power of 30 kW that can move a maximum flow rate of 600 m³/h. Both pumps were controlled by two electronic inverters. The whole system works as a close circuit, suctioning the water from a recirculation tank of 5 m³ and driving it upwards to the hydraulic testing channel. At the end of the channel, a metallic gate controlled by a gear system was installed to induce low-velocity hydrokinetic conditions.

The description of the water flume is shown in Figure 8, where (1) is the hydraulic pumps, (2) is the electronic system, (3) is the reassuring tank, (4) is the channel test section including torque sensor and rotor, (5) is the water gate, and (6) is the suction tank.

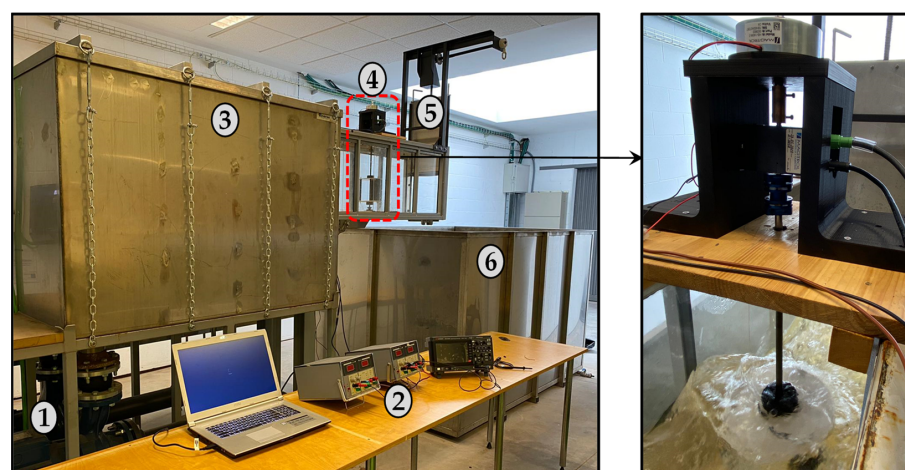


Figure 8. Water flume including the turbine rotor.

To test the turbine, a water-resistant methacrylate box was designed and built. This structure has in its submerged part a waterproof radial bearing that allows for the rotation of the axis in optimal conditions. In the upper part and out of the water current, a lid is

available as the location of the torque meter and the electric brake. It should be noted that this structure can be easily installed and removed thanks to the anchoring system based on slide clamps.

3.4. Testing Procedure

To study the power stage of the described turbine, a high-precision torque meter was used together with an electromagnetic brake. This procedure was used both in the wind tunnel and in the water current flume. The torque transducer used was an integrated high-precision torque and rotational speed sensor (Magtrol TS-103, 0.5 Nm of rated torque, accuracy <0.1% and 15,000 rpm max. speed, accuracy <0.015%) calibrated in accordance with the standards of the Swiss Federal Institute of Metrology (METAS).

This device allows for measurements of torque, rotational speeds, and relative position of the blades with data-taking frequencies up to 80 data per second, thereby collecting a good range of sampling. All collected data were sent to a database for further processing. The variation in the braking force was directly controlled by a power supply device. The characterization procedure (Figure 9) started with an initial measurement where no braking force was applied, so the rotor had its maximum rotational speed but did not generate power.

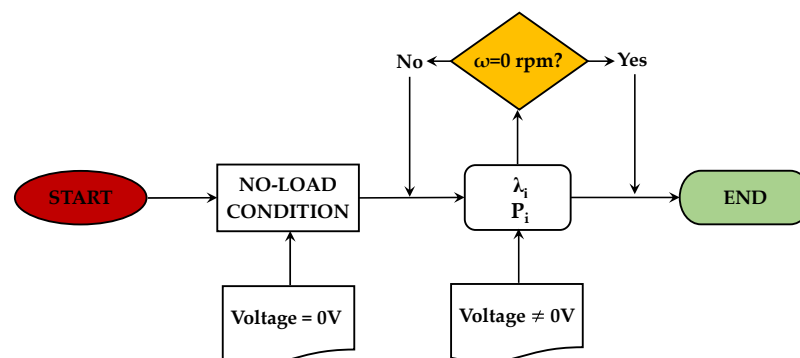


Figure 9. Experimental test procedure.

This step is called “no-load condition”. Subsequently, the resistive torque of the electric brake was sequentially changed, in different “*i*” steps, through voltage variations at the power supply device, obtaining different extracted powers (P_i) and tip speed ratios (λ_i).

The turbine was tested at different wind and water velocities as well as various blockage conditions (see Table 1). In fact, this rotor was tested for flow velocities higher than 10 m/s, reaching 20 m/s and proved stability, reliability, and durability, but it should be borne in mind that these higher velocities are somewhat rare, particularly in an urban environment, indicating that our research is largely focused on real-world performance and on not an artificial one.

Table 1. Different wind and water testing conditions.

	Flow Velocity (m/s)	Blockage Ratio (BR%)
Wind tests	7.1, 8, 9, and 10	6.8
Water tests	0.71, 0.73, 0.75, and 0.78	20, 25.1, 31.8, and 34.1

4. Results and Discussion

During the different tests, continuous measurements of the parameters, including torque and angular velocity, were carried out. Thus, it was possible to check if the turbine reached stability before starting the power test in each point, thereby minimizing discontinuities. After loading the turbine rotor, it proved preferable to wait and watch the

rotational speed variation of the turbine rotor before recording the results to ensure that the turbine was working under stable conditions. Figure 10 illustrates the stability condition during one of the proposed tests.

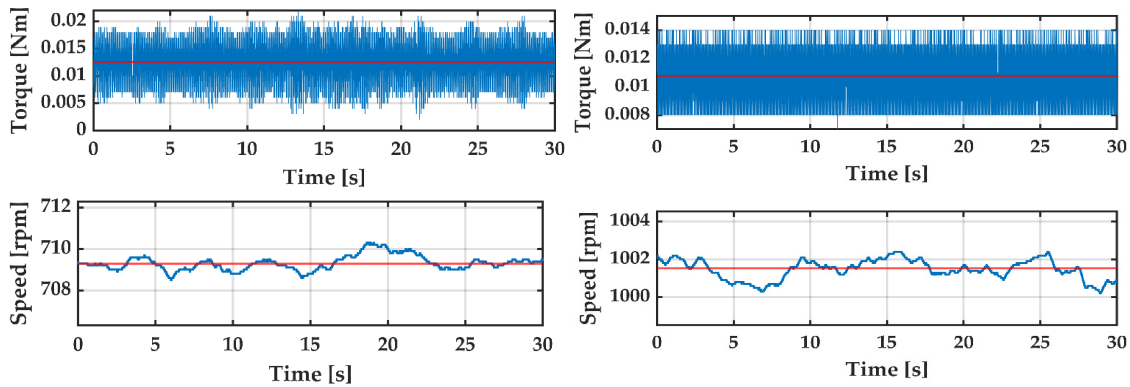


Figure 10. Stability conditions for low and high rotational speeds test conditions at a wind speed of 8 m/s.

The variation in the power output with the rotational speed of the turbine rotor for different upstream wind velocities are shown in Figure 11. All tested speeds show the same tendency. When loading the turbine rotor, the rotational speed decreased and the output power increased dramatically until reaching the maximum power point. After that, the power output started to decline up until it reached the point where the turbine stopped and was not able to produce more power. In fact, for high flow velocities, the power curve was almost complete after reaching the *MPP*, but for low velocities, the power curve nearly reached the *MPP* and does not reach the completion point. This is due to the power-to-friction ratio, since for high flow velocity, the turbine is able to produce power to overcome the friction and to pass the *MPP*. On the other hand, for low velocities, the rotor is not able to pass this point and to characterize this part of the power curve.

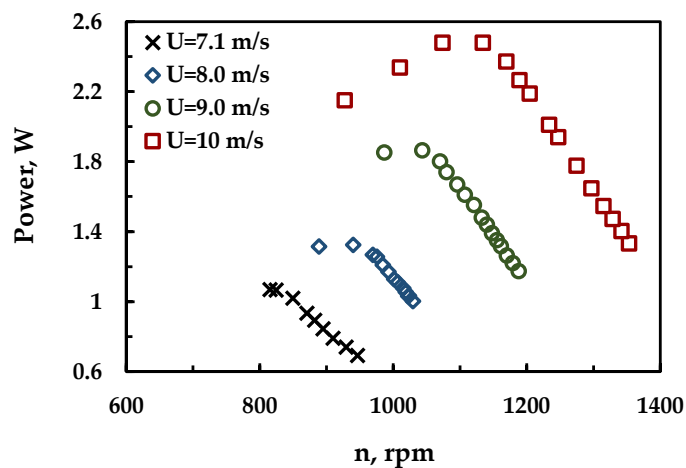


Figure 11. Wind tunnel power curves at different upstream velocities.

By tracking the maximum power point *MPP* variation with the upstream wind velocity (Figure 12), it was found that the maximum power increases approximately with the cube of the upstream wind velocity, as Equation (3) indicates, to reach its maximum value of 2.5 W at a wind velocity of 10 m/s.

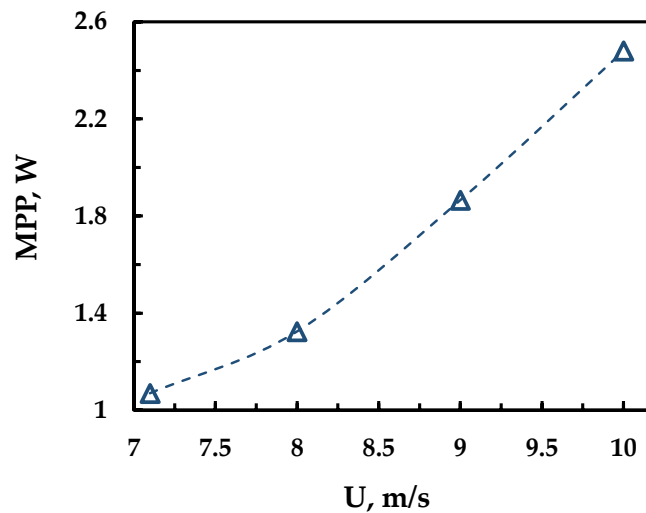


Figure 12. Maximum power point variation with wind velocities.

The characteristic curve of the turbine inside the wind tunnel is shown in Figure 13. The rotor is observed as working in a stable C_p range of approximately 0.13, this being the maximum point reached at a λ of 1.1. Additionally, all curves seem to be identical, which means that the turbine rotor works properly under open-field conditions without the existence of other factor such as blockage. In fact, the value of tip speed ratio is considered paltry compared with other similar turbines; this is due to the high solidity value that was selected in the proposed rotor to allow for self-starting under low flow velocities.

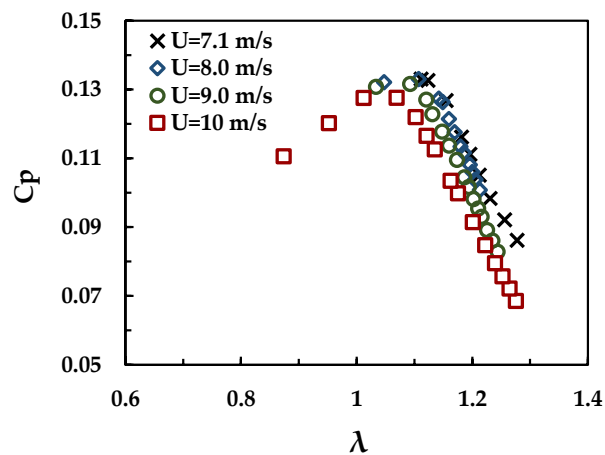


Figure 13. Characteristic curve for the turbine rotor at different wind velocities.

To study the effects of blockage conditions and their correction to open-field behavior, the turbine was tested in the open-surface water flume. Four tests were carried out for similar velocities and different blockage values ranging from 0.2 to 0.34. Figure 14a shows the variation in the characteristic curves with blockage. Different curves were obtained for the same rotor, while for wind tests, only one curve was drawn. This is due to the existence of flow blockage conditions that affect the rotor performance. By increasing the blockage value, the performance curves shifted to higher values of tip speed ratios and power coefficients. This is a direct consequence of the flow acceleration around the turbine rotor while the blockage increased. As shown in Figure 14b, with a turbine rotor blockage value of 6.8% inside the wind tunnel, which is considered an open-field condition, the

maximum power coefficient value is of 0.13. By increasing the blockage value from 6.8% to 34.1%, the maximum power coefficient increased to reach its maximum value of 0.97.

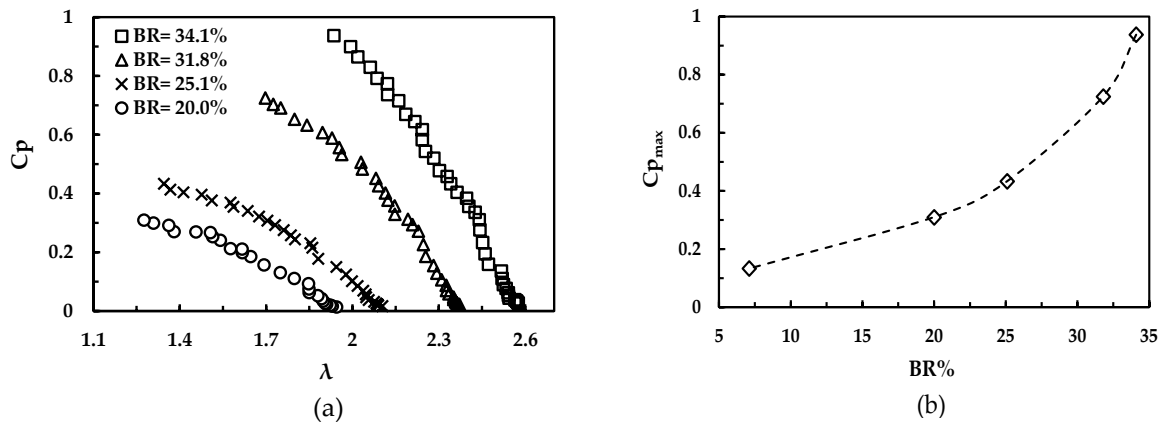


Figure 14. (a) Characteristic curves at different water blockage values and (b) variation in $C_{p_{max}}$ with Blockage ratio.

The extrapolation of blockage to open-field conditions was performed using the flow velocity of 0.71 m/s with a BR of 0.2. Under these conditions, the rotor works at Reynolds number of 3.5×10^4 approximately, so that results between wind and water can be compared. After applying the formulation of Gauvin et al. and Werle, the U_F of 0.92 m/s and 0.875 m/s were extracted, respectively. Figure 15 compares the results: obtained at wind tunnel, confined water flume, and calculated for an open field (open waters) with the blockage corrections (Werle and Gauvin) and with the results of the experiments carried out by Patel et al. [45] using the same profile and solidity in open waters.

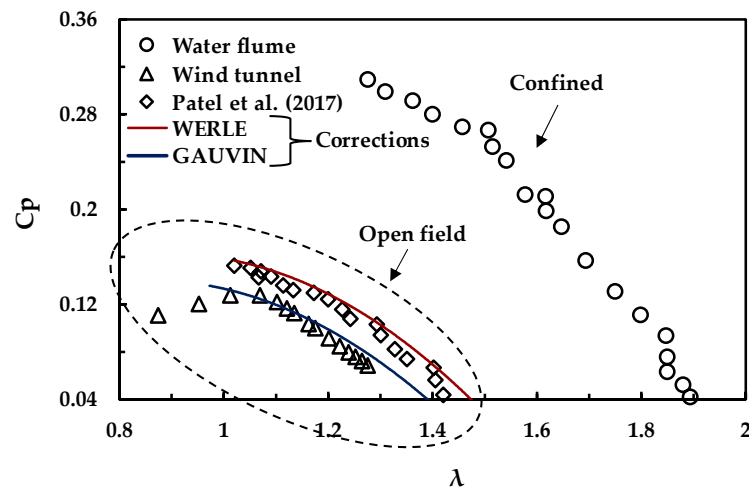


Figure 15. Turbine characteristic curves in wind tunnel and water flume ($Re = 3.5 \times 10^4$ approximately).

The peak power coefficient for the confined flow condition reached a value of 0.31, while in the wind tunnel, the obtained value is 0.13, which demonstrates the effect of blockage on the energy extraction. In fact, the corrected results (Werle and Gauvin) are quite similar to the results obtained from the wind tunnel and Patel et al. [45] tests (validating the results obtained). However, Werle’s formulations gives slightly higher results, reaching a C_p value of nearly 0.16. Moreover, the tip speed ratio that corresponds to the maximum power coefficient values coincide in all open-field cases being greater than 1.

Therefore, maintaining the Reynolds number value between experiments in a wind tunnel (no blockage) and a water flume (with blockage), which is wind velocity approximately 10 times water velocity, demonstrates that the wind power characteristic obtained is similar to the one that corresponds to open-water conditions.

5. Conclusions

The combined use of hydrokinetic and wind turbines farms is considered a modern development in the energy sector for urban communities and smart cities that will be able to provide energy to nearby consumption points. The use of a vertical-axis crossflow turbine design is considered one of the best options from the economic and technical points of view.

A compact Darrieus turbine designed to operate in both water and air was presented and tested in a wind tunnel and water flume. The wind tunnel tests reproduced real open-field conditions at four wind velocities varying from 7 to 10 m/s. Power curves were obtained for each tested wind velocity, showing that the maximum power point increases approximately with the cube of the upstream wind velocity, up to a value of 2.5 W at a wind velocity of 10 m/s.

Characteristic curves for the rotor inside the wind tunnel at different upstream wind velocities seem to be identical, which means that the turbine rotor works properly under open-field conditions without blockage.

The turbine was tested at an open-surface water flume for different blockage values ranging from 0.2 to 0.34. Increasing the blockage value shifts the performance curves to higher values of tip speed ratios and power coefficients due to the flow acceleration around the turbine rotor while the blockage increased, reaching a value of 0.97 for a blockage ratio of 0.34.

The curves obtained in the wind tunnel (open field conditions) are similar to those obtained in the water current flume (confined conditions) as long as the same Reynolds number is maintained and the blockage corrections are applied. That opens the door to accurately estimating the power characteristics for different water current scenarios (blockage and velocities) from the results obtained in a wind tunnel or vice versa.

Author Contributions: Conceptualization, A.G.-Y.; methodology, E.B.-M.; software, A.F.-J.; validation, A.G.-Y., A.F.-J.; formal analysis, E.B.-M., E.Á.-Á.; investigation, A.G.-Y.; resources, R.E.-V.; data curation, R.E.-V.; writing—original draft preparation, A.G.-Y.; writing—review and editing, E.Á.-Á.; visualization, A.G.-Y.; supervision, E.B.-M.; project administration, R.E.-V. All authors have read and agreed to the published version of the manuscript.

Funding: This research received no external funding.

Institutional Review Board Statement: Not applicable.

Informed Consent Statement: Not applicable.

Acknowledgments: The authors would like to express their gratitude to the Egyptian Cultural Affairs and Missions Sector (the Egyptian Ministry of Higher Education and Scientific Research) along with Port Said University and to the project HYDROCIMAR II financed by the Institute of Economic Development of the Principality of Asturias (Spain).

Conflicts of Interest: The authors declare no conflict of interest.

References

1. Espejo-Marín, C.; Aparicio-Guerrero, A.E. La Producción de Electricidad con Energía Solar Fotovoltaica en España en el Siglo XXI. *Cuad. Sobre Vico* **2020**, *66*–93. [CrossRef]
2. Díaz, H.; Soares, C.G. Review of the current status, technology and future trends of offshore wind farms. *Ocean Eng.* **2020**, *209*, 107381. [CrossRef]
3. IEA. Energy Technology Perspectives 2020. Available online: <https://www.iea.org/reports/energy-technology-perspectives-2020> (accessed on 8 May 2020).
4. REN21. Renewables 2020 Global Status Report 2020. Available online: <https://www.ren21.net/gsr-2020/> (accessed on 8 May 2020).

5. IRENA. Global Renewables Outlook: Energy Transformation 2050; 2020. Available online: <https://www.irena.org/publications/2020/Apr/Global-Renewables-Outlook-2020#:~:{}:text=Global%20Renewables%20Outlook%3A%20Energy%20transformation%202050,-April%202020&text=The%20Global%20Renewables%20Outlook%20shows,challenges%20faced%20by%20different%20regions> (accessed on 8 May 2020).
6. Oreste, F.; Vittorio, M.G.; Francesco, P. Numerical assessment of the vulnerability to impact erosion of a pump as turbine in a water supply system. *J. Hydroinform.* **2020**, *22*, 691–712. [[CrossRef](#)]
7. Malael, I.; Gherman, G.B.; Porumbel, I. Increase the Smart Cities Development by Using an Innovative Design for Vertical Axis Wind Turbine. In Proceedings of the 27th DAAAM International Symposium on Intelligent Manufacturing and Automation, Vienna, Austria, 26–29 October 2016; pp. 506–513.
8. Alvarez, E.A.; Rico-Secades, M.; Corominas, E.; Huerta-Medina, N.; Guitart, J.S. Design and control strategies for a modular hydrokinetic smart grid. *Int. J. Electr. Power Energy Syst.* **2018**, *95*, 137–145. [[CrossRef](#)]
9. Yuan, Z.; Wang, W.; Fan, X. Back propagation neural network clustering architecture for stability enhancement and harmonic suppression in wind turbines for smart cities. *Comput. Electr. Eng.* **2019**, *74*, 105–116. [[CrossRef](#)]
10. Mohammadi, S.; Hassanalian, M.; Arionfard, H.; Bakhtiyarov, S. Optimal design of hydrokinetic turbine for low-speed water flow in Golden Gate Strait. *Renew. Energy* **2020**, *150*, 147–155. [[CrossRef](#)]
11. Lee, J.H.; Park, S.; Kim, D.H.; Rhee, S.H.; Kim, M.-C. Computational methods for performance analysis of horizontal axis tidal stream turbines. *Appl. Energy* **2012**, *98*, 512–523. [[CrossRef](#)]
12. Consul, C.A.; Willden, R.H.J.; Ferrer, E.; Mcculloch, M.D. Influence of Solidity on the Performance of a Cross-Flow Turbine. In Proceedings of the 8th European Wave and Tidal Energy Conference, Uppsala, Sweden, 7–10 September 2009; pp. 484–493.
13. Khan, M.; Bhuyan, G.; Iqbal, M.; Quaioco, J. Hydrokinetic energy conversion systems and assessment of horizontal and vertical axis turbines for river and tidal applications: A technology status review. *Appl. Energy* **2009**, *86*, 1823–1835. [[CrossRef](#)]
14. Kaprawi, S.; Santoso, D.; Sipahutar, R. Performance of combined water turbine darrieus-savonius with two stage savonius buckets and single deflector. *Int. J. Renew. Energy Res.* **2015**, *5*, 217–221.
15. Vermaak, H.J.; Kusakana, K.; Koko, S.P. Status of micro-hydrokinetic river technology in rural applications: A review of literature. *Renew. Sustain. Energy Rev.* **2014**, *29*, 625–633. [[CrossRef](#)]
16. Le Hocine, A.E.B.; Lacey, R.J.; Poncet, S. Multiphase modeling of the free surface flow through a Darrieus horizontal axis shallow-water turbine. *Renew. Energy* **2019**, *143*, 1890–1901. [[CrossRef](#)]
17. Balduzzi, F.; Zini, M.; Molina, A.C.; Bartoli, G.; De Troyer, T.; Runacres, M.C.; Ferrara, G.; Bianchini, A. Understanding the Aerodynamic Behavior and Energy Conversion Capability of Small Darrieus Vertical Axis Wind Turbines in Turbulent Flows. *Energies* **2020**, *13*, 2936. [[CrossRef](#)]
18. Sinagra, M.; Sammartano, V.; Aricò, C.; Collura, A.; Tucciarelli, T. Cross-flow Turbine Design for Variable Operating Conditions. *Procedia Eng.* **2014**, *70*, 1539–1548. [[CrossRef](#)]
19. Yosry, A.G.; Fernández-Jiménez, A.; Álvarez-Álvarez, E.; Marigorta, E.B. Design and characterization of a vertical-axis micro tidal turbine for low velocity scenarios. *Energy Convers. Manag.* **2021**, *237*, 114144. [[CrossRef](#)]
20. Glauert, H. Wind Tunnel Interference on Wings, Bodies and Airscrews. *Aeronaut. Res. Comm.* **1933**, *1566*, 1–52.
21. Gauvin-Tremblay, O.; Dumas, G. Two-way interaction between river and deployed cross-flow hydrokinetic turbines. *J. Renew. Sustain. Energy* **2020**, *12*, 034501. [[CrossRef](#)]
22. Schluntz, J.; Willden, R. The effect of blockage on tidal turbine rotor design and performance. *Renew. Energy* **2015**, *81*, 432–441. [[CrossRef](#)]
23. Vennell, R. Exceeding the Betz limit with tidal turbines. *Renew. Energy* **2013**, *55*, 277–285. [[CrossRef](#)]
24. Bahaj, A.; Molland, A.; Chaplin, J.; Batten, W. Power and thrust measurements of marine current turbines under various hydrodynamic flow conditions in a cavitation tunnel and a towing tank. *Renew. Energy* **2007**, *32*, 407–426. [[CrossRef](#)]
25. Werle, M.J. Wind Turbine Wall-Blockage Performance Corrections. *J. Propuls. Power* **2010**, *26*, 1317–1321. [[CrossRef](#)]
26. Soerensen, H.C.; Weinstein, A. Ocean Energy: Position Paper for IPCC. In Proceedings of the Scoping Meeting on Renewable Energy Sources and Climate Change Mitigation, Lübeck, Germany, 20–25 January 2008; pp. 93–102.
27. Birjandi, A.H.; Bibeau, E.L.; Chatoorgoon, V.; Kumar, A. Power measurement of hydrokinetic turbines with free-surface and blockage effect. *Ocean Eng.* **2013**, *69*, 9–17. [[CrossRef](#)]
28. Bachant, P.; Wosnik, M. Performance measurements of cylindrical- and spherical-helical cross-flow marine hydrokinetic turbines, with estimates of exergy efficiency. *Renew. Energy* **2015**, *74*, 318–325. [[CrossRef](#)]
29. Kolekar, N.; Vinod, A.; Banerjee, A. On Blockage Effects for a Tidal Turbine in Free Surface Proximity. *Energies* **2019**, *12*, 3325. [[CrossRef](#)]
30. A Consul, C.; Willden, R.H.J.; McIntosh, S.C. Blockage effects on the hydrodynamic performance of a marine cross-flow turbine. *Philos. Trans. R. Soc. A Math. Phys. Eng. Sci.* **2013**, *371*, 20120299. [[CrossRef](#)] [[PubMed](#)]
31. Brochier, G.; Fraunie, P.; Beguier, C.; Paraschivoiu, I. Water channel experiments of dynamic stall on Darrieus wind turbine blades. *J. Propuls. Power* **1986**, *2*, 445–449. [[CrossRef](#)]
32. Fujisawa, N.; Shibuya, S. Observations of dynamic stall on Darrieus wind turbine blades. *J. Wind. Eng. Ind. Aerodyn.* **2001**, *89*, 201–214. [[CrossRef](#)]
33. Sherry, M.; Sheridan, J.; Jacono, D.L. Horizontal Axis Wind Turbine Tip and Root Vortex Measurements. *Exp. Fluids* **2013**, *54*, 3. [[CrossRef](#)]

34. Iungo, G.V.; Viola, F.; Camarri, S.; Porté-Agel, F.; Gallaire, F. Linear stability analysis of wind turbine wakes performed on wind tunnel measurements. *J. Fluid Mech.* **2013**, *737*, 499–526. [[CrossRef](#)]
35. Hiraki, K.; Wakita, R.; Inoue, M. Improvement of straight-bladed vertical-axis water turbine for tidal current power generation. In Proceedings of the 9th ISOPE Pacific/Asia Offshore Mechanics Symposium (PACOMS-2010), Busan, Korea, 14–17 November 2010; pp. 169–174.
36. Shahsavarifard, M.; Bibeau, E.L.; Chatoorgoon, V. Effect of shroud on the performance of horizontal axis hydrokinetic turbines. *Ocean Eng.* **2015**, *96*, 215–225. [[CrossRef](#)]
37. Jeong, H.; Lee, S.; Kwon, S.-D. Blockage corrections for wind tunnel tests conducted on a Darrieus wind turbine. *J. Wind. Eng. Ind. Aerodyn.* **2018**, *179*, 229–239. [[CrossRef](#)]
38. Ruiz, S.N. *Aerogeneradores de Media Potencia*; CIEMAT: Madrid, Spain, 2020.
39. Betz, A. Der Maximum der theoretisch möglichen Ausnutzung des Windes durch Windmotoren. *Z. Gesamte Turbinenwes* **1920**, *26*, 307–309.
40. Nishino, T.; Willden, R.H.J. The efficiency of an array of tidal turbines partially blocking a wide channel. *J. Fluid Mech.* **2012**, *708*, 596–606. [[CrossRef](#)]
41. Draper, S.; Houlsby, G.T.; Oldfield, M.L.G.; Borthwick, A.G.L. Modelling tidal energy extraction in a depth-averaged coastal domain. *IET Renew. Power Gener.* **2010**, *4*, 545. [[CrossRef](#)]
42. Houlsby, G.T.; Vogel, C.R. The power available to tidal turbines in an open channel flow. *Proc. Inst. Civ. Eng. Energy* **2017**, *170*, 12–21. [[CrossRef](#)]
43. Espina-Valdés, R.; Fernández-Jiménez, A.; Francos, J.F.; Marigorta, E.B.; Álvarez-Álvarez, E. Small cross-flow turbine: Design and testing in high blockage conditions. *Energy Convers. Manag.* **2020**, *213*, 112863. [[CrossRef](#)]
44. Álvarez-Álvarez, E.; Rico-Secades, M.; Fernández-Jiménez, A.; Espina-Valdés, R.; Corominas, E.L.; Calleja-Rodríguez, A.J. Hydrodynamic water tunnel for characterization of hydrokinetic microturbines designs. *Clean Technol. Environ. Policy* **2020**, *22*, 1843–1854. [[CrossRef](#)] [[PubMed](#)]
45. Patel, V.; Eldho, T.; Prabhu, S. Experimental investigations on Darrieus straight blade turbine for tidal current application and parametric optimization for hydro farm arrangement. *Int. J. Mar. Energy* **2017**, *17*, 110–135. [[CrossRef](#)]
46. Burton, T.; Jenkins, N.; Sharpe, D.; Bossanyi, E. *Wind Energy Handbook*; John Wiley & Sons, Ltd.: Chichester, UK, 2011.
47. Calignano, F.; Lorusso, M.; Roppolo, I.; Minetola, P. Investigation of the Mechanical Properties of a Carbon Fibre-Reinforced Nylon Filament for 3D Printing. *Machines* **2020**, *8*, 52. [[CrossRef](#)]

4.6 Journal Metrics

The following data are based on the last updated one from the Web of Science database for the year of 2023.

Article No. 3	
Journal	SUSTAINABILITY
Title	Wind–water experimental analysis of small sc-darrieus turbine: an approach for energy production in urban systems
Category Quartile	Q2
Impact Factor	3.889
Impact Factor (5 years)	4.089
CiteScore	5.0
No. of Citations [May 2021 - May 2023]	6

Chapter 5

Efficiency Enhancement Varying the Channel Geometry

5.1 Overview

In the previous chapters, the design and the performance of the lift-based hydrokinetic turbine have been investigated. These kinds of turbines are considered more efficient than the drag-based ones. However, recommendations can still be applied to improve the performance of the drag-based types. Thus, the current investigation has been extended to include the drag-based turbine and examine potential methods to enhance its efficiency. This chapter focuses on improving the performance of the drag-based hydrokinetic turbine installed in a hydraulic channel through the use of an obstacle on the channel bottom, which is a cost-effective and maintenance-free solution. Experiments have been carried out using two obstacles, with heights of 3 *cm* and 5 *cm*, that are designed to occupy all the channel width. Numerically, a multiphase model is developed to investigate the impact of the height of the obstacle on the flow rate passing through the turbine rotor, and the forces exert on the blades.

5.2 The Turbine Model Configuration

A basic drag-based hydrokinetic turbine has been designed and fabricated to be tested inside the water channel for different obstacle configurations at the channel bottom. Table 5.1 presents the main design parameters of the turbine model. As illustrated in Figure 5.1, the rotor contains 12 blades that are made of AISI 304 stainless steel to resist corrosion and humid environments. The connection between the blades, the upper and the lower plates has been made by a Shielded Metal Arc Welding (SMAW), which provides a good finishing and adhesion at a low cost. The semi-circular section blades have a beveled edge (at angle of 30°) to improve the hydrodynamic profile, as it reduces the losses when

Table 5.1: General specifications of the drag-based turbine rotor.

Parameter	Specification
Rotor diameter (D)	0.23 m
Blade profile	semi-circular
Chord length (C)	0.042 m
Rotor height (H)	0.3 m
Number of blades (n)	12
Bevel angle (ϕ)	30°
Shaft diameter (d_s)	0.03 m

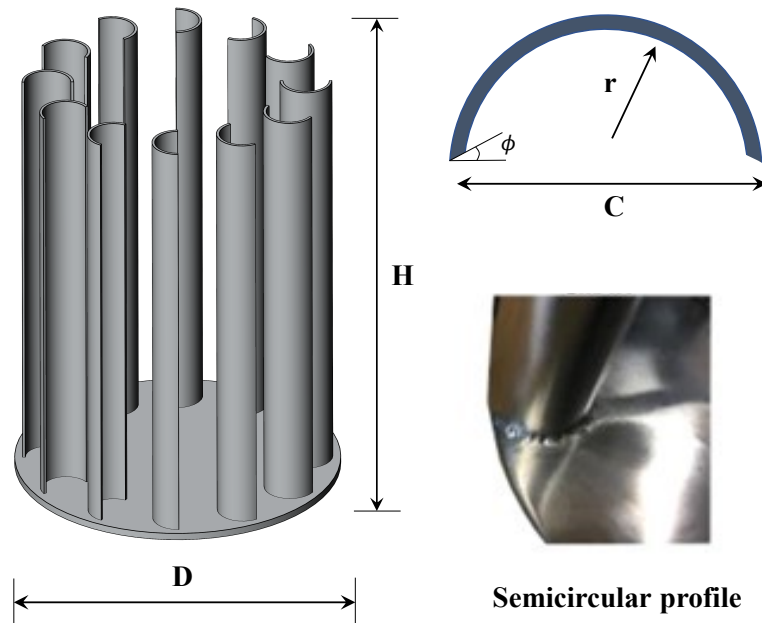


Figure 5.1: A detailed schematic of the drag-based turbine model.

the water stream approaches the turbine blade. The two ending plates are also made of stainless steel, containing a hollow center to facilitate coupling to the rotational axis. The upper cover has a 30 mm hole through which the metal shaft stem passes, while the lower cover has a 13 mm hole. It is in the lower base where the rotor is tightened by nut and bolt so that the axis rotates in conjunction with the rotor. The two obstacles (see Fig. 5.2) have been made out of aluminium due to its low weight and firmness, designed to occupy all the channel width with heights of 3 cm and 5 cm.

The turbine model, with its all components, has been mounted on a steel shaft and coupled with a 300 W commercial (Gimbal-GM8112H) Permanent Magnet Generator (PMG) with the characteristics indicated in Table 5.2. To increase the electrical voltage of the PMG, a mechanical multiplier system of belts and pulleys has been installed. Thus, the rotational speed of the generator is increased 8 times. The rotor and the generator arrangements are shown in details in Fig. 5.3.

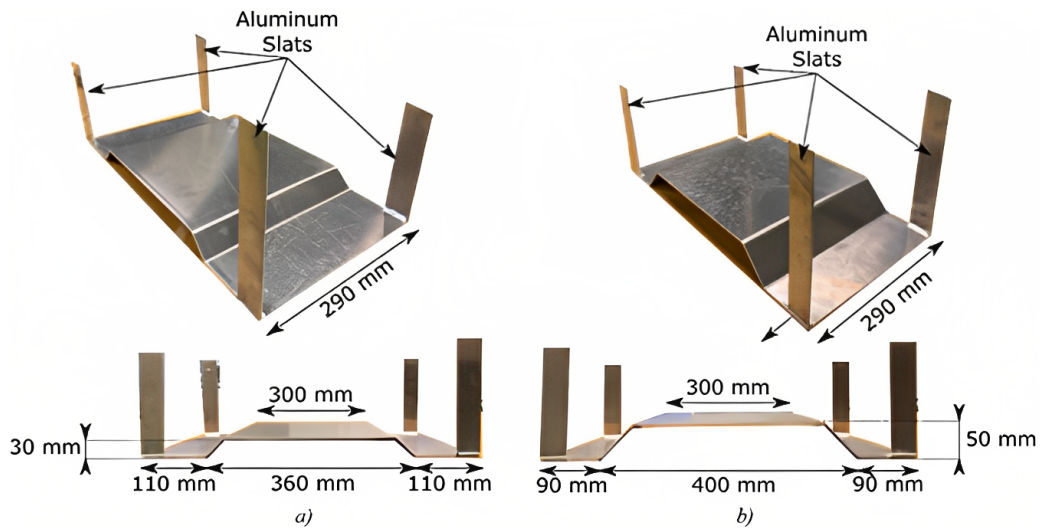


Figure 5.2: A detailed schematic of the two metallic obstacles.

Table 5.2: PMG main characteristics.

Feature	Value
Pair of poles	21
Resistance per phase	7 Ω
Series inductance per phase	3 mH
Maximum nominal voltage	28 V

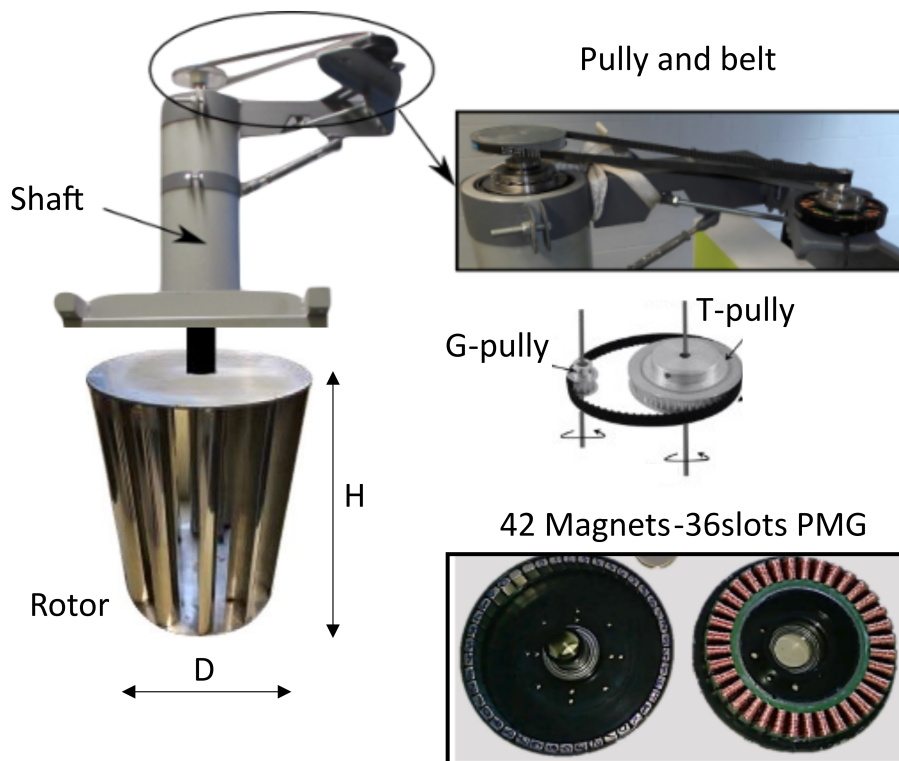


Figure 5.3: Turbine-Generator coupling system.

5.3 The Numerical Model

A three-dimensional multiphase numerical model has been developed to simulate the drag-based turbine for different channel bed obstacles. The model includes the turbine, the settling tank, and the test channel. The numerical model has been created with the actual dimensions of the hydrodynamic flume, which includes a rectangular prism-shaped area for water discharge from the channel (outlet), and two water inlet holes located in the lower part of the settling tank. As presented in Fig. 5.4, the whole domain has been discretized using a fully unstructured mesh with a tetrahedral shape cells. A structured mesh comprised of rectangular prisms has been applied in the water discharge area due to its cubic shape. To simulate the rotational motion of the turbine rotor, the sliding mesh technique has been used in the current simulation.

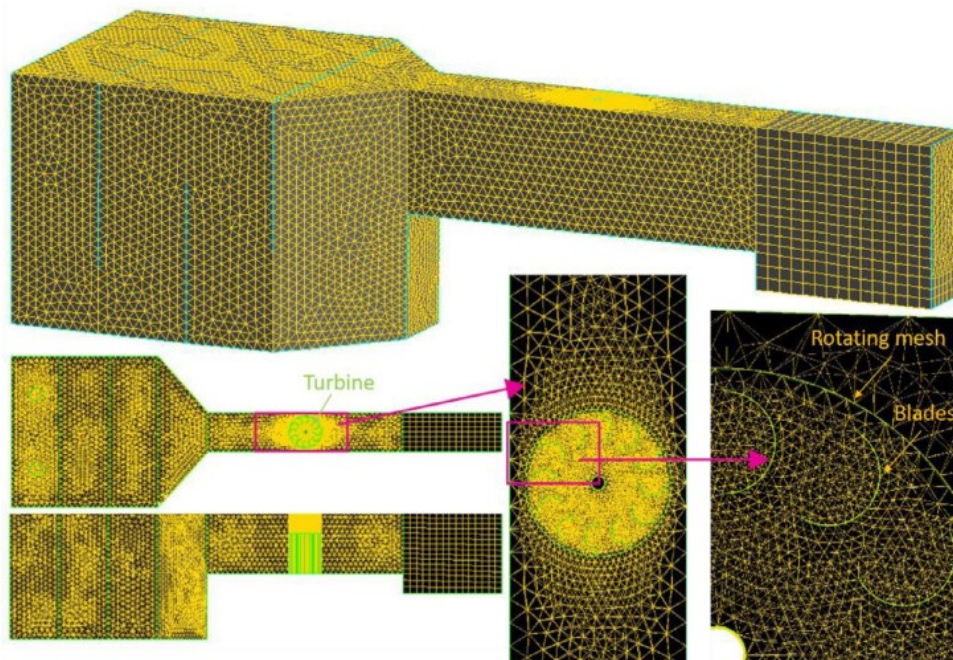


Figure 5.4: The computational grid visualization.

In order to investigate the mesh sensitivity, five different mesh sizes of (200K, 500K, 800K, 1,200K, and 1,500K cells) have been tested using the same flow rate and under the same operating conditions. The mesh size of 1,200K cells has been selected as it provided a good balance between the accuracy and the computational cost. This mesh exhibits a high quality as 99.99 %of cells have a skewness value below 0.7. Also, to simplify the numerical model and to reduce computational times, grid simplifications have been made. The blades are represented as surfaces without thickness with a sharp blade inlet, detecting flow separation at the leading edge correctly without the need for a finer mesh around the blade. additionally, no finer meshes have been included to achieve a more accurate description of the near wall boundary layers. These are significantly reduced due to the increment of the velocity near the turbine as a consequence of the flow blockage.

5.4 Objectives

The main objective in the current chapter is to investigate the power output increase and the efficiency enhancement of a drag-based hydrokinetic turbine by varying the channel geometry. This increase is achieved by implementing an obstacle on the bottom of the water channel. By means of experimental and numerical methodologies, the the power output and the flow behaviour have been investigated to evaluate the effectiveness of this approach.

5.5 Peer-reviewed Journal Publication

5.5.1 Increased Efficiency of Hydrokinetic Turbines Through the Use of an Obstacle on The Channel Bottom



Contents lists available at ScienceDirect

Ocean Engineering

journal homepage: www.elsevier.com/locate/oceaneng

Increased efficiency of hydrokinetic turbines through the use of an obstacle on the channel bottom

R. Espina-Valdés^{a,*}, V.M. Fernández-Álvarez^a, A. Gharib-Yosry^b, A. Fernández-Jiménez^a, E. Álvarez-Álvarez^a^a GIFD Group, EP Mieres, University of Oviedo, Mieres, Spain^b Mechanical Power Department, Faculty of Engineering, Port Said University, Port-Said, Egypt

ARTICLE INFO

Keywords:

Hydrokinetic
Cross-flow
Obstacle
Rotor flow rate
Maximum-power-point

ABSTRACT

Nowadays, the growing demand for energy and the current shift towards the eradication of fossil fuels has led to continuous research into and development of alternative clean energies. Among these, one of the least investigated is the extraction of hydrokinetic energy in hydraulic channels. This article highlights an investigation focused on improving the performance of a hydrokinetic turbine installed in a hydraulic channel through the use of an obstacle on the channel bottom, thus providing a solution involving minimum investment and without the need for maintenance. It was found through a series of tests carried out in a hydrodynamic water tunnel that the power produced increases with the height of the obstacle. In addition, a validated numerical model facilitated the completion of the research by studying the influence of the height of the obstacle on the flow rate that passes through the turbine rotor. The latter representing the key factor in the generation of power together with the forces acting on the blades. Under conditions analogous to those of the literature examples (with the turbine fully submerged), a power increase of about 25% was obtained in the tests.

1. Introduction

The renewable energy sector has not been spared from the effects of the COVID-19 (International Energy Agency, 2021). Pandemic and manufacturing processes, supply chains and investments have been affected, leading, once again, to a slowdown in the transition to a sustainable global energy model (Hosseini, 2020). Nevertheless, our responsibility as a society is to continue the path towards finding new, cleaner, and more sustainable sources of energy.

In addition to conventional renewable energies, there are other types of small-scale energy utilization that may be of great interest, such as systems for utilizing the energy present in river currents, artificial water channels or marine currents or tides. The energy that exists in flowing water currents is considered a low-carbon resource with an enormous power potential (Moran, Lopez, Moore, Müller, Hyndman). In fact, the International Energy Agency (IEA) has estimated a world energy potential of 120,000 TWh in the case of tidal currents (Caballero Santos, 2011) and more than 840 TWh in the case of low-velocity water currents of rivers and channels (IDAE, 2011). At present, the state of development of the use of the energy present in the currents is conducted by

hydrokinetic turbines with know-how derived from the wind industry. The development of these devices is still in its embryonic stage, with demonstration applications to supply electrical energy in not connected to the electricity grid areas (Kumar and Sarkar, 2016). The power generated by a hydrokinetic turbine depends on the water velocity cubed, the area swept by blades, the water density and the efficiency of the conversion equipment (Mohammadi et al., 2020). The rated electrical power of the marine hydrokinetic turbines is generally much higher (>100 kW) than river and channel turbines (1–10 kW) (Roberts et al., 2016). Until now, the use of hydrokinetic turbines has been restricted mainly to water velocities higher than 1 m/s (Güney and Kaygusuz, 2010).

Hydrokinetic turbines can be classified according to the direction of flow and the position of the axis in two main groups: axial turbines with parallel axis and flow (similar to the designs of two-bladed and three-bladed horizontal axis wind turbines), and crossflow with perpendicular axis (horizontal or vertical in relation to the free surface) and flow, like the Savonius or Darrieus designs (Vermaak et al., 2014) (Patel et al., 2017a). In the existing developments to date, axial turbines present better conversion efficiency than crossflow ones, but these allow better use of the wet section. Additionally, vertical axis crossflow turbines

* Corresponding author.

E-mail address: espinarodolfo@uniovi.es (R. Espina-Valdés).<https://doi.org/10.1016/j.oceaneng.2022.112872>

Received 18 March 2022; Received in revised form 13 September 2022; Accepted 8 October 2022

Available online 18 October 2022

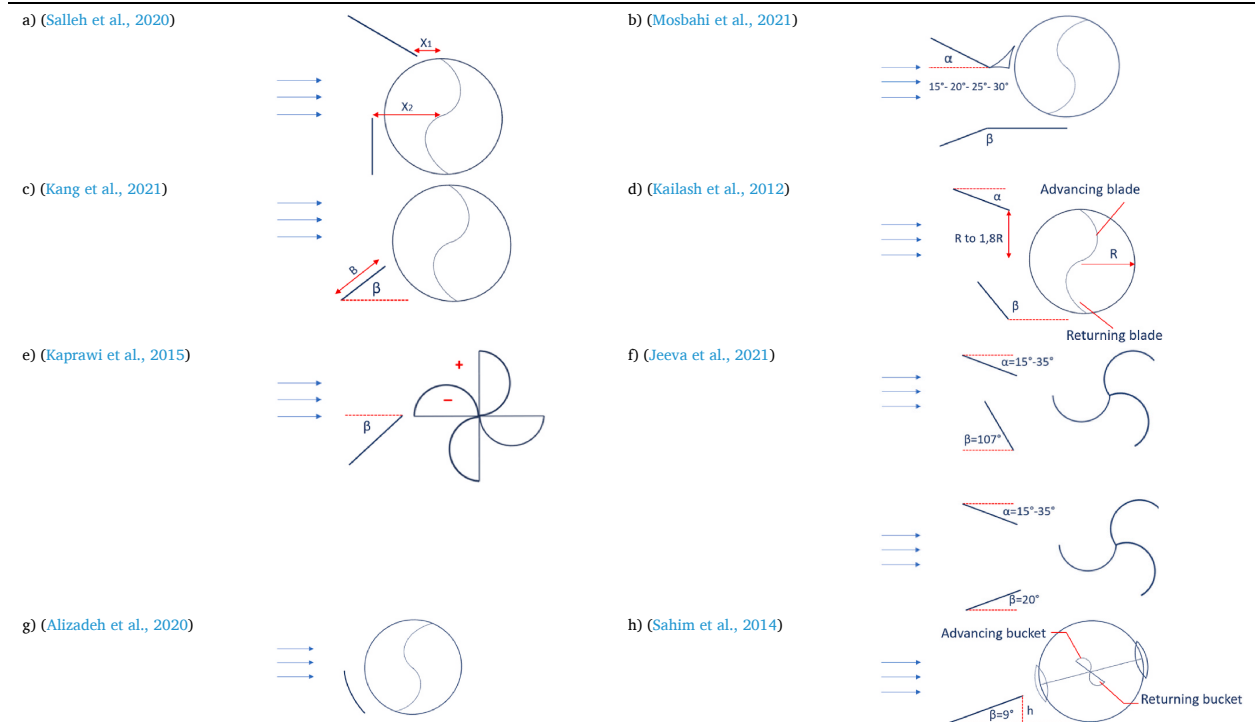
0029-8018/© 2022 The Authors. Published by Elsevier Ltd. This is an open access article under the CC BY-NC-ND license (<http://creativecommons.org/licenses/by-nc-nd/4.0/>).

Nomenclature		Greek symbols	
A_u	Turbine useful area, m^2	η_e	Electrical efficiency
D	Turbine diameter, m	η_m	Mechanical efficiency
F_D	Drag forces, N	μ	Water viscosity, Kg/m·s
F_L	Lift forces, N	ρ	Water density, kg/m^3
F_T	Thrust forces, N		
g	Gravitational acceleration, m/s^2	Abbreviation	
h	Water height, m	AFD	Adjustable frequency drive
H_r	Turbine hydraulic head, m	AISI	American iron and steel institute
L	Blade length, m	CFD	Computational fluid dynamics
n	Turbine rotational speed, rpm	HWT	Hydrodynamic water tunnel
p	Pressure, Pa	MPP	Maximum power point
P_e	Electrical power, W	MPPT	Maximum power point continuously
P_r	Hydraulic power, W	O&M	Operation and maintenance
P_{rMPP}	Maximum hydraulic power, W	PMG	Permanent magnet generator
Q	Water flow rate, m^3/s	SCADA	Supervisory control and data acquisition
Q_r	Rotor flow rate, m^3/s	SIMPLE	Semi-implicit method for pressure-linked equations
Q_{rMPP}	Flow rate in maximum power production, m^3/s	SST	Shear stress transport
Re	Reynolds number	TURTLE	Turbine test laboratory equipment
v	Velocity, m/s	URANS	Unsteady Reynolds-Average-Navier-Stokes
y	Upstream water depth, m	VOF	volume of fluid
y_c	Critical depth, m	3D	three-dimensional
z	Obstacle height, cm		

allow electrical and electronic control equipment to be located out of the water, unlike axial turbines, whose equipment must be encapsulated when submerged. As analyzed by Patel et al. (2017b) through experimental investigations, the Darrieus turbine is one of the best options that can be used as a hydrokinetic turbine due to its high power coefficient.

Therefore, the use of vertical axis cross-flow turbines reduces the initial investment, minimizes maintenance costs and increases the availability of the system (Hunt et al., 2020). The new technological challenge for the development of this type of turbines is the improvement of their efficiency even in operating conditions with very low speeds, for which

Table 1
Flow modifiers schemes.



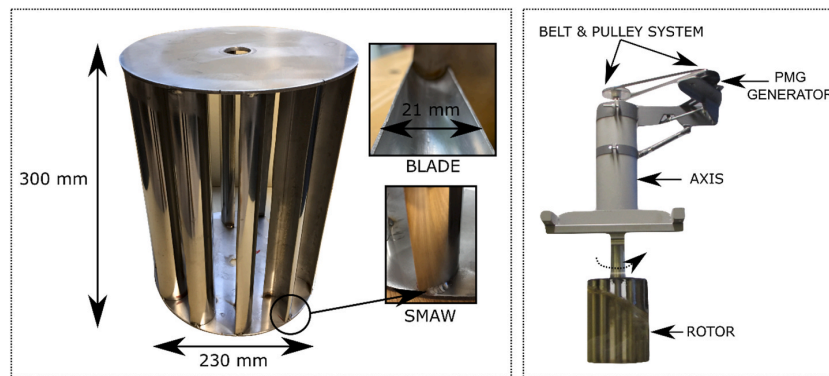


Fig. 1. Turbine design.

various methods have been studied.

Firstly, the development of a control algorithm which ensure that the maximum power of the turbine is continuously secured, named Maximum Power Point Tracking (MPPT) algorithm. For example, the research presented in (Alvarez et al., 2018) that proposes a simple solution based on a low cost power electronics control board running simple software. Additionally, the studies carried out by Jia et al. (2002) and Bundi et al. (2020) propose MPPT algorithms embedded in a low-cost electronic board for its application in turbines operating in high torque conditions.

Secondly, taking advantage of the variation of the current characteristics caused by the blockage generated by the turbine when the flow passes (Houlsby and Vogel, 2016). This results in three phenomena: an increase in the velocity of the fluid around the rotor, a change of the pressure in the wake, and the appearance of longitudinal pressure gradients due to the effects of the boundary layer (Glauert, 1933). Daskiran et al. (2016) investigated the blockage ratio effect on turbine performance and they found that the increment in blockage ratio from 0.03 to 0.98 enhanced its power coefficient from 0.437 to 2.254 and increased power generation from 0.56 kW to 2.86 kW. Kolekar et al. carried out experiments to understand the influence of free surface proximity on blockage effects and near-wake flow field, and therefore in the power obtained (Kolekar et al., 2019). Honnasiddaiah et al. (C M et al., 2021) analyzed the performance of a Savonius rotor for small-scale hydro-power generation by modifying the bed slope, and they found power coefficient and torque coefficient improvements of up to 40% and 10%, respectively.

Thirdly, installing flow modifiers to increase the turbine performance, mainly in drag-based rotors. The simpler ones are vertical plates located upstream from the turbine. Different examples of studies in the research line of vertical plates with drag-based rotor turbines, are shown in Table 1 (elaborated by the authors) represented by horizontal two-dimensional models. The study of the influence of a double obstacle scheme in the performance of a turbine (Table 1-a) was done by Salleh et al. (2020) finding increments up to 30%. Mosbahi et al. (2021) analyzed the effect of an upstream deflector system (Table 1-b) in the performance of a twisted rotor by numerical simulations and experimental tests. Results showed that the proposed deflector improved its efficiency by 14%. Kang et al. (2021) described the effects of an upstream baffle on the flow characteristics and starting performance of a drag-type hydrokinetic rotor (Table 1-c). The results show that the negative torque is eliminated due to the introduction of the deflector.

Other experimental studies carried out showed that two deflectors placed in their optimal positions upstream of the flow increased the energy obtained (Kailash et al., 2012) (Table 1-d) and revealed that the angle of the deflector with regard to the current flow influences the performance of the turbine (Kaprawi et al., 2015) (Table 1-e) (Jeeva et al., 2021) (Table 1-f). For a Savonius model design, Alizadeh et al.

(2020) investigated (using CFD model) the power generation improvement made by an upstream barrier (with at least the turbine height) that deviated the fluid flow from the reversing bucket (Table 1-g). The results of this analysis revealed that utilizing a barrier to its optimum length increases the maximum power generated by about 18%. Also, the experimental work carried out by Sahim et al. (2014) concluded that a single deflector plate placed upstream from a Darrieus-Savonius turbine increases the energy that it produces (Table 1-h).

Despite the increase in power production that the flow modifiers produce, their installation brings about a rise in solution costs and complicates the O&M tasks, i.e., causing the accumulation of residues and sediments (Martin-Short et al., 2015).

This research reveals an analysis and study of how an obstacle in the channel bottom, below the turbine, increases the power generated by a cross flow drag-based hydrokinetic turbine operating in high blockage conditions. The obstacle has a remarkably simple design which minimizes the cost of its installation, prevents any possible obstruction of the current flow, maintains the directions of the stream flow lines across the turbine, finally obtaining an increase in power in keeping with the height of the obstacle. The inclusion of the obstacle in the channel when designing a new project would not require specific maintenance. In the case of acting on existing channels, it would mean a slight modification in the structure of the channel, which would not require an increase in the maintenance cost of the original channel, since it is only a modification of the slopes of the bottom of the channel. If this solution of the obstacle at the bottom is compared with the use of deflectors, an elimination of the sediment problems can be seen in the low speed zones that affect the deflectors, where periodic maintenance work is necessary and takes up time of operation and raises costs.

In this work, two obstacle heights plus the no obstacle case have been studied to obtain sufficient information to achieve a consistent validation of the numerical model. Experimental studies with a larger number of obstacle heights studied can be found in the literature, such as the analyses of Patel et al. (Patel, Eldho, Prabhu).

In terms of blockage, the obstruction caused by the presence of the turbine rotor plays an important role. The flow characteristics are altered and therefore, the power results obtained will vary if the turbine is installed in another location with different dimensions than the test channel. Thus, if one wished to extrapolate these results to another installation, it would be necessary to apply a velocity correction method. Patel et al. introduced the methodology of correcting the velocity and efficiency of hydrokinetic turbines with a highly blocked channel geometry (Patel et al., 2019).

The study was carried out in the running water channel of the EPM of the University of Oviedo, and the results obtained have been used to validate a Computational Fluid Dynamics (CFD) numerical model. This numerical model was used to perform a parametric study with different obstacle heights and to analyze the causes of the increase in power

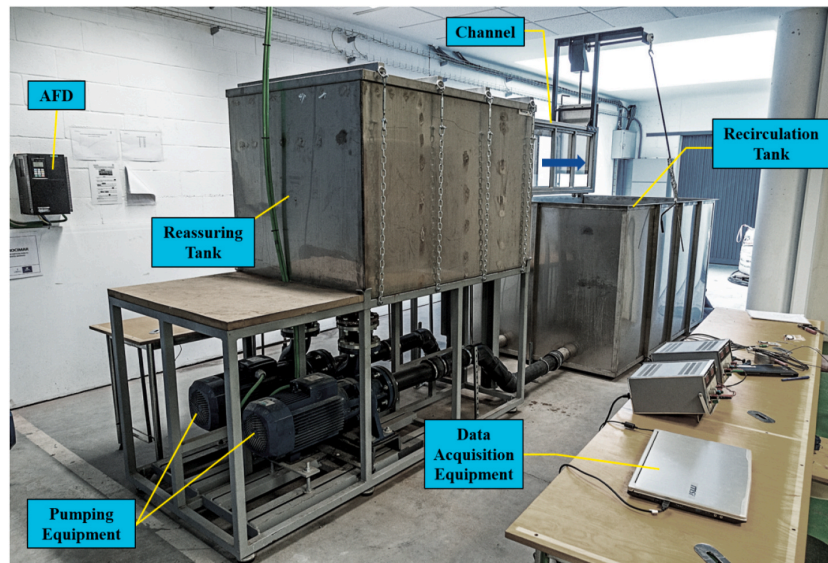


Fig. 2. Hydrodynamic water tunnel.

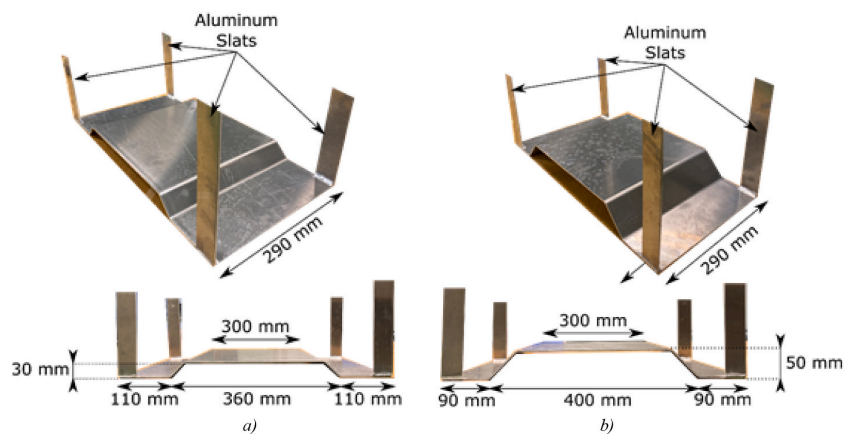


Fig. 3. Geometry of bed obstacles: a) 3 cm height and b) 5 cm height.

produced.

2. Laboratory materials

The elements used to carry out the tests were a turbine, a hydrodynamic water tunnel, two obstacles (same design and different heights) and a control system. The turbine rotor has 12 semi-circular blades 0.3 m high and 0.23 m wide, built with AISI 304 stainless steel to resist corrosion and dynamic forces, and shielded at the top and bottom to ensure adhesion even at fast rotational speeds. The blades have an angular separation of 30° with a semicircular section of 21 mm of diameter (Fig. 1). This type of turbine was selected because it has sufficient starting torque at low flow rates and has already been characterized in the laboratory and in the field.

The turbine is coupled to a vertical axis with radial and axial high standard waterproof bearings installed at a metallic bushing. This axis has in its upper part a belt and pulley system designed to multiply the rotational speed mechanically connected to a permanent magnet generator (PMG).

The experimental tests have been conducted in a hydrodynamic

water tunnel (HWT) (Fig. 2) made up of tanks (reassuring and recirculation), hydraulic pumps, adjustable frequency drive (AFD), glass channel (0,5 m height, 0,3 m width and 1,5 length) and a monitoring-control system. The HWT can recirculate water flows up to $300 \text{ m}^3/\text{h}$.

The monitoring and control system, named TURbine Test Laboratory Equipment, TURTLE (designed by the researches of University of Oviedo Hydraulic Engineering Group) is made up of hardware components – two ultrasonic water height sensors (HC-SR04), two pump drives converters, electronic board to control the turbine operation, and PC- and a specially designed software which runs in the PC to perform the test and collect the data obtained (Álvarez-Álvarez et al., 2020).

The two obstacles (Fig. 3) have been made out of aluminium due to its low weight and firmness, designed to occupy all the channel width with heights of 3 cm and 5 cm.

3. CFD numerical model

To develop the numerical model, a complete three-dimensional geometry was generated incorporating the turbine, the reassuring tank, and the test channel (Fig. 4). The geometrical design has the real

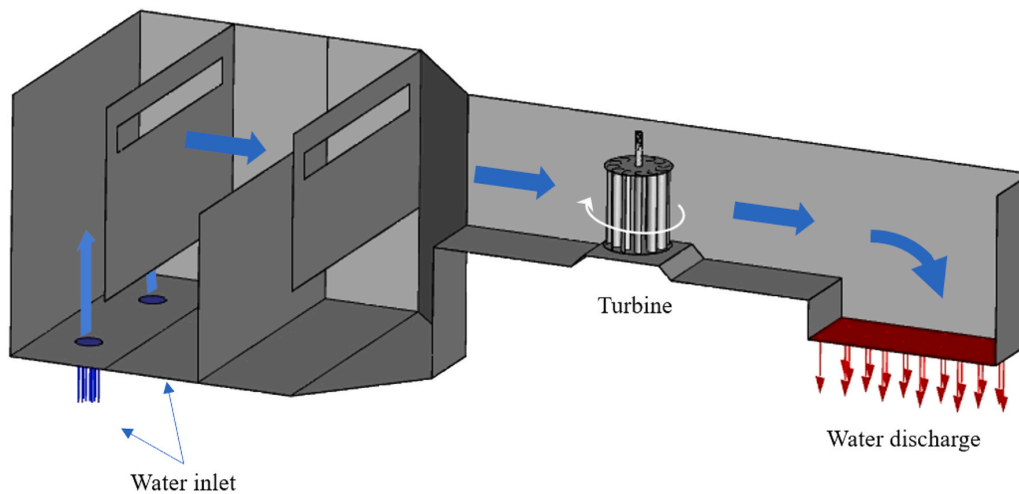


Fig. 4. HWT geometry.

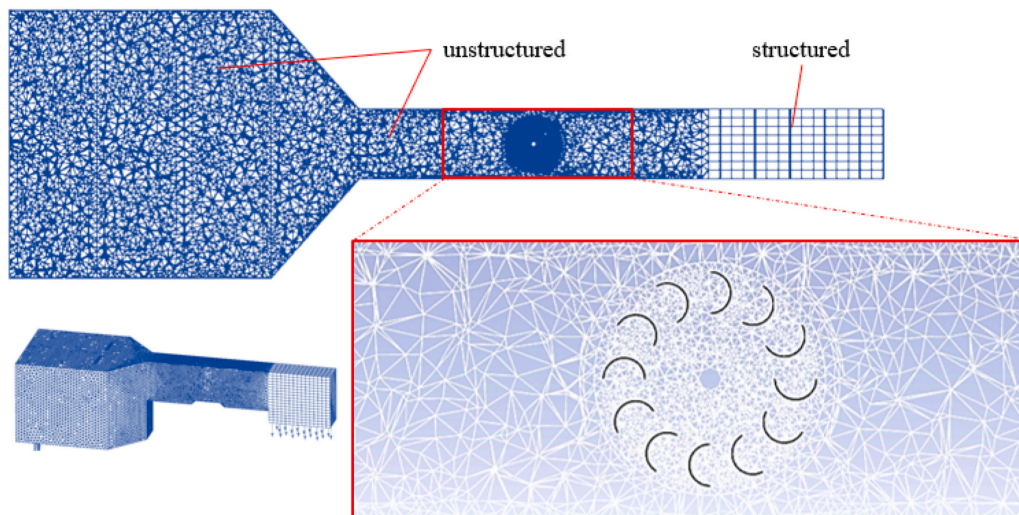


Fig. 5. Numerical model mesh.

dimensions of the hydrodynamic tunnel, including a rectangular prism-shaped area for the discharge of water from the channel (outlet) and two water inlet holes in the lower part of the reassuring tank. In addition, to guarantee the proper functioning of the model, the upper section of the domain was completely exposed to the air with a view to replicating the water flow free surface.

This same geometry was employed in the different simulations incorporating the different bed obstacles which were the object of the investigation. To obtain the numerical CFD model a cell mesh was built where the flow equations were solved (Fig. 5). For that purpose, the geometry was divided into 8 different volumes where an unstructured mesh based on tetrahedra (which has a good adaptation to complex geometries) was used, except for the water discharge area where a structured mesh based on rectangular prisms was employed due to its cubic shape. Incorporating the turbine in a cylindrical volume which rotates helped simulate the movement of the turbine with a good degree of accuracy as the unstructured mesh adapts perfectly to the turbine blades.

The number of cells of the mesh was set to 1,200,000 with

satisfactory quality: 99.99% of the cells had a skewness value under 0.7. To study the dependence of the mesh with the power results and its influence on the computational time, five numbers of cells, 200,000, 500,000, 800,000, 1,200,000 and 1,500,000 were evaluated with the same flow rate and the range of rotational speeds that define the turbine power characteristics. With 1,200,000 cells a compromise between accuracy and computational time was reached.

The fluid volume model (VOF) has been selected to track the air-water free surface (Hirt and Nichols, 1981). The model solved the Unsteady Reynolds-Average-Navier-Stokes (URANS) for each cell of the entire domain (Riglin et al., 2015).

To obtain a turbine power characteristic from the no-load to the maximum load condition for a certain flow rate value, three steps were taken a) filling the canal with water (which was empty at the beginning) until the free surface stabilized; b) applying the condition of movement to the rotating mesh defined by introducing the inertial terms of the centrifugal forces and the Coriolis acceleration in the flow equations (Lanzafame et al., 2013); c) moving the rotating mesh with the different rotational speeds measuring the torque needed to maintain them

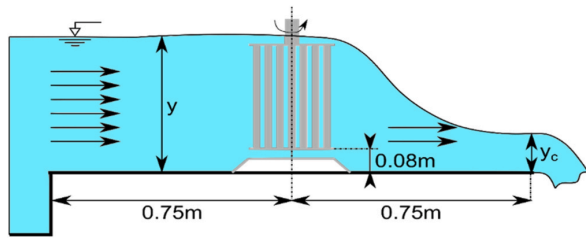


Fig. 6. Experimental test scheme.

constant. In the first two stages, convergence was achieved with 1000 iterations since they are stationary processes, while in the final phase, due to the mesh movement and its non-stationary condition, the convergence was achieved through a stabilization of the torque in 10 complete revolutions of the rotor. In this case, the value of the time step corresponding to a rotation of 3° was set, thereby varying it as a function of the rotational speed.

The boundary conditions applied were mass flow at the water inlets, pressure outlet at the discharge, and the upper part of the model (tank

and channel) with normal atmospheric pressure (101.325 Pa). The surfaces of the tank, the channel and the turbine blades were defined as walls with no-slip condition. Water and air densities and viscosities were set to constant values (water: 1.025 kg/m^3 and $1.003 \cdot 10^{-3} \text{ kg/m}\cdot\text{s}$; air: 1.225 kg/m^3 and $1.789 \cdot 10^{-5} \text{ kg/m}\cdot\text{s}$).

To resolve the URANS equations the solver Pressure-Implicit with splitting of Operators algorithm was used. Second order schemes were also applied for the discretization of the spatial and temporal derivatives in the equations. The semi-implicit method for pressure-linked equations (SIMPLE) was used in order to resolve the velocity-pressure coupling. The turbulence was simulated using the shear stress transport (SST) $k-\omega$ turbulence model, a combination of a $k-\omega$ model and a $k-\epsilon$ model suitable for complex flows (Bardina et al., 1997). This turbulence model is chosen since the average y^+ is 0.93, and empowers accurate predictions of flow separation under adverse pressure gradients (Gorle et al., 2016). In addition, in the blade zone the meshing has cells within the boundary layer. To carry out the simulations of the numerical model, the ANSYS FLUENT V18.0 software was used (Ansys, 2018).

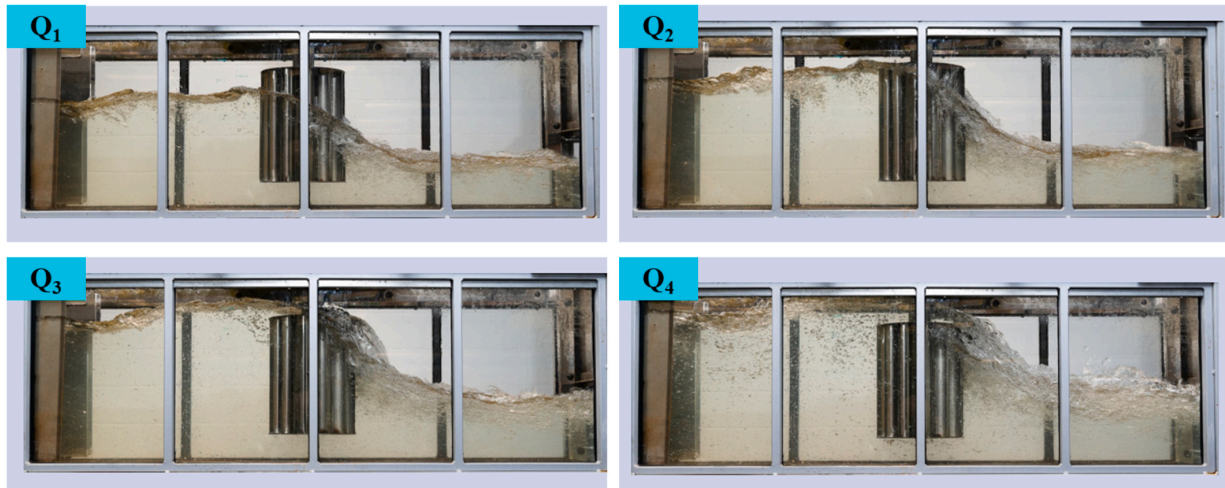


Fig. 7. Scenarios without bed obstacle.

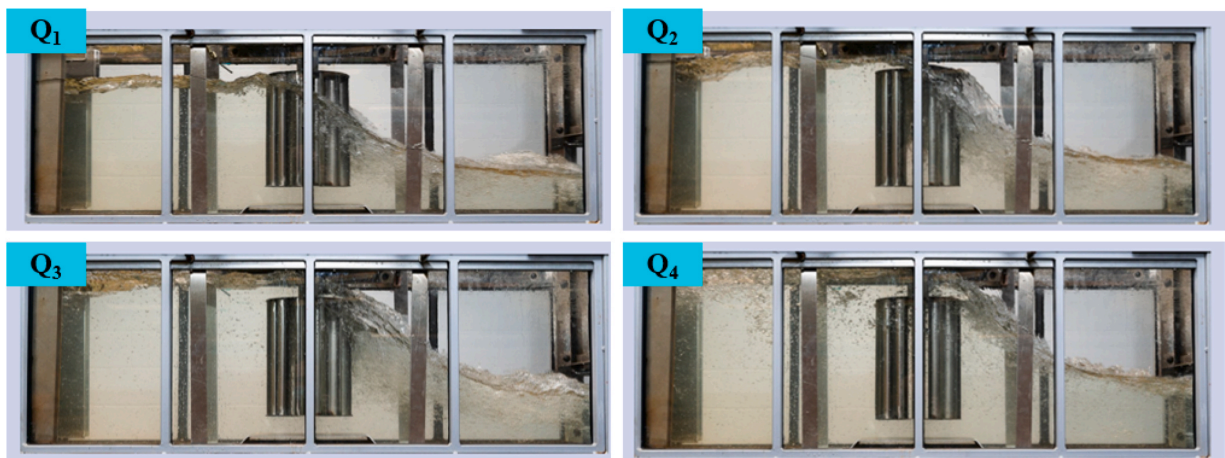


Fig. 8. Scenarios with 3 cm obstacle.

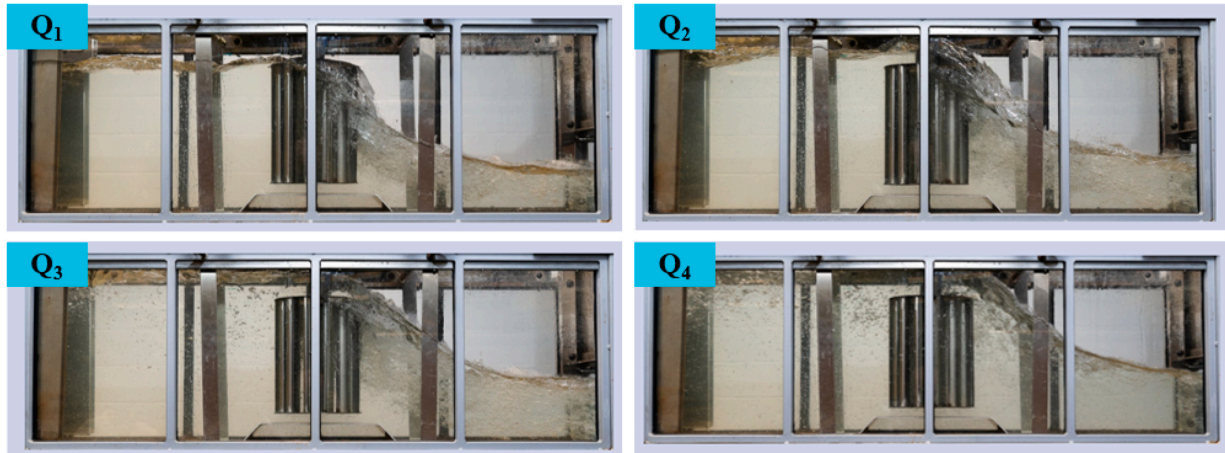


Fig. 9. Scenarios with 5 cm obstacle.

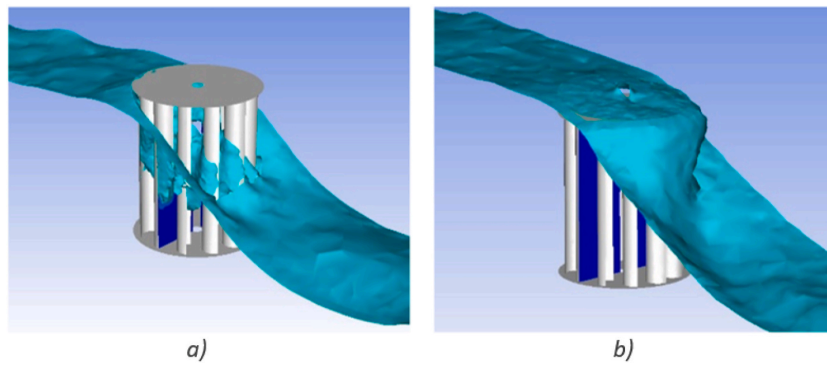


Fig. 10. Free surface and A_w for Q_3 : a) no obstacle; b) 5 cm obstacle.

4. Experimental tests methodology

Three different set of tests were conducted: without bed obstacle, and with the 3 cm and the 5 cm height bed obstacles; each set with four flow rates: $0.055 \text{ m}^3/\text{s}$ (Q_1), $0.064 \text{ m}^3/\text{s}$ (Q_2), $0.072 \text{ m}^3/\text{s}$ (Q_3) and $0.076 \text{ m}^3/\text{s}$ (Q_4).

The position of the turbine and the obstacle in the tests are shown in Fig. 6, both elements upstream from the channel discharge at which critical flow conditions are reached. The channel slope is zero and the Reynolds number - $Re_D = \frac{\rho v D}{\mu}$ where ρ is water density, v is upstream

water velocity, D is turbine diameter and μ is the water viscosity-in the experiment as a function of the diameter of the turbine is around $0.7 \cdot 10^6$.

The different scenarios evaluated corresponding to the different flow rates and obstacles are shown in Figs. 7-9.

In scenarios Q_1 and Q_2 the presence of the obstacle increases the proportion of the turbine rotor that is submerged.

For all tests conducted the blockage ratio calculated as the wet transversal areas of turbine plus obstacle divided by that of the channel was kept within a range between 40% and 50%. The results are

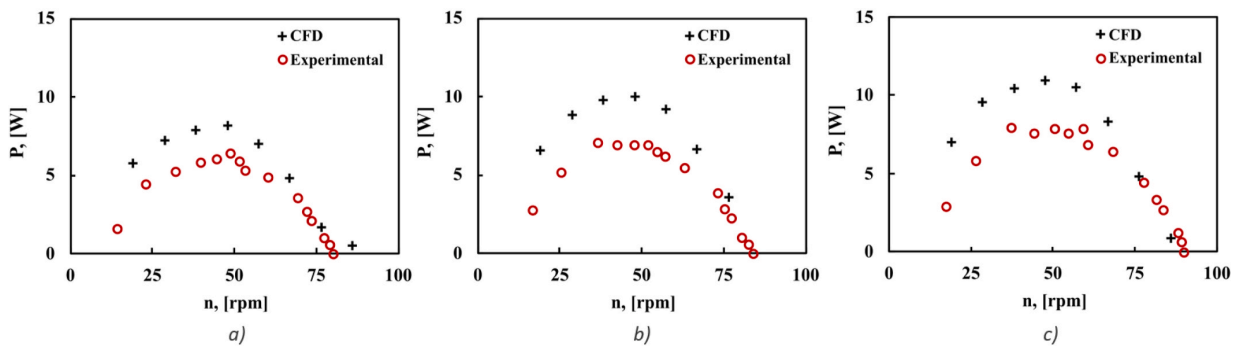


Fig. 11. Power characteristics experimental vs CFD for Q_4 : a) no bed obstacle; b) 3 cm obstacle; c) 5 cm obstacle.

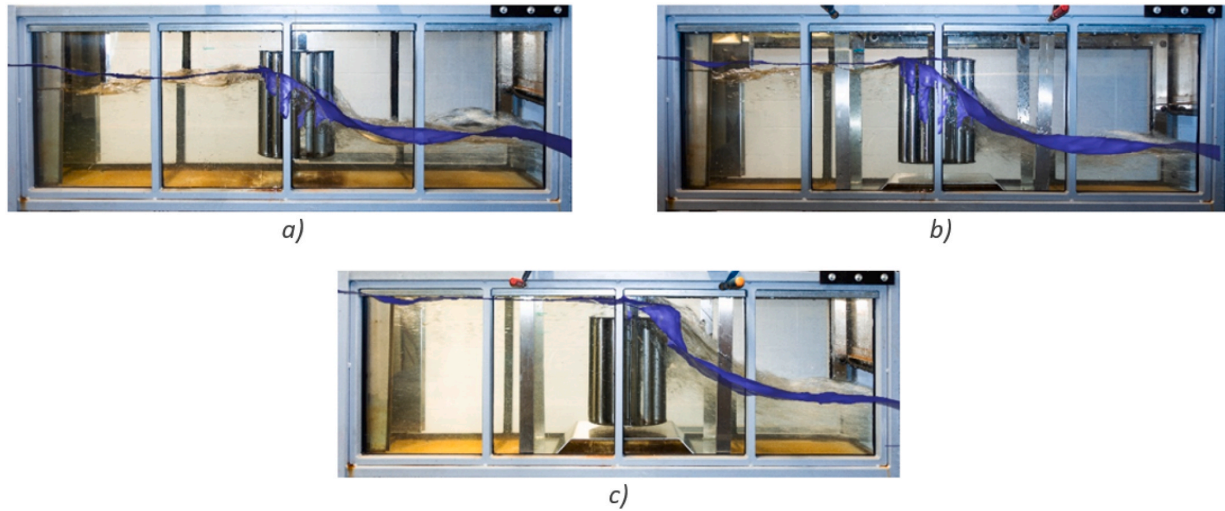


Fig. 12. Free surface experimental vs CFD results for Q_3 : a) no obstacle; b) 3 cm obstacle; c) 5 cm obstacle.

conditioned by the size of the channel. The velocities and heights are the result of the size of the channel. Obviously, if this turbine configuration is tested in another scenario, the results will be different. To predict the real power of the turbine if it works in a river or canal with a large flow region, it would be necessary to take into account the velocity corrections widely studied in the literature, which are mainly due to the blockage effect.

5. Numerical model validation

The numerical model was validated with the experimental one by comparing their degree of similarity between results of power characteristics and free surfaces positions.

The power obtained with the CFD model consists of the rotor power (P_r) hereafter to be known as the hydraulic power:

$$P_r = \rho g H_r Q_r \tag{1}$$

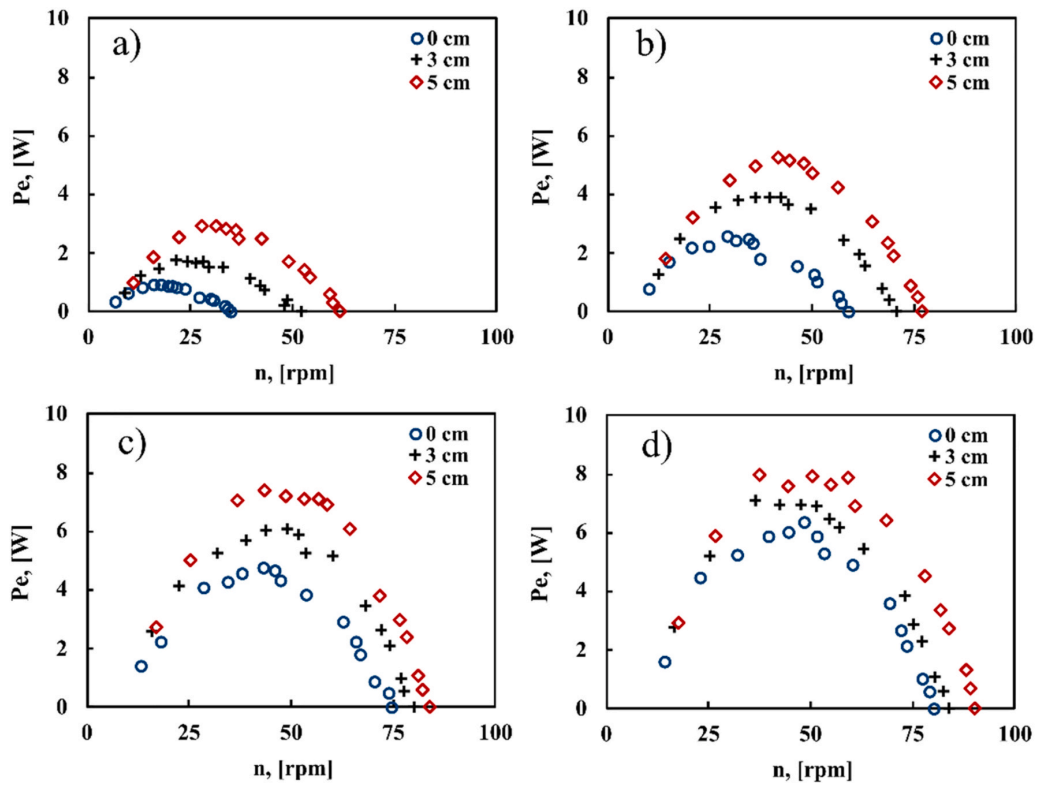
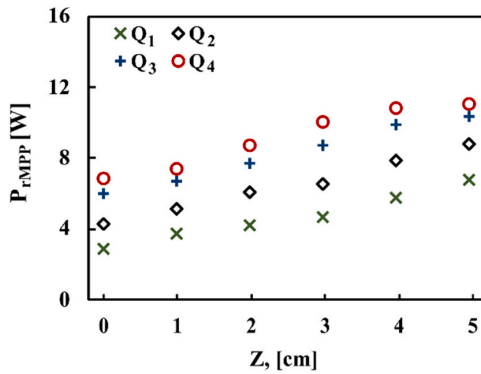


Fig. 13. Electrical power characteristics: a) Q_1 ; b) Q_2 ; c) Q_3 ; d) Q_4 .


 Fig. 14. Variation of P_{rMPP} with the obstacle height.

where ρ is the density of the fluid, g is the gravity acceleration, H_r is the hydraulic head and Q_r is the rotor flow rate. The value of Q_r is determined by calculating the flow rate through the rotor-soaked area in a transversal-to-the-flow plane located in the middle of the turbine, named as useful area (A_u). Fig. 10 shows the free surface and A_u obtained for Q_3 with 3 and 5 cm obstacle heights.

However, the power obtained in the experimental tests corresponds to electrical power (P_e) that comprises the P_r and the mechanical and electrical performances of the installation, in accordance with the following expression:

$$P_e = \eta_e \eta_m P_r \quad (2)$$

where η_e is the electrical efficiency, η_m is the mechanical efficiency and P_r is the hydraulic power.

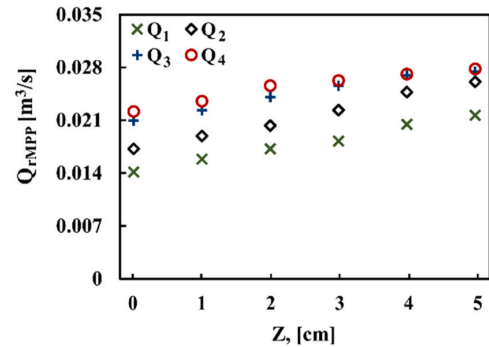
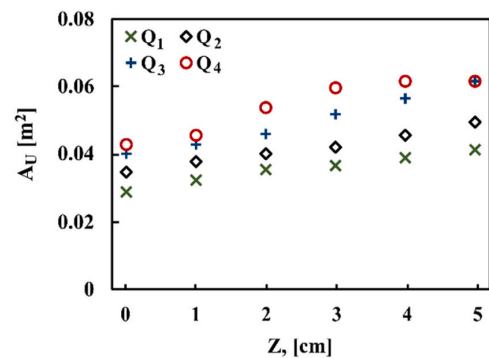
The results obtained for the different scenarios (example with Q_4 in Fig. 11) show that the power values obtained with the CFD model are significantly higher than the experimental ones. The differences increase as the rotational speed decreases from no load condition, where the maximum rotational speed is reached. The reason for that, is because the rotational speed reduction is induced to a progressive increment of the resistant torque implying higher mechanical losses in the pulley system (mechanical efficiency). The similarity between results provided full validation of the numerical model (see Fig. 12).

6. Results and discussion

Three types of tests have been conducted in the laboratory where the performance of the turbine has been studied in each of the planned scenarios. In the same way, these tests have been reproduced using validated CFD models. With the data obtained during the entire process, the behavior of the turbine and the power output were investigated and the consequences of introducing the obstacles were studied. In this section the results obtained in the experimental tests and in the simulations are shown and analyzed.

6.1. Electrical power characteristics

The tests to determine the characteristics of electrical power (P_e) plotted against rotational speed in experimental form (n) were performed from the no load (or no torque with maximum rotational speed) condition up to that of maximum torque (where the turbine stops) for the different flow rates. The results of the power features obtained show that the power values increase with the height of the obstacle for each value of rotational speed (Fig. 13). Also, for Q_1 and Q_2 (Fig. 13, a-b) the rotational speed range obtained for each feature is different as there is a considerable variation of the part not submerged with the obstacle height and the magnitude of the frictional power losses due to the pulley


 Fig. 15. Variation of Q_{rMPP} with the obstacle height.

 Fig. 16. Variation of A_u with the obstacle height.

system. For each feature the point at which the turbine produces the maximum power known as MPP is of maximum interest as the turbine control systems will continuously ensure operability at those conditions (Alvarez et al., 2018).

6.2. Evolution of the maximum hydraulic power with the height of the obstacle

With the validated CFD model, it was possible to assess more cases by varying obstacle heights without performing physical tests in the laboratory channel. Thus, six cases have been simulated corresponding to obstacles from a height of 0 cm (without obstacle) to 5 cm in steps of 1 cm in height. Fig. 14 shows the evolution of the maximum hydraulic power (P_{rMPP}) versus the obstacle height always observing a linear dependence between variables with a nearly constant slope (around 0,5 W per 1 cm of obstacle height increment), for Q_1 and Q_2 scenarios. The same tendency is noted for Q_3 and Q_4 and obstacle heights up to 3 cm height, with a smooth increment of the maximum power for higher obstacles (4 and 5 cm).

6.3. Evolution of the rotor flow rate with the height of the obstacle

The same tendencies are observed with the Q_r in MPP (Q_{rMPP}) conditions and the height of the obstacle (Fig. 15): for Q_1 and Q_2 scenarios, the relationship between variables is linear with a constant slope, while for Q_3 and Q_4 the relationship is similar only for obstacle heights under 3 cm while for the greater ones, the increment of Q_{rMPP} with the obstacle height is lower.

For all cases, it was clear that the height of the obstacle implies a practically proportional rise of the upstream water free surface as a consequence of the high flow blockage conditions instigated by the

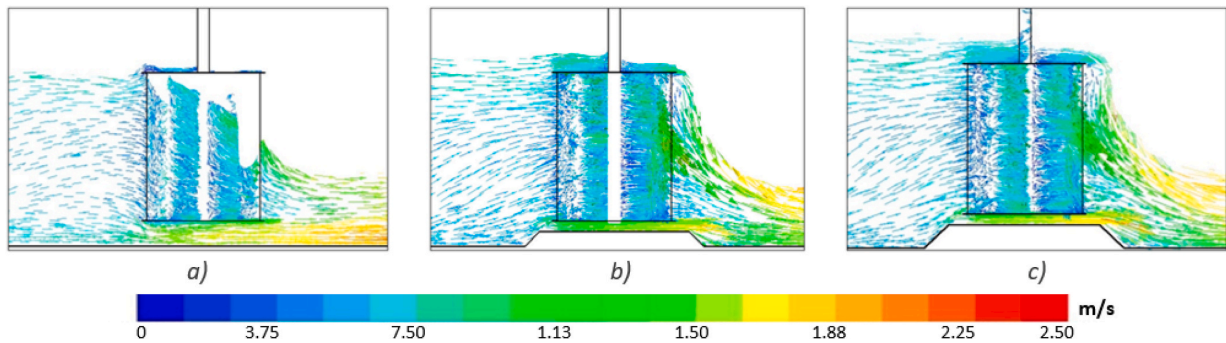


Fig. 17. Velocity vectors in the mid-transversal section for Q_3 and MPP conditions: a) no obstacle; b) 3 cm obstacle; c) 5 cm obstacle.

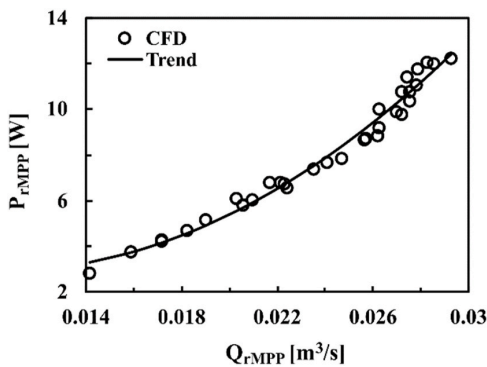


Fig. 18. Variation of P_{rMPP} with Q_{rMPP} .

turbine. The evolution of A_{li} with the height of the obstacle (Fig. 16) justifies the rotor flow rate trends observed for Q_1 , Q_2 , Q_3 and Q_4 , with obstacle heights lower than 3 cm in the last two, as the height of the obstacle increases significantly the transversal area leading to a similar tendency in the rotor flow rate. While for the cases with A_{li} values close to the maximum one – Q_3 and Q_4 for obstacle heights higher than 3 cm – the influence of the obstacle height in the rotor flow rate is only produced by the increment of the water velocity through the turbine due to the proximity of the critical point of discharge, that makes that the rise of the elevation of the water surface is lower than height of the obstacle; as an example, Fig. 17 shows the water velocity vectors in the mid-transversal section of the turbine.

6.4. Evolution of maximum hydraulic power and rotor flow rate

Fig. 18 represents the relationship between the P_{rMPP} and Q_{rMPP} for all cases simulated in this study. This curve shows a slightly quadratic relationship between both variables which indicates that increments in the power production by the height of the obstacle are brought about by two factors: the rotor flow rate itself and the turbine head always bearing in mind that the upstream height increases with the height of the obstacle while the downstream critical height is kept constant for each water flow rate.

6.5. Forces actuating on the turbine blades

From the results of the CFD simulations, it was possible to study the fields of relative water velocities and pressure for the different flow rates at each MPP conditions, thereby determining the effects of the height of the obstacle in the forces actuating on the blades. These fields have been analyzed in a horizontal section located at 150 mm from the upper

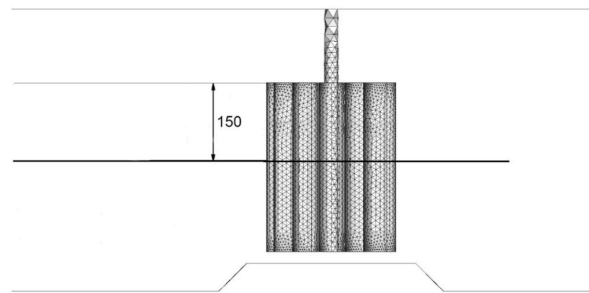


Fig. 19. Horizontal section location (mm).

turbine section (Fig. 19), which is considered representative of the submerged sections.

Initially it can be detected that the values of the pressure around the blades increase in magnitude with the height of the obstacle, see for example the case of Q_3 (Fig. 20), where the white color represents air.

The increase in pressure is derived from the variation in the height of the water free surface upstream when the obstacle is placed, which induces a greater speed through the turbine (the variation of the free surface height is less in the turbine than upstream). This phenomenon was analyzed by Patel et al. (2018) and is based on the concept of increased stagnation pressure in the turbine blades and impulse momentum principle.

The study of the pressure and relative velocity fields also determine the forces present in the turbine blades. In order to carry out an analysis of the forces and in the absence of aerodynamic profiles of the blades, the study is conducted on the convex and concave faces of each blade, defining different forces: drag forces (F_D) in areas of both low pressure and relative water velocities (appear in the blades due to the wake generated by the rotational movement); thrust forces (F_T), in high pressure zones due to the flow stagnation (no water velocity); and lift forces (F_L), in zones of low pressure and high flow velocity in a direction parallel to the blade. As a representative example, Fig. 21 shows the pressure and relative velocity fields for the scenario of Q_3 , 3 cm height obstacle, and MPP conditions, as well as the forces on the blades aligned to the flow direction (1 and 7), and those offering resistance (4 and 10). Note that these blades have been chosen because they represent the extreme conditions, while the rest of the blades are set to more intermediate ones.

F_T and F_D forces are present on blades 4 and 10. In blade 4 the F_T force acts on the concave face while F_D on the convex one, both generate torque in the direction of the turbine rotation (positive torque), while in blade 10, F_T and F_D are on the convex and concave faces respectively generating torque resisting the rotational movement (negative torque). In the case of blades 1 and 7, the F_T and F_L forces appeared on the convex

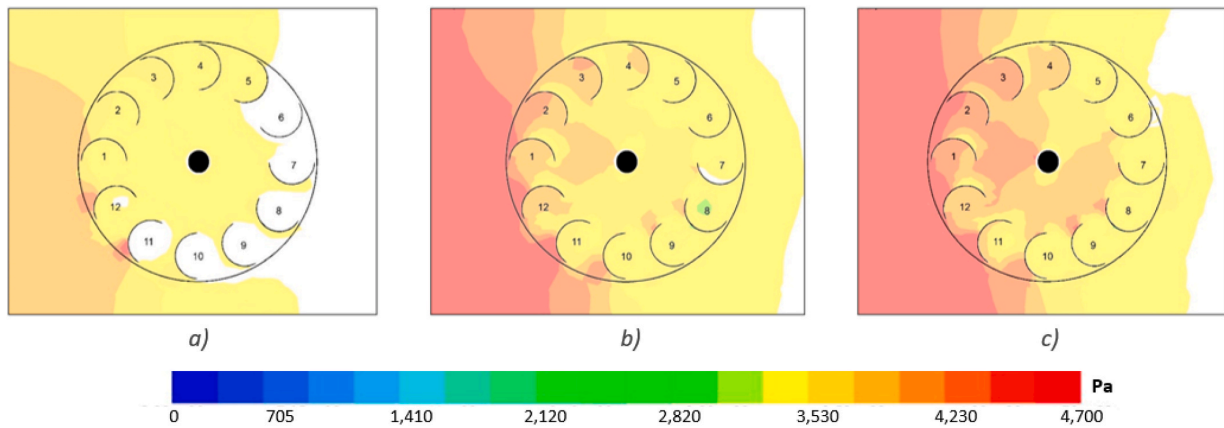


Fig. 20. Pressure field for Q_3 and MPP conditions: a) no obstacle; b) 3 cm obstacle; c) 5 cm obstacle.

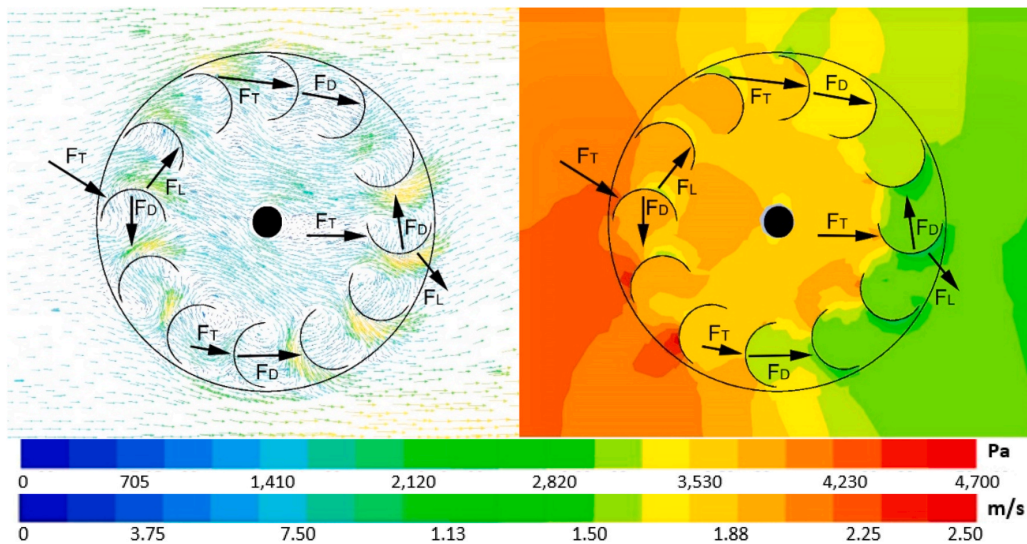


Fig. 21. Forces, relative velocity, and pressure fields (Q_3 , 3 cm obstacle and MPP).

faces generating positive torque, while F_D forces appear on the concave ones creating negative torque. Figs. 22 and 23 show the pressure distribution along blades 1–7, and 4–10 respectively, with important variations in the cases in which F_T and F_L appear on the same face.

With the pressure distribution along the faces of the blade considered as positive pressure when it creates positive torque and negative in the opposite case, Figs. 24 and 25 represent the net pressure along blades 1–7 and 4–10 for Q_3 at MPP conditions with no obstacle, 3 cm and 5 cm height obstacle. In general, it can be observed that the higher the height of the obstacle the greater the pressure values on the blades which in turn increases the torque in the sense of rotation. Additionally, it can be seen in Fig. 24, that on blades 1 and 7 the distribution of net pressure, half with negative values and half with positive values all along the blades result in a very low force and therefore torque. Therefore blades 1 and 7 have little influence on the turbine rotation and the obstacle presence does not produce any effect. However, blades 4 and 10 (Fig. 25) are crucial in order to generate movement and are significantly affected by the height of the obstacle.

7. Conclusions

The research provides an analysis of the increment in the power production of a drag-based water hydrokinetic turbine obtained by using a simple design of an obstacle on the bottom of the channel where the turbine is installed. Also, the turbine was located upstream at a critical discharge point and due to its dimensions prompted a high flow blockage (around 50%) The simplicity of the inclusion of this obstacle and the lack of O&M present this alternative as something which may feasibly be included in new industrial scale installations.

In a set of laboratory tests and by using a validated CFD model it was found that the power produced by the turbine increases with the height of the obstacle. The numerical model provided sufficient evidence to suggest that the water flow rate through the turbine rotor was the key factor which attributed to this increment in power production as it is largely dependent on the height of the obstacle, with the same tendencies observed with the power generation. For a fixed flow rate, the height of the obstacle entails an elevation of the water free surface upstream from the turbine which leads to an increment of rotor flow by increasing the wetted turbine transversal area up to its maximum, and when it is reached, for higher obstacles, increasing the water velocity

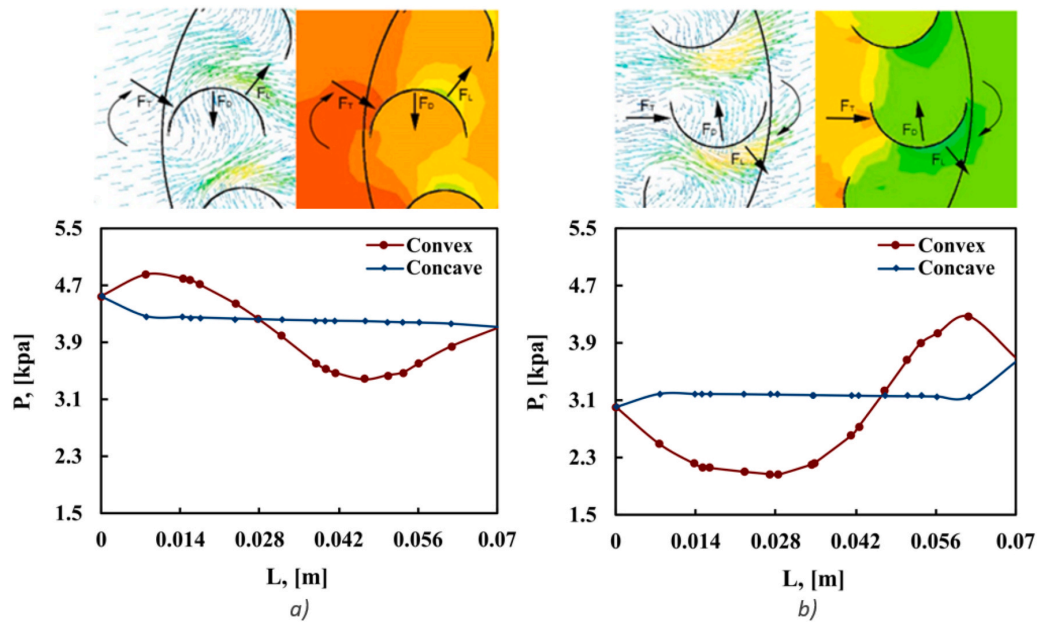


Fig. 22. Pressure distributions along (a) blade 1 and (b) blade 7 (Q_3 , 3 cm obstacle and MPP).

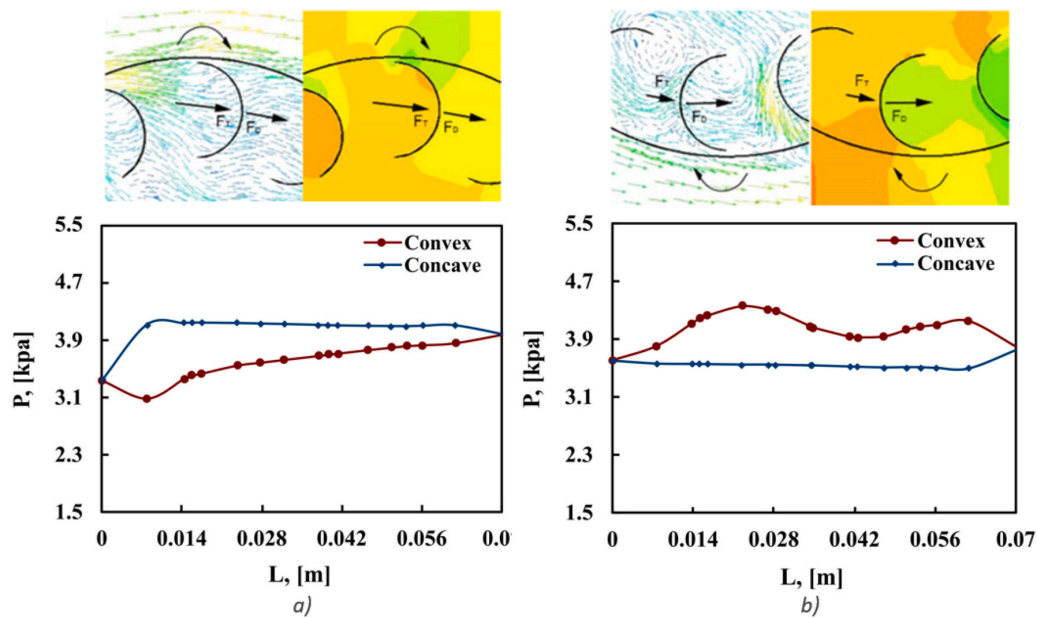


Fig. 23. Pressure distributions along (a) blade 4 and (b) blade 10 (Q_3 , 3 cm obstacle and MPP).

due to the effect of the downstream critical point, as the water elevation is lower than the height of the obstacle.

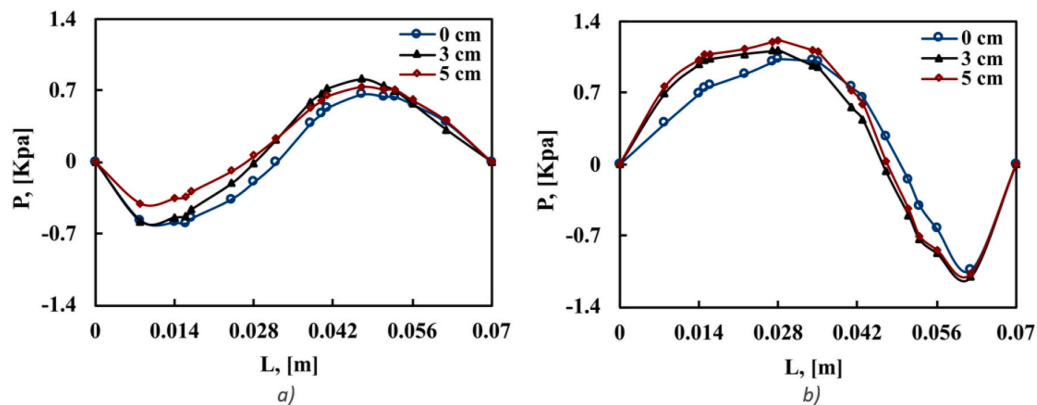
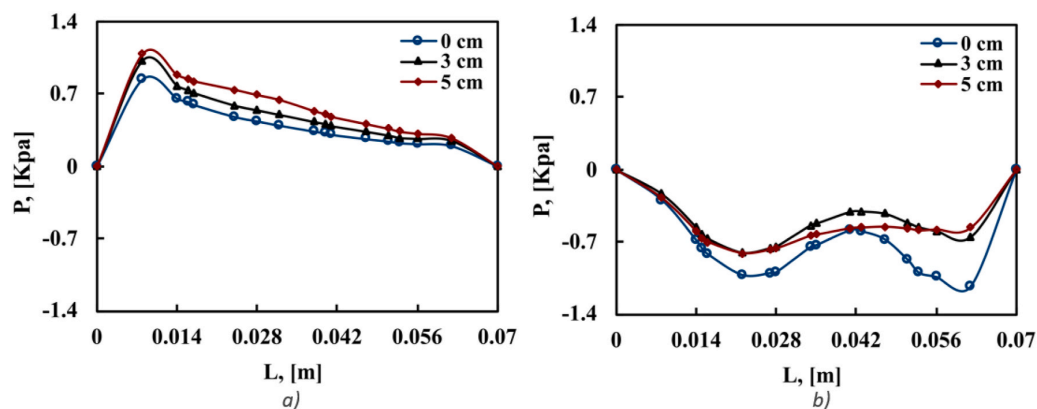
The rise in the flow rate also occasions the same effect in the turbine hydraulic head, due to the high blockage conditions of installation, resulting both in a multiplication of the power production. Under conditions analogous to those of the literature examples (with the turbine fully submerged), a power increase of about 25% was obtained in the tests.

In addition, from the tests conducted the forces on the rotor blades have been studied from the pressure and velocity fields obtained in the

numerical model. The effect of the height of the obstacles in the forces was identified and highlighted the fact that the obstacle height increased the net pressure, and therefore the torque produced on the blades, as they are placed transversally to the flow.

CRediT authorship contribution statement

R. Espina-Valdés: Investigation, Methodology, Validation, Formal analysis, Writing – original draft. **V.M. Fernández-Álvarez:** Investigation, Methodology, Data curation, Validation, Formal analysis. **A.**

Fig. 24. Net pressure along (a) blade 1 and (b) blade 7 (Q_3 and MPP).Fig. 25. Net pressure along (a) blade 4 and (b) blade 10 (Q_3 and MPP).

Gharib-Yosry: Investigation, Methodology, Formal analysis. **A. Fernández-Jiménez:** Investigation, Methodology, Data curation, Validation, Formal analysis. **E. Álvarez-Álvarez:** Conceptualization, Ideas, Writing – original draft, Writing – review & editing, Formal analysis, Supervision.

Declaration of competing interest

The authors declare that they have no known competing financial interests or personal relationships that could have appeared to influence the work reported in this paper.

Data availability

Data will be made available on request.

References

- Alizadeh, H., Jahangir, M.H., Ghasempour, R., 2020. CFD-based improvement of Savonius type hydrokinetic turbine using optimized barrier at the low-speed flows. *Ocean. Eng.* 202 (March), 107178.
- Álvarez-Álvarez, E., Rico-Secades, M., Corominas, E.L., Huerta-Medina, N., Soler Guitart, J., 2018. Design and control strategies for a modular hydrokinetic smart grid. *Int. J. Electr. Power Energy Syst.* 95, 137–145.
- Álvarez-Álvarez, E., Rico-Secades, M., Fernández-Jiménez, A., Espina-Valdés, R., Corominas, E.L., Calleja-Rodríguez, A.J., 2020. Hydrodynamic water tunnel for characterization of hydrokinetic microturbines designs. *Clean Technol. Environ. Policy* 22 (9), 1843–1854.
- Ansys, 2018. ANSYS Fluent User's Guide, 18.1. Canonsburg, PA.

- Bardina, J.E., Huang, P.G., Coakley, T.J., 1997. Turbulence modeling validation, testing, and development. NASA Tech. Memo. 110446, 8–20.
- Bundi, J.M., Ban, X., Wekesa, D.W., Sun, Y., 2020. Advanced gain-scheduled control of A DFIG based on a H-Darrieus wind turbine for maximum power tracking and frequency support. *Control Eng. Appl. Informat.* 22 (2), 23–32.
- C M, S., Honnasiddaiah, R., Hindasageri, V., Madav, V., 2021. Studies on application of vertical axis hydro turbine for sustainable power generation in irrigation channels with different bed slopes. *Renew. Energy* 163, 845–857.
- Caballero Santos, C., 2011. Estudio de plantas de producción de energías renovables con aprovechamiento de la energía del mar. Universidad Carlos III de Madrid, Leganés.
- Daskiran, C., Riglin, J., Oztekin, A., 2016. Numerical analysis of blockage ratio effect on a portable hydrokinetic turbine. In: *Fluids Engineering*, vol. 7. V007T09A064.
- Glauert, H., 1933. Wind tunnel interference on wings, bodies and airscrews. *Aeronaut. Res. Comm.* 1566, 1–52.
- Gorle, J.M.R., Chatellier, L., Pons, F., Ba, M., 2016. Flow and performance analysis of H-Darrieus hydroturbine in a confined flow: a computational and experimental study. *J. Fluid Struct.* 66, 382–402.
- Güney, M.S., Kaygusuz, K., 2010. Hydrokinetic energy conversion systems: a technology status review. *Renew. Sustain. Energy Rev.* 14 (9), 2996–3004. Elsevier Ltd.
- Hirt, C., Nichols, B., 1981. Volume of fluid (VOF) method for the dynamics of free boundaries. *J. Comput. Phys.* 39 (1), 201–225.
- Hosseini, S.E., 2020. An outlook on the global development of renewable and sustainable energy at the time of COVID-19. *Energy Res. Social Sci.* 68 (April), 101633.
- Houlsby, G.T., Vogel, C.R., 2016. The power available to tidal turbines in an open channel flow. *Proc. Inst. Civ. Eng. - Energy* 170 (1), 12–21.
- Hunt, A., Stringer, C., Polagye, B., 2020. Effect of aspect ratio on cross-flow turbine performance. *J. Renew. Sustain. Energy* 12 (5).
- IDAIE, 2011. Plan de Energías Renovables 2011–2020.
- International Energy Agency, 2021. Global energy review 2021. *Glob. Energy Rev.* 2020, 1–36.
- Jeeva, B., Sandeep, S.J., Ramsundram, N., Prasanth, M., Praveen, B., 2021. Experimental investigation of three bladed inclined savonius hydrokinetic turbine by using deflector plate. *IOP Conf. Ser. Mater. Sci. Eng.* 1146 (1), 012009.
- Jia, Y., Yang, Z., Cao, B., 2002. A new maximum power point tracking control scheme for wind generation. In: *PowerCon 2002 - 2002 International Conference on Power System Technology*, Proceedings, vol. 1, pp. 144–148.

- Kailash, G., Eldho, T.I., Prabhu, S.V., 2012. Performance study of modified savonius water turbine with two deflector plates. *Int. J. Rotating Mach.* 2012.
- Kang, C., Zhao, H., Zhang, Y., Ding, K., 2021. Effects of upstream deflector on flow characteristics and startup performance of a drag-type hydrokinetic rotor. *Renew. Energy* 172, 290–303.
- Kaprawi, S., Santoso, D., Sipahutar, R., 2015. Performance of combined water turbine darrieus- savonius with two stage savonius buckets and single deflector. *Int. J. Renew. Energy Resour.* 5, 217–221.
- Kolekar, N., Vinod, A., Banerjee, A., 2019. On blockage effects for a tidal turbine in free surface proximity. *Energies* 12 (17), 3325.
- Kumar, D., Sarkar, S., 2016. A review on the technology, performance, design optimization, reliability, techno-economics and environmental impacts of hydrokinetic energy conversion systems. *Renew. Sustain. Energy Rev.* 58, 796–813.
- Lanzafame, R., Mauro, S., Messina, M., 2013. Wind turbine CFD modeling using a correlation-based transitional model. *Renew. Energy* 52, 31–39.
- Martin-Short, R., Hill, J., Kramer, S.C., Avidis, A., Allison, P.A., Piggott, M.D., 2015. Tidal resource extraction in the Pentland Firth, UK: potential impacts on flow regime and sediment transport in the Inner Sound of Stroma. *Renew. Energy* 76, 596–607.
- Mohammadi, S., Hassanalian, M., Arionfard, H., Bakhtiyarov, S., 2020. Optimal design of hydrokinetic turbine for low-speed water flow in Golden Gate Strait. *Renew. Energy* 150, 147–155.
- Moran, E.F., Lopez, M.C., Moore, N., Müller, N., Hyndman, D.W., 2018. Sustainable hydropower in the 21st century. *Proc. Natl. Acad. Sci. USA* 115 (47), 11891–11898.
- Mosbahi, M., et al., 2021. Performance improvement of a drag hydrokinetic turbine. *Water* 13 (3), 273.
- Patel, V., Eldho, T.I., Prabhu, S.V., 2019. Velocity and performance correction methodology for hydrokinetic turbines experimented with different geometry of the channel. *Renew. Energy* 131, 1300–1317.
- Patel, V., Bhat, G., Eldho, T.I., Prabhu, S.V., 2017a. Influence of overlap ratio and aspect ratio on the performance of Savonius hydrokinetic turbine. *Int. J. Energy Res.* 41 (6), 829–844.
- Patel, V., Eldho, T.I., Prabhu, S.V., 2017b. Experimental Investigations on Darrieus Straight Blade Turbine for Tidal Current Application and Parametric Optimization for Hydro Farm Arrangement, vol. 17. Elsevier Ltd.
- Patel, V., Eldho, T.I., Prabhu, S.V., 2018. Theoretical study on the prediction of the hydrodynamic performance of a Savonius turbine based on stagnation pressure and impulse momentum principle. *Energy Convers. Manag.* 168, 545–563.
- Patel, V., Eldho, T.I., Prabhu, S.V., 2019. Performance enhancement of a Darrieus hydrokinetic turbine with the blocking of a specific flow region for optimum use of hydropower. *Renew. Energy* 135, 1144–1156.
- Riglin, J., Chris Schleicher, W., Liu, L.-H., Oztekin, A., 2015. Characterization of a micro-hydrokinetic turbine in close proximity to the free surface. *Ocean. Eng.* 110, 270–280.
- Roberts, A., Thomas, B., Sewell, P., Khan, Z., Balmain, S., Gillman, J., 2016. Current tidal power technologies and their suitability for applications in coastal and marine areas. *J. Ocean Eng. Mar. Energy* 2 (2), 227–245.
- Sahim, K., Ihtisan, K., Santoso, D., Sipahutar, R., 2014. Experimental study of darrieus-savonius water turbine with deflector: effect of deflector on the performance. *Int. J. Rotating Mach.* 2014.
- Salleh, M.B., Kamaruddin, N.M., Mohamed-Kassim, Z., 2020. The effects of deflector longitudinal position and height on the power performance of a conventional Savonius turbine. *Energy Convers. Manag.* 226 (August), 113584.
- Vermaak, H.J., Kusakana, K., Koko, S.P., 2014. Status of Micro-hydrokinetic River Technology in Rural Applications: A Review of Literature. *Renewable and Sustainable Energy Reviews.*

5.6 Journal Metrics

The following data are based on the last updated one from the Web of Science database for the year of 2023.

Article No. 4	
Journal	OCEAN ENGINEERING
Title	Increased efficiency of hydrokinetic turbines through the use of an obstacle on the channel bottom
Category Quartile	Q1
Impact Factor	4.372
Impact Factor (5 years)	4.5
CiteScore	6.5
No. of Citations [Oct 2022 - May 2023]	1

Chapter 6

Results and General Discussion

6.1 Overview

As mentioned in Chapter 1, the main objective of this dissertation is to address the design and the characterization of a small vertical-axis hydrokinetic turbine inside an open water channel, under low flow velocities. The experimental characterization allows to assess the effect of different parameters, including the turbine blockage and the upstream velocity on the overall performance of the turbine. Moreover, the numerical complementary study outlines an intensive three-dimensional multiphase simulation of the turbine model with free-surface variations to investigate the interactions between the turbine rotor and the channel section.

Additionally, experimental tests have been carried out in an open-jet subsonic wind tunnel under open-field conditions (with no blockage), keeping the same Reynolds number value as in the previous water channel experiments, to enable a comparison between the results obtained from both tests. Finally, the evaluation of the characteristics of a drag-based hydrokinetic turbine has been performed, experimentally and numerically, focusing on improving the efficiency in water channels, by varying the channel bed geometry.

6.2 Experimental Assessment of the Turbine Model

As mentioned in Chapter 2, the turbine model has three straight blades with fixed pitch and a NACA-0015 profile. A solidity of 2.0 together with an aspect ratio of 1.0 has been selected, looking for self-starting and efficient operation with low flow velocities. The experimental measurements are used to assess the effect of different parameters on the overall performance of the hydrokinetic turbine model. The Maximum Power Point (*MPP*) and peak power coefficient are compared with one-dimensional actuator disc

theory. Additionally, an analysis is carried out to study the effect of the slope in an inclined channel.

Tests have been performed in an open channel rig at three flow rates of $0.05 \text{ m}^3/\text{s}$, $0.06 \text{ m}^3/\text{s}$ and $0.065 \text{ m}^3/\text{s}$, with inlet velocities ranging from 0.33 m/s to 0.69 m/s . For each flow rate value, the power produced from the turbine model is obtained for different flow conditions. As illustrated in the upper part of Fig. 6.1, by increasing upstream velocity values, the power produced increases and the rotational speeds are shifted to higher values. The power increase is higher than the cube of the upstream velocity which would match the change in kinetic energy. This is a consequence of the intensification of the blockage as the velocity increases. Increasing the load beyond the maximum power point, decreases the output from the turbine with a decline of the rotational speed. Operation and measurement on this unstable zone would require an active control system.

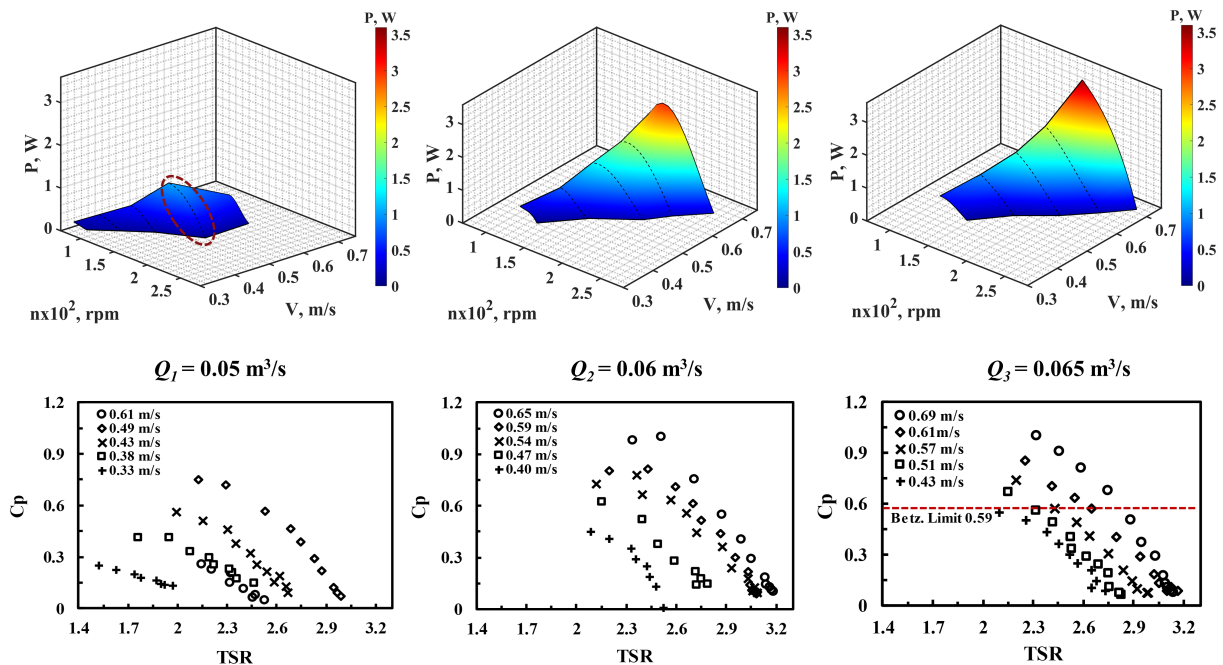


Figure 6.1: Turbine power and characteristic curves for different upstream velocities.

The non-dimensional parameters tip speed ratio (λ) and power coefficient C_p have been used to compare the performance of different flow rates and upstream velocities. As shown in the lower part of Fig. 6.1, the power coefficient achieved with greater flow rates is higher. However, the upstream velocity has the most obvious effect on the turbine performance. With the lowest upstream velocity tested (0.33 m/s), the peak power coefficient is 0.25 with $\lambda = 1.52$, with the highest upstream velocity (0.69 m/s), the peak power coefficient reaches 0.99 with $\lambda = 2.32$. If the turbine is partially submerged under certain flow conditions, a significant decline in power output occurs, exceeding 40 %. For a constant flow rate, the increase in the peak power coefficient with the upstream velocity is linked to the increase in the blockage ratio. The blockage accelerates the flow around the turbine rotor, resulting in a higher power output compared with an unrestricted flow.

Furthermore, for a sub-critical flow, the water height goes down as the energy is extracted, increasing the blockage effect. In fact, the difference in static head around the turbine rotor makes the total available energy greater than the kinetic one.

To further explore the phenomena, the experimental results are compared with the calculations of the Linear Momentum Actuator Disk Theory (LMADT) adjusted for open channel flow and presented in Fig. 6.2. A reasonably good match between the experimental power measurements and the analytical calculations is found for the whole ranges of upstream velocities (see Fig. 6.2a). However, the experimental results are somewhat lower than the analytical ones because the model does not consider friction losses from the channel walls.

In the analytical results in Fig. 6.2b, the lines corresponding to different flow rates diverge for high upstream velocities, due to the different increase in the blockage ratio. In the experimental results, this separation is not so evident, most likely due to the higher losses caused by the blockage. Also, it is found that, Betz limit is not applicable to channel turbines, and this hypothesis has been confirmed experimentally.

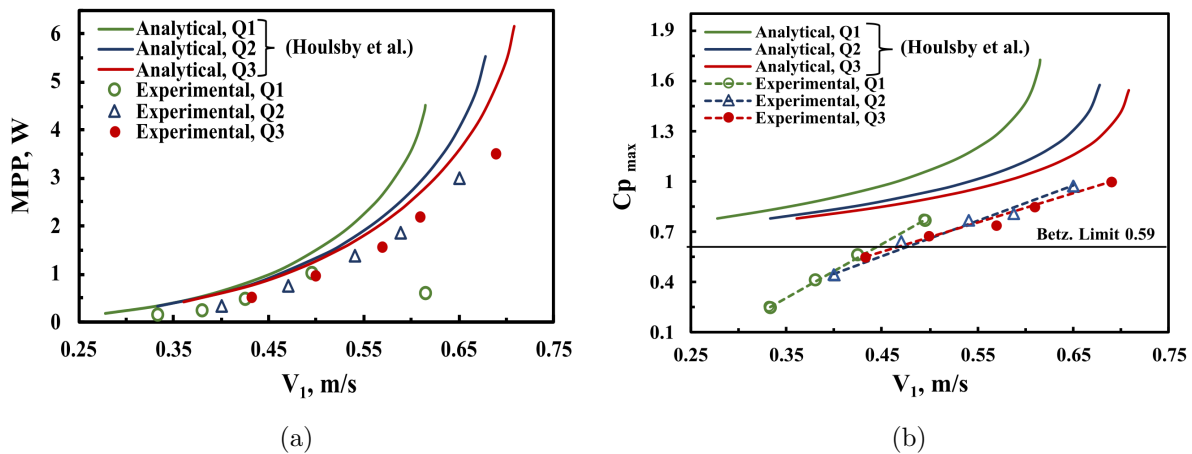


Figure 6.2: Experimental results and analytical model predictions.

The turbine efficiency has been defined in relation to the maximum theoretical power obtainable. As presented in Fig. 6.3, small upstream velocities have only marginal efficiencies. However, from 0.45 m/s upwards, the efficiency is over 70 %, and as high as 81 %. Finally, the relation between slope and performance in an inclined channel has been assessed in the current study. The variation of the maximum power point is proportional to the square value of the channel slope. Also, the tip speed ratios that obtain the maximum power output have a slight dispersion, but they fit an equation proportional to the fourth root of the slope.

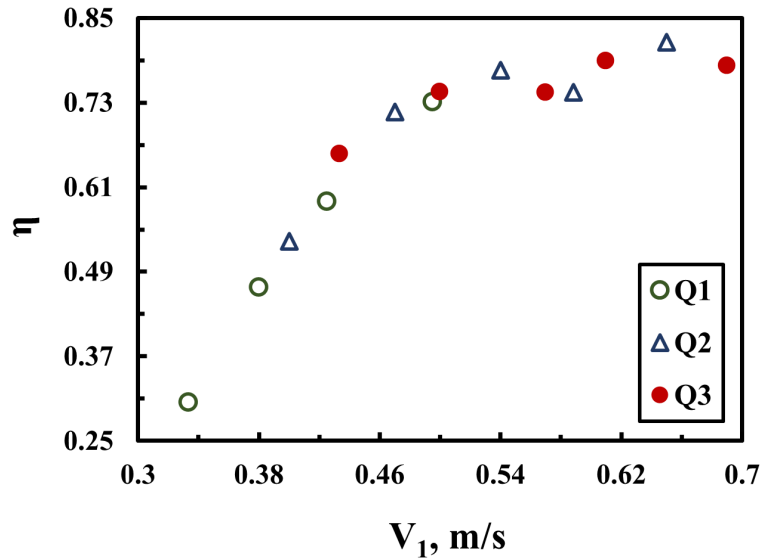


Figure 6.3: Experimental turbine efficiency with respect to the analytical model.

6.3 Turbine Modeling with Free-surface Variations

As stated in Chapter 3, the flow field characteristics and free-surface flow analysis of the turbine model inside an open channel have been investigated. An intensive three-dimensional multiphase simulation has been carried out to understand the complex free-surface flow around the turbine and its relevance on the overall performance. From the experimental results, three different cases have been selected for the simulation. The first case (C_1) in which the channel is fully-filled with water and the control gate is slightly opened, with an upstream velocity value of 0.43 m/s ; the second case (C_2) with an intermediate opening and an upstream velocity value of 0.57 m/s ; finally, the third case (C_3), where the control gate is fully opened and the upstream velocity value reaches 0.69 m/s .

The numerical model has been validated with the experimental data by comparing the turbine characteristic curve, that is obtained experimentally, with the multiphase and single-phase simulations for the first case (C_1) as shown in Fig. 6.4. A reasonably good match has been found between the experimental and the numerical results. The power coefficients obtained are much closer to the experimental ones for the whole range of tip speed ratios. However, the single-phase model values are somewhat higher, as it does not consider the free-surface deformations around the rotor.

In a more qualitative mode, the three-dimensional shape adopted by the free-surfaces results of the VOF model has been compared to the experiments as presented in Fig. 6.5. The VOF model is able to simulate not only the free-surface longitudinal variations, but also the interactions with the channel wall boundaries, even when the flow becomes supercritical as in the C_3 case.

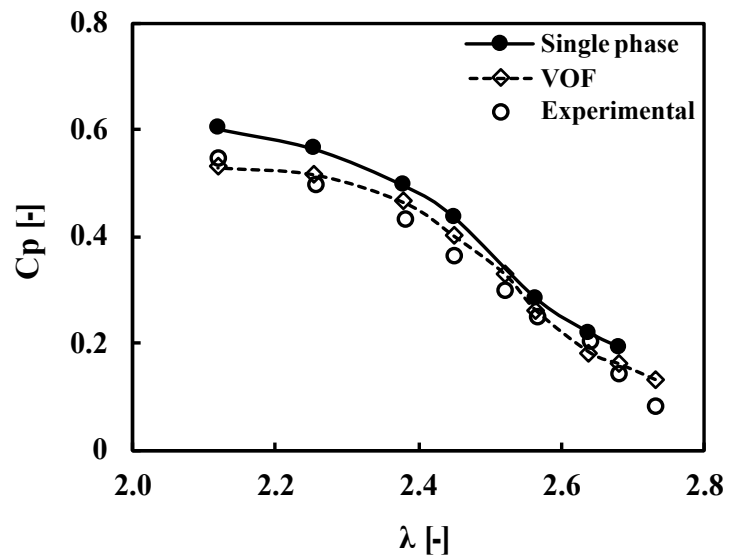


Figure 6.4: characteristic curve validation for (C_1).

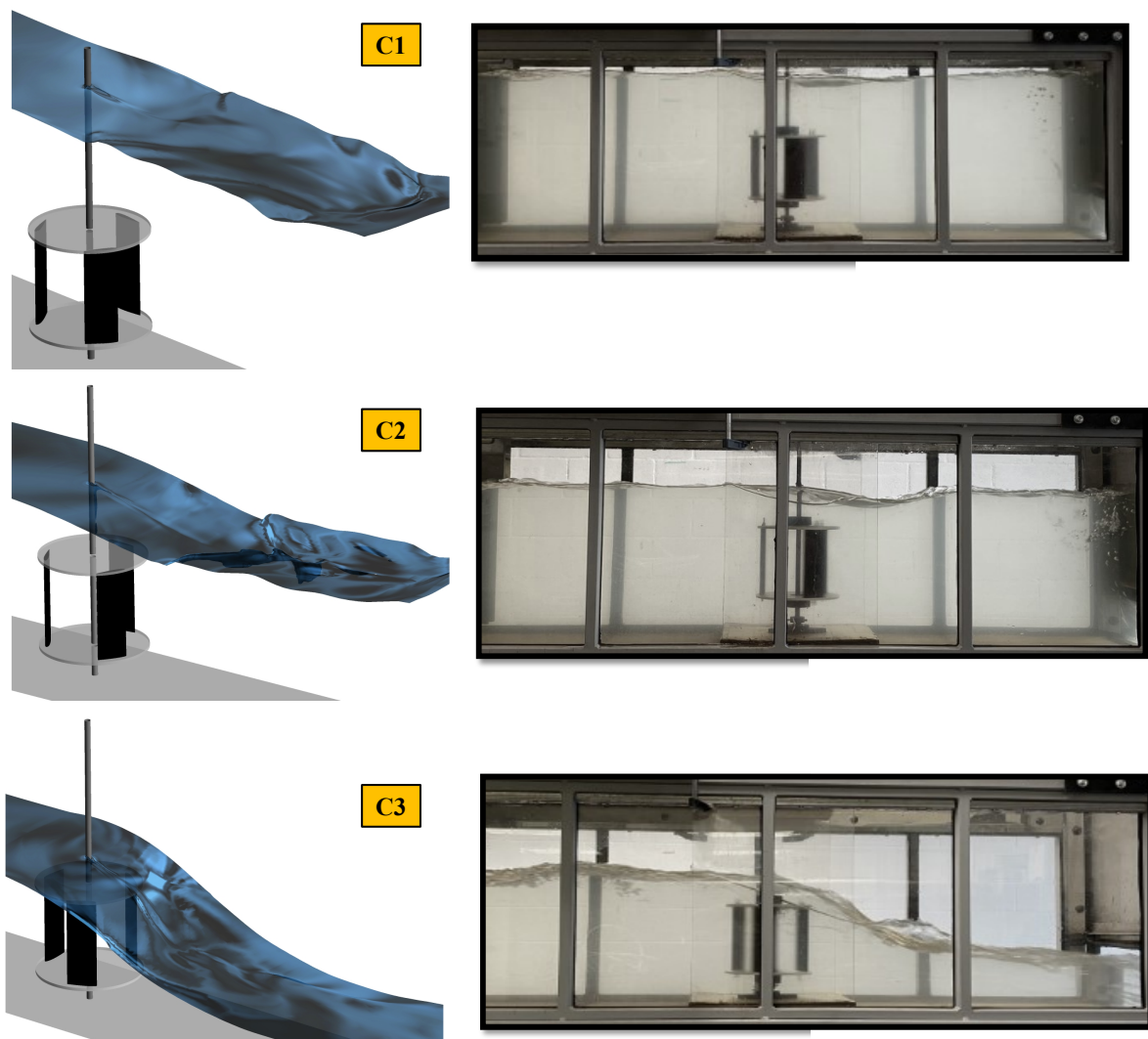


Figure 6.5: Free-surface shape around the rotor (isosurface water fraction of 0.5) at $\lambda = 2.3$.

In C_1 case, it can be observed that there is a slight decrease of the free-surface just after the turbine, which recovers quickly. In the C_2 case, the drop after the turbine is deeper, corresponding to a higher energy extraction. The subsequent recovery is also more abrupt and turbulent, although the original level is also recovered. In both cases, the free-surface drop is quite smooth covering the whole width of the channel, while the recovery shows more disturbances and wave reflections from the channel walls. In the C_3 case, corresponding to the maximum inlet velocity, the energy extraction is also the highest, which requires the flow to go from a subcritical regimen before the turbine to a supercritical one after the turbine.

Moreover, polar plot diagrams have been used in this study to represent and compare the contribution of each blade on the output torque as shown in Fig. 6.6. The three lobes are very clearly defined, which implicitly means that the positive effect of each blade is limited to a relatively small angular range. The peaks coincide in all cases indicating that the angular zone of maximum effect does not change with the upstream flow velocity nor the tip speed ratio, but is geometrically defined. In this kind of polar figures, the total torque coefficient of the turbine is equivalent to the area enclosed by each curve.

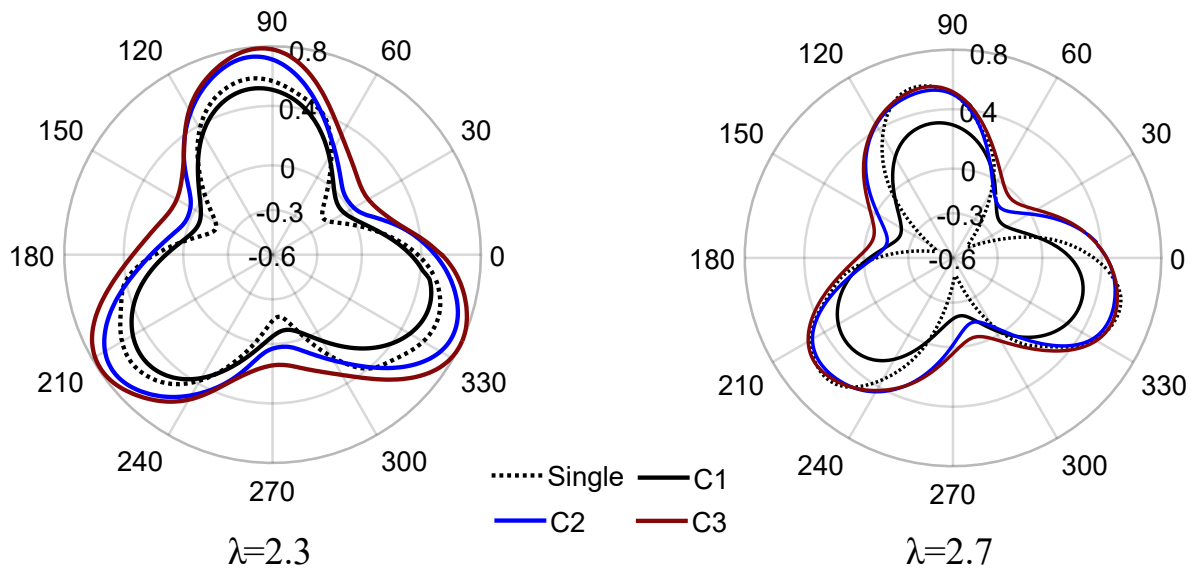


Figure 6.6: The polar distributions of the instantaneous torque coefficient.

The variation in the total torque coefficient between the two tip speed ratios is clearly seen, for instance, the total torque coefficient for the C_1 case is 0.225 for $\lambda = 2.3$ and 0.083 for $\lambda = 2.7$. The average difference between both tip speed ratios is about 52%, as the lower tip speed ratio ($\lambda = 2.3$) always producing more power. The difference in area is also evident between the three cases for each tip speed ratio. For instance, at $\lambda = 2.3$, the torque coefficient of C_2 case is 38% higher than C_1 one, while the C_3 case is 49 % higher. Also the lobes are less defined as the power increases, denoting an increase in the positive angular range.

To further explore the effect of the free-surface on the blade hydrodynamics, the relative streamlines around the turbine blade at various azimuth angular positions from $\theta = 60^\circ$ to $\theta = 300^\circ$ are examined and illustrated in Fig 6.7. The incidence angle of the relative streamline velocity at the leading edge increases by lowering the free-surface from C_1 to C_3 , especially in the positive production zone (the angles of 60° and 120°), where the lift force direction increases the torque values and the hydrodynamic efficiency.

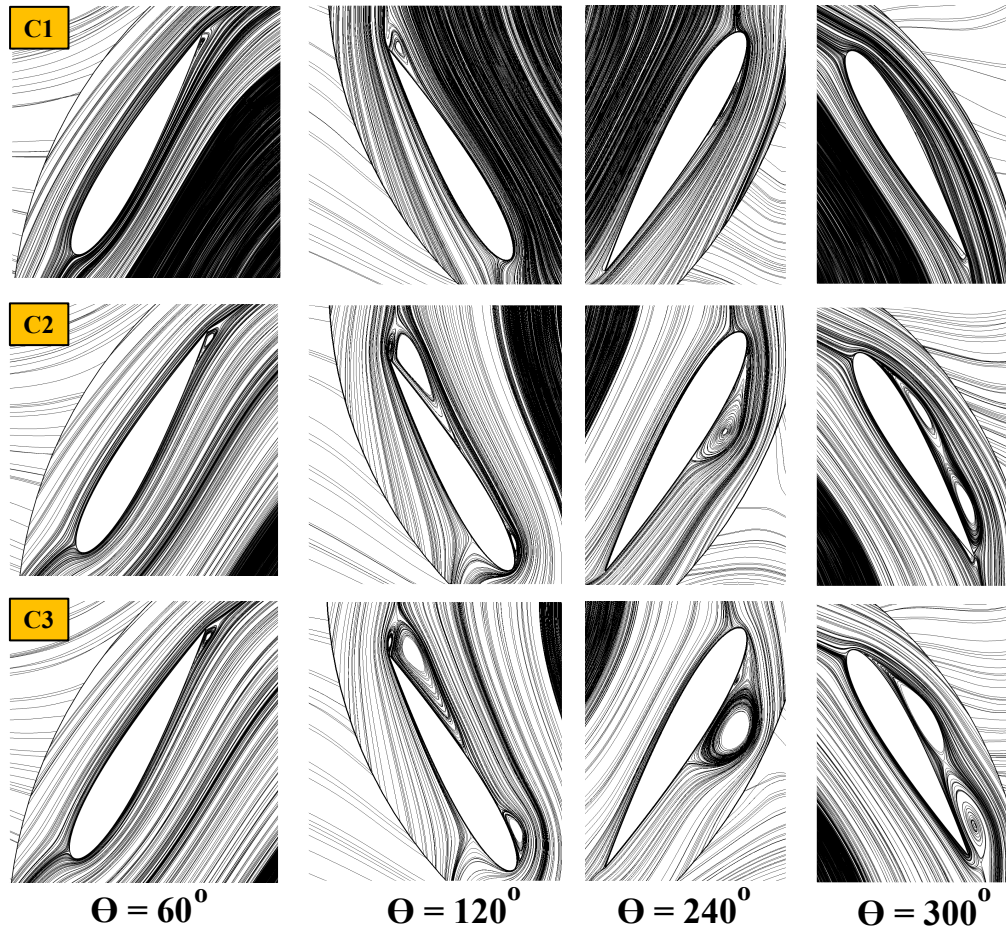


Figure 6.7: Instantaneous streamlines around the hydrofoil at various azimuth angular positions.

In the C_1 case, the incidence angles are the lowest -very close to zero but still enough to obtain a positive torque at 60 degrees- and there is no separation at any point. This is favorable in the positive production zone but not in the rest where a noticeable resistant torque is attained. In the cases of C_2 and C_3 , the free-surface is nearer to the turbine and the relative flow angles have a larger variation range which even leads to the flow separation. Specifically, for the C_3 case, it can be seen how the separation is quite strong with clear separation bubbles.

The detachment of the flow at the angle range between 240° and 300° , reduces the forces that generate the rotation resistance, so that the torque does not even become negative in spite of the increased drag. This type of hydrodynamic stall is very specific for these cross-flow turbines but does not exist in axial ones.

However, for the model in the current study, the C_3 case has extreme free-surface deformation, but the separation is already detected in the C_2 case where the shape change of the free surface is not so pronounced. Although further study is needed, it seems that the increase of the incidence angle that generates the positive torque is quite gradual, but the separation of the flow in the resistance zone produces a sudden increase of the power obtained. This indicates that the change in performance is more related to the depth of the free surface than the change in shape.

The pressure coefficient distribution around the blades have been analyzed with different azimuth angles and have provided a better insight into the positive torque production zones and their relation with the flow separation. As presented in Fig. 6.8, an abnormal behaviour of the pressure coefficient -a crossover from the pressure to the suction side- have been detected for some cases at specific angular positions. This has been caused by the low pressure zone inside the rotor, due to the high solidity of the blades.

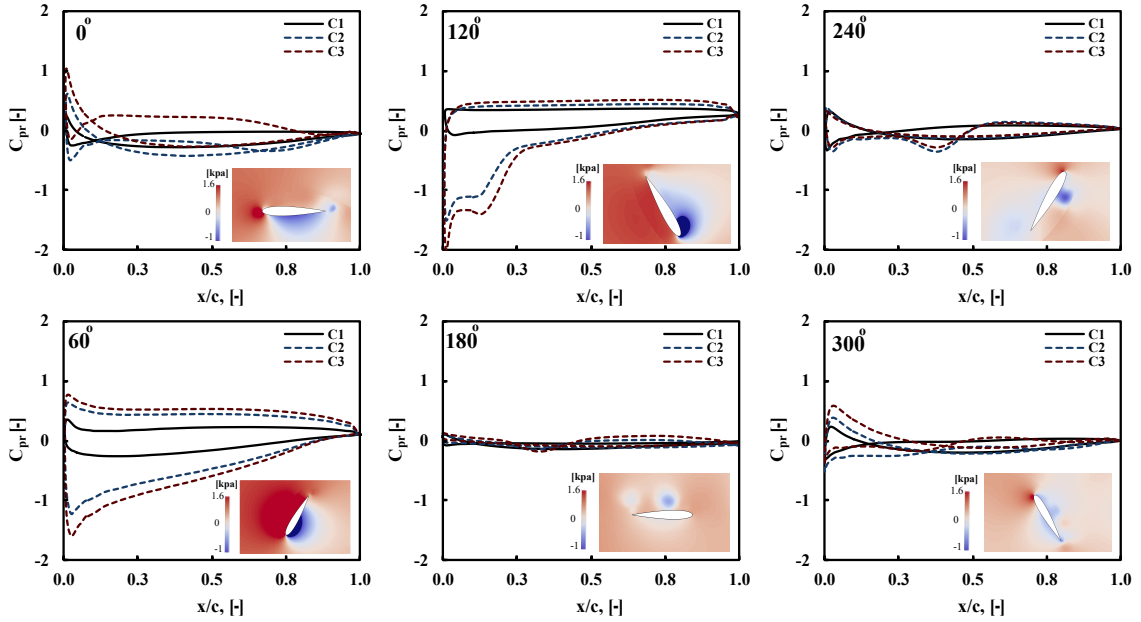


Figure 6.8: Pressure coefficient for all cases and pressure contour samples of C_2 on a single blade at $\lambda = 2.3$.

The normalized vorticity fields around the turbine rotor are also presented in Fig. 6.9. The vortices generated by the lower and upper turbine plates have been visualized, straddling the wake behind the turbine. The intensity of these vortices and their downstream extension increase with the free-surface lowering. Also, the two ending plates cause the flow to be more bi-dimensional between them reducing the vertical drift. Additionally, the flow field is found to be similar in any section inside the turbine except near the plates. These plates seem to increase the complexity and the losses in the wake zone, the plates are very useful from the mechanical point of view to support the turbine blades, and actually improve the hydrodynamic performance. Apart from reducing the blade-tip effects, the plates prevent air from entering the turbine when the surface drops significantly.

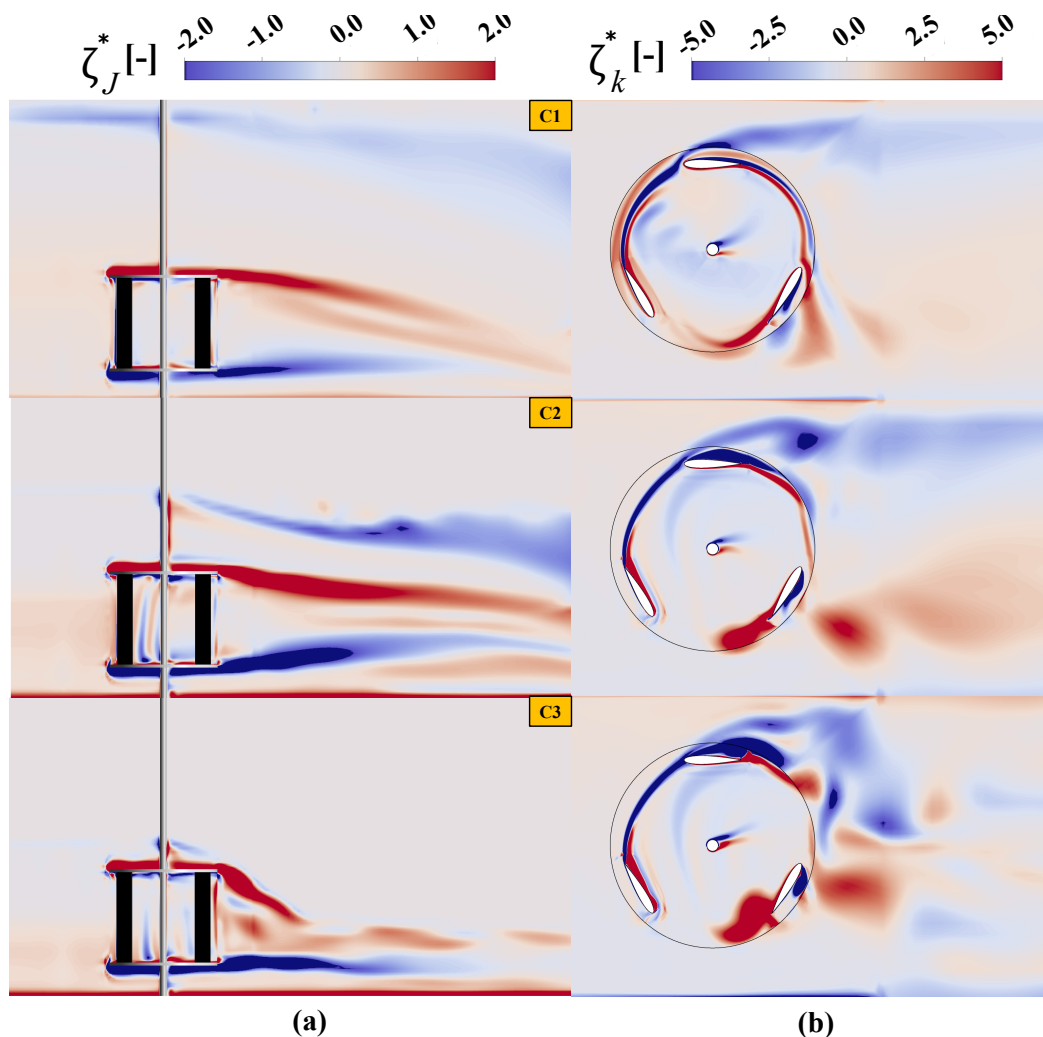


Figure 6.9: Normalized vorticity fields ($J - K$) at the middle sections for all cases.

6.4 Open-field Testing Approach

As mentioned in Chapter 4, experimental runs have been carried out on the turbine model in an open-jet wind tunnel to simulate the open-field operation conditions. Tests have been performed using the same Reynolds number value (around 3.5×10^4) as in previous water channel tests, to enable a comparison between both results. The wind tunnel runs have been carried out for different wind velocities: 7.0 m/s , 8.0 m/s , 9.0 m/s and 10.0 m/s . For each velocity, the turbine rotates freely without any loading until reaching the steady state condition where the rotational speed is nearly constant. Thereafter, the turbine is gradually loaded by changing the input current to the brake. Subsequently, the rotational speed decreases and the torque produced rises till reaching the maximum power point. From that point onwards, the power output from the turbine decreases with the decline of the rotational speed until the turbine reaches an unstable condition and stops.

As presented in Fig. 6.10, the maximum power coefficient values corresponding to each upwind velocity are quite similar, with only a slight shift in the tip speed ratio value. This confirms that the blockage effect on the turbine performance is negligible. However, the small discrepancy observed in the experimental results is most likely attributed to mechanical losses in the system, which become more significant at higher upwind velocities. This effect is particularly noticeable in small turbine models like the one used in our study. The tip speed ratio values are considered lower for the current turbine model compared with other similar turbines. This is due to the high solidity value which is selected to avoid the starting issue.

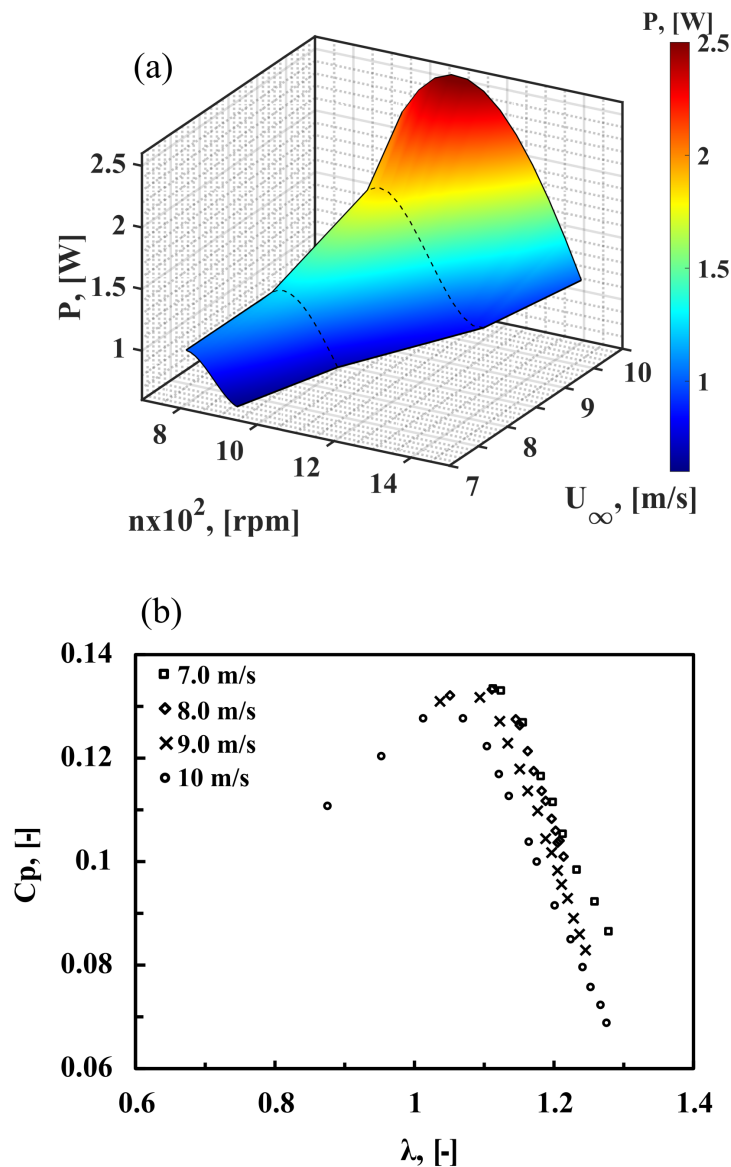


Figure 6.10: Turbine characteristic curves for different upwind velocities.

The extrapolation of blockage to open-field conditions has been performed using a Reynolds number of 3.5×10^{-4} approximately, so that results between wind and water are comparable. To check the validity of this approach, two blockage correction equations

(Werle and Gauvin) are applied to the water channel tests to estimate the operational behavior in open water and to be compared with the wind tunnel tests along with other experimental findings (using the same profile and solidity in open waters) [33]. The corrected results are quite similar to the results obtained from the wind tunnel tests. However, Werle's formulations gives slightly higher results in the power coefficient values. The tip speed ratio that corresponds to the maximum power coefficient values coincide in all open-field cases being greater than 1.0.

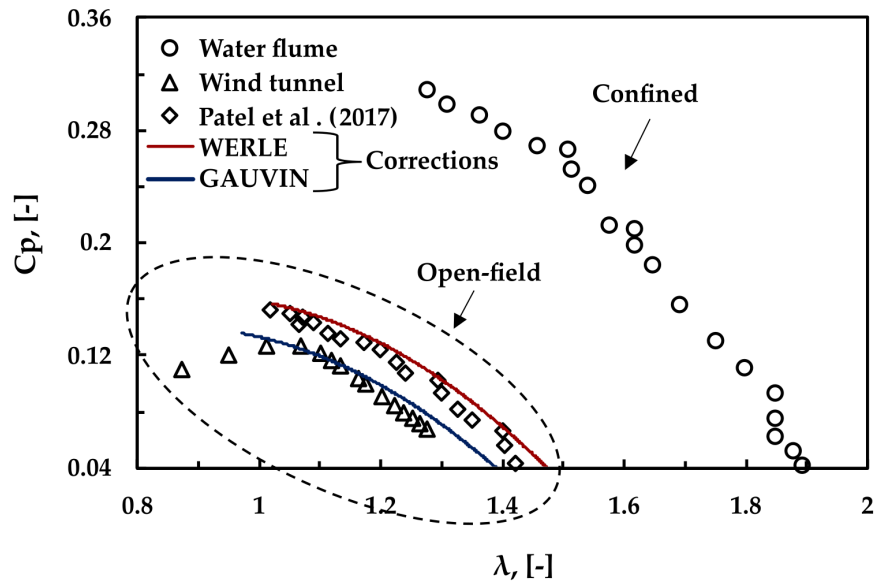


Figure 6.11: Turbine characteristic curves in wind tunnel and water flume ($Re=3.5 \times 10^{-4}$).

6.5 Efficiency Enhancement Experiments

As mentioned in Chapter 5, the efficiency improvement of hydrokinetic turbines is investigated. The research provides an analysis of the increment in the power production of a hydrokinetic turbine obtained by using a simple design of an obstacle on the bottom of the channel where the turbine is installed. The turbine is located upstream at a critical discharge point and due to its dimensions prompted a high flow blockage (around 50 %). The simplicity of the inclusion of this obstacle and the lack of present this alternative as something which may feasibly be included in new industrial scale installations. By means of experimental and multiphase numerical methodologies, the the power output and the flow behaviour have been studied to evaluate the effectiveness of this approach. Three different set of tests have been conducted: without bed obstacle, and with the 3cm and the 5cm height bed obstacles; each set with four flow rates: $0.055 \text{ m}^3/\text{s}$ (Q_1), $0.064 \text{ m}^3/\text{s}$ (Q_2), $0.072 \text{ m}^3/\text{s}$ (Q_3) and $0.076 \text{ m}^3/\text{s}$ (Q_4).

As presented in Fig. 6.12, the electrical power produced by the turbine increases with the height of the obstacle. The numerical model provided sufficient evidence to suggest that the water flow rate through the turbine rotor is the key factor which attributed to

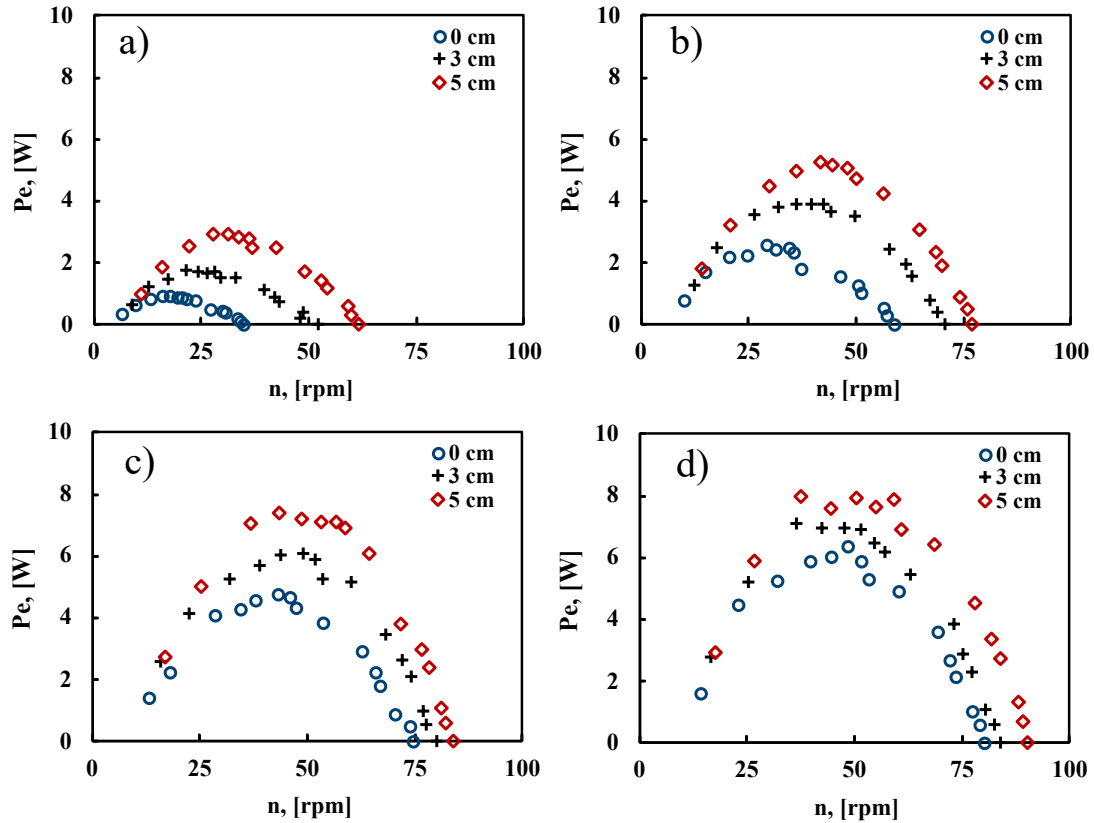


Figure 6.12: Electrical power characteristics: a) Q1; b) Q2; c) Q3; d) Q4.

this increment in power production as it is largely dependent on the height of the obstacle, with the same tendencies observed with the power generation.

For a fixed flow rate, the height of the obstacle entails an elevation of the water free surface upstream from the turbine. This leads to an increment of rotor flow by increasing the wetted transversal area of the rotor (the portion of the turbine that is in contact with water and experiencing hydrodynamic forces) up to its maximum. For this condition of higher obstacles, increasing the water velocity is due to the effect of the downstream critical point, as the water elevation is lower than the height of the obstacle. The rise in the flow rate also occasions the same effect in the turbine hydraulic head, due to the high blockage conditions of installation, resulting both in a multiplication of the power production.

The forces acting on the rotor blades have been studied, and the pressure and the velocity fields obtained from the multiphase numerical model have been analyzed. As a result of this comprehensive investigation, it is found that the height of the obstacles has a significant impact on the forces exerted on the blades, as it directly influences the net pressure on the blades, thereby increasing the amount of torque generated by the rotor.

Chapter 7

Conclusions and Future Work

7.1 Conclusions

The process of harvesting hydrokinetic energy involves capturing energy from various sources such as tides, ocean currents, or river flow. Vertical-axis hydrokinetic turbines are promising option to harness the low velocity currents. However, operating these turbines under realistic flow velocities and understanding the complex flow behaviour remain a great challenge.

This dissertation gives an insightful overview of the vertical-axis hydrokinetic turbines, with a special focus on the design and the characterization inside open water channels and under low flow velocity conditions. The influence of different parameters including flow rate, upstream velocity, Froud number, blockage and free-surface variations on the turbine performance is presented and discussed. Moreover, a cost-effective novel method to test hydrokinetic turbine models under open-field conditions (no blockage effects) has been investigated. Finally, an approach for the efficiency improvement by varying the channel geometry is presented.

The work presented regarding the design and the experimental testing of the Hydrokinetic turbine model can be summarized as follows:

- The NACA-0015 blade profile and a solidity of 2.0 together with an aspect ratio of 1.0 has been selected for the turbine model design, looking for self-starting and efficient operation with low flow velocities.
- With higher upstream velocity, the power rises, and the rotational speeds shift to higher values. The power increase is higher than the cube of the upstream velocity as a consequence of the intensification of the blockage.

- Increasing the load beyond the maximum power point, decreases the output from the turbine with a decline of the rotational speed. Operation and measurement on this unstable zone would require an active control system.
- The upstream velocity has the most obvious effect on the turbine performance. However, if the turbine is partially submerged, the power output drops sharply (more than 40 %).
- For a constant flow rate, the increase in the peak power coefficient with the upstream velocity is linked to the increase in the blockage ratio. The blockage accelerates the flow around the turbine rotor, resulting in a higher power output compared with an unrestricted flow. Furthermore, for a sub-critical flow, the water height goes down as the energy is extracted, increasing the blockage effect.
- By Comparing the experimental results with the calculations of the actuator disc theory adjusted for open channel flow. A reasonably good match between experimental and analytical results has been found for the whole ranges of upstream velocities. However, the experimental results are somewhat lower than the analytical ones because the model does not consider friction losses from the channel walls.
- Betz limit is not applicable to channel turbines, and this hypothesis has been confirmed experimentally.
- The turbine efficiency for small upstream velocities are marginal. However, from 0.45 m/s upwards, the efficiency is over 70 %, and as high as 81 %.
- The variation of the maximum power point is proportional to the square value of the channel slope. Also, the tip speed ratios that obtain the maximum power output have a slight dispersion, but they fit an equation proportional to the fourth root of the slope.

The work presented regarding the multiphase simulation of the turbine inside the open channel, with the free-surface variations, can be summarized as follows:

- The power coefficients obtained from the single-phase model are somewhat higher than the experimental ones, as it does not consider the free-surface deformations around the rotor. However, the VOF model values are much closer to the experimental ones for the whole range of tip speed ratios.
- The VOF model is able to simulate not only the free-surface longitudinal variations, but also the interactions with the channel wall boundaries.
- The energy extraction is found to be directly linked to the magnitude of the velocity in the turbine, specifically around the blades, and increasing with the free-surface drop. The surface change is also responsible for the wake recovery behaviour.

- An abnormal behaviour of the pressure coefficient have been detected for some cases at specific angular positions. This has been caused by the low pressure zone inside the rotor, due to the high solidity of the blades.
- The vorticity generated by the blades and the ending plates has been clearly analyzed. The interaction between both of them develops horseshoe vortices that separate from the rotor forming a vortex street.

The work presented regarding the open-field testing of the turbine inside the open-jet wind tunnel, can be summarized as follows:

- The open-field operating condition has been confirmed as the maximum power coefficient values corresponding to each upwind velocity are quite similar.
- The results obtained from the two blockage correction equations (Werle and Gauvin) are quite similar to the results obtained from the wind tunnel tests, which confirms the validity of the approach.

Finally, the work presented regarding the efficiency enhancement by varying the channel geometry, can be summarized as follows:

- The turbine power is boosted as the height of the obstacle increases. The flow rate through the turbine rotor is found largely dependent on the height of the obstacle.
- The height of the obstacle entails an elevation of the water free-surface upstream the turbine, which increases the wetted transversal area of the rotor and produces the effect of the downstream critical point.
- The height of the obstacles has a significant impact on the forces exerted on the blades, as it directly influences the net pressure on the blades.

7.2 Conclusions (Spanish)

El proceso de aprovechamiento de la energía hidrocínética consiste en capturar energía de diversas fuentes, como las mareas, las corrientes oceánicas o el caudal de los ríos. Las turbinas hidrocínéticas de eje vertical son una opción prometedora para aprovechar las corrientes de baja velocidad. Sin embargo, el funcionamiento de estas turbinas a velocidades de flujo realistas y la comprensión del complejo comportamiento del flujo siguen siendo un gran reto.

Esta tesis ofrece una visión general de las turbinas hidrocínéticas de eje vertical, con especial atención al diseño y la caracterización dentro de canales de agua abiertos y en condiciones de baja velocidad de flujo. Se presenta y discute la influencia de diferentes

parámetros como el caudal, la velocidad aguas arriba, el número de Froud, el bloqueo y las variaciones de la superficie libre en el rendimiento de la turbina. Además, se ha investigado un método novedoso y rentable para probar modelos de turbinas hidrocínicas en condiciones de campo abierto (sin efectos de bloqueo). Por último, se presenta un enfoque para la mejora de la eficiencia mediante la variación de la geometría del canal.

El trabajo realizado en relación con el diseño y las pruebas experimentales del modelo de turbina hidrocínica puede resumirse como sigue:

- Para el diseño del modelo de turbina se ha seleccionado el perfil de álabe NACA-0015 y una solidez de 2,0 junto con una relación de aspecto de 1,0, buscando el autoarranque y un funcionamiento eficiente con velocidades de flujo bajas.
- A mayor velocidad aguas arriba, la potencia aumenta y las velocidades de giro se desplazan hacia valores más altos. El aumento de potencia es mayor que el cubo de la velocidad aguas arriba como consecuencia de la intensificación del bloqueo.
- Al aumentar la carga por encima del punto de máxima potencia, disminuye la producción de la turbina con un descenso de la velocidad de giro. El funcionamiento y la medición en esta zona inestable requerirían un sistema de control activo.
- La velocidad aguas arriba es la que más influye en el rendimiento de la turbina. Sin embargo, si la turbina está parcialmente sumergida, la potencia disminuye bruscamente (más del 40 %).
- Para un caudal constante, el aumento del coeficiente de potencia pico con la velocidad aguas arriba está ligado al aumento de la relación de bloqueo. El bloqueo acelera el flujo alrededor del rotor de la turbina, lo que se traduce en una mayor potencia en comparación con un flujo sin restricciones. Además, para un flujo subcrítico, la altura del agua desciende a medida que se extrae la energía, lo que aumenta el efecto de bloqueo.
- Comparando los resultados experimentales con los cálculos de la teoría del disco actuador ajustada para flujo en canal abierto. Se ha encontrado una coincidencia razonablemente buena entre los resultados experimentales y los analíticos para todo el rango de velocidades aguas arriba. Sin embargo, los resultados experimentales son algo inferiores a los analíticos porque el modelo no tiene en cuenta las pérdidas por fricción de las paredes del canal.
- El límite de Betz no es aplicable a las turbinas de canal, y esta hipótesis se ha confirmado experimentalmente.
- La eficiencia de la turbina para velocidades pequeñas aguas arriba es marginal. Sin embargo, a partir de 0,45 m/s , la eficiencia es superior al 70 %, y llega hasta el 81 %.

- La variación del punto de máxima potencia es proporcional al cuadrado de la pendiente del canal. Asimismo, las relaciones de velocidad de punta que obtienen la potencia máxima tienen una ligera dispersión, pero se ajustan a una ecuación proporcional a la raíz cuarta de la pendiente.

Los trabajos presentados relativos a la simulación multifásica de la turbina en el interior del canal abierto, con las variaciones de superficie libre, pueden resumirse como sigue:

- Los coeficientes de potencia obtenidos a partir del modelo monofásico son algo superiores a los experimentales, ya que no tiene en cuenta las deformaciones de la superficie libre alrededor del rotor. Sin embargo, los valores del modelo VOF se aproximan mucho más a los experimentales para toda la gama de relaciones de velocidad de punta.
- El modelo VOF es capaz de simular no sólo las variaciones longitudinales de la superficie libre, sino también las interacciones con los límites de la pared del canal.
- Se comprueba que la extracción de energía está directamente relacionada con la magnitud de la velocidad en la turbina, concretamente alrededor de los álabes, y que aumenta con la caída de la superficie libre. El cambio de superficie también es responsable del comportamiento de recuperación de la estela.
- En algunos casos se ha detectado un comportamiento anormal del coeficiente de presión en determinadas posiciones angulares. Esto ha sido causado por la zona de baja presión en el interior del rotor, debido a la alta solidez de las palas.
- Se ha analizado claramente la vorticidad generada por las palas y las placas de terminación. La interacción entre ambas desarrolla vórtices en herradura que se separan del rotor formando una calle de vórtices.

El trabajo presentado en relación con las pruebas en campo abierto de la turbina dentro del túnel de viento de chorro abierto, puede resumirse como sigue:

- La condición de funcionamiento a campo abierto se ha confirmado, ya que los valores del coeficiente de potencia máxima correspondientes a cada velocidad de ceñida son bastante similares.
- Los resultados obtenidos a partir de las dos ecuaciones de corrección del bloqueo (Werle y Gauvin) son bastante similares a los obtenidos en las pruebas del túnel de viento, lo que confirma la validez del planteamiento.

Por último, el trabajo presentado en relación con la mejora de la eficiencia mediante la variación de la geometría del canal, puede resumirse como sigue:

- La potencia de la turbina aumenta a medida que aumenta la altura del obstáculo. El caudal que atraviesa el rotor de la turbina depende en gran medida de la altura del obstáculo.
- La altura del obstáculo implica una elevación de la superficie libre de agua aguas arriba de la turbina, lo que aumenta el área transversal mojada del rotor y produce el efecto del punto crítico aguas abajo.
- La altura de los obstáculos tiene un impacto significativo en las fuerzas ejercidas sobre las palas, ya que influye directamente en la presión neta sobre las palas.

7.3 Contributions

The main contributions made during the development of this dissertation are:

- Designing and manufacturing a small vertical-axis hydrokinetic turbine model that able to rotate and produce power under low flow velocity conditions. The turbine and all of its components are fabricated using the additive manufacturing technology precisely at a fraction of the cost offered by traditional machining technologies.
- Investigating the effect of different operational parameters including the blockage ratio, the Froud number and the upstream velocity on the overall performance of the turbine inside an open water channel.
- Developing a three-dimensional multiphase model to simulate the turbine rotor under different free-surface variations and to investigate the interactions between the turbine and the channel section, including the free-surface.
- Implementing and validating a novel a approach to evaluate the performance of the hydrokinetic turbine model under open-field conditions using wind tunnel tests. It is achieved by unifying the Reynolds number value in both experiments.
- Improving the overall performance of hydrokinetic turbines by varying the water channel geometry, through the use of an obstacle on the channel bed.

7.3.1 Contributions of the Dissertation Published in International Journals

1. **Ahmed Gharib Yosry**, Eduardo Álvarez Álvarez, Rodolfo Espina Valdés, Adrián Pandal, and Eduardo Blanco Marigorta. “Experimental and multiphase modeling of small vertical-axis hydrokinetic turbine with free-surface variations”. In *Renewable Energy*, 203 (2023), pp. 788-801, [doi.org/10.1016/j-renene-2022.12.114]

2. **A. Gharib Yosry**, A. Fernández-Jiménez, E. Álvarez-Álvarez, and E. Blanco Marigorta. “Design and characterization of a vertical-axis micro tidal turbine for low velocity scenarios”. In: *Energy Conversion and Management*, 237 (2021), p. 114, [doi.org/10.1016/j.enconman.2021.114144]
3. **A. Gharib Yosry**, E. Blanco-Marigorta, A. Fernández-Jiménez, R. Espina-Valdés, and E. Álvarez-Álvarez. “Wind–Water Experimental Analysis of Small SC-Darrieus Turbine: An Approach for Energy Production in Urban Systems”. In: *Sustainability* 13.9 (2021), p. 5256, [doi.org/10.3390/su13095256]
4. R Espina-Valdés, VM Fernández-Álvarez, **A Gharib-Yosry**, A Fernández-Jiménez, and E Álvarez-Álvarez. “Increased efficiency of hydrokinetic turbines through the use of an obstacle on the channel bottom”. In: *Ocean Engineering*, 266 (2022), p. 112872, [doi.org/10.1016/j.oceaneng.2022.112872]
5. A. Fernández-Jiménez, E. Álvarez-Álvarez, M. López, M. Fouz, Iván López, **A. Gharib Yosry**, Rubén Claus, and R. Carballo. “Power Performance Assessment of Vertical-Axis Tidal Turbines Using an Experimental Test Rig”. In: *Energies*, (2021), p. 6686, [doi.org/10.3390/en14206686]
6. Rodolfo Espina-Valdés, Aitor Fernández-Jiménez, Victor Manuel Fernández- Pacheco, **Ahmed Gharib Yosry**, and Eduardo Eduardo. “Experimental analysis of the influence of the twist angle of the blades of hydrokinetic Darrieus helical turbines”. In: *Ingenieria del agua* 26.3 (2022), pp. 205–216, [doi.org/10.4995/ia.2022.17696]
7. Aitor Fernández-Jiménez, Eduardo Blanco-Marigorta, **Ahmed Gharib Yosry**, Victor- Manuel Fernández-Pacheco, and Eduardo Álvarez-Álvarez. “Evaluation of a vertical axis hydrokinetic turbine for water channels.” In: *DYNA-Ingenieria e Industria*, (2021), [doi.org/10.6036/9883]
8. Rodolfo Espina-Valdés, Victor M Fernández-Álvarez, **Ahmed Gharib Yosry**, Aitor Fernández-Jiménez, and Eduardo Álvarez-Álvarez. “Influence of a Simple Baffle Plate on the Efficiency of a Hydrokinetic Turbine”. In: *Environmental Sciences Proceedings* 21.1 (2022), p. 4, [doi.org/10.3390/enviro21004]
9. Roberta Ferraiuolo, **Ahmed Gharib Yosry**, Aitor Fernández-Jiménez, Rodolfo Espina- Valdés, Eduardo Álvarez-Álvarez, Giuseppe Del Giudice, and Maurizio Giugni. “Design and Experimental Performance Characterization of a Three-Blade Horizontal- Axis Hydrokinetic Water Turbine in a Low-Velocity Channel”. In: *Environmental Sciences Proceedings*, 21.1 (2022), p. 62, [doi.org/10.3390/env22021062]
10. Rodolfo Espina-Valdés, **Ahmed Gharib Yosry**, Roberta Ferraiuolo, Aitor Fernández-Jiménez, and Victor Manuel Fernández-Pacheco. “Experimental Comparison between Hydrokinetic Turbines: Darrieus vs. Gorlov”. In: *Environmental Sciences Proceedings* 21.1 (2022), p. 26, [doi.org/10.3390/env2021026]

7.3.2 Contributions of the Dissertation Published in International Conferences

11. **A. Gharib Yosry**, R. Espina-Valdes, E. Blanco-Marigorta, and E. Álvarez-Álvarez. “An approximation of using vertical-axis tidal turbine for water desalination in the Suez Canal waterway”. In: *Proceedings of the ASME 2022 16th International, Conference on Energy Sustainability*, ES2022, Philadelphia, PA, USA (2022), [doi.org/10.1115/ES2022-85533]
12. **A. Gharib Yosry**, E. Blanco-Marigorta, R. Espina-Valdes, and E. Álvarez-Álvarez. “Performance Evaluation of a Small Darrieus Turbine Working with Low Flow Velocity.” In: *6th IAHR Europe Congress, June 30th – July 2nd, Marsaw, Poland* (2020), [iahr2020.pl/2021/02/12/the-book-of-abstracts]
13. **A. Gharib Yosry**, A. Fernández-Jiménez, M. Pacheco Víctor, and M. Rico-Secades. “Internet of energy applied to water hydrokinetic smart-grids: A test rig example.” In: *Proceedings of the ASME 2022 16th International, Conference on Energy Sustainability*, ES2022, Philadelphia, PA, USA (2022), [doi.org/10.1115/ES202285552]
14. L Santamaria, M Garcia, **A. Gharib**, M Galdo, E Blanco, JM Fernández, and S Velarde. “Training program for researchers in design and manufacturing of experimental prototypes for fluids engineering using additive technologies”. In: *IOP Conference Series: Materials Science and Engineering*, Vol. 1193. 1. IOP Publishing. 2021, p. 012096, [[doi:10.1088/1757899X/1193/1/012096](https://doi.org/10.1088/1757899X/1193/1/012096)]
15. A. Fernández-Jiménez, M. Rico-Secades, A. Calleja-Rodríguez, **A. Gharib Yosry**, and E. Álvarez-Álvarez. “Obtaining energy in a water distribution system using a small vertical axis hydrokinetic turbine: a practical example.” In: *6th IAHR Europe Congress, June 30th – July 2nd, Marsaw, Poland* (2020). [iahr2020.pl/2021/02/12str]
16. **A. Gharib Yosry**, A. Jiménez, M. Pacheco Víctor, and M. Rico-Secades. “Wind tunnel and OpenFOAM flow analysis of high solidity vertical-axis wind turbine.” In: *Proceedings of ASME Turbo Expo 2023, Turbomachinery Technical Conference and Exposition*, GT2023, Boston, Massachusetts USA (2023). [[Accepted May-2023](#)]
17. E. Álvarez-Álvarez, **A. Gharib Yosry**, A. Fernández-Jiménez, Antonio C. Rodríguez, and M. Rico-Secades. “Diagnostic Strategies for Microturbines Operating Status Applied to Predictive Maintenance: Experimental Test Case.” In: *Proceedings of ASME Turbo Expo 2023, Turbomachinery Technical Conference and Exposition*, GT2023, Boston, Massachusetts USA (2023). [[Accepted May-2023](#)]

7.4 Future Work

There are several points that can be addressed in the future to continue the research line of this dissertation:

- Expanding the investigation to include the design and testing of helical vertical-axis hydrokinetic turbines with different twisting angles. A comparison between the straight and the helical-bladed ones will be provide a further knowledge in this field.
- Analysing the starting behaviour of the straight-bladed turbine model for different angular positions, using a stepper motor and torque sensor.
- Testing the lift-based VAHT in the water channel with the obstacle and comparing the performance enhancement with tested drag-based turbine.
- More numerical investigation, including Delay Detached Eddy Simulation (DDES) and Improved Delay Detached Eddy Simulation (IDDES), of the flow field around the blade profile using the open-source simulation tool (OpenFOAM).
- Exploring the possibility of implementing a simple methodology that uses the energy data produced by the turbine generator to develop predictive maintenance strategies for these kinds of turbines in remote areas.

7.5 Dissertation Funding

This work is fully funded and supported by the Egyptian Government, the Ministry of Higher Education and Scientific Research along with Port-Said University, Egypt. Scholarship call 2019/2020.

Bibliography

- [1] J. Zheng, J. Du, B. Wang, J. J. Klemeš, Q. Liao, and Y. Liang, “A hybrid framework for forecasting power generation of multiple renewable energy sources,” *Renewable and Sustainable Energy Reviews*, vol. 172, p. 113046, 2023.
- [2] “Irena (2022), world energy transitions outlook 2022: 1.5°C pathway, international renewable energy agency.” <https://www.irena.org/Digital-Report/World-Energy-Transitions-Outlook-2022>. Accessed: 2023-01-29.
- [3] “Renewable energymarket update, outlook for 2022 and 2023.” <https://www.iea.org/reports/renewable-energy-market-update-may-2022>. Accessed: 2023-01-29.
- [4] A. K. Aliyu, B. Modu, and C. W. Tan, “A review of renewable energy development in africa: A focus in south africa, egypt and nigeria,” *Renewable and Sustainable Energy Reviews*, vol. 81, pp. 2502–2518, 2018.
- [5] “Irena (2022), irena’s energy transition support to strengthen climate action.” <https://www.irena.org/publications>. Accessed: 2023-02-12.
- [6] M. T. Tigabu, D. D. Guta, and B. T. Admasu, “Economics of hydro-kinetic turbine for off-grid application: A case study of gumara river, upper blue Nile, Amhara, Ethiopia,” *International Journal of Renewable Energy Research (IJRER)*, vol. 9, no. 3, pp. 1368–1375, 2019.
- [7] M. El-Sawy, A. S. Shehata, A. A. Elbatran, and A. Tawfiq, “Numerical simulation of flow in hydrokinetic turbine channel to improve its efficiency by using first and second-law efficiency analysis,” *Ocean Engineering*, vol. 244, p. 110400, 2022.
- [8] “Renewable capacity statistics 2021, irena (2021).” <https://www.irena.org/publications/2021/March/Renewable-Capacity-Statistics-2021>. Accessed: 2023-02-22.
- [9] S. Klein and E. Fox, “A review of small hydropower performance and cost,” *Renewable and Sustainable Energy Reviews*, vol. 169, p. 112898, 2022.
- [10] C. M. Niebuhr, M. Van Dijk, V. S. Neary, and J. N. Bhagwan, “A review of hydrokinetic turbines and enhancement techniques for canal installations: Technology,

- applicability and potential,” *Renewable and Sustainable Energy Reviews*, vol. 113, p. 109240, 2019.
- [11] M. J. Khan, M. T. Iqbal, and J. E. Quaicoe, “A technology review and simulation based performance analysis of river current turbine systems,” in *2006 Canadian Conference on Electrical and Computer Engineering*, pp. 2288–2293, 2006.
- [12] P. K. Talukdar, V. Kulkarni, and U. K. Saha, “Field-testing of model helical-bladed hydrokinetic turbines for small-scale power generation,” *Renewable Energy*, vol. 127, pp. 158–167, 2018.
- [13] Y. Li, B. J. Lence, and S. M. Calisal, “An integrated model for estimating energy cost of a tidal current turbine farm,” *Energy Conversion and Management*, vol. 52, no. 3, pp. 1677–1687, 2011.
- [14] C. Boccaletti, G. Fabbri, L. J. Marco Garcia, and E. Santini, “An overview on renewable energy technologies for developing countries: the case of guinea bissau,” *Renewable Energy and Power Quality*, 2008.
- [15] K. Sornes, “Small-scale water current turbines for river applications,” *Zero Emission Resource Organisation (ZERO)*, pp. 1–19, 2010.
- [16] H. J. Vermaak, K. Kusakana, and S. P. Koko, “Status of micro-hydrokinetic river technology in rural applications: A review of literature,” *Renewable and Sustainable Energy Reviews*, vol. 29, pp. 625–633, 2014.
- [17] M. S. Güney and K. Kaygusuz, “Hydrokinetic energy conversion systems: A technology status review,” *Renewable and Sustainable Energy Reviews*, vol. 14, no. 9, pp. 2996–3004, 2010.
- [18] G. Saini and R. P. Saini, “A review on technology, configurations, and performance of cross-flow hydrokinetic turbines,” *International Journal of Energy Research*, vol. 43, no. 13, pp. 6639–6679, 2019.
- [19] M. M. Elsakka, D. B. Ingham, L. Ma, and M. Pourkashanian, “Cfd analysis of the angle of attack for a vertical axis wind turbine blade,” *Energy Conversion and Management*, vol. 182, pp. 154–165, 2019.
- [20] D. Saeidi, A. Sedaghat, P. Alamdari, and A. A. Alemrajabi, “Aerodynamic design and economical evaluation of site specific small vertical axis wind turbines,” *Applied energy*, vol. 101, pp. 765–775, 2013.
- [21] S. Kefi, A. Joneja, T. KT Tse, and S. Li, “Channel geometry optimization for vertical axis wind turbines in skyscrapers,” *Computer-Aided Design and Applications*, vol. 15, no. 2, pp. 211–218, 2018.

- [22] P. Punys, I. Adamonyte, A. Kvaraciejus, E. Martinaitis, G. Vyciene, and E. Kasiulis, “Riverine hydrokinetic resource assessment. a case study of a lowland river in lithuania,” *Renewable and Sustainable Energy Reviews*, vol. 50, pp. 643–652, 2015.
- [23] I. F. S. dos Santos, R. G. R. Camacho, G. L. Tiago Filho, A. C. B. Botan, and B. A. Vinent, “Energy potential and economic analysis of hydrokinetic turbines implementation in rivers: An approach using numerical predictions (cfd) and experimental data,” *Renewable Energy*, vol. 143, pp. 648–662, 2019.
- [24] N. Mehmood, Z. Liang, and J. Khan, “Harnessing ocean energy by tidal current technologies,” *Research Journal of Applied Sciences, Engineering and Technology*, vol. 4, no. 18, pp. 3476–3487, 2012.
- [25] C. Vogel, R. Willden, and G. Houlby, “Tidal stream turbine power capping in a head-driven tidal channel,” *Renewable Energy*, vol. 136, pp. 491–499, 2019.
- [26] I. G. Bryden, S. Couch, A. Owen, and G. Melville, “Tidal current resource assessment,” *Proceedings of the Institution of Mechanical Engineers, Part A: Journal of Power and Energy*, vol. 221, no. 2, pp. 125–135, 2007.
- [27] R. Kumar and S. Sarkar, “Effect of design parameters on the performance of helical darrieus hydrokinetic turbines,” *Renewable and Sustainable Energy Reviews*, vol. 162, p. 112431, 2022.
- [28] M. Shiono, K. Suzuki, and S. Kiho, “Output characteristics of darrieus water turbine with helical blades for tidal current generations,” in *The twelfth international offshore and polar engineering conference*, OnePetro, 2002.
- [29] A. Verbruggen, M. Fishedick, W. Moomaw, T. Weir, A. Nadaï, L. J. Nilsson, J. Nyboer, and J. Sathaye, “Renewable energy costs, potentials, barriers: Conceptual issues,” *Energy policy*, vol. 38, no. 2, pp. 850–861, 2010.
- [30] C. Consul, R. Willden, E. Ferrer, and M. McCulloch, “Influence of solidity on the performance of a cross-flow turbine,” in *Proceedings of the 8th European wave and tidal energy conference, Uppsala, Sweden*, pp. 7–10, 2009.
- [31] M. Mohamed, “Impacts of solidity and hybrid system in small wind turbines performance,” *Energy*, vol. 57, pp. 495–504, 2013.
- [32] P. Mohan Kumar, K. Sivalingam, T.-C. Lim, S. Ramakrishna, and H. Wei, “Strategies for enhancing the low wind speed performance of h-darrieus wind turbine—part 1,” *Clean Technologies*, vol. 1, no. 1, pp. 185–204, 2019.
- [33] V. Patel, T. Eldho, and S. Prabhu, “Experimental investigations on darrieus straight blade turbine for tidal current application and parametric optimization for hydro farm arrangement,” *International journal of marine energy*, vol. 17, pp. 110–135, 2017.

-
- [34] M. Singh, A. Biswas, and R. Misra, "Investigation of self-starting and high rotor solidity on the performance of a three s1210 blade h-type darrieus rotor," *Renewable energy*, vol. 76, pp. 381–387, 2015.
- [35] T. Maeda, Y. Kamada, J. Murata, K. Furukawa, M. Yamamoto, *et al.*, "Effect of number of blades on aerodynamic forces on a straight-bladed vertical axis wind turbine," *Energy*, vol. 90, pp. 784–795, 2015.
- [36] I. B. Mabrouk and A. El Hami, "Effect of number of blades on the dynamic behavior of a darrieus turbine geared transmission system," *Mechanical Systems and Signal Processing*, vol. 121, pp. 562–578, 2019.
- [37] I. B. Mabrouk, A. El Hami, L. Walha, B. Zghal, and M. Haddar, "Dynamic vibrations in wind energy systems: Application to vertical axis wind turbine," *Mechanical Systems and Signal Processing*, vol. 85, pp. 396–414, 2017.
- [38] M. Mohamed, A. Dessoky, and F. Alqurashi, "Blade shape effect on the behavior of the h-rotor darrieus wind turbine: Performance investigation and force analysis," *Energy*, vol. 179, pp. 1217–1234, 2019.
- [39] M. Mohamed, "Performance investigation of h-rotor darrieus turbine with new airfoil shapes," *Energy*, vol. 47, no. 1, pp. 522–530, 2012.
- [40] N. Ma, H. Lei, Z. Han, D. Zhou, Y. Bao, K. Zhang, L. Zhou, and C. Chen, "Airfoil optimization to improve power performance of a high-solidity vertical axis wind turbine at a moderate tip speed ratio," *Energy*, vol. 150, pp. 236–252, 2018.
- [41] M. Claessens, "The design and testing of airfoils for application in small vertical axis wind turbines, master of science thesis," *Aerospace Engineering*, 2006.
- [42] O. Eboibi, *The influence of blade chord on the aerodynamics and performance of vertical axis wind turbines*. PhD thesis, University of Sheffield, 2013.
- [43] M. H. Khanjanpour and A. A. Javadi, "Optimization of the hydrodynamic performance of a vertical axis tidal (vat) turbine using cfd-taguchi approach," *Energy Conversion and Management*, vol. 222, p. 113235, 2020.
- [44] R. Gosselin, G. Dumas, and M. Boudreau, "Parametric study of h-darrieus vertical-axis turbines using cfd simulations," *Journal of Renewable and Sustainable Energy*, vol. 8, no. 5, p. 053301, 2016.
- [45] F. Kanyako and I. Janajreh, "Numerical investigation of four commonly used airfoils for vertical axis wind turbine," in *ICREGA'14-Renewable Energy: Generation and Applications*, pp. 443–454, Springer, 2014.
- [46] G. Bangga, S. Hutani, and H. Heramarwan, "The effects of airfoil thickness on dynamic stall characteristics of high-solidity vertical axis wind turbines," *Advanced Theory and Simulations*, vol. 4, no. 6, p. 2000204, 2021.

- [47] C. Liang and H. Li, “Effects of optimized airfoil on vertical axis wind turbine aerodynamic performance,” *Journal of the Brazilian Society of Mechanical Sciences and Engineering*, vol. 40, pp. 1–9, 2018.
- [48] S. Bhuyan and A. Biswas, “Investigations on self-starting and performance characteristics of simple h and hybrid h-savonius vertical axis wind rotors,” *Energy Conversion and Management*, vol. 87, pp. 859–867, 2014.
- [49] A. Sengupta, A. Biswas, and R. Gupta, “Studies of some high solidity symmetrical and unsymmetrical blade h-darrieus rotors with respect to starting characteristics, dynamic performances and flow physics in low wind streams,” *Renewable Energy*, vol. 93, pp. 536–547, 2016.
- [50] M. Mosbahi, A. Ayadi, Y. Chouaibi, Z. Driss, and T. Tucciarelli, “Performance improvement of a novel combined water turbine,” *Energy Conversion and Management*, vol. 205, p. 112473, 2020.
- [51] Y. Kyojuka, H. Akira, D. Duan, and Y. Urakata, “An experimental study on the darrieus-savonius turbine for the tidal current power generation,” in *The Nineteenth International Offshore and Polar Engineering Conference*, OnePetro, 2009.
- [52] J. Jacob and D. Chatterjee, “Design methodology of hybrid turbine towards better extraction of wind energy,” *Renewable Energy*, vol. 131, pp. 625–643, 2019.
- [53] M. Alam, M. Iqbal, *et al.*, “A low cut-in speed marine current turbine,” *the journal of Ocean Technology*, vol. 5, no. 4, pp. 49–61, 2010.
- [54] G. Saini and R. Saini, “Comparative investigations for performance and self-starting characteristics of hybrid and single darrieus hydrokinetic turbine,” *Energy Reports*, vol. 6, pp. 96–100, 2020.
- [55] K. Sahim, D. Santoso, and R. Sipahutar, “Performance of combined water turbine darrieus-savonius with two stage savonius buckets and single deflector,” *International Journal of Renewable Energy Research*, vol. 5, no. 1, pp. 217–221, 2015.
- [56] T. Bouhal, O. Rajad, T. Kousksou, A. Arid, T. El Rhafiki, A. Jamil, A. Benbassou, *et al.*, “Cfd performance enhancement of a low cut-in speed current vertical tidal turbine through the nested hybridization of savonius and darrieus,” *energy Conversion and Management*, vol. 169, pp. 266–278, 2018.
- [57] C. Li, Y. Xiao, Y.-l. Xu, Y.-x. Peng, G. Hu, and S. Zhu, “Optimization of blade pitch in h-rotor vertical axis wind turbines through computational fluid dynamics simulations,” *Applied Energy*, vol. 212, pp. 1107–1125, 2018.
- [58] Y. Yang, Z. Guo, Q. Song, Y. Zhang, and Q. Li, “Effect of blade pitch angle on the aerodynamic characteristics of a straight-bladed vertical axis wind turbine based on experiments and simulations,” *Energies*, vol. 11, no. 6, p. 1514, 2018.

-
- [59] Y.-X. Peng, Y.-L. Xu, and S. Zhan, “A hybrid dmst model for pitch optimization and performance assessment of high-solidity straight-bladed vertical axis wind turbines,” *Applied Energy*, vol. 250, pp. 215–228, 2019.
- [60] Y.-L. Xu, Y.-X. Peng, and S. Zhan, “Optimal blade pitch function and control device for high-solidity straight-bladed vertical axis wind turbines,” *Applied Energy*, vol. 242, pp. 1613–1625, 2019.
- [61] B. Chen, S. Su, I. M. Viola, and C. A. Greated, “Numerical investigation of vertical-axis tidal turbines with sinusoidal pitching blades,” *Ocean Engineering*, vol. 155, pp. 75–87, 2018.
- [62] I. Paraschivoiu, O. Trifu, and F. Saeed, “H-darrieus wind turbine with blade pitch control,” *International Journal of Rotating Machinery*, vol. 2009, 2009.
- [63] N. Kolekar and A. Banerjee, “Performance characterization and placement of a marine hydrokinetic turbine in a tidal channel under boundary proximity and blockage effects,” *Applied Energy*, vol. 148, pp. 121–133, 2015.
- [64] M. J. Najafi, S. M. Naghavi, and D. Toghraie, “Numerical simulation of flow in hydro turbines channel to improve its efficiency by using of lattice boltzmann method,” *Physica A: Statistical Mechanics and its Applications*, vol. 520, pp. 390–408, 2019.
- [65] A. H. Birjandi, E. L. Bibeau, V. Chatoorgoon, and A. Kumar, “Power measurement of hydrokinetic turbines with free-surface and blockage effect,” *Ocean Engineering*, vol. 69, pp. 9–17, 2013.
- [66] D. Medici, S. Ivanell, J.-Å. Dahlberg, and P. H. Alfredsson, “The upstream flow of a wind turbine: blockage effect,” *Wind Energy*, vol. 14, no. 5, pp. 691–697, 2011.
- [67] T. Chen and L. Liou, “Blockage corrections in wind tunnel tests of small horizontal-axis wind turbines,” *Experimental Thermal and Fluid Science*, vol. 35, no. 3, pp. 565–569, 2011.
- [68] V. Patel, T. Eldho, and S. Prabhu, “Performance enhancement of a darrieus hydrokinetic turbine with the blocking of a specific flow region for optimum use of hydropower,” *Renewable Energy*, vol. 135, pp. 1144–1156, 2019.
- [69] R. Espina-Valdés, A. Fernández-Jiménez, J. F. Francos, E. B. Marigorta, and E. Álvarez-Álvarez, “Small cross-flow turbine: Design and testing in high blockage conditions,” *Energy Conversion and Management*, vol. 213, p. 112863, 2020.
- [70] J. I. Whelan, J. Graham, and J. Peiro, “A free-surface and blockage correction for tidal turbines,” *Journal of Fluid Mechanics*, vol. 624, pp. 281–291, 2009.
- [71] G. T. Houlsby and C. R. Vogel, “The power available to tidal turbines in an open channel flow,” *Proceedings of Institution of Civil Engineers: Energy*, vol. 170, no. 1, pp. 12–21, 2017.

- [72] C. Vogel, G. Houlby, and R. Willden, “Effect of free surface deformation on the extractable power of a finite width turbine array,” *Renewable Energy*, vol. 88, pp. 317–324, 2016.
- [73] C. Vogel, R. Willden, and G. Houlby, “Power available from a depth-averaged simulation of a tidal turbine array,” *Renewable Energy*, vol. 114, pp. 513–524, 2017.
- [74] S. Yagmur, F. Kose, and S. Dogan, “A study on performance and flow characteristics of single and double h-type darrieus turbine for a hydro farm application,” *Energy Conversion and Management*, vol. 245, p. 114599, 2021.
- [75] P. Ouro, S. Runge, Q. Luo, and T. Stoesser, “Three-dimensionality of the wake recovery behind a vertical axis turbine,” *Renewable Energy*, vol. 133, pp. 1066–1077, 2019.
- [76] N. Guillaud, G. Balarac, E. Goncalves, and J. Zanette, “Large eddy simulations on vertical axis hydrokinetic turbines-power coefficient analysis for various solidities,” *Renewable Energy*, vol. 147, pp. 473–486, 2020.
- [77] P. Ouro and T. Stoesser, “An immersed boundary-based large-eddy simulation approach to predict the performance of vertical axis tidal turbines,” *Computers & Fluids*, vol. 152, pp. 74–87, 2017.
- [78] T. Kinsey and G. Dumas, “Impact of channel blockage on the performance of axial and cross-flow hydrokinetic turbines,” *Renewable energy*, vol. 103, pp. 239–254, 2017.
- [79] I. A. Tunio, M. A. Shah, T. Hussain, K. Harijan, N. H. Mirjat, and A. H. Memon, “Investigation of duct augmented system effect on the overall performance of straight blade darrieus hydrokinetic turbine,” *Renewable Energy*, vol. 153, pp. 143–154, 2020.
- [80] K. Sun, R. Ji, J. Zhang, Y. Li, and B. Wang, “Investigations on the hydrodynamic interference of the multi-rotor vertical axis tidal current turbine,” *Renewable Energy*, vol. 169, pp. 752–764, 2021.
- [81] S. Zanforlin, “Advantages of vertical axis tidal turbines set in close proximity: A comparative cfd investigation in the english channel,” *Ocean Engineering*, vol. 156, pp. 358–372, 2018.
- [82] Y. Nishi, G. Sato, D. Shiohara, T. Inagaki, and N. Kikuchi, “Performance characteristics of axial flow hydraulic turbine with a collection device in free surface flow field,” *Renewable Energy*, vol. 112, pp. 53–62, 2017.
- [83] J. Yan, X. Deng, A. Korobenko, and Y. Bazilevs, “Free-surface flow modeling and simulation of horizontal-axis tidal-stream turbines,” *Computers & Fluids*, vol. 158, pp. 157–166, 2017.

-
- [84] A. Benavides-Morán, L. Rodríguez-Jaime, and S. Laín, “Numerical investigation of the performance, hydrodynamics, and free-surface effects in unsteady flow of a horizontal axis hydrokinetic turbine,” *Processes*, vol. 10, no. 1, p. 69, 2021.
- [85] X. Sun, J. Chick, and I. Bryden, “Laboratory-scale simulation of energy extraction from tidal currents,” *Renewable Energy*, vol. 33, no. 6, pp. 1267–1274, 2008.
- [86] J. Riglin, W. C. Schleicher, I.-H. Liu, and A. Oztekin, “Characterization of a micro-hydrokinetic turbine in close proximity to the free surface,” *Ocean Engineering*, vol. 110, pp. 270–280, 2015.
- [87] Y. Nishi, G. Sato, D. Shiohara, T. Inagaki, and N. Kikuchi, “A study of the flow field of an axial flow hydraulic turbine with a collection device in an open channel,” *Renewable energy*, vol. 130, pp. 1036–1048, 2019.
- [88] M. Nakajima, S. Iio, and T. Ikeda, “Performance of savonius rotor for environmentally friendly hydraulic turbine,” *Journal of Fluid Science and Technology*, vol. 3, no. 3, pp. 420–429, 2008.
- [89] Z. Yin and M. Esmailpour, “The hydrodynamic performance of a turbine in shallow free surface flow,” *Journal of Hydrodynamics*, vol. 33, no. 4, pp. 804–820, 2021.
- [90] A. E. B. Le Hocine, R. J. Lacey, and S. Poncet, “Multiphase modeling of the free surface flow through a darrieus horizontal axis shallow-water turbine,” *Renewable Energy*, vol. 143, pp. 1890–1901, 2019.
- [91] S.-C. Roh and S.-H. Kang, “Effects of a blade profile, the reynolds number, and the solidity on the performance of a straight bladed vertical axis wind turbine,” *Journal of Mechanical Science and Technology*, vol. 27, no. 11, pp. 3299–3307, 2013.
- [92] A. Sengupta, A. Biswas, and R. Gupta, “Studies of some high solidity symmetrical and unsymmetrical blade h-darrieus rotors with respect to starting characteristics, dynamic performances and flow physics in low wind streams,” *Renewable Energy*, vol. 93, pp. 536–547, 2016.
- [93] C. Navier, “Mémoire sur les lois du mouvement des fluides,” *Mémoires de l’Académie Royale des Sciences de l’Institut de France*, vol. 6, no. 1823, pp. 389–440, 1823.
- [94] O. Reynolds, “On the two manners of motion of water,” in *Proc. R. Instn Gt Brit*, vol. 11, pp. 44–52, 1884.
- [95] D. C. Wilcox, “Reassessment of the scale-determining equation for advanced turbulence models,” *AIAA journal*, vol. 26, no. 11, pp. 1299–1310, 1988.
- [96] F. R. Menter, “Two-equation eddy-viscosity turbulence models for engineering applications,” *AIAA journal*, vol. 32, no. 8, pp. 1598–1605, 1994.

- [97] C. Hirt and B. Nichols, “Volume of fluid (vof) method for the dynamics of free boundaries,” *Journal of Computational Physics*, vol. 39, no. 1, pp. 201–225, 1981.
- [98] P. J. Roache, “Perspective: A Method for Uniform Reporting of Grid Refinement Studies,” *Journal of Fluids Engineering*, vol. 116, pp. 405–413, 09 1994.

List of Figures

- 1.1 The energy transition vision for 2050. 2
- 1.2 Renewable net capacity additions by region, 2019-2021. 2
- 1.3 Fossil and Renewable electricity generation in Egypt 2022. 3
- 1.4 Global map of the annual hydropower generation in 2022. 5
- 1.5 Hydrokinetic turbine classifications 5
- 1.6 Hydrokinetic turbine examples: a) Axial-flow model and b) Cross-flow model. 6
- 1.7 The working concept of lift-based vertical axis turbine. 7
- 1.8 Schematic of boosting the solidity through number of blades and chord length. 8
- 1.9 Different configurations of symmetric and non-symmetric airfoils. 10
- 1.10 The hybrid system configuration and tests inside the towing tank 12
- 1.11 Diagrammatic representation of the asynchronous hybrid system 12
- 1.12 Sketch of the pitch control system. 13
- 1.13 Layout of the augmentation channel and the pontoon profile details. 14

- 2.1 A detailed schematic of the turbine model. 20
- 2.2 Snapshots of the blade profile slicing and printing processes. 21
- 2.3 Snapshots of the different components of the turbine model. 22
- 2.4 A detailed schematic of the experimental test rig. 23
- 2.5 A photo of the water channel with the measuring instruments. 24
- 2.6 The water height measuring sensors. 24
- 2.7 The torque sensor measuring and control configurations. 25
- 2.8 One-dimensional LMADT in an open channel flow. 27

- 4.1 A detailed schematic of the open-jet wind tunnel. 68
- 4.2 The turbine model position in the tunnel. 69

4.3	A photo of the test rig with different instrumentation.	70
4.4	The model failure test inside the wind tunnel.	70
4.5	Snapshots of the blade profile slicing (layers orientation).	71
5.1	A detailed schematic of the drag-based turbine model.	92
5.2	A detailed schematic of the two metallic obstacles.	93
5.3	Turbine-Generator coupling system.	93
5.4	The computational grid visualization.	94
6.1	Turbine power and characteristic curves for different upstream velocities. . .	114
6.2	Experimental results and analytical model predictions.	115
6.3	Experimental turbine efficiency with respect to the analytical model. . . .	116
6.4	characteristic curve validation for (C_1).	117
6.5	Free-surface shape around the rotor (isosurface water fraction of 0.5) at $\lambda = 2.3$	117
6.6	The polar distributions of the instantaneous torque coefficient.	118
6.7	Instantaneous streamlines around the hydrofoil at various azimuth angular positions.	119
6.8	Pressure coefficient for all cases and pressure contour samples of C_2 on a single blade at $\lambda = 2.3$	120
6.9	Normalized vorticity fields ($J - K$) at the middle sections for all cases. . .	121
6.10	Turbine characteristic curves for different upwind velocities.	122
6.11	Turbine characteristic curves in wind tunnel and water flume ($Re=3.5 \times 10^4$).123	
6.12	Electrical power characteristics: a) Q1; b) Q2; c) Q3; d) Q4.	124

List of Tables

- 1.1 Renewable power capacities over the world for three consecutive years. 4

- 2.1 General specifications of the turbine rotor. 20
- 2.2 Measurement uncertainties for the experimental tests. 26

- 5.1 General specifications of the drag-based turbine rotor. 92
- 5.2 PMG main characteristics. 93

- A.1 Configuration parameters for the additive manufacturing process. 153
- A.2 CFD configuration parameters for the VOF model in ANSYSFLUENT. . . 154

Acronyms

VAHT	Vertical Axis Hydrokinetic Turbine
HAHT	Horizontal Axis Hydrokinetic Turbine
LES	Large Eddy Simulation
MRF	Moving Reference Frame
RANS	Reynolds Averaged Navier-Stokes
VOF	Volume Of Fluid
FDM	Fused Deposition Modeling
SCADA	Supervisory Control and Data Acquisition
LMADT	Linear Momentum Actuator Disc Theory
PMG	Permanent Magnet Generator
SMAW	Shielded Metal Arc Welding
GCI	Grid Conversion Index
MPP	Maximum Power Point

List of Symbols

ω	Angular velocity
V_R	Relative flow velocity
u_∞	Upstream flow velocity
u	Blade velocity
F_L	Lift force
F_D	Drag force
N	Normal force
T	Tangential force
θ	Azimuth angle
n	Number of blades
C	Chord length
R	Rotor radius
C_p	Power coefficient
C_{pw}	Mixing zone power dissipation
λ	Tip speed ratio
A_T	Turbine total area
A	Channel cross-sectional area
B	Blockage ratio
σ	Turbine solidity
D	Rotor diameter
d_s	Shaft diameter
F_r	Froud number
h_1	Upstream water height
α_4	Wake velocity coefficient
α_2	Turbine velocity coefficient
β_4	Bypass velocity coefficient
Δh	Free-surface drop
C_T	Thrust coefficient
η	Turbine efficiency
N	Rotational speed
u_c	Confined flow velocity

u_f	Open-field flow velocity
λ_f	Corrected tip speed ratio
C_{pf}	Corrected power coefficient
m	Empirical correction factor
ρ	Fluid density
P	Fluid pressure
μ	Dynamic viscosity
α	Water volume fraction
V_w	Water volume
V	Mixture volume
r	Grid refinement ratio
F_s	Factor of safety

Appendix A

Appendix: Additive Manufacturing and CFD Parameters

A.1 3-D Slicing and Printing Parameters

Table A.1: Configuration parameters for the additive manufacturing process.

	Parameter	Value/Spec
Quality	Layer height	0.1 mm
	Initial layer height	0.3 mm
	Line width	0.39 mm
Shell	Wall line count	3
	Skin overlap	5%
	Outer wall distance	0.2 mm
Infill	Overlap percentage	10%
	Pattern shape	lines
	Infill density	35%
Material	Type	PLA
	Build plate temperature	55°c
	Printing temperature	200°c
Speed (*)	Travel speed	120 mm/s
	Acceleration	1750 mm/s ²
	Printing speed	45 : 60 mm/s

(*) The printing speed is varied depending on the printed part complexity .

A.2 Simulation Setup

Table A.2: CFD configuration parameters for the VOF model in ANSYSFLUENT.

Setup	Parameter	Value/Spec
General	Solver	<i>pressure – based</i>
	Velocity formulation	<i>absolute</i>
	Gravity	$z = -9.81\text{m/s}^2$
	Time	<i>transient</i>
Models	Multiphase	<i>VOF</i>
	Formulation	<i>implicit</i>
	Viscous	<i>K – ω SST</i>
Material	Fluid	<i>Air – Water</i>
Cell zones	Rotor	<i>fluid</i>
	Channel	<i>fluid</i>
Solution Methods	P-V coupling	<i>coupled</i>
	Gradient	<i>Least Squares</i>
	Pressure	<i>Presto!</i>
	Momentum	<i>Second Order Upwind</i>
	T.K.E	<i>Second Order Upwind</i>
	Volume Fraction	<i>Compressive</i>
Under-Relaxation Factors	Transient Formulation	<i>Second Order Implicit</i>
	Pressure	0.3
	Body Forces	1.0
	Momentum	0.7
Initialization	Volume Fraction	0.5
	Overlap percentage	10%
	Pattern shape	<i>lines</i>
Calculation	Hybrid	<i>absolute – R.F</i>
	Time step	$1^\circ/\text{step}$
	No. Time steps	10080
	Max.Iteration/Step	25
	Stepping Method	<i>fixed</i>

Appendix B

Appendix: Linear Momentum Actuator Disc Theory, LMADT

B.1 Houlsby's Analytical Model Equations

9. LINEAR MOMENTUM ACTUATOR DISC THEORY IN AN OPEN CHANNEL FLOW

9.1 Geometry of the flow

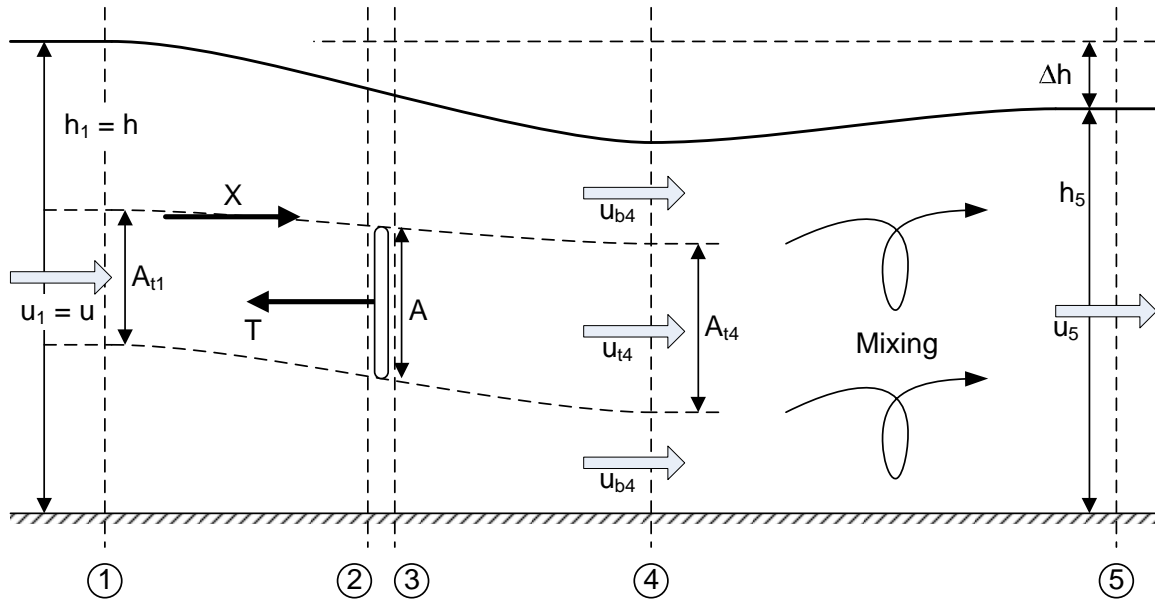


Figure 4: One dimensional linear momentum actuator disc theory in an open channel flow

5. NOMENCLATURE

Symbol	Definition
u	Stream velocity (uniform)
ρ	Fluid density
g	Gravity
p	Pressure (gauge)
h	Stream height/hydrostatic head
α_2	Turbine flow velocity coefficient
α_4	Turbine wake flow velocity coefficient
β_4	Bypass flow velocity coefficient
A	Area of the turbine defined as an actuator disc
R	Area ratio
b	Width of flow (open channel)
B	§8: Blockage ratio ($1/R$) §9: Blockage ratio (A/bh)
T	Thrust from the actuator disc to the fluid
X	Reaction between the turbine flow and bypass flow
P	Power extracted by the turbine
P_w	Power dissipate in downstream mixing
C_p	Dimensionless power coefficient, normalised by upstream kinetic flux
C_{p^*}	Dimensionless power coefficient, normalised by upstream kinetic flux and the pressure drop across the actuator disc
C_{pw}	Dimensionless power dissipation in downstream mixing, normalised by upstream kinetic flux
C_T	Dimensionless thrust coefficient, normalised by upstream kinetic pressure
C_{TL}	Dimensionless thrust coefficient, normalised by turbine kinetic pressure
η	Efficiency of a turbine in a finite flow
F_r	Froude number = u/\sqrt{gh}

Subscripts	Definition
t	Turbine flow
b	Bypass flow
1,2,3...	Station of the flow

9.2 Continuity relations

Region		Station 1	Station 2	Station 3	Station 4	Station 5
Turbine	Area	$A_{1t} = bhB\alpha_2$	$A_{2t} = A_{3t} = bhB$		$A_{4t} = bhB \frac{\alpha_2}{\alpha_4}$	
	Velocity	$u_{1t} = u$	$u_{2t} = u_{3t} = u\alpha_2$		$u_{4t} = u\alpha_4$	
	Volumetric flow	$q_{1t} = q_t$ $= ubhB\alpha_2$	$q_{2t} = q_{3t}$ $= ubhB\alpha_2$		$q_{4t} = ubhB\alpha_2$	
	Elevation head	$h_{1t} = h$	h_{2t}	h_{3t}	$h_{4t} = h_4$	
By-pass	Area	$A_{1b} =$ $bh(1 - B\alpha_2)$			$A_{4b} = bh \frac{(1 - B\alpha_2)}{\beta_4}$	
	Velocity	$u_{1b} = u$			$u_{4b} = u\beta_4$	
	Volumetric flow	$q_{1b} = q_b$ $= uhb(1 - B\alpha_2)$			$q_{4b} = uhb(1 - B\alpha_2)$	
	Elevation head	$h_{1b} = h$			$h_{4b} = h_4$	
Total	Depth	$h_1 = h$			h_4	$h_5 = h - \Delta h$
	Velocity	$u_1 = u$	Varies		Varies	$u_5 = \frac{uh}{(h - \Delta h)}$
	Volumetric flow	$q_1 = q = ubh$			$q_4 = ubh$	$q_5 = ubh$
	Pressure force	$p_1 = \frac{1}{2}\rho gh^2$	Varies	Varies	$p_4 = \frac{1}{2}\rho gh_4^2$	$p_5 =$ $\frac{1}{2}\rho g(h - \Delta h)^2$

Table 4

9.3 Commentary and derivation

The open channel flow calculation follows a similar pattern to before, except that in the Bernoulli calculation the total head is now employed. We assume that at stations 1, 4, and 5 the pressure can be treated as hydrostatic. In some senses the calculation is a hybrid between the calculation at constant pressure and the one in a fixed tube: the downstream dimensions of the flow are not fixed, but there are relationships between dimension and velocity and between dimension and pressure force.

We start by noting that in the by-pass flow:

$$h + \frac{u^2}{2g} = h_4 + \frac{u^2\beta_4^2}{2g} \quad \dots(29)$$

As before, Bernoulli in the turbine flow upstream and downstream of the turbine gives:

$$h + \frac{u^2}{2g} = h_{2t} + \frac{u^2\alpha_2^2}{2g} \quad \dots(30)$$

$$h_{3t} + \frac{u^2\alpha_2^2}{2g} = h_4 + \frac{u^2\alpha_4^2}{2g} \quad \dots(31)$$

And the equilibrium of the turbine gives:

$$\rho g(h_{2t} - h_{3t})Bbh = T \quad \dots(32)$$

Combining equations (29), (30), (31) and (32) gives:

$$h_{2t} - h_{3t} = \frac{T}{\rho g B b h} = \frac{u^2}{2g} (\beta_4^2 - \alpha_4^2) \quad \dots(33)$$

$$T = \frac{\rho u^2 B b h}{2} (\beta_4^2 - \alpha_4^2) \quad \dots(34)$$

Now consider the momentum equation between stations 1 and 4, which gives:

$$\frac{1}{2} \rho g b (h^2 - h_4^2) - T = \rho u^2 b h B \alpha_2 (\alpha_4 - 1) + \rho u^2 h b (1 - B \alpha_2) (\beta_4 - 1) \quad \dots(35)$$

Eliminating T between (34) and (35) gives

$$\frac{1}{2} g (h^2 - h_4^2) - B h \frac{u^2}{2} (\beta_4^2 - \alpha_4^2) = u^2 h B \alpha_2 (\alpha_4 - 1) + u^2 h (1 - B \alpha_2) (\beta_4 - 1) \quad \dots(36)$$

And we can make use of the continuity relationship

$$h_4 = B h \frac{\alpha_2}{\alpha_4} + h \frac{(1 - B \alpha_2)}{\beta_4} \quad \dots(37)$$

Note also the following forms

$$\beta_4 = h(1 - B \alpha_2) / (h_4 - B h \alpha_2 / \alpha_4) \quad \dots(38)$$

$$\alpha_2 = \frac{\alpha_4 (h(1 - \beta_4) + \beta_4 (h - h_4))}{B h (\alpha_4 - \beta_4)} \quad \dots(39)$$

To eliminate (in principle) h_4 and β_4 between (29), (36) and (37), leaving, as previously, a relationship between α_2 and α_4 . First eliminate h_4 to give:

$$\left(1 - \left(\frac{B \alpha_2}{\alpha_4} + \frac{(1 - B \alpha_2)}{\beta_4} \right) \right) = \frac{u^2}{2gh} (\beta_4^2 - 1) \quad \dots(40)$$

and

$$\begin{aligned} \left(1 - \left(\frac{B \alpha_2}{\alpha_4} + \frac{(1 - B \alpha_2)}{\beta_4} \right) \right)^2 &= \frac{u^2}{gh} \left(2B \alpha_2 (\alpha_4 - 1) + 2(1 - B \alpha_2) (\beta_4 - 1) + B (\beta_4^2 - \alpha_4^2) \right) \\ &= \frac{u^2}{gh} \left(2B \alpha_2 (\alpha_4 - \beta_4) + 2(\beta_4 - 1) + B (\beta_4^2 - \alpha_4^2) \right) \end{aligned} \quad \dots(41)$$

It is convenient later to write the results in terms of the upstream Froude number $F_r = u / \sqrt{gh}$.

Dividing (41) by (40) we obtain

$$\left(1 + \frac{B \alpha_2}{\alpha_4} + \frac{(1 - B \alpha_2)}{\beta_4} \right) = \frac{2}{(\beta_4^2 - 1)} \left(2B \alpha_2 (\alpha_4 - \beta_4) + 2(\beta_4 - 1) + B (\beta_4^2 - \alpha_4^2) \right) \quad \dots(42)$$

which re-arranges to

$$B\alpha_2(\beta_4 - \alpha_4) \left(4 + \frac{(\beta_4^2 - 1)}{\alpha_4\beta_4} \right) = 2B(\beta_4^2 - \alpha_4^2) + \frac{(1 - \beta_4)^3}{\beta_4} \quad \dots(43)$$

leading to the solution:

$$\alpha_2 = \frac{2(\beta_4 + \alpha_4) - \frac{(\beta_4 - 1)^3}{B\beta_4(\beta_4 - \alpha_4)}}{4 + \frac{(\beta_4^2 - 1)}{\alpha_4\beta_4}} \quad \dots(44)$$

Rewriting (40) as

$$B\alpha_2 \frac{(\beta_4 - \alpha_4)}{\alpha_4\beta_4} = \frac{(\beta_4 - 1)}{\beta_4} - \frac{u^2}{2gh} (\beta_4^2 - 1) \quad \dots(45)$$

And dividing (44) and (45) to eliminate α_2 we obtain after some manipulation:

$$\left(4\alpha_4\beta_4 + (\beta_4^2 - 1) \right) \left((\beta_4 - 1) - \frac{F_r^2}{2} (\beta_4^2 - 1)\beta_4 \right) = 2B(\beta_4^2 - \alpha_4^2)\beta_4 - (\beta_4 - 1)^3 \quad \dots(46)$$

Which is a quartic in β_4

$$\frac{F_r^2}{2}\beta_4^4 + 2\alpha_4 F_r^2 \beta_4^3 - (2 - 2B + F_r^2)\beta_4^2 - (4\alpha_4 + 2\alpha_4 F_r^2 - 4)\beta_4 + \left(\frac{F_r^2}{2} + 4\alpha_4 - 2B\alpha_4^2 - 2 \right) = 0 \quad \dots(47)$$

As $B \rightarrow 0$ and $\beta_4 \rightarrow 1$ note the limit

$$\frac{B}{(\beta_4 - 1)} = \frac{2\alpha_4}{(1 - \alpha_4^2)} \left(1 - \frac{u^2}{gh} \right) \quad \dots(48)$$

The downstream head drop can be calculated from overall momentum:

$$\frac{1}{2}\rho g b (h^2 - (h - \Delta h)^2) - T = \rho b h u \left(\frac{uh}{h - \Delta h} - u \right) \quad \dots(49)$$

$$\frac{1}{2} \left(2 \frac{\Delta h}{h} - \left(\frac{\Delta h}{h} \right)^2 \right) - \frac{T}{\rho b g h^2} = \frac{u^2}{gh} \left(\frac{\Delta h}{h - \Delta h} \right) \quad \dots(50)$$

$$\frac{1}{2} \left(2 \frac{\Delta h}{h} - \left(\frac{\Delta h}{h} \right)^2 \right) - \frac{T}{\rho b g h^2} = F_r^2 \left(\frac{\Delta h/h}{1 - \Delta h/h} \right) \quad \dots(51)$$

Where $C_T = \frac{T}{\frac{1}{2}\rho B b h u^2}$ so that $\frac{T}{\rho b g h^2} = \frac{C_T B F_r^2}{2}$. This is a cubic in $\Delta h/h$:

$$\frac{1}{2} \left(\frac{\Delta h}{h} \right)^3 - \frac{3}{2} \left(\frac{\Delta h}{h} \right)^2 + \left(1 - F_r^2 + \frac{C_T B F_r^2}{2} \right) \frac{\Delta h}{h} - \frac{C_T B F_r^2}{2} = 0 \quad \dots(52)$$

The power lost in the mixing is calculated as:

$$\begin{aligned}
 P_W &= \frac{1}{2}\rho u^3 b h B \alpha_2 \alpha_4^2 + \frac{1}{2}\rho u^3 b h (1 - B \alpha_2) \beta_4^2 - \frac{1}{2}\rho u^3 b h \left(\frac{h}{h - \Delta h} \right)^2 + h b u (h_4 - h_5) \rho g \\
 &= \frac{1}{2}\rho u^3 B b h \left(\alpha_2 \alpha_4^2 + \frac{(1 - B \alpha_2)}{B} \beta_4^2 - \frac{1}{B} \left(\frac{1}{1 - \Delta h/h} \right)^2 + \frac{2(h_4 - h_5)g}{u^2 B} \right) \dots(53)
 \end{aligned}$$

Alternatively it can be useful simply to calculate the total power taken out of the flow:

$$\begin{aligned}
 P + P_W &= \frac{1}{2}\rho u^3 b h - \frac{1}{2}\rho u^3 b h \left(\frac{h}{h - \Delta h} \right)^2 + h b u (h - h_5) \rho g \\
 &= \frac{1}{2}\rho u^3 b h \left(1 - \left(\frac{1}{1 - \Delta h/h} \right)^2 + \frac{2\Delta h/h}{F_r^2} \right) = \rho g u b h \Delta h \left(1 - F_r^2 \frac{1 - \Delta h/2h}{(1 - \Delta h/h)^2} \right) \dots(54)
 \end{aligned}$$

Therefore the efficiency of the turbine is simply:

$$\eta = \frac{P}{P + P_W} = \frac{P}{\rho g u b h \Delta h} \left(1 - F_r^2 \frac{1 - \Delta h/2h}{(1 - \Delta h/h)^2} \right)^{-1} \dots(55)$$

For small Froude number flows this may be approximated by $\eta \approx \frac{P}{\rho g u b h \Delta h}$.

9.4 Calculation sequence

1. Specify principal dimensioning parameters ρ , g and h
2. (Optionally specify width b , which acts as purely scaling term on power and force)
3. Specify upstream Froude number $F_r = u/\sqrt{gh}$, blockage ratio $0 \leq B \leq 1$ and dimensionless velocity factor $0 \leq \alpha_4 \leq 1$
4. Calculate dimensionless quantities:
 - a. Solve for β_4 from:

$$\frac{F_r^2}{2} \beta_4^4 + 2\alpha_4 F_r^2 \beta_4^3 - (2 - 2B + F_r^2) \beta_4^2 - (4\alpha_4 + 2\alpha_4 F_r^2 - 4) \beta_4 + \left(\frac{F_r^2}{2} + 4\alpha_4 - 2B\alpha_4^2 - 2 \right) = 0$$

such that $\beta_4 > 1$ and $1 > \alpha_2 > \alpha_4$.

$$\text{b. } \alpha_2 = \frac{2(\beta_4 + \alpha_4) - \frac{(\beta_4 - 1)^3}{B\beta_4(\beta_4 - \alpha_4)}}{4 + \frac{(\beta_4^2 - 1)}{\alpha_4\beta_4}}$$

$$\text{c. } C_T = (\beta_4^2 - \alpha_4^2)$$

$$\text{d. } C_{TL} = \frac{C_T}{\alpha_2^2}$$

- e. Solve for $\Delta h/h$ from:

$$\frac{1}{2} \left(\frac{\Delta h}{h} \right)^3 - \frac{3}{2} \left(\frac{\Delta h}{h} \right)^2 + \left(1 - F_r^2 + \frac{C_T B F_r^2}{2} \right) \frac{\Delta h}{h} - \frac{C_T B F_r^2}{2} = 0$$

$$\text{f. } C_P = \alpha_2 C_T$$

$$g. \quad C_P + C_{PW} = \frac{1}{B} \left(1 - \left(\frac{1}{1 - \Delta h/h} \right)^2 + \frac{2\Delta h/h}{F_r^2} \right)$$

$$h. \quad \eta = \frac{C_P}{C_P + C_{PW}} = \frac{P}{P + P_W}$$

5. Calculate dimensioned quantities:

$$i. \quad T = \frac{1}{2} \rho u^2 B b h C_T$$

$$j. \quad P = \frac{1}{2} \rho u^3 B b h C_P$$

$$k. \quad P_W = \frac{1}{2} \rho u^3 B b h C_{PW}$$

$$l. \quad \Delta h = h \frac{\Delta h}{h}$$

$$m. \quad \text{Pressure drop across turbine } \Delta p_T = \frac{T}{B b h}$$

9.5 Solution space of the model

The quartic defined by equation (47) will yield real solutions for β_4 only for a subset of input variables F_r, B, α_4 . To determine the range of this subset we can reconsider the equations derived in §9.3. It is clear that both equation (29) and equation (35) express quantities that will have a minimum value when plotted against h_4 . These minimum values indicate that the flow within the bypass and the far wake, respectively, will be exactly critical. If h_4 is specified as less than this critical point no real solutions will exist for a given upstream discharge rate. More specifically the turbine will 'block' the flow and a hydraulic jump will result.

To determine the critical point consider equation (29). Mathematically the condition of critical flow can be expressed as

$$\frac{dE}{dh_4} = \frac{d}{dh_4} \left(\frac{\beta_4^2 V^2}{2g} + h_4 \right) = \frac{h F_r^2}{2} \frac{d}{dh_4} \beta_4^2 + 1 = 0 \quad \dots(56)$$

Giving the condition

$$\frac{d(\beta_4^2)}{dh_4} = -\frac{2}{h F_r^2} \quad \dots(57)$$

A similar exercise can be done for equation (35) to determine the minimum momentum. However it can be shown numerically that in all cases the bypass condition given by (57) is reached at the point when solutions to the quartic (47) become complex. The far wake will never reach critical conditions before the bypass flow.

Therefore the solution space of this open channel model is bounded by the requirement that the bypass flow remains sub-critical, or mathematically $\frac{d(\beta_4^2)}{dh_4} < -\frac{2}{h F_r^2}$.

Appendix C








Appendix: Complementary Publications

C.1 Complementary Peer-reviewed Journal Publications

C.1.1 Power Performance Assessment of Vertical-axis Tidal Turbines Using an Experimental Test Rig

Article

Power Performance Assessment of Vertical-Axis Tidal Turbines Using an Experimental Test Rig

Aitor Fernández-Jiménez ^{1,*} , Eduardo Álvarez-Álvarez ¹ , Mario López ² , Mateo Fouz ³ , Iván López ³ , Ahmed Gharib-Yosry ⁴ , Rubén Claus ²  and Rodrigo Carballo ³

¹ Hydraulic R&D Group, University of Oviedo, Gonzalo Gutiérrez Quirós St, 33600 Mieres, Spain; edualvarez@uniovi.es

² DyMAST R&D Group, Department of Construction and Manufacturing Engineering, University of Oviedo, Gonzalo Gutiérrez Quirós St, 33600 Mieres, Spain; mario.lopez@uniovi.es (M.L.); clausruben@uniovi.es (R.C.)

³ Área de Ingeniería Hidráulica, University of Santiago de Compostela, Benigno Ledo St, 2, 27002 Lugo, Spain; davidmateo.fouz.varela@usc.es (M.F.); ivan.lopez@usc.es (I.L.); rodrigo.carballo@usc.es (R.C.)

⁴ Mechanical Power Department, Port Said University, Port Said 42526, Egypt; ahmed.gharib@eng.psu.edu.eg

* Correspondence: uo216958@uniovi.es

Abstract: This article presents the characteristic curves of a vertical-axis hydrokinetic tidal turbine of the Darrieus subtype aimed at meeting the electricity demand of port facilities located at harbors and estuaries with low water-speed conditions. The turbine was tested in the water-current flume of the University of Santiago de Compostela for several flow conditions with different water heights and water speeds. Blockage conditions were tested by examining the results from two groups of tests: with and without an accelerator device that restricts the flow around the rotor. The tip speed ratio and the power coefficient were used to characterize the performance of the turbine for each test. Finally, the results for open-field conditions were obtained by applying empirical expressions, which allowed us to assess the performance of the device in estuaries and harbors with known water-flow regimes.

Keywords: marine renewable energy; tidal energy; laboratory tests; tidal turbine



Citation: Fernández-Jiménez, A.; Álvarez-Álvarez, E.; López, M.; Fouz, M.; López, I.; Gharib-Yosry, A.; Claus, R.; Carballo, R. Power Performance Assessment of Vertical-Axis Tidal Turbines Using an Experimental Test Rig. *Energies* **2021**, *14*, 6686. <https://doi.org/10.3390/en14206686>

Academic Editor: Elhoussin Elbouchikhi

Received: 7 September 2021

Accepted: 12 October 2021

Published: 15 October 2021

Publisher's Note: MDPI stays neutral with regard to jurisdictional claims in published maps and institutional affiliations.



Copyright: © 2021 by the authors. Licensee MDPI, Basel, Switzerland. This article is an open access article distributed under the terms and conditions of the Creative Commons Attribution (CC BY) license (<https://creativecommons.org/licenses/by/4.0/>).

1. Introduction

Port facilities utilize a series of key services which promote the economic and social development of regions. There are a number of key activities which demand significant consumption of energy, existing important activities that demand big amounts of energy. Therefore, improvements in energy consumption are essential in order to ensure the most favorable use of electricity. It should be borne in mind that, due to their nature, there are diverse renewable hypo-carbon energies that could be used at these facilities, such as tidal currents or wave energy [1].

The total amount of energy consumed at ports represents 75% of all the energy used by the transport sector worldwide, which equates to 221 million tons of oil equivalent (MTOE) [2]. This represents 2.7% of global CO₂ emissions. Unless drastic measures are taken to reduce these emissions, it is expected that in the coming years, as a consequence of the growth of international trade, they will continue to increase, reaching 7% of all CO₂ emissions by 2040 [2].

The International Maritime Organization (IMO) has proposed different measures to reduce today's emissions by 50% up to 2050. Some such proposals include the use of renewable fuels, such as hydrogen or ammonia, or electric generation from low-carbon resources [3]. It should be noted that even some private concerns, such as the Maersk shipping company, have set a zero-emissions target for the year 2050 [4].

In the case of ports, the incorporation of electricity generation technologies from low-carbon resources will be a reality in 2030 [5]. Some examples are the port of Houston

(United States), where, in 2020, a solar panel farm was set up to supply electricity for harbor activity [6] or the port of Gothenburg (Sweden), where 80% of the electricity generated comes from a mixed plant of solar panels and windmills [7].

In this context, the development and implementation of other electric generation technologies from renewable resources, such as vertical-axis hydrokinetic turbines to harness water currents, are an excellent alternative to provide green energy to port facilities and reach the zero-emissions target set by the IMO for 2050. These devices are low-pressure turbines which generate electricity from the kinetic term (velocity) of a flowing stream with low potential energy, where the difference between upstream and downstream height is less than 0.2 m [8]. The generated energy can be used directly in the port, optimizing the environmental benefits of renewable energy, constituting a nearby point of consumption, and thereby reducing transport, operation, and maintenance costs.

The use of hydrokinetic turbines for their application in harbor areas is based on the electrical generation from the energy of tidal currents. These streams are a renewable, clean, and largely foreseeable resource which could be used to contribute to the decarbonization of port facilities. It has been estimated that tidal currents have a global energy potential of 800 TWh/year [9], meaning that their development and implementation would have a considerable niche in the world market. To date, this technology has been studied from various perspectives. These include: energy storage [10], their effects in the electrical market [11], and their economic optimization of operation [12]. Additionally, on many occasions, auxiliary mechanical elements, such as flow accelerators, need to be installed to increase velocity and ensure satisfactory operation [13].

Hitherto, the two main types of hydrokinetic turbines used to supply energy to harbor areas have been axial turbines (flow and axis parallel) and crossflow turbines (flow and axis perpendicular). Some of the real projects carried out using axial turbines include the RITE system based in New York (USA) that can generate 70 MWh/year [14] and the Kvalsund project installed in Finnmark (Norway) with a total power of 500 kW [15]. As regards crossflow rotor-based projects, the most noteworthy are the Blue Energy system settled in Canada with a total power of 2 kW [16] and the Oryon Watermill project located in the Netherlands with 150 kW of power [17], both with diameters greater than 2 m. In addition, the OceanQuest project should be highlighted, in which the testing of a 1 MW H-Darrieus prototype was carried out on the coast of Brittany (France) [18]. All of them are still in an embryonic stage, but recent results have been successful, which augers well for the future.

From a scientific point of view, the study of crossflow turbines has been based mainly on the development of numerical models. This is due to existing difficulties in the experimental characterization of these devices, such as problems with starting rotation at low water velocities and obtaining measurements of their power stage since, at these low speeds, torque is small [19]. In this sense, some studies stand out, such as the study carried out by Behroui et al. [20] where a Savonius rotor was characterized using Computational Fluid Dynamic (CFD) techniques, obtaining the mechanical performance. Another study of interest is the work of Kumar and Saini [21], which presents a numerical methodology for optimizing the blade size of a Savonius rotor taking into account the hydrodynamic parameters of the water stream.

As regards Darrieus typology, the studies presented by Kirke [22] and Benchikh Le Hocine et al. [23] stand out. Both publications considered the influence of the blockage effect on the power stage of a crossflow turbine. Thus, in the initial study, a deflector was numerically tested to observe its influence on the energy production of a rotor, while in the second publication, two numerical models were used together (CFD and Blade Element Method, BEM) to study the influence of the position of the water-free sheet on the turbine's performance.

This article presents an analysis and study of a Darrieus vertical-axis crossflow turbine in a current water flume, under blocking effects induced by a flow-accelerator device and with low water-velocity conditions (<1 m/s). The study was carried out in a water-current

flume installed in the laboratory of the Hydraulic Engineering Area at the Polytechnic School of Engineering of Lugo (University of Santiago de Compostela, USC).

2. Materials and Methods

2.1. Experimental Set-Up

A Darrieus rotor (Hydraulic R&D Group, Mieres, Spain) design was used, geometrical characteristics of which are shown in Figure 1.

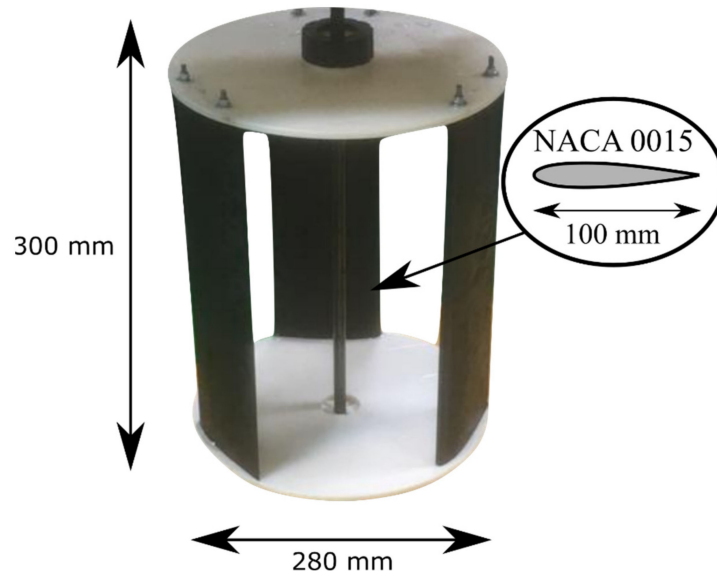


Figure 1. Darrieus rotor design tested, with the geometrical characteristics.

Using Equation (1), the solidity of this design was 0.34. This solidity value was selected because, since the rotor would work under low water-velocity conditions, having a high solidity made it easier to start the rotation of the turbine [24]. In fact, some other studies such as Singh et al. [25] and Mohammed et al. [26] show that Darrieus rotors improve their starting capacity when solidity is high since the static torque is increased, although there may be a downturn in performance.

$$\sigma = \frac{N \cdot c}{2 \cdot \pi \cdot R} \quad (1)$$

where σ is the solidity (dimensionless), N is the number of blades (dimensionless), c is the blade chord (m), and R is the rotor's radius (m).

The rotor was printed using 3D additive technology, attending to lift designs criteria to maximize performance. The material used was nylon filament (PA) due to its resistance against stresses, lightness, and non-degradation under water presence. The surface roughness of the elements that made up the rotor was reduced due to the high precision and excellent final finish of the printing equipment used (BCN3D SigmaxR19) (BCN3D, Barcelona, Spain). Additionally, after printing, the elements were subjected to sanding and sealing primer with plastic material. In consequence, the surface was completely smooth and there were no effects of turbulence in the flow due to the roughness of the turbine.

The turbine was placed in a stainless-steel metal case, in the lower part of which a radial bearing was located to ensure rotation, and the rotors were coupled to a 1.20 m-long stainless-steel shaft with a diameter measuring 10 mm. This structure was 0.62 m wide, 0.70 m long, and 1 m high, and could be found inside the water-current flume (Figure 2). In addition, two lateral windows of 0.24 m² were built so that the tests could be filmed.

The turbine was located at 0.175 m above the floor of the channel, using the lower rotor cover as a reference.

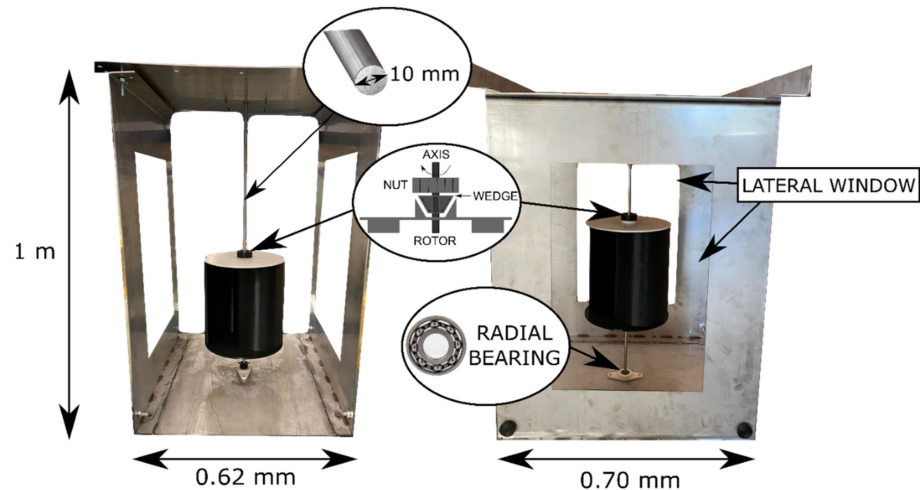


Figure 2. Structure used to couple the different rotor designs.

The structure was designed in such a way that it was possible to add and easily remove the rotor and the accelerator device by using two sets of sprats. The accelerator device was based on a symmetrical NACA profile (0015), being placed on each side of the turbine. This element allowed the incident speed to be increased by 1.6 times as the cross-section was reduced (from 0.65 m to 0.39 m). Furthermore, the use of this standardized profile for the accelerator allowed a gradual reduction in the passage section, avoiding detachments and directing the flow of water towards the rotor, minimizing the appearance of turbulent effects [27]. Figure 3 shows the accelerator device (Hydraulic R&D Group, Mieres, Spain) geometry.

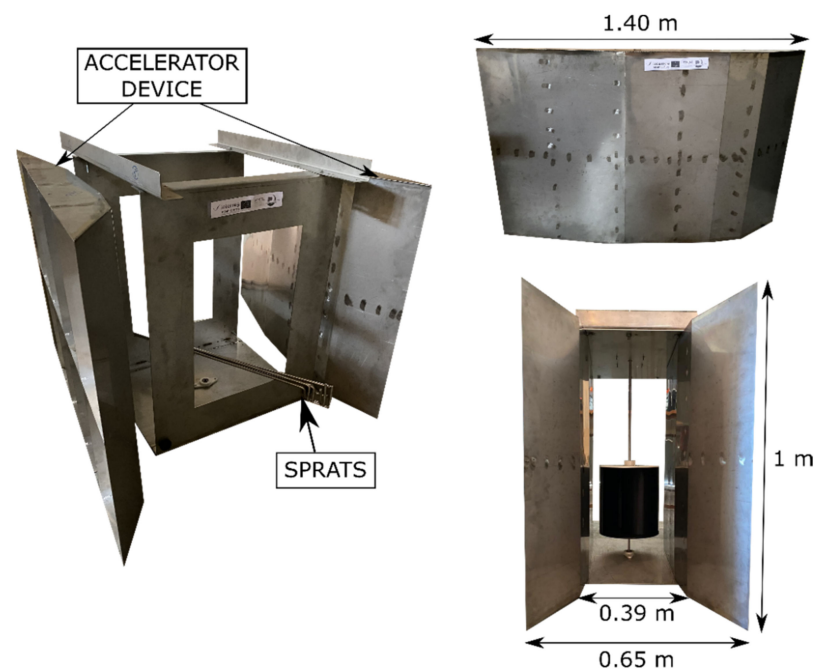


Figure 3. Geometry of the accelerator device.

A 20 m-long water-current flume, which was 0.65 m wide and 1 m high with transparent crystal walls, was used to carry out the power characterization of the selected rotor. The movement of the water inside the channel was forced by a hydraulic pump (Pedrollo Spa, San Bonifacio VR, Italy) with 22 kW of power (IDEAL-RNL-150-250/264 series). There was no free-discharge point on the circuit (Figure 4). The flow inside the channel was controlled by means of several valves that were calibrated with an ultrasonic flow meter. In this manner, different water speeds and heights could be reproduced under controlled conditions.

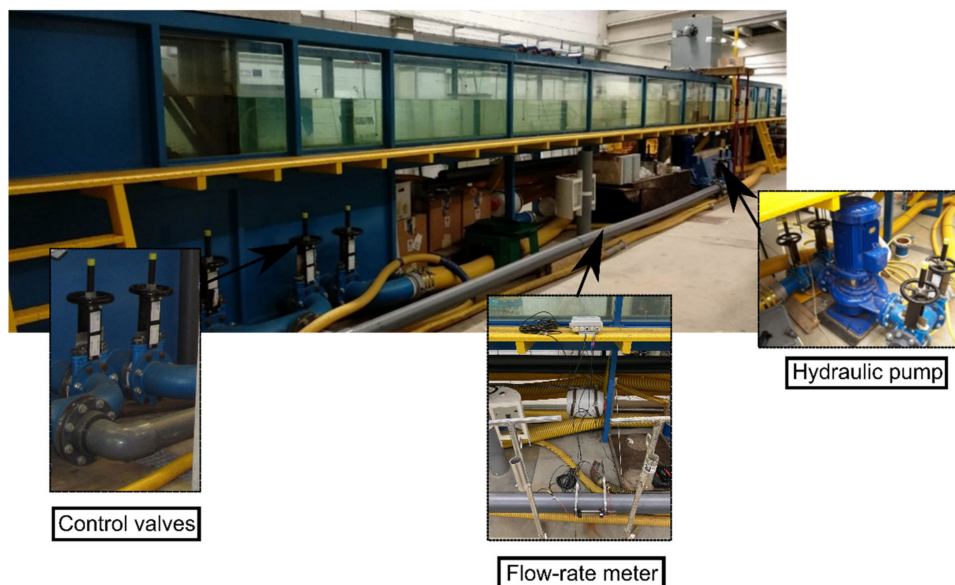


Figure 4. Water-current flume with the hydraulic control devices.

To monitor the hydraulic parameters during the tests such as flow rate, water velocity, and height variation, different sensors were used, including water-pressure devices, electric and ultrasonic water-height sensors, and an Acoustic Doppler Velocimeter (ADV) (Sontek, San Diego, CA, USA). The ADV was located just at the inlet zone of the turbine so that the speed upstream the rotor was known (Figure 5).

The power characterization simulation process of the rotor was based on variation of the resistive torque of the electric brake. In this way, for each value induced on the electric brake, a rotational speed (n) and mechanical torque (T) in the turbine were obtained, so that the rotor's power stage could be fully and satisfactorily simulated. Figure 6 shows an outline of the procedure adopted.

The characterization began with an initial measurement, called "no load", where the electric brake did not offer resistance so that the turbine would rotate at its maximum speed but would not generate mechanical torque (Step 1). Then, by using a power-supply unit, the brake voltage was progressively varied, increasing the braking torque and obtaining, for each voltage, an n and T value of the turbine (Step 2). The test ended when the turbine stopped its rotation (Step 3).

The measurements were recorded with a high-precision torque meter (MAGTROL TS 103 series, Buffalo, NY, USA) and an electrical brake (MAGTROL HB140M series, Buffalo, NY, USA). This system measured instant torque (N·m) and rotational speed (rpm), storing and processing all data using the manufacturer's software (MAGTROL TORQUE Version 10, Buffalo, NY, USA).

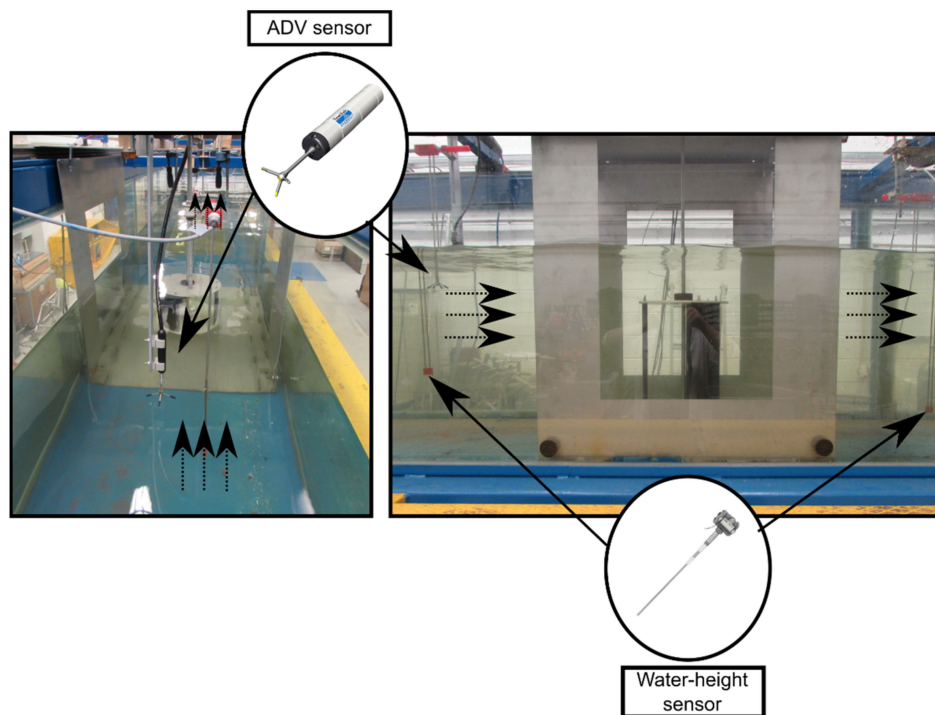


Figure 5. Hydraulic sensors' locations during tests.

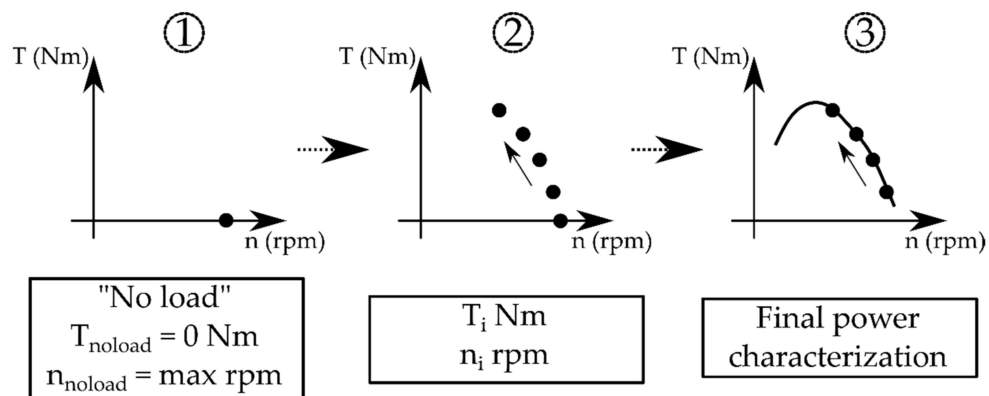


Figure 6. Scheme of the experimental characterization procedure.

2.2. Performance Indicators

The power characterization of the turbine was carried out from the raw data obtained by the torque meter. Subsequently, these data were processed, and several performance indicators were obtained. The relation of the speed at the tip of the blade with the upstream flow speed—i.e., the Tip Speed Ratio (*TSR*), was obtained by applying:

$$TSR = \frac{\omega \cdot R}{U} \quad (2)$$

with ω the rotational speed of the rotor (rad/s), and U the average water speed in the uniform zone upstream of the turbine at the channel (m/s). In addition, the power coefficient of the turbine (dimensionless) was obtained by applying:

$$Cp = \frac{P_m}{P_t} \quad (3)$$

where P_m is the average mechanical power in a complete turn of the turbine (W), obtained using:

$$P_m = \omega \cdot T \quad (4)$$

with T the torque force at the shaft (N·m), and P_t the average hydraulic power of the current during a given test (W), obtained via:

$$P_t = \frac{1}{2} \cdot \rho \cdot A_t \cdot U^3 \quad (5)$$

with ρ the fluid density (kg/m³), and A_t the area swept by the blades (m²), which was calculated by multiplying the height of the turbine (h) by the transverse width occupied by the rotor ($2R$).

2.3. Open-Field Conditions

In the presence of any blockage, the fluid is forced to pass through the rotor and the flow is accelerated [28]. This may be applied to experiments in current flumes such as those carried out in this study, but not to estuaries where the flow is unrestricted by walls near the rotor—i.e., open-field conditions. On this basis, the performance of the turbine for open-field conditions is required to assess the power production of the turbine for a possible location of interest in the vicinity of a port.

To characterize the performance of the turbine in open-field conditions, the modified values of Cp and TSR were obtained by applying:

$$Cp_F = Cp \left(\frac{U}{U_F} \right)^3 \quad (6)$$

$$TSR_F = TSR \left(\frac{U}{U_F} \right) \quad (7)$$

respectively, where U_F is the open-field flow speed corresponding to each value of water speed tested in the flume under blocked conditions (m/s). The relation between velocities, applied velocity relationship, is based on the expression proposed by Gauvin et al. [28]. This Equation (8) was selected since it performs well with blockage coefficients greater than 20%, as indicated in the case studied [28]:

$$\left(\frac{U_F}{U} \right)^2 = \frac{1}{1 - (m \cdot B)} \quad (8)$$

where B (dimensionless) is the blockage coefficient provided by:

$$B = \frac{2 \cdot R \cdot h}{b \cdot y} \quad (9)$$

with h the height of the rotor (m), b the flume width (m), y the water height at the flume (m), and m an empirical coefficient provided by [28]:

$$m = 8.14 \cdot B^2 - 7.31 \cdot B + 3.23 \quad (10)$$

A complete power characterization of the rotor was carried out to study the influence of blockage phenomena during the power stage of the turbine under low water-speed

conditions (<1 m/s). For each velocity, three water heights (0.5, 0.55, and 0.6 m) were induced with and without an accelerator device, carrying out a total of six tests. Under these conditions, values of B of 0.21, 0.23, and 0.25 were obtained for the tests without an accelerator and of 0.38, 0.41, and 0.45 when this element was placed. In both cases, the variation of blockage was made by varying the water level, although each situation was different because of changes in the hydrodynamic behavior due to the presence of the accelerator. Figure 7 shows an outline of the tests carried out.

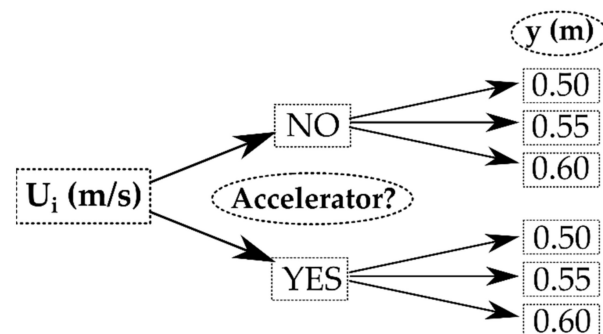


Figure 7. Outline showing how the tests were carried out.

An initial water velocity of $U_1 = 0.174$ m/s was selected because it was the cut-in speed of the rotor, while $U_3 = 0.246$ m/s was the maximum water speed of the current flume. $U_2 = 0.210$ m/s was selected as an intermediate speed. It should be noted that the position of the rotor, water-height sensors, and the ADV speed meter were invariably located in the same place during all tests. More specifically, all sensors were located at a height of 0.30 m from the bottom of the channel, and the ADV located at 0.70 m upstream of the rotor axis. Figure 8 shows a diagram with the main distances.

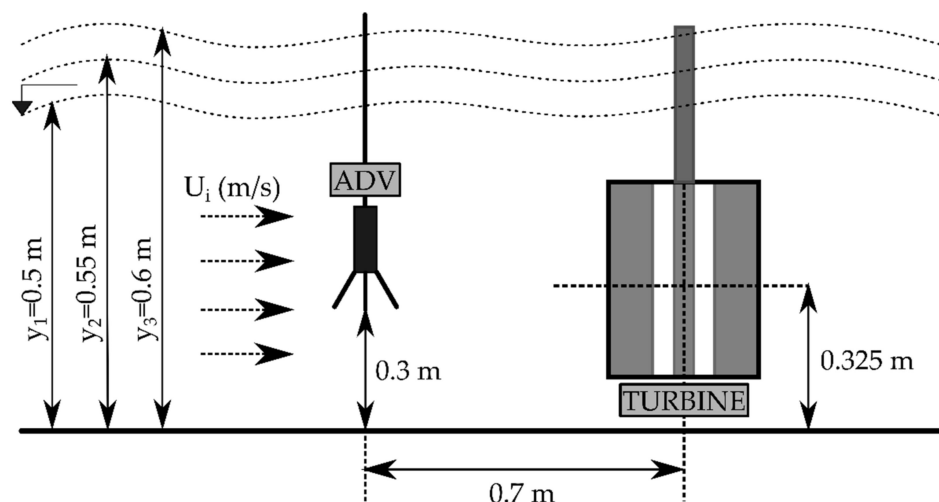


Figure 8. Diagram with the position of the different elements used in tests.

3. Results and Discussion

The proposed Darrieus water-current turbine was studied following the power characterization procedure described in previous sections. On the one hand, Figure 9 shows the variation of P_m versus the rotational speed of the turbine (n) for tests without an accelerator represented as being (a–c) whilst the different water speeds used were of 0.174, 0.210, and 0.246 m/s, respectively. On the other hand, Figure 10 shows the same tests but

using the accelerator device represented as (a–c) with water speeds of 0.174, 0.210, and 0.246 m/s, respectively.

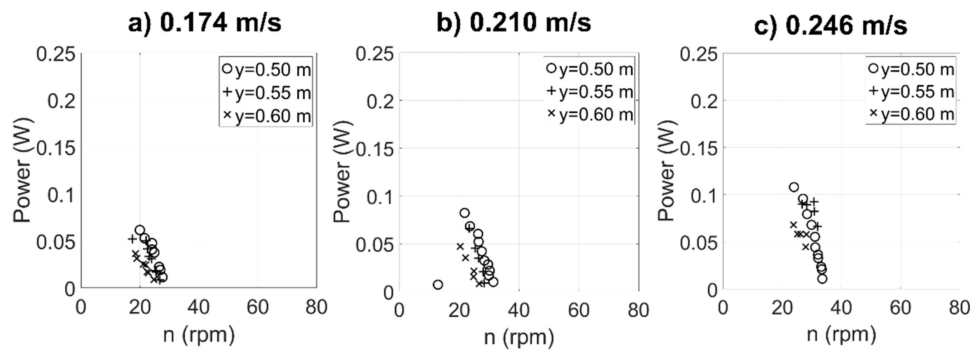


Figure 9. Variation of power vs. n for the different tests without an accelerator device.

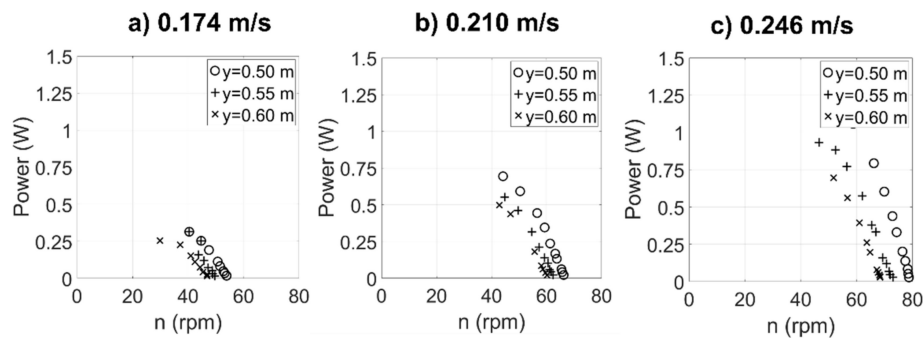


Figure 10. Variation of power vs. n for the different tests with an accelerator device.

The characteristic curves show how power values were affected by variations in the current speed and in water height. More specifically, when the current velocity increased or the water height decreased, the power of the rotor went up. This produces an increase of blockage conditions, which has direct consequences on energy extraction. In fact, the effects of blockage were noticeable when the accelerator device was installed, producing a significant increase in the rotational speed and power, even under the low water velocities of the tests.

It could also be observed how the recorded values reached a point of maximum power (maximum power point, MPP) and then the turbine stopped its rotation. The reason was that the left part of the C_p vs. TSR curve corresponds to an unstable operating zone of the turbine caused by the loss of lift force on blades (the turbine was the Darrieus NACA 0015 type that works mainly under lift forces). In the case that the rotor had a design based on drag forces (for example a Savonius type) it would be possible to obtain those points of the instability zone. [29].

Using the dimensionless coefficients of TSR and C_p it was possible to obtain an initial approximation of the operation of the designed turbine. Figure 11 shows these power parameters only with the results of the tests where the accelerator device was used since these tests conditions allow for a better visualization of the behavior of the turbine.

For the three water velocities, maximum TSR values higher than 4.5 were attained, which indicates a significant acceleration of the speed at the tip of the blade with respect to the current velocity. Furthermore, in all tests the maximum C_p values were greater than 1 due to the great blockage existing during the tests ($B > 0.38$). Therefore, it is evident that the results obtained were strongly influenced by blockage phenomenon but were not consistent with the behavior of the turbine under open-field conditions. To

obtain its characteristics without considering the blockage effects, the previously indicated Equations (6) and (7) were applied, showing in Figure 12 the C_{pF} and TSR_F values for the same tests.

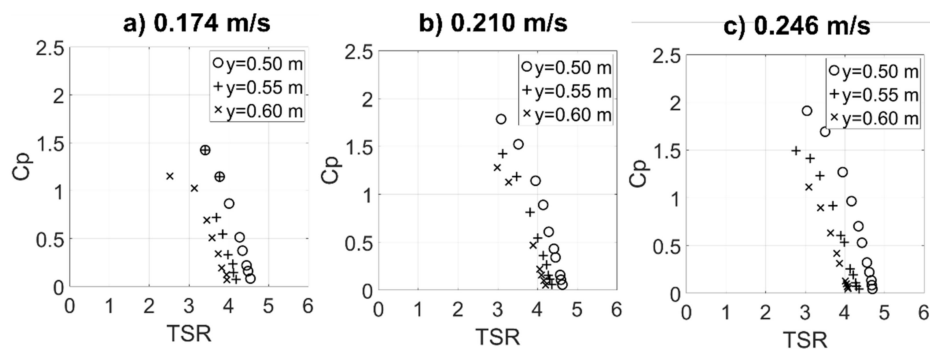


Figure 11. C_p vs. TSR curves for the three water velocities tested using the accelerator device.

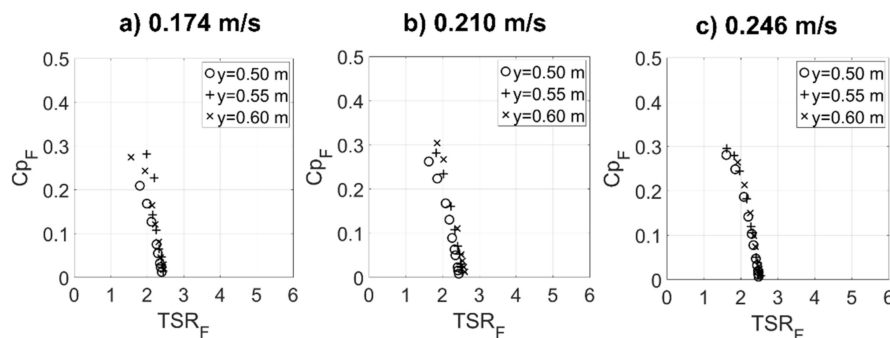


Figure 12. C_{pF} vs. TSR_F curves for the three water velocities tested using the accelerator device under open-field conditions.

The values of C_p and TSR at open-field conditions suffered a marked decrease with respect to the values under confined flow. Be that as it may, TSR values greater than 1 showed an increase in the speed at the tip of the blade, which indicates, in a preliminary way, that the rotor worked mainly at lift, so the performance of the turbine was better [21]. Further, the maximum values of C_p reached 0.29, which corresponds with more realistic values than the previous values. It should be noted that, considering the low water velocities, the turbine performed well and had good behavior due to those high-power coefficient values. Finally, and especially for the maximum water velocity, it may be observed how the characteristic curve of the turbine tended to be unique, thus eliminating the influence of the height.

4. Conclusions

In this study, the power characterization of a vertical-axis hydrokinetic tidal turbine based on the Darrieus subtype was put forward. The device under scrutiny was designed to supply electricity to port facilities located at harbors and estuaries with low water-velocity conditions. The turbine was tested in the water-current flume of the University of Santiago de Compostela to evaluate its performance under several flow conditions with three different current speeds. Moreover, the blockage effects on the performance of the turbine were examined by varying the water height and installing an accelerator device that restricted the flow around the rotor. Once the laboratory experiments were concluded, the performance of the turbine in confined and open-field conditions was satisfactorily assessed. The procurement of unrestricted results was made possible by applying empirical expressions to experimental data.

Several conclusions of interest and future research lines can be drawn from the results of this work. As expected, the power coefficient of the turbine increased when the accelerator device was installed in the water-current flume for all the flow conditions examined. This happened since blockage conditions produced changes in the water-current regime that favored the extraction of energy via by the turbine. More specifically, for the highest water velocity ($U = 0.246$ m/s) values of $C_p = 1.91$ were attained, although this result was obtained under confined flow conditions.

While the confined results were promising, open-field conditions were examined to assess the potential of this device under realistic conditions. After applying empirical expressions, C_p values decreased, reaching a maximum of 0.29 at non-restricted conditions. This result points to an excellent performance of the turbine, and possibly more, considering the low water velocities of the tests.

Future research should include the application of numerical modeling to analyze other aspects of the performance of the turbine both under blockage and open-field conditions. Furthermore, the study of flow regimes in locations of interest may be considered to assess the performance of the turbine under real conditions.

Author Contributions: Conceptualization, software, validation, investigation, resources, writing—original draft preparation, writing—review and editing, A.F.-J.; conceptualization, methodology, formal analysis, visualization, supervision, E.Á.-Á.; conceptualization, methodology, formal analysis, visualization, supervision, project administration, funding acquisition, M.L.; software, validation, investigation, resources, M.F.; software, validation, investigation, resources, I.L.; software, validation, investigation, resources, A.G.-Y.; software, validation, investigation, resources, R.C. (Rubén Claus); conceptualization, methodology, formal analysis, visualization, supervision, project administration, funding acquisition, R.C. (Rodrigo Carballo). All authors have read and agreed to the published version of the manuscript.

Funding: This research was funded by PORTOS project co-financed by the Interreg Atlantic Area Programme through the European Regional Development Fund, grant number EAPA_784/2018.

Institutional Review Board Statement: Not applicable.

Informed Consent Statement: Not applicable.

Data Availability Statement: Not applicable.

Acknowledgments: Not applicable.

Conflicts of Interest: The authors declare no conflict of interest.

References

1. Cavallaro, L.; Iuppa, C.; Castiglione, F.; Musumeci, R.; Foti, E. A Simple Model to Assess the Performance of an Overtopping Wave Energy Converter Embedded in a Port Breakwater. *J. Mar. Sci. Eng.* **2020**, *8*, 858. [CrossRef]
2. IEA. *Renewables 2020. Analysis and Forecast to 2025*; IEA: New York, NY, USA, 2020.
3. Nuchturee, C.; Li, T.; Xia, H. Energy efficiency of integrated electric propulsion for ships—A review. *Renew. Sustain. Energy Rev.* **2020**, *134*, 110145. [CrossRef]
4. Maersk. Towards a Zero-Carbon Future | Maersk. Available online: <https://www.maersk.com/news/articles/2019/06/26/towards-a-zero-carbon-future> (accessed on 4 January 2021).
5. Global Wind Energy Council. Global Wind Energy Council—GWEC: Global Wind Report 2009. 2009. Available online: <http://www.gwec.net/index.php?id=167&L=0> (accessed on 4 January 2021).
6. Port of Houston. Port Commission Approves Move on Renewable Energy | Business Wire. Available online: <https://www.businesswire.com/news/home/20191023005777/en/Port-Commission-Approves-Move-on-Renewable-Energy> (accessed on 4 January 2021).
7. Port of Gotenburg. New agreement between Swedegas and FordonsGas—Liquefied Biogas Brings Further Climate Benefits to Gothenburg Shipping | Hellenic Shipping News Worldwide. Available online: <https://www.hellenicshippingnews.com/new-agreement-between-swedegas-and-fordonsgas-liquefied-biogas-brings-further-climate-benefits-to-gothenburg-shipping/> (accessed on 4 January 2021).
8. Khan, M.J.; Bhuyan, G.; Iqbal, M.T.; Quaicoe, J.E. Hydrokinetic energy conversion systems and assessment of horizontal and vertical axis turbines for river and tidal applications: A technology status review. *Appl. Energy* **2009**, *86*, 1823–1835. [CrossRef]

9. Soerensen, H.C.; Weinstein, A. *Ocean Energy: Position Paper for IPCC*; Intergovernmental Panel on Climate Change: Lubeck, Germany, 2009.
10. Bahmani-Firouzi, B.; Azizipanah-Abarghoee, R. Optimal sizing of battery energy storage for micro-grid operation management using a new improved bat algorithm. *Int. J. Electr. Power Energy Syst.* **2014**, *56*, 42–54. [[CrossRef](#)]
11. Gburczyk, P.; Wasiak, I.; Mienski, R.; Pawelek, R. Energy management system as a mean for the integration of distributed energy sources with low voltage network. In Proceedings of the International Conference on Electrical Power Quality and Utilisation, EPQU, Lisbon, Portugal, 17–19 October 2011; pp. 488–492. [[CrossRef](#)]
12. Alvarez, E.A.; Campos-Lopez, A.M.; Gutiérrez-Trashorras, A.J. OCCAM: On-line cost-function based control algorithm for microgrids. *J. Renew. Sustain. Energy* **2012**, *4*, 033101. [[CrossRef](#)]
13. Elbatran, A.H.; Ahmed, Y.M.; Shehata, A.S. Performance study of ducted nozzle Savonius water turbine, comparison with conventional Savonius turbine. *Energy* **2017**, *134*, 566–584. [[CrossRef](#)]
14. Verdant Power. Technology Evaluation of Existing and Emerging Technologies. *Water Curr. Turbines River Appl.* **2006**, *3502*, 1–48.
15. Kvalsund. Kvalsund Tidal Turbine Prototype | Tethys. Available online: <https://tethys.pnnl.gov/project-sites/kvalsund-tidal-turbine-prototype> (accessed on 4 January 2021).
16. BlueEnergy Canada INC. Blue Energy Turbine. 2020. Available online: <http://www.blueenergy.com/> (accessed on 8 January 2021).
17. Oryon. ORYON WATERMILL. Available online: <https://www.oryonwatermill.com/> (accessed on 4 January 2021).
18. “OceanQuest—HydroQuest,” 2021. Available online: <https://www.hydroquest.fr/en/oceanquest/> (accessed on 22 June 2021).
19. Espina-Valdés, R.; Fernández-Jiménez, A.; Francos, J.F.; Marigorta, E.B.; Álvarez-Álvarez, E. Small cross-flow turbine: Design and testing in high blockage conditions. *Energy Convers. Manag.* **2020**, *213*, 112863. [[CrossRef](#)]
20. Behrouzi, F.; Nakisa, M.; Maimun, A.; Ahmed, Y.M.; Souf-Aljen, A.S. Performance investigation of self-adjusting blades turbine through experimental study. *Energy Convers. Manag.* **2019**, *181*, 178–188. [[CrossRef](#)]
21. Kumar, A.; Saini, R. Performance parameters of Savonius type hydrokinetic turbine—A Review. *Renew. Sustain. Energy Rev.* **2016**, *64*, 289–310. [[CrossRef](#)]
22. Kirke, B. Tests on ducted and bare helical and straight blade Darrieus hydrokinetic turbines. *Renew. Energy* **2011**, *36*, 3013–3022. [[CrossRef](#)]
23. Le Hocine, A.E.B.; Lacey, R.J.; Poncet, S. Multiphase modeling of the free surface flow through a Darrieus horizontal axis shallow-water turbine. *Renew. Energy* **2019**, *143*, 1890–1901. [[CrossRef](#)]
24. Yosry, A.G.; Fernández-Jiménez, A.; Álvarez-Álvarez, E.; Marigorta, E.B. Design and characterization of a vertical-axis micro tidal turbine for low velocity scenarios. *Energy Convers. Manag.* **2021**, *237*, 114144. [[CrossRef](#)]
25. Singh, M.; Biswas, A.; Misra, R. Investigation of self-starting and high rotor solidity on the performance of a three S1210 blade H-type Darrieus rotor. *Renew. Energy* **2015**, *76*, 381–387. [[CrossRef](#)]
26. Chong, W.T.; Muzammil, W.K.; Wong, K.H.; Wang, C.-T.; Gwani, M.; Chu, Y.J.; Poh, S.-C. Cross axis wind turbine: Pushing the limit of wind turbine technology with complementary design. *Appl. Energy* **2017**, *207*, 78–95. [[CrossRef](#)]
27. Sarraf, C.; Djeridi, H.; Prothin, S.; Billard, J. Thickness effect of NACA foils on hydrodynamic global parameters, boundary layer states and stall establishment. *J. Fluids Struct.* **2010**, *26*, 559–578. [[CrossRef](#)]
28. Gauvin-Tremblay, O.; Dumas, G. Two-way interaction between river and deployed cross-flow hydrokinetic turbines. *J. Renew. Sustain. Energy* **2020**, *12*, 034501. [[CrossRef](#)]
29. Álvarez-Álvarez, E.; Rico-Secades, M.; Fernández-Jiménez, A.; Espina-Valdés, R.; Corominas, E.L.; Calleja-Rodríguez, A.J. Hydrodynamic water tunnel for characterization of hydrokinetic microturbines designs. *Clean Technol. Environ. Policy* **2020**, *22*, 1843–1854. [[CrossRef](#)] [[PubMed](#)]

C.1.2 Influence of a Simple Baffle Plate on the Efficiency of a Hydrokinetic Turbine



Proceeding Paper

Influence of a Simple Baffle Plate on the Efficiency of a Hydrokinetic Turbine [†]

Rodolfo Espina-Valdés ^{1,*}, Victor M. Fernández-Álvarez ¹, Ahmed Gharib-Yosry ², Aitor Fernández-Jiménez ¹ and Eduardo Álvarez-Álvarez ¹¹ GIFD Group—EP Mieres, University of Oviedo, 33600 Mieres, Spain² Mechanical Power Department, Faculty of Engineering, Port Said University, Port-Said 42526, Egypt* Correspondence: espinarodolfo@uniovi.es[†] Presented at the International Conference EWaS5, Naples, 12–15 July 2022.

Abstract: The research presented analyzes the influence exerted on the efficiency of a vertical axis cross-flow hydrokinetic microturbine by modifying the geometry of the channel by means of a deflector located upstream of the turbine. To this end, a series of laboratory tests were carried out in the water tunnel at the University of Oviedo, including the measurement of electrical power and the rotational speeds of the turbine. Additionally, the results obtained were used to adjust a computational fluid dynamics model that allows studying the pressure and velocity fields of the water, where to delve into the analysis of the different types of forces applied to the faces of the blades. The results clearly indicate that the baffle increases the turbine power output up to 250% more than without including any device in the water flow.

Keywords: hydrokinetic microturbine; enhancement; efficiency; low cost; validated CFD

Citation: Espina-Valdés, R.; Fernández-Álvarez, V.M.; Gharib-Yosry, A.; Fernández-Jiménez, A.; Álvarez-Álvarez, E. Influence of a Simple Baffle Plate on the Efficiency of a Hydrokinetic Turbine. *Environ. Sci. Proc.* **2022**, *21*, 4. <https://doi.org/10.3390/environsciproc2022021004>

Academic Editors:

Vasilis Kanakoudis, Maurizio Giugni, Evangelos Keramaris and Francesco De Paola

Published: 17 October 2022

Publisher's Note: MDPI stays neutral with regard to jurisdictional claims in published maps and institutional affiliations.



Copyright: © 2022 by the authors. Licensee MDPI, Basel, Switzerland. This article is an open access article distributed under the terms and conditions of the Creative Commons Attribution (CC BY) license (<https://creativecommons.org/licenses/by/4.0/>).

1. Introduction

The energy obtained from hydrokinetic turbines depends mainly on the speed of the water [1] and to achieve the profitability necessary to compete with conventional energy sources, speeds from 1–2 m/s are required [2]. Usually, the water that circulates through canals or riverbeds does not reach these magnitudes; thus, currently, obtaining energy in this type of installation does not represent a real alternative to the current energy system [3]. Considering that the energy potential available in the case of low-velocity water currents of rivers and channels is greater than 840 TWh [4], progress should be made towards the development of these types of turbines to improve their efficiency, even in operating conditions with very low speeds.

To date, different solutions have been studied to increase the efficiency of a turbine in a channel, such as developing control algorithms to guarantee the maximum power of the turbine at any time [5,6], study in depth the effects of the blockage caused by the turbine in [7–9], or the installation of flow modifiers to increase the performance of the turbine [10–12].

This study analyzes the consequences derived from placing a baffle plate in a channel, in order to direct the flow of water to improve the rotational speed of the turbine (N) and therefore, the power generated (P). The original idea for this app was inspired by the ancient Persian windmills of Nashtifan, northwestern Iran [13]. These windmills are considered the oldest in the world and have been in operation since the 7th century.

The mills are wooden turbines included in a structure that acts as a conduit for the wind. In order to maximize the wind power gain, its structure has a deflector plate that directs the wind to the area in favor of the rotation of the turbine [14].

2. Materials and Methods

Lab Tests

The elements used to carry out the tests were a vertical axis turbine, a hydrodynamic water tunnel, a baffle plate, and a control system. The turbine is made up of 12 semicircular stainless-steel blades, 0.3 m high and 0.23 m wide (Figure 1). The blades have an angular separation of 30° with a semicircular section of 21 mm in diameter. At the top of the shaft is a system of belts and pulleys designed to multiply the speed of rotation mechanically connected to a permanent magnet generator (PMG).

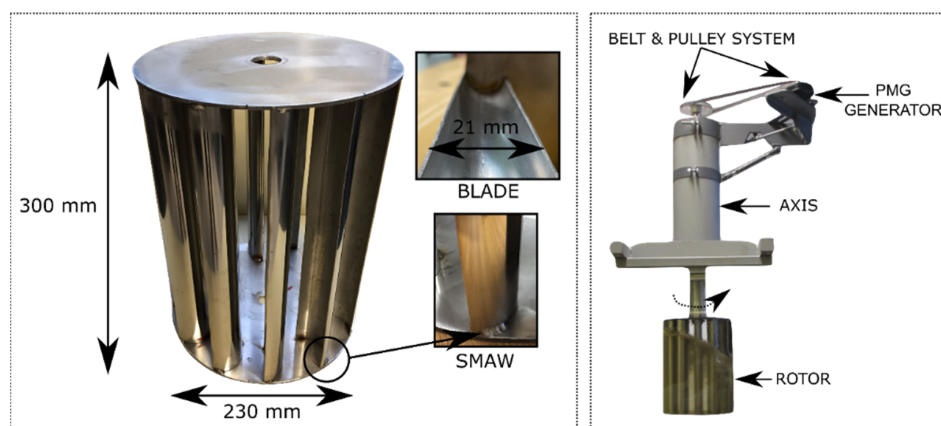


Figure 1. Turbine design.

The experimental tests were carried out in a hydrodynamic water tunnel (HWT) (Figure 2) made up of tanks (reassuring and recirculation), hydraulic pumps, adjustable frequency drive (AFD), glass channel (0.5 m height, 0.3 m width and 1.5 length) and a monitoring-control system. This system, called TURbine Test Laboratory Equipment, TURTLE, is made up of ultrasonic water height sensors, an electronic board and a PC, which together with specially designed software allow the test to be carried out and the data obtained to be collected.

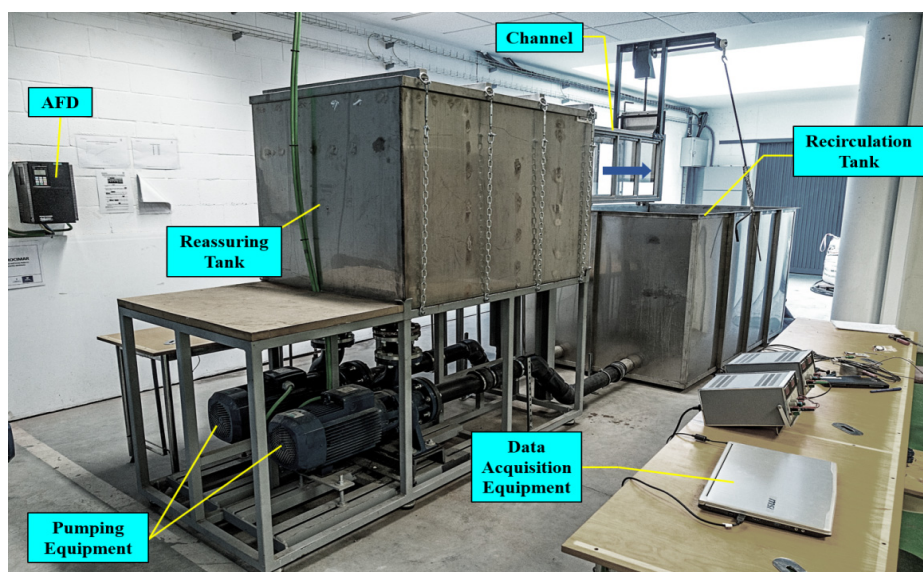


Figure 2. Hydrodynamic water tunnel.

The tests were carried out with two flow rates: $0.055 \text{ m}^3/\text{s}$ (Q_1) and $0.064 \text{ m}^3/\text{s}$ (Q_2). First, the channel was tested without modifying its geometry (scenario 1) (Figure 3), and then, the baffle was added (scenario 2) (Figure 4).

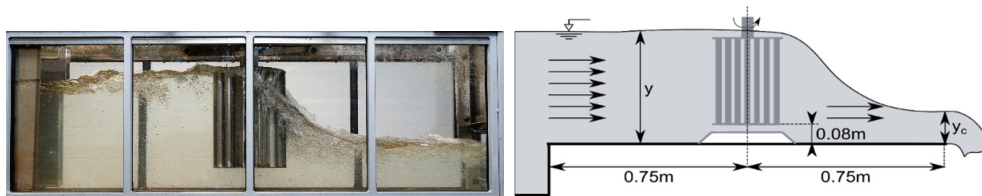


Figure 3. Scenario 1.



Figure 4. Scenario 2.

The main elements of the test are located upstream of the discharge channel where the critical flow conditions are reached. Table 1 shows the main values of the operating ranges.

Table 1. Operative ranges.

	Flow Rates (m^3/s)	Upstream Height (m)	Upstream Velocity (m/s)
Scenario 1	0.055	0.44	0.42
Scenario 2	0.064	0.49	0.44

3. Lab Results

The results obtained for the two flows in the two proposed scenarios are shown in Figures 5 and 6.

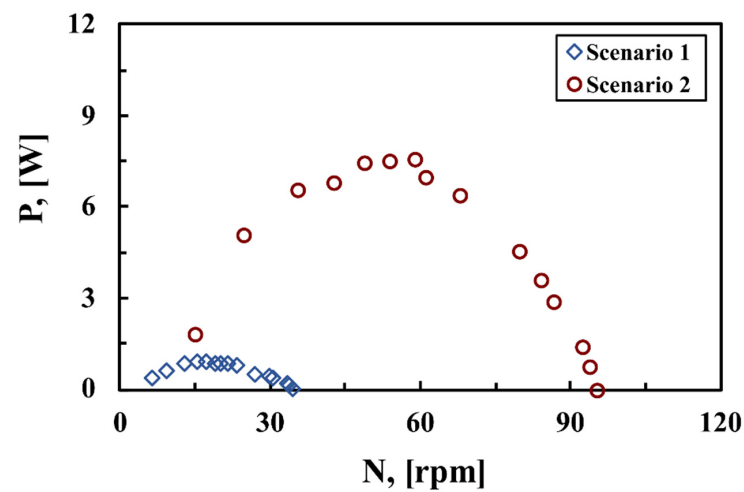


Figure 5. P vs. N comparison of scenarios 1 and 2 with Q_1 flow.

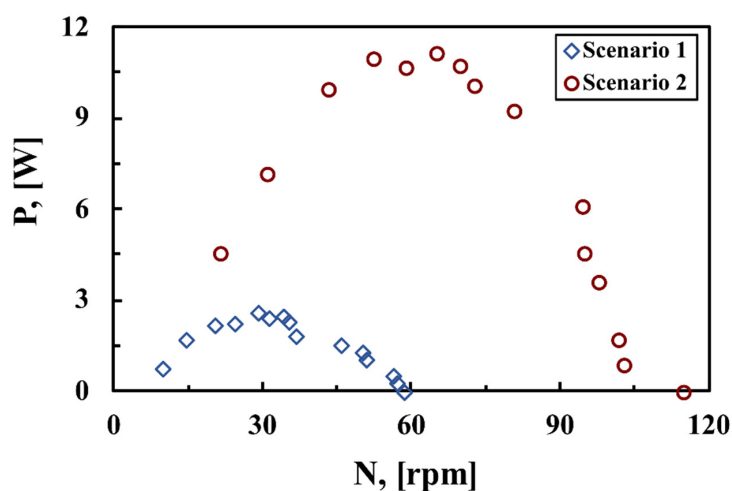


Figure 6. P vs. N comparison of scenarios 1 and 2 with Q_2 flow.

The tests carried out with the plate inclined at 22 degrees achieved the best results both in power increase and in the turbine speed range.

4. CFD Numerical Model

To build the numerical model, a complete three-dimensional geometry was generated incorporating the turbine, the stilling tank, the test flume, and the baffle. The geometric design has the actual dimensions of the hydrodynamic tunnel, including a rectangular prism-shaped area for the discharge of water from the channel (outlet) and two water inlet holes at the bottom of the reassuring tank. Furthermore, to ensure the correct functioning of the model, the upper part of the domain was completely exposed to air in order to replicate the free surface of water flow (Figure 7).

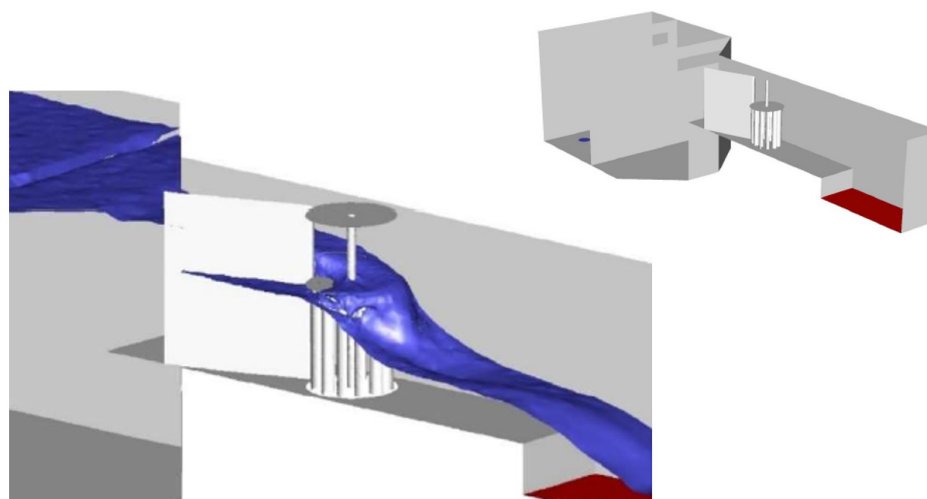


Figure 7. HWT geometry and free surface detail.

To obtain the numerical CFD model, a grid of cells was prepared where the flow equations were solved. To solve the rotation of the turbine, the geometry was divided into eight different volumes in which an unstructured mesh based on tetrahedrons was used to achieve a good adaptation to the complex areas, except in the water discharge area where a structured mesh based on rectangular prisms was used due to its simple cubic shape. A

cylindrical volume was incorporated that helped to simulate the movement of the turbine with a good degree of precision (Figure 8), as the unstructured mesh adapts perfectly to the turbine blades. The number of grid cells was set at 1,200,000 with satisfactory quality: 99.99% of the cells had an asymmetry value of less than 0.7. To study the dependence of the grid on the power results and its influence on the calculation time, four numbers of cells were evaluated: 200,000, 500,000, 800,000, 1,200,000, and 1,500,000 with the same flow rate and the range of rotational speeds that define the turbine power characteristics. With 1,200,000 cells, the ideal compromise between accuracy and calculation time was achieved.

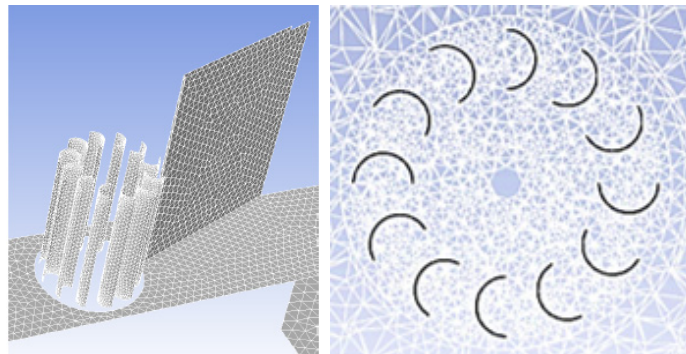


Figure 8. Meshing around the rotor.

The volume of fluid (VOF) model was selected to resolve the behavior of the free surface at its boundary between air and water (Figure 9). The model solved the unsteady Reynolds-average Navier–Stokes (URANS) for each cell included in the domain. The boundary conditions applied were mass flow at the water inlets, pressure outlet at the discharge, and the upper part of the model (tank and channel) with normal atmospheric pressure (101,325 Pa). The surfaces of the tank, the channel, and the turbine blades were defined as walls with a no-slip condition. Water and air densities and viscosities were set to constant values (water: 1.025 Kg/m^3 and $1.003 \times 10^{-3} \text{ Kg/m}\cdot\text{s}$; air: 1.225 Kg/m^3 and $1.789 \times 10^{-5} \text{ Kg/m}\cdot\text{s}$). To solve the URANS equations, the pressure-implicit solver algorithm with splitting of operators was used. In addition, second-order schemes were applied for the discretization of the spatial and temporal derivatives in the equations. The semi-implicit method for pressure-bound equations (SIMPLE) was used to solve the velocity–pressure coupling and turbulence was simulated using the shear stress transport (SST) $k\text{-}\omega$ turbulence model, suitable for complex flows. ANSYS FLUENT V18.0 software was used to perform the simulations of the numerical model [15].

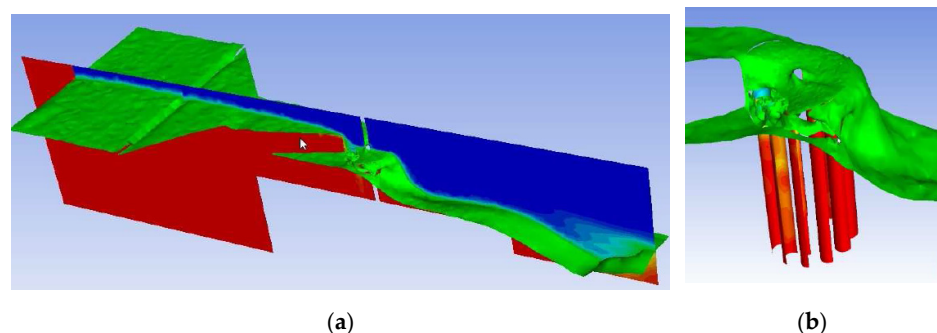


Figure 9. (a) Longitudinal section of the channel with the free surface; (b) detail of the free surface in the turbine.

5. Validation of the Numerical Model

The numerical model was validated with the experimental model (scenario 2) by comparing its degree of similarity between the results of the rotational speed (N) and power characteristics, and the positions of the free surfaces.

The experimental and numerical results of N (rpm) and power (W) for the two flow rates tested were analyzed for Q_1 (Figure 10) and Q_2 (Figure 11).

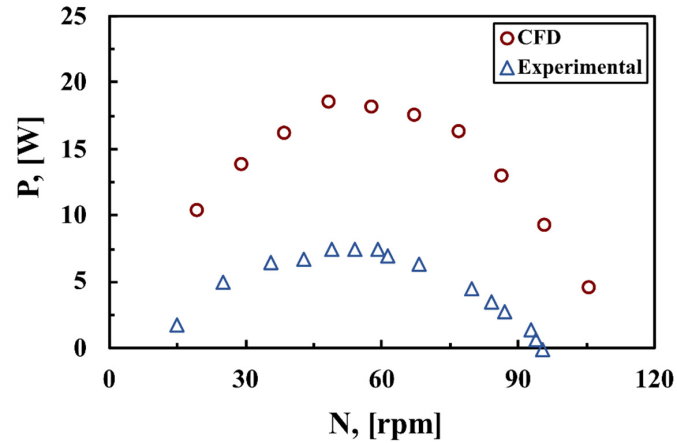


Figure 10. P vs. N comparison in scenario 2 and Q_1 .

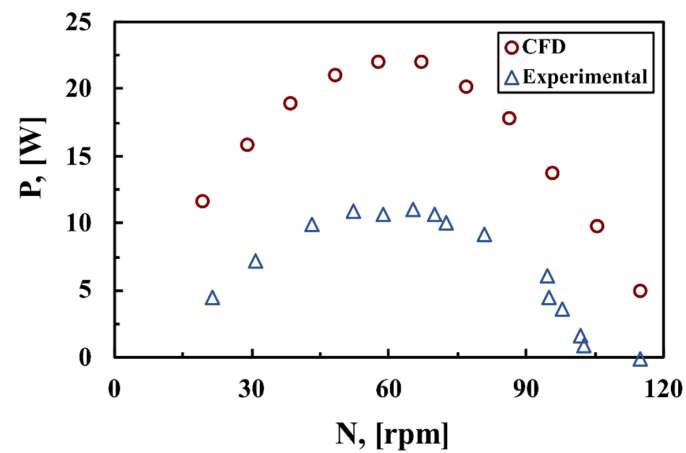


Figure 11. P vs. N comparison in scenario 2 and Q_2 .

In addition, the profiles of the free surface of the experimental and the numerical model were compared (Figure 12). The high similarity between both confirms the analytical results.

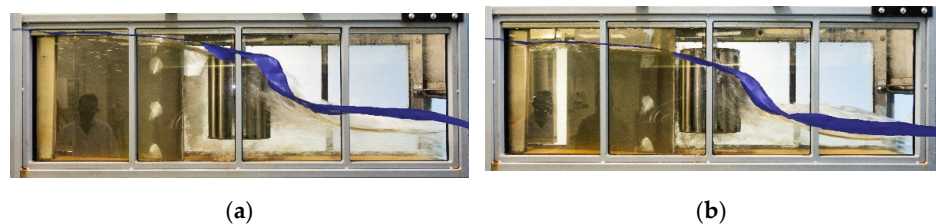


Figure 12. (a) Experimental vs. CFD for Q_1 ; (b) experimental vs. CFD for Q_2 .

6. Conclusions

Tests of a vertical axis hydrokinetic turbine were carried out in the hydrodynamic channel of the University of Oviedo under two scenarios: (a) with the original configuration of the channel; and (b) introducing a baffle plate oriented 22° towards the center of the turbine with respect to the channel wall.

The tests carried out with the baffle plate inclined at 22° achieved an increase in the results both in terms of power increase (greater than 250%) and in the speed range of the turbine. It was proven that simply inserting the plate increases the efficiency of the turbine considerably.

In addition, a CFD model was built and validated with the results of the experiment. Thanks to this, in future works, it is possible to deepen the study of how the forces work around the blades from the analysis of the speed and pressure field, as well as to carry out parametric studies on the ideal inclination of the baffle plate to optimize the installation.

Author Contributions: R.E.-V.: investigation, methodology, validation, formal analysis, and writing—original draft. V.M.F.-Á.: investigation, methodology, data curation, validation, and formal analysis. A.G.-Y.: investigation, methodology, and formal analysis. A.F.-J.: investigation, methodology, data curation, validation, and formal analysis. E.Á.-Á.: conceptualization ideas, writing—original draft, writing—review and editing, formal analysis, and supervision. All authors have read and agreed to the published version of the manuscript.

Funding: This research received no external funding.

Institutional Review Board Statement: Not applicable.

Informed Consent Statement: Not applicable.

Data Availability Statement: Not applicable.

Conflicts of Interest: The authors declare no conflict of interest.

References

1. Mohammadi, S.; Hassanalian, M.; Arionfard, H.; Bakhtiyarov, S. Optimal Design of Hydrokinetic Turbine for Low-Speed Water Flow in Golden Gate Strait. *Renew. Energy* **2020**, *150*, 147–155. [[CrossRef](#)]
2. Güney, M.S.; Kaygusuz, K. Hydrokinetic Energy Conversion Systems: A Technology Status Review. *Renew. Sustain. Energy Rev.* **2010**, *14*, 2996–3004. [[CrossRef](#)]
3. Kumar, D.; Sarkar, S. A Review on the Technology, Performance, Design Optimization, Reliability, Techno-Economics and Environmental Impacts of Hydrokinetic Energy Conversion Systems. *Renew. Sustain. Energy Rev.* **2016**, *58*, 796–813. [[CrossRef](#)]
4. IDAE Plan de Energías Renovables 2011–2020. Available online: https://www.idae.es/sites/default/files/documentos/publicaciones_idae/documentos_11227_per_2011-2020_def_93c624ab.pdf (accessed on 7 February 2022).
5. Syahputra, R.; Soesanti, I. Performance Improvement for Small-Scale Wind Turbine System Based on Maximum Power Point. *Energies* **2019**, *12*, 3938. [[CrossRef](#)]
6. Nicolaie, S.; Tudor, E.; Dumitru, C. Improving the Energy Conversion Efficiency for Hydrokinetic Turbines Using MPPT Controller. *Appl. Sci.* **2020**, *10*, 7560. [[CrossRef](#)]
7. Vogel, C.R.; Houlby, G.T.; Willden, R.H.J. Effect of Free Surface Deformation on the Extractable Power of a Finite Width Turbine Array. *Renew. Energy* **2016**, *88*, 317–324. [[CrossRef](#)]
8. Houlby, G.T.; Vogel, C.R. The Power Available to Tidal Turbines in an Open Channel Flow. *Proc. Inst. Civ. Eng.-Energy* **2016**, *170*, 12–21. [[CrossRef](#)]
9. Kolekar, N.; Vinod, A.; Banerjee, A. On Blockage Effects for a Tidal Turbine in Free Surface Proximity. *Energies* **2019**, *12*, 3325. [[CrossRef](#)]
10. Salleh, M.B.; Kamaruddin, N.M.; Mohamed-Kassim, Z. The Effects of Deflector Longitudinal Position and Height on the Power Performance of a Conventional Savonius Turbine. *Energy Convers. Manag.* **2020**, *226*, 113584. [[CrossRef](#)]
11. Mosbahi, M.; Lajnef, M.; Derbel, M.; Mosbahi, B.; Aricò, C.; Sinagra, M.; Driss, Z. Performance Improvement of a Drag Hydrokinetic Turbine. *Water* **2021**, *13*, 273. [[CrossRef](#)]
12. Sahim, K.; Ihtisan, K.; Santoso, D.; Sipahutar, R. Experimental Study of Darrieus-Savonius Water Turbine with Deflector: Effect of Deflector on the Performance. *Int. J. Rotating Mach.* **2014**, *2014*. [[CrossRef](#)]
13. Naiemi, A.H.; Yeganehfarzand, S. Nashtifan Windmills in Their Environmental Context, Khurasan, Iran. *Vernac. Archit.* **2019**, *50*, 57–77. [[CrossRef](#)]

14. Ramin Nashtifan Windmills. Available online: <http://historicaliran.blogspot.com/2012/03/nashtifan-windmills.html> (accessed on 17 February 2022).
15. Ansys. *ANSYS Fluent User's Guide*; 18.1; ANSYS: Canonsburg, PA, USA, 2018; Available online: <http://users.abo.fi/rzevenho/ansys%20fluent%2018%20tutorial%20guide.pdf> (accessed on 10 February 2022).

C.1.3 Design and Experimental Performance Characterization of a Three-blade Horizontal-axis Hydrokinetic Water Turbine in a Low Velocity Channel



Proceeding Paper

Design and Experimental Performance Characterization of a Three-Blade Horizontal-Axis Hydrokinetic Water Turbine in a Low-Velocity Channel [†]

Roberta Ferraiuolo ^{1,*} , Ahmed Gharib-Yosry ² , Aitor Fernández-Jiménez ³, Rodolfo Espina-Valdés ³ , Eduardo Álvarez-Álvarez ⁴ , Giuseppe Del Giudice ¹ and Maurizio Giugni ¹

¹ Department of Civil, Architectural and Environmental Engineering, University of Naples Federico II, 80125 Naples, Italy

² Mechanical Power Department, Faculty of Engineering, Port Said University, Port-Said 42526, Egypt

³ GIFD Group—EP Mieres, University of Oviedo, 33600 Mieres, Spain

⁴ Energy Department, University of Oviedo, Wifredo Ricart s/n, 33204 Gijón, Spain

* Correspondence: roberta.ferraiuolo@unina.it

[†] Presented at the International Conference EWaS5, Naples, Italy, 12–15 July 2022.

Abstract: The present work describes the design process of a 3D-printed prototype of a three-blade horizontal-axis hydrokinetic water turbine (HAHWT). The employed blade profile is an EPLER818, which was previously studied through the Q-Blade software according to the velocity range presumed ($v < 1$ m/s) in the experiments. The prototype performance was studied in a recirculating water channel at the Polytechnic Engineering School of Mieres (Oviedo University), with a gate of variable height at the channel end, which allows for performing different hydrodynamic scenarios upon varying the considered flow rate. The results show that the extracted power increases due to the equally increased blockage ratio, which represents the ratio between the turbine area and the channel area. However, an excessive increase in the blockage ratio corresponds to a power reduction effect due to the reduction in the effective area and the generation of a two-phase air-water condition.

Keywords: HAHWT; 3D printing; blockage ratio; turbine performance



Citation: Ferraiuolo, R.; Gharib-Yosry, A.; Fernández-Jiménez, A.; Espina-Valdés, R.; Álvarez-Álvarez, E.; Del Giudice, G.; Giugni, M. Design and Experimental Performance Characterization of a Three-Blade Horizontal-Axis Hydrokinetic Water Turbine in a Low-Velocity Channel. *Environ. Sci. Proc.* **2022**, *21*, 62. <https://doi.org/10.3390/environsciproc2022021062>

Academic Editors: Vasilis Kanakoudis, Evangelos Keramaris and Francesco De Paola

Published: 1 November 2022

Publisher's Note: MDPI stays neutral with regard to jurisdictional claims in published maps and institutional affiliations.



Copyright: © 2022 by the authors. Licensee MDPI, Basel, Switzerland. This article is an open access article distributed under the terms and conditions of the Creative Commons Attribution (CC BY) license (<https://creativecommons.org/licenses/by/4.0/>).

1. Introduction

Traditional hydroelectric plants are vastly used worldwide to provide electricity to densely populated areas. In 2020, global net hydropower additions reached 21 GW (+40% from 2019), reversing the five-year trend of growth decline. Almost 60% of the new capacity was commissioned through several large-scale projects in China, the country that has led global hydropower growth since 1996 [1]. Furthermore, the impacts of the COVID-19 outbreak and the actual energy crises triggered by the current conflict between Russia and Ukraine have demonstrated the resilience of renewable sources and their fundamental role in the future of ecological transition. In such a context, the global electricity demand is expected to grow by approximately 5% in 2021 and 4% in 2022, driven by global economic recovery [2]. This is why, currently, several researchers are investigating micro-hydrokinetic turbines to perform an alternative for renewable energy production, especially at locations where conventional hydropower cannot provide a feasible solution [3–8]. Hydrokinetic turbines are devices that transform the kinetic energy of water flow into mechanical energy in a shaft and, finally, into electrical energy in a generator. These kinds of turbines usually are classified into horizontal and vertical axes according to the mutual position of the rotation axis and flow direction. Namely, in the horizontal one, the axis of rotation is parallel to the flow direction, whereas, in the vertical one, the axis is orthogonal to the flow direction [9,10]. The design of axial flow micro-turbines is similar to the wind flow and tidal turbines; specifically, these kinds of rotors are more efficient than drag devices with a

vertical axis because they harness energy from the lift force, for this reason, they are defined as lifting devices [11].

1.1. Rotor Performance

Lift and drag are the components of the force perpendicular and parallel to the direction of relative water speed, respectively. In order to quantify the entity of lift and drag force, it is useful to take into account two important coefficients: C_L and C_D , which can be defined as:

$$C_L = \frac{L}{1/2\rho V_\infty^2 c} \quad (1)$$

$$C_D = \frac{D}{1/2\rho V_\infty^2 c} \quad (2)$$

where ρ is the water density $\cong 1000 \text{ kg/m}^3$ and c is the airfoil length, often denoted by the chord, which can be defined as the line that connects the leading edge with the trailing edge of the airfoil. The unit for the lift and the drag in Equations (1) and (2) is a force per length N/m. To offer a complete description of the forces, it is also necessary to define the moment M regarding a point in the airfoil. This point is conventionally located on the chord line at $c/4$ from the leading edge, and it is assumed that, in this specific point, the resultant of the aerodynamic forces are applied. The C_L and C_D are functions of α and Reynolds number. α is the angle of attack defined as the angle between the chord line and the velocity of the oncoming flow. The Reynolds number is proportional to the ratio between inertia and viscous forces. It is responsible for the boundary layer transition from laminar to turbulent flow, provoking the airfoil stall condition, which completely depends on geometry [12–14]. In the case of an airfoil, the Reynolds number is usually defined as:

$$Re = \frac{cV_\infty}{\nu} \quad (3)$$

where ν is the kinematic viscosity, which for water at 20 °C is approximately equal to $\cong 1.00 \times 10^{-6} \text{ m}^2/\text{s}$; c is the chord, and V_∞ is the relative velocity. For a given airfoil, the behaviors of C_L and C_D are computed and plotted in so-called polars: C_L, α ; C_D, α , and $C_L/C_D, \alpha$; the latter represents profile's performance according to the variation of the angle of attack. Q-Blade is open-source software that allows us to understand the performance of wind/water turbines and the blade design. It is also useful for plotting the airfoil polar according to the Reynolds number variation that each blade section has. For the specific case presented, the Reynolds number varies in the range of $1.00 \times 10^{-4} \div 1.00 \times 10^{-5}$. As visible from Figure 1, the best angle that maximizes the efficiency of the overall profile is equal to 6°.

Another important concept is the available energy P_{max} that is obtained if, theoretically, the water speed could be reduced to zero, as in Equation (4):

$$P_{max} = \frac{1}{2}\dot{m}V_0^2 = \frac{1}{2}\rho AV_0^3 \quad (4)$$

where \dot{m} is the mass flow, V_0 is the water speed, ρ is the water density, and A is the area where the water speed was reduced. The equation for the maximum available power is very important since it shows that power increases with the cube of the water speed and only linearly with density and area. To evaluate the power production performance of the system, the non-dimensional power coefficient is defined as:

$$C_p = \frac{P}{\frac{1}{2}\rho V^3 A} \quad (5)$$

where P is the output mechanical power, V is the current velocity m/s upstream to the turbine, A is the reference surface (the turbine area), and ρ is the water density. The power

coefficient is the ratio between the power produced by the rotor in Watts and the power produced from the fluid flow. The power coefficient is usually reported as a function of the Tip Speed Ratio (TSR), another non-dimensional quantity representing the speed at the blade tip normalized to the upstream flow velocity.

$$TSR = \frac{\omega R}{V} \quad (6)$$

where R is the turbine radius and ω is the rotational speed. Each turbine generates a force perpendicular to the rotor plane, e.g., the thrust, which can be non-dimensionalized as:

$$C_T = \frac{T}{\frac{1}{2}\rho V^3 A} \quad (7)$$

where T is the trust acting on the rotor. Once the relation of mechanical power and the thrust coefficient with TSR is found, the turbine hydrodynamic performance is known.

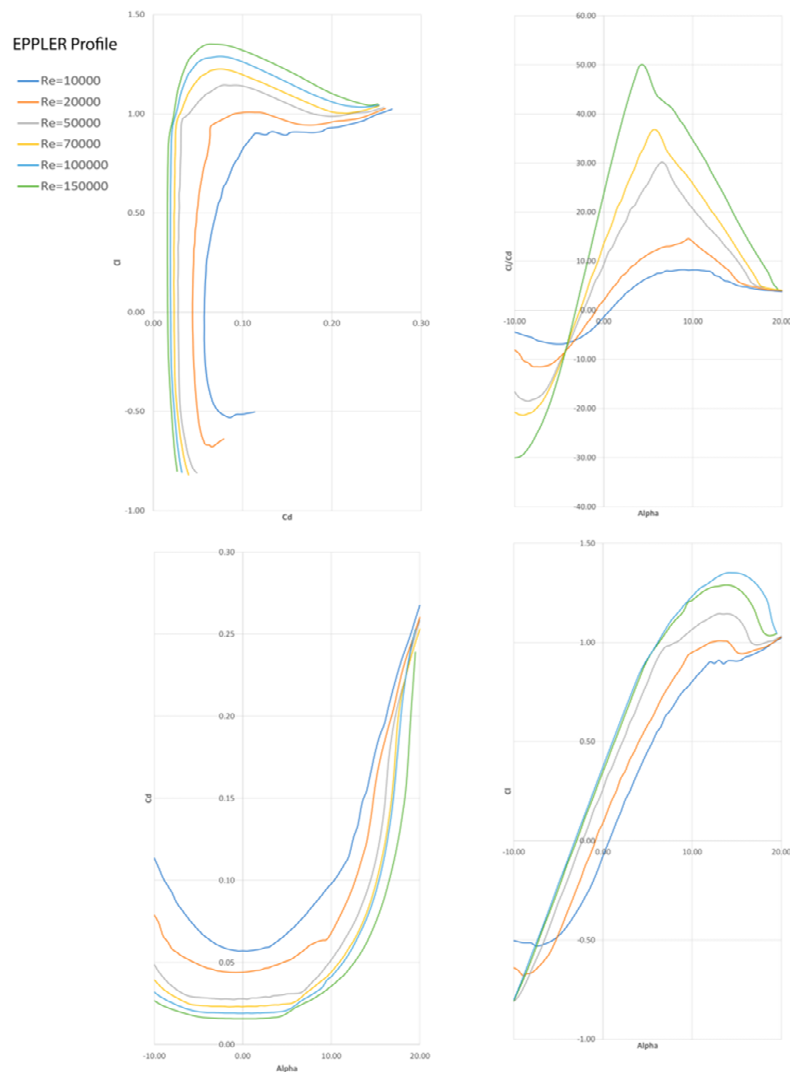


Figure 1. Polar of the EPPLER profile extracted from Q-Blade.

1.2. Blade Design

The airfoil profile chosen for the present study was an EPPLER818, as shown in Figure 2.

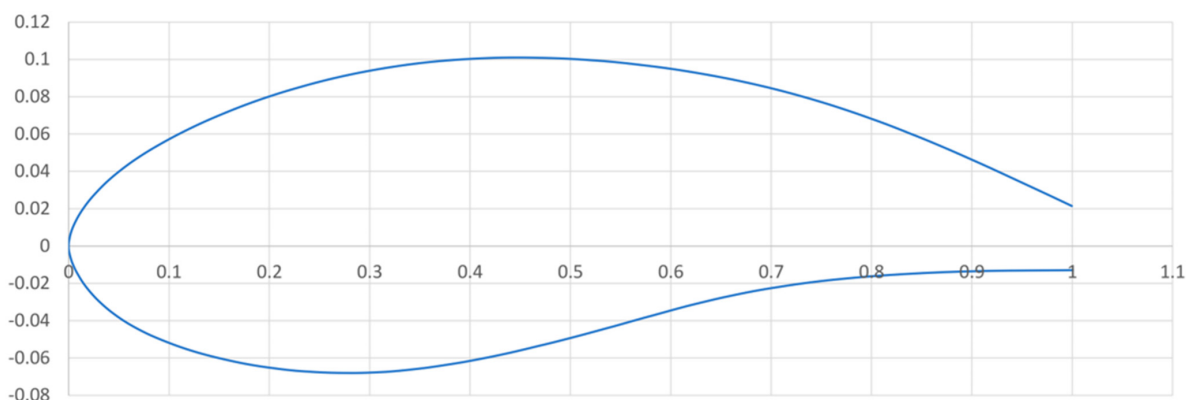


Figure 2. Chosen airfoil profile.

The first necessary assumptions to define the blade design are the definition of a velocity range, the blade radius, and the number of blades. The velocity range must be compatible with the experimental limitation regarding acceptable velocity in the water channel in which the turbine was tested. Furthermore, for this study, the representative chord was assumed to be equal to $R/4$, corresponding to a fixed value of solidity of 0.10 at 75% of the blade span. Solidity is the ratio between the overall area of the blades and the swept area of the turbine (function of rotor radius) and the number of blades, chosen equal to $N = 3$, and it is often identified by the Greek letter σ :

$$\sigma = \frac{cN}{2\pi R} \quad (8)$$

To design the blade, it is common practice to divide it into different sections along the blade span and, for each one, the size of the chord and twist angle are defined. The twist angle is between the zero-lift angle and the zero-lift angle of the root airfoil. The methodology applied for designing the present blade has the objective of optimizing the profile to have a quite linear distribution of the chord from the root to the tip of the blade, keeping in mind the hub size. The turbine's hub is the component that connects the blades to the main shaft and ultimately to the rest of the drive train. The geometrical characteristics of the studied turbine are summarized in Table 1 below:

Table 1. Turbine geometry characteristics.

Velocity Range (m/s)	Blade Radius (m)	Chord $R/4$ (m)	Hub Radius (m)	Number of Blades (-)
0.43 ÷ 0.68	0.084	0.03	0.025	3

It is worth noting that fixing a range of possible TSR (Equation (6)), which in this specific case are considered to vary in the range from 2 to 8, and knowing both the velocity range and the turbine radius, it is easy to obtain the angular velocity ω rad/s. Furthermore, the relative velocity that each section has along the blade span is the vectorial composition of an axial velocity (strictly dependent on the inlet velocity) and the rotational velocity component, which depends on the angular velocity and the distance from the blade root (r/R), is at its maximum value at the blade tip. To impose that each section of the blade span have the same angle, an assumption that maximizes the efficiency of the profile,

approximately being equal to 6° , it is possible to obtain the distribution of twist by the tangent of the angle of inflow ϕ . Moreover, the tangent of the angle of inflow is the ratio between the axial and rotational velocity components. Therefore, the twist angle is the difference between the inflow attack angle. Table 2 summarizes the twist and chord angle distribution, chosen for the blade design.

Table 2. Blade discretization with chord and twist angle assumed.

Number of Section	Local Solidity $\sigma = cN/2\pi R$	r/R	Chord (m)	Twist ($^\circ$)
1	0.1400	0.0000	0.03000	45.7500
2	0.1200	0.0080	0.02900	41.2500
3	0.1200	0.0168	0.02800	36.2175
4	0.1100	0.0252	0.02700	30.2750
5	0.1100	0.0336	0.02600	23.9550
6	0.1100	0.0420	0.02500	18.5950
7	0.1000	0.0504	0.02375	14.7925
8	0.1000	0.0588	0.02200	11.9775
9	0.0900	0.0670	0.02100	9.0000
10	0.0800	0.0755	0.01950	8.5000
11	0.0800	0.0840	0.01800	8.0000

2. Rotor Design and Experimental Set-Up

The whole prototype was drawn in the SOLIDWORKS 2019 software with the purpose of realizing a flexible prototype able to be modified potentially, creating a special squared lock system for the blade into the hub. The adaptation draws inspiration from similar research [15] with a different scope, which is equally applicable to the present study. Figure 3a shows the geometric characteristic of the studied joint, which was graphically realized by a revolution solid that follows the airfoil. The total dimension of the rotor is the sum of the blade radius of 0.084 m, the hub radius 0.025 m, and the height of the joint of 0.009 m, making the turbine radius equal to 0.118 m. A sort of pillar with a squared ending acts as a joint between the extremities of the two plates. The designed turbine was printed with a 3D printer in polylactic acid, also known as PLA, and was composed of six pieces attached to each other by three M3 screws. Figure 3b is the CAD project showing each rotor part in detail.

The HAHWT was tested under low water velocity conditions in a recirculating water channel of 0.30 m in width, 0.5 m in height and 3.5 m in length with a transparent glass wall located at the Polytechnic Engineering School of Mieres (Oviedo University in Spain). As shown in Figure 4, water recirculation was provided by two centrifugal pumps (1) of 15 KW each, with a nominal flow rate of 300 m³/h, controlled by two inverters. The water flows through the channel and falls in the recirculating tank downstream (2), where a variable height gate (3) allows for performing different operating conditions, varying the velocity from 0.14 to 0.9 m/s at the maximum flow rate. The turbine was inserted into a wooden box (4) with transparent walls and a cutting steel foil in the middle, allowing the horizontal axis rotation. On the top of the box, there was a high precision torque and rotational speed meter (5) Magtrol TS103 (0.5 Nm of rated torque, accuracy < 0.1% and 1.5 rpm max. speed, accuracy < 0.015%) with an electrical brake (6) Magtrol HB-140M-2 controlled by DC (7). Moreover, a vertical axis connected to the horizontal one through a bevel gear allows transmitting the rotation to the torque meter and, due to the software provided by the manufacturer TORQUE V10, recording the mechanical parameters (torque, rotation speed, angle, mechanical power, and test time) necessary for the characterization of the curves along the power stage. Due to the fluctuation of the water surface, the height of water was measured upstream of the turbine at the x-coordinate of 0.54 m from the beginning of the channel and downstream of the turbine at the x-coordinate of 0.65 m.

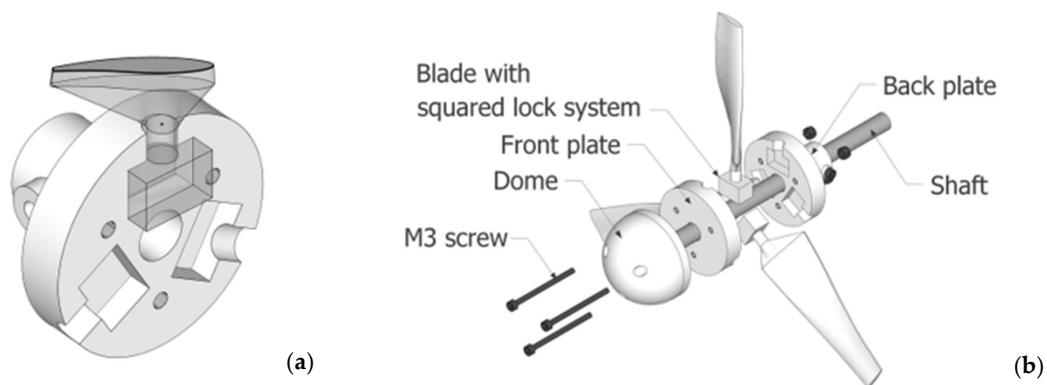


Figure 3. The designed squared lock system (a). The turbine axonometric projection (b).

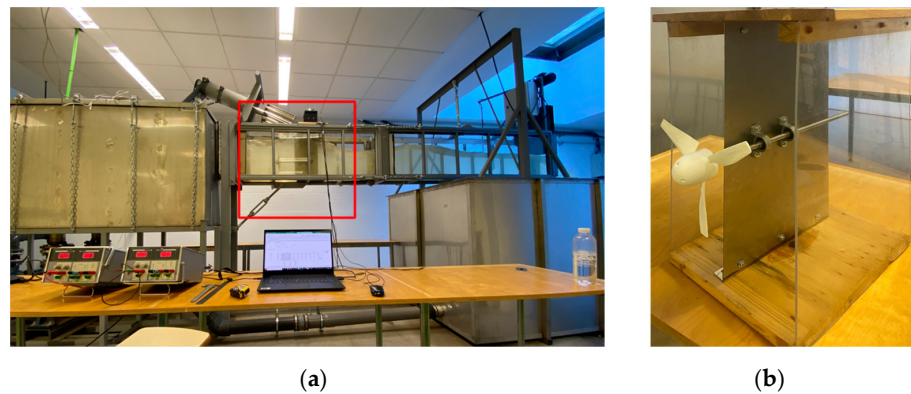


Figure 4. Experimental set-up (a). Wooden box where the Turbine is located (b).

2.1. Methodology

The experimental tests were organized considering three different values of flow rates, knowing the calibration law that links the frequency engine of the pump system and the corresponding flow rate. The three values of flow rates considered were $Q_1 = 0.052 \text{ m}^3/\text{s}$ (23 Hz), $Q_2 = 0.059 \text{ m}^3/\text{s}$ (27 Hz), and $Q_3 = 0.065 \text{ m}^3/\text{s}$ (31 Hz), respectively; for each one, 5 different downstream heights of the gate were tested, starting from the nearly closed to the nearly open condition. In this regard, 5 velocity points were analyzed, starting from the minimum to the maximum possible velocity (critical flow condition at which the channel outlet is achieved), to assess the turbine behavior in the same velocity points, increasing the flow rate value. Furthermore, due to the fluctuation of the free surface, the measurement of the water height upstream H_1 and downstream H_2 of the rotor allows calculating of the correspondent average velocity, $v = Q/(b \times h_1)$, at the cross-section. Due to the presence of HAHWT, which harnesses the kinetic part of the energy contained in the water flow, the velocity upstream of the rotor slows down, producing an increase in pressure gradient at the turbine inlet, whereas, at the outlet, a rising in velocity and turbulence corresponds to a decreasing in pressure gradient. In that regard, the blockage ratio, namely the ratio between the turbine area (A_t) and the channel area (A_c) $B = A_t/A_c$, tends to increase the power produced due to the reduction in water height caused by the consequent raising in the height gate and inflow velocity. This blockage ratio produces an effect on the power extracted through the turbine, better explained in the Results section. The methodology was applied to obtain the curve along the power stage, starting from the so-called “zero loads” condition, where no braking torque is applied to the turbine, i.e., the voltage of the electric brake is equal to 0 V. Under this condition, the power extracted is zero, but the rotation velocity is equal to the maximum value (n_{max}). Successively, the turbine is

gradually loaded, increasing the voltage by 0.5 V step up to the value of resistive torque able to arrest the turbine, immediately. This point coincides with the maximum power point (MPP) as in Equation (4), which corresponds to the minimum value of rotational velocity (n_{\min}). Table 3 summarizes the experimental tests conducted in this paper.

Table 3. Experimental tests.

Test 1 $Q_1 = 0.052 \text{ m}^3/\text{s}$					
H gate (m)	0.12	0.13	0.14	0.15	0.16
H1 upstream (x 0.54 m)	0.40	0.38	0.37	0.28	0.27
V1 upstream (m/s)	0.43	0.45	0.47	0.62	0.64
$B = At/A_c$	0.36	0.38	0.39	0.52	0.54
Test 2 $Q_2 = 0.059 \text{ m}^3/\text{s}$					
H gate (m)	0.15	0.16	0.17	0.18	0.19
H1 upstream (x 0.54 m)	0.45	0.42	0.39	0.31	0.30
V1 upstream (m/s)	0.43	0.47	0.50	0.63	0.65
$B = At/A_c$	0.36	0.35	0.37	0.47	0.49
Test 3 $Q_3 = 0.065 \text{ m}^3/\text{s}$					
H gate (m)	0.16	0.17	0.18	0.19	0.20
H1 upstream (x 0.54 m)	0.50	0.44	0.43	0.33	0.32
V1 upstream (m/s)	0.44	0.50	0.51	0.66	0.68
$B = At/A_c$	0.29	0.33	0.34	0.44	0.46

2.2. Results and Conclusions

For each upstream velocity V_1 , the maximum rotational speed corresponds to the zero-load condition (0V in the brake). On the other hand, with the increase in the turbine load, the rotational speed decreases, which also produces an increase in the angle between the flow and the blades so that an increase in power and in the lift is produced up to a certain value, after which the airfoil reaches the stall condition and the drag forces increase more rapidly than the lift one. This phenomenon produces a decrease in power and rotational speed up to the complete turbine arresting. Therefore, the experimental points are located in the unstable part of the curve (on the left side), which is not visible in Figure 5 because they are beyond the recording experimental data point. The comparison between Test 1 and 3 shown in the P-n charts (a) and (b) of Figure 5 reveals how the power output variation increases with the upstream flow velocity and blockage ratio. However, it is evident how, in correspondence with the highest value of blockage ratio produced in the channel, 0.46 in Test 1 and 0.54 in Test 3, it determines a decrease in power extracted. Moreover, Figure 5 (c) and (d) show the start with the lowest flow rate Q_1 , which corresponds to an upstream velocity equal to 0.62 m/s and a C_p maximum equal to 0.52 for a TSR of 5.16; this coincides with the fully filled channel condition where the blockage ratio (At/A_c) is minimal, $B = 0.52$. The peak of the power coefficient reaches its maximum value of 0.62 at a TSR of 5.91 with a corresponding velocity of 0.63 m/s and $B = 0.47$ in the Q_2 flow rate condition. On the contrary, with the Q_3 and an upstream velocity of 0.66 m/s, it produces a reduction in C_p , equal to 0.56 because, in this case, the channel gate is fully opened with a critical outlet flow condition. Therefore, the blockage ratio positively affects the turbine performance, because it compresses the flow and produces an increase in the power coefficient. Still, it could also determine a decrease in C_p due to the interference between water and air when the gate is nearly open. What happens is that the water level on the upstream side is nearly at the same elevation as the turbine, and, due to the surface drop on the downstream side, the backside of the rotor is exposed to the air. The drop in the power coefficient depends on two factors: the turbine is not completely covered with water, reducing the effective area, and the partial flow separation occurs as the air enters the suction side of the blade, as reported by [16]. A future objective of the present study is to validate the experimental results with a Computational Fluid Dynamics (CFD) model in order to

investigate air–water interferences with the Volume of Fluid (VOF) model, which could better interpret the water–air interference and the flow around the HAWT [17,18].

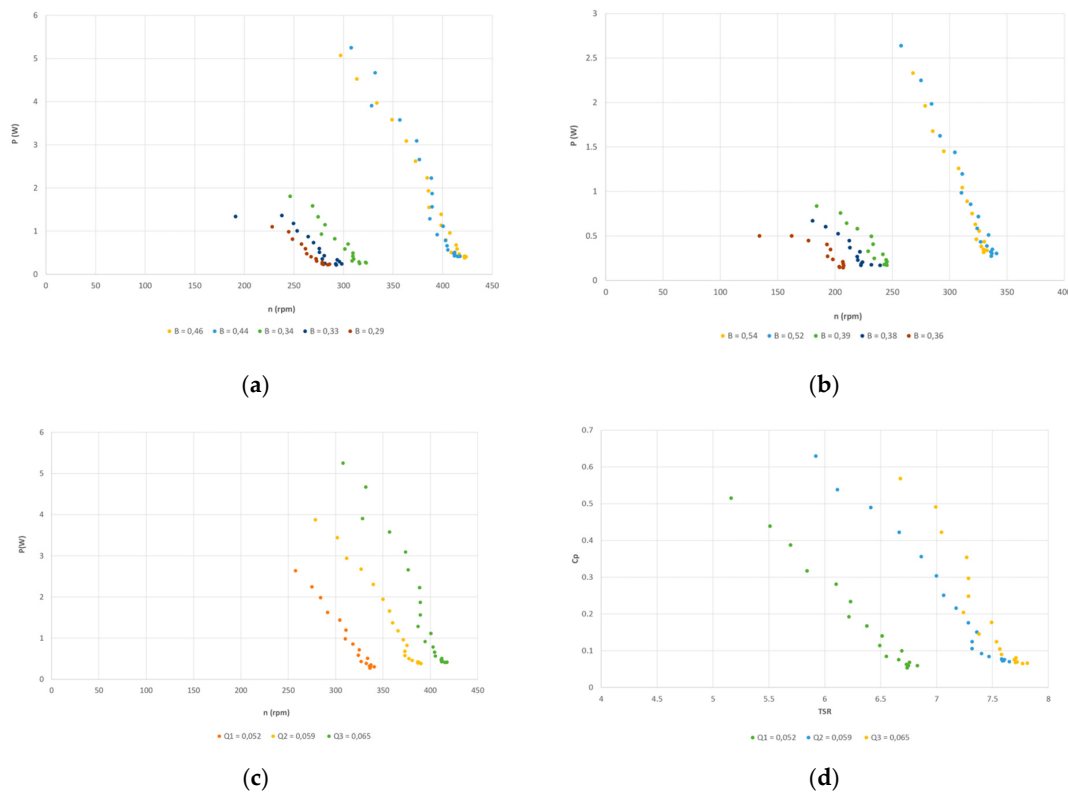


Figure 5. P-n Q_1 (a). P-n Q_3 (b). P-n comparison (c). C_p -TSR comparison (d).

Author Contributions: R.F.: Investigation, Methodology, Validation, Formal analysis, and Writing—original draft. A.G.-Y.: Methodology, Validation, and Formal analysis. A.F.-J.: Investigation and Methodology. E.Á.-Á.: Conceptualization, Writing—review and editing, Formal analysis, and Supervision. R.E.-V.: Methodology. G.D.G.: Formal analysis and Supervision. M.G.: Supervision. All authors have read and agreed to the published version of the manuscript.

Funding: This research received no external funding.

Institutional Review Board Statement: Not applicable.

Informed Consent Statement: Not applicable.

Data Availability Statement: Not applicable.

Conflicts of Interest: The authors declare no conflict of interest.

References

1. IEA. *Renewables 2019—Analysis-IEA*; International Energy Agency: Paris, France, 2019.
2. IEA. *Electricity Market Report-July 2021*; International Energy Agency: Paris, France, 2021.
3. Elbatran, A.H.; Yaakob, O.B.; Ahmed, Y.M.; Shabara, H.M. Operation, performance and economic analysis of low head micro-hydropower turbines for rural and remote areas: A review. *Renew. Sustain. Energy Rev.* **2015**, *43*, 40–50. [[CrossRef](#)]
4. dos Santos, I.F.S.; Camacho, R.G.R.; Tiago Filho, G.L.; Botan, A.C.B.; Vinent, B.A. Energy potential and economic analysis of hydrokinetic turbines implementation in rivers: An approach using numerical predictions (CFD) and experimental data. *Renew. Energy* **2019**, *143*, 648–662. [[CrossRef](#)]
5. Lago, L.I.; Ponta, F.L.; Chen, L. Advances and trends in hydrokinetic turbine systems. *Energy Sustain. Dev.* **2010**, *14*, 287–296. [[CrossRef](#)]

6. Loots, I.; Van Dijk, M.; Barta, B.; Van Vuuren, S.J.; Bhagwan, J.N. A review of low head hydropower technologies and applications in a South African context. *Renew. Sustain. Energy Rev.* **2015**, *50*, 1254–1268. [[CrossRef](#)]
7. Tian, W.; Mao, Z.; Ding, H. Design, test and numerical simulation of a low-speed horizontal axis hydrokinetic turbine. *Int. J. Nav. Archit. Ocean Eng.* **2018**, *10*, 782–793. [[CrossRef](#)]
8. Gasnier, P.; Saoutieff, E.; Soriano, O.; Alessandri, B.; Ojer-Aranguren, J.; Boisseau, S. Cm-scale axial flow water turbines for autonomous flowmeters: An experimental study. *Smart Mater. Struct.* **2018**, *27*, 115035. [[CrossRef](#)]
9. Khan, M.J.; Bhuyan, G.; Iqbal, M.T.; Quaioco, J.E. Hydrokinetic energy conversion systems and assessment of horizontal and vertical axis turbines for river and tidal applications: A technology status review. *Appl. Energy* **2009**, *86*, 1823–1835. [[CrossRef](#)]
10. Cardona-Mancilla, C.; Del Río, J.S.; Chica-Arrieta, E.; Hincapié-Zuluaga, D. Horizontal axis hydrokinetic turbines: A literature review. *Tecnol. Ciencias Agua* **2018**, *9*, 180–197. [[CrossRef](#)]
11. Castelli, M.R.; Benini, E. Comparison between Lift and Drag-Driven VAWT Concepts on Low-Wind Site AEO. *Int. J. Environ. Ecol. Eng.* **2011**, *5*, 1677–1682. [[CrossRef](#)]
12. Barbarić, M.; Guzović, Z. Investigation of the possibilities to improve hydrodynamic performances of micro-hydrokinetic turbines. *Energies* **2020**, *13*, 4560. [[CrossRef](#)]
13. Kolekar, N.; Banerjee, A. Performance characterization and placement of a marine hydrokinetic turbine in a tidal channel under boundary proximity and blockage effects. *Appl. Energy* **2015**, *148*, 121–133. [[CrossRef](#)]
14. Grasso, F.; Coiro, D.; Bizzarrini, N.; Calise, G. Design of advanced airfoil for stall-regulated wind turbines. *Wind Energy Sci.* **2017**, *2*, 403–413. [[CrossRef](#)]
15. Bahaj, A.S.; Molland, A.F.; Chaplin, J.R.; Batten, W.M.J. Power and thrust measurements of marine current turbines under various hydrodynamic flow conditions in a cavitation tunnel and a towing tank. *Renew. Energy* **2007**, *32*, 407–426. [[CrossRef](#)]
16. Birjandi, A.H.; Bibeau, E.L.; Chatoorgoon, V.; Kumar, A. Power measurement of hydrokinetic turbines with free-surface and blockage effect. *Ocean Eng.* **2013**, *69*, 9–17. [[CrossRef](#)]
17. Benavides-Morán, A.; Rodríguez-Jaime, L.; Laín, S. Numerical Investigation of the Performance, Hydrodynamics, and Free-Surface Effects in Unsteady Flow of a Horizontal Axis Hydrokinetic Turbine. *Processes* **2022**, *10*, 69. [[CrossRef](#)]
18. Gharib Yosry, A.; Fernández-Jiménez, A.; Álvarez-Álvarez, E.; Blanco Marigorta, E. Design and characterization of a vertical-axis micro tidal turbine for low velocity scenarios. *Energy Convers. Manag.* **2021**, *237*, 114144. [[CrossRef](#)]

C.2 Conference publications

C.2.1 An Approximation of Using Vertical-axis Tidal Turbine for Water Desalination in the SUEZ Canal Waterway

Proceedings of the ASME 2022 16th International
Conference on Energy Sustainability
ES2022
July 11-13, , Philadelphia, PA, USA

ES2022-85533

**AN APPROXIMATION OF USING VERTICAL-AXIS TIDAL TURBINE FOR WATER
DESALINATION IN THE SUEZ CANAL WATERWAY**

Ahmed Gharib-Yosry*

Dept. of Mechanical Power Engineering
Port Said University
Port-Said 42526
Egypt
Email: ahmed.gharib@eng.psu.edu.eg

Rodolfo Espina Valdes

Dept. of Energy Engineering
University of Oviedo
Mieres 33600
Spain
Email: espinarodolfo@uniovi.es

Eduardo Blanco-Marigorta

Dept. of Energy Engineering
University of Oviedo
Gijón 33204
Spain
Email: eblanco@uniovi.es

Eduardo Alvarez-Alvarez

Dept. of Energy Engineering
University of Oviedo
Mieres 33600
Spain
Email: edualvarez@uniovi.es

ABSTRACT

Many countries are suffering from water shortage, especially Egypt, which is considered one of the limited regions in fresh-water resources. Desalination has been proven a feasible and promising technology for supplying potable water. However, the main challenge inhibiting the wider use of desalination technologies is the high economic cost especially due to the energy consumption. The main goal of this research is to provide an approach on the possibility of using vertical-axis turbines to harness the periodical tidal current and the hydrokinetic flow from ships and vessels, which run continuously in the Suez Canal waterway, for a desalination process. The turbine rotor type and the design parameters have been selected carefully looking for self-starting and best performance under low flow velocities with independency of the flow direction. Experimentally, the model has been fabricated using additive manufacturing process, and tested in a water flume under different upstream flow velocities. Power curves have been obtained for each operating condition.

Additionally, the non-dimensional tip speed ratio and power coefficient curve have been characterized. Numerically, an intensive three-dimensional simulation has been carried out in order to obtain a better understanding of the complex hydrodynamic flow phenomena around the turbine rotor.

Keywords: Hydrokinetic Turbine, Desalination, Tidal Turbine, CFD, Water Channel.

NOMENCLATURE

A Turbine cross-sectional area, m².
C Blade chord length, m.
C_{pr} Pressure coefficient.
D Turbine diameter, m.
d_s Shaft diameter, m.
H Blade height, m.
N Rotational speed, rpm.
P Power output, W.
λ Tip speed ratio.

*Address all correspondence to this author.

INTRODUCTION

The desalination of seawater is a key element in the solution of the water demand for many regions in the world. In 2005, there were approximately 8,000 desalination plants with total capacity of 30 million m^3/day [1]. Thanks to the continuous research and development in this sector, nowadays these numbers have risen to almost 16,000 plants with total capacity of 96 million m^3/day . However, only 130 desalination plants are operated by sources of renewable energy, which represents less than 1% of the total desalination capacity [2], while the majority are powered by fossil fuels [3].

Generally, there are two main desalination methods, the first one is based on thermal conversion process, while the other one -which we are interested in- is based on the membrane process and specifically that works with reverse osmosis (RO) technique [4]. The main challenge inhibiting the wider use of this desalination technologies is the high economic cost especially due to the energy consumption. Many research projects have been applied to investigate the possibility of the use of hybrid renewable energy systems as a power resource for (RO) desalination, specially, in off-grid regions. For example, a hybrid system consisting of a 10 Kw wind turbine, a 20 kW photovoltaic solar panel (PV) panel and a diesel generator with a rated power of 8.90 kW has been utilized in a small scale (RO) unit in a Turkish island to produce $1\text{m}^3/\text{h}$ of fresh water with cost of $\$2.20/\text{m}^3$ of water [5]. This water price cost has been lowered in another study using two alternatives [6], the first one combines a 10 kW wind turbine, 4.9 kW diesel generator, and 20 kW (PV) to produce fresh water with a price of $\$1.10/\text{m}^3$, while the second alternative uses a 5 kW hydrokinetic turbine, 4.9 kW diesel generator and 2.8 kW (PV) with a corresponding water cost of $\$0.56/\text{m}^3$. Although, these two studies offered a fresh water with lower price, they involved a fossil fuel source of energy which make them to lose the sustainability in the desalination process.

In fact, the use of tidal energy in the (RO) water desalination is already under investigation, as this source of energy is more predictable than other sources and has a higher energy intensity. The investigation of Elgado-Torres et al. [7] calculated that the use of tidal turbine along with (PV) increases the operating time of the desalination plant at nominal capacity between 1.8 and 2.8 times compared to the process driven by solar (PV) alone, with total capacity of $5.1\text{m}^3/\text{day}$ for each 10 MW hydrokinetic turbine. In [8], a horizontal axis tidal turbine has been designed and optimized to be used for powering (RO) desalination unit through coupling it directly with the high pressure pump in the desalination plant, for each $1\text{m}^3/\text{h}$, the energy required has been estimated to be $3440\text{Wh}/\text{m}^3$. A similar turbine has been tested in both laboratory and field conditions, coupled with a plunger pump as a component of the desalination unit, and as able to reach the 35 bar needed for the reverse osmosis [9]. However, these results are not very practical, as the turbine started to produce energy when the current flow exceeded 1.0 m/s, which

makes this system viable only for high velocity tidal currents. The vertical-axis turbine type is considered convenient option to harness the energy in the water current, due to its simple design, low maintenance cost and the flow direction insensitivity [10]. Especially in the Suez Canal, where ships pass all day long in both directions, producing constant changes in the direction of the local currents. The southern entrance of the Suez canal waterway has been selected as a preliminary location (Fig.1), because all the ships pass through a single branch, and the section is narrow but with side sections suitable for the placement of turbines (Fig.2). Statistically, about 1500 ships pass through this area every month, with an average speed of 3 m/s. It has been calculated that, in the area where the turbines would be located, fluctuating currents are produced continuously, with speeds between 0.2 and 1.5 m/s, and with oscillation periods of around half an hour.

Many investigations have been carried out to characterize and study the flow field around the vertical-axis turbine rotor inside open channels [11], under low velocity conditions [12]. Experimentally, the performance and wake structure of the three blades vertical-axis turbine with NACA-4418 blade profile have been studied in an open water channel using torque sensor and Particle Image Velocimetry (PIV) [13]. For further understating of the phenomena, this study has been complemented by a Large Eddy Simulation (LES) of the flow around the rotor. The same simulation mechanism has been applied to study the effect of changing the blade solidity (which is calculated as $\sigma = n.C/R$, where n is the number of blades, C is the chord length and R is the radius of the turbine rotor) on the turbine performance [14]. The increase in the power coefficient has been found to be linked to the decrease in the solidity value up to a critical limit, in which the turbine is still able to produce positive torque and flow separation is avoided. The performance of the vertical-axis turbine has been also reported under different channel circumstances in-

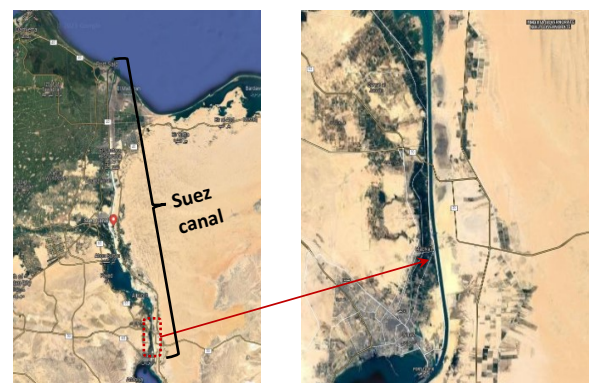


FIGURE 1: The southern entrance of the Suez Canal (the selected location).

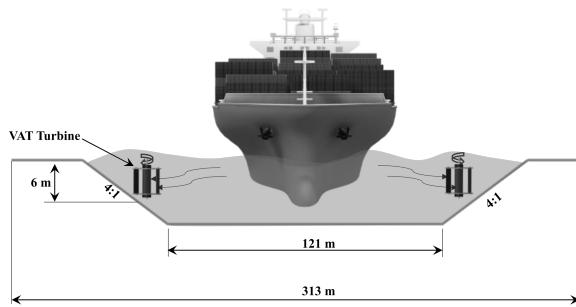


FIGURE 2: An approach for the turbine in the Suez Canal waterway (Not to scale).

cluding open flow conditions [15] and confined ones [16]. The wake recovery downstream the turbine rotor inside open channel has been also investigated, it is divided into three different regions; the near zone which is located just behind the rotor, the transitional zone that begins at two diameters of the turbine rotor and the far-wake region which is after five diameters value downstream the turbine [17].

One of the main problems of the vertical-axis turbine operation is the low starting torque. Many investigations has been carried out to offer solutions that can help to overcome this issue. Among of them, the hybrid turbine system in which a drag-based type like Savonius turbine is used on the same axis with the left-based type one [18]. Increasing the turbine solidity is considered one of the simplest solutions, as for high solidity value ($\sigma = 2.0$) a sufficient starting torque with a maximum power coefficient value have been obtained [19]. This design aspect has been applied to the purposed turbine model in the current study for a better starting characteristics under low velocity conditions.

Taking this into account, the main objective of this article is to design and test, experimentally and numerically, a small vertical axis turbine under low flow velocity conditions as the most suitable as a complementary power source in a reverse osmosis water purification unit to be inserted in the Suez canal waterway.

TURBINE MODEL DESIGN AND FABRICATION

A vertical-axis, straight blades, turbine model has been designed and manufactured to be tested and characterized experimentally in a water flume. A 3D schematic and images of the turbine model are shown in Fig. 3. The turbine consists of a slotted-chuck holding system (i), three fixed-pitch NACA 0015 straight blades (ii), two ending plates (iii) and ball bearing support (iv). The turbine parameters have been selected carefully looking for a self-starting and efficient operation. Typically, the NACA 4-digit series is employed for vertical-axis turbines with

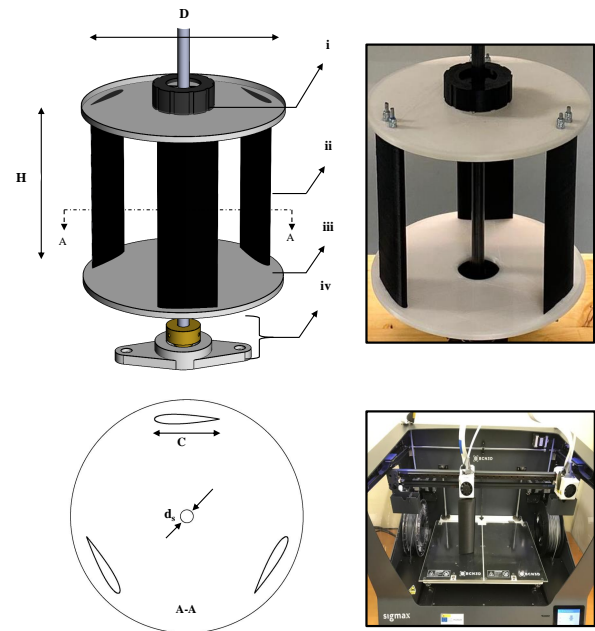


FIGURE 3: Schematic and manufacturing details of the model.

good performance in water [20]. Specifically, the NACA-0015 symmetrical airfoil has been selected among the other profiles due to its good performance at low Reynolds number [21]. For low flow velocities, increasing the blade thickness is preferable from the separation point of view [22]. Additionally, the ratio between the turbine height to the diameter (aspect ratio) has been set to 1.0, which gives the best performance for small turbines [23]. Based on all the design aspects mentioned above, the turbine model has an equal diameter (D) and height (H) of 0.15 m, and a chord length (C) of 0.05 m. The model was designed using 3D-CAD software and manufactured with 3D printing technology using Polylactic acid (PLA) material for its flexibility and high strength. The turbine model, with all its components, has been mounted on a steel shaft of diameter ($d_s = 10\text{mm}$).

METHODOLOGY

Experimental Methodology

Tests have been carried out in a recirculating hydraulic flume under low flow velocity conditions (Fig. 4). Water recirculation is provided by two 15 kW centrifugal pumps (1), each with a nominal flow rate of $300\text{ m}^3/\text{hr}$, controlled by two drive converters (2). The water flows from the tank (3) through the glass channel-which contains the turbine rotor (4)-and falls into the recirculating tank (5) at the end. The facility has also control and



FIGURE 4: Experimental set-up configuration.

measuring devices (6) connected to the turbine rotor.

The channel has a rectangular section (0.5 m high, 0.3 m wide and 1.5 m long) obtaining flow velocities varying from 0.14 m/s to 0.9 m/s at the maximum flow rate condition. The brake-torque arrangement consists of an integrated high precision torque and rotational speed sensor, Magtrol TS103 (0.5 Nm of rated torque, accuracy $<0.1\%$ and 1,5000 rpm max. speed, accuracy $<0.015\%$ and a hysteresis brake, Magtrol HB-140M-2 controlled by DC current. Mechanically, they are connected to the turbine shaft through flexible couplings. Furthermore, three ultrasonic sensor (HC-SR04) are used, covering the width of the channel, to obtain the water height and hence estimate the water flow velocity. Experimental tests have been carried out under three upstream flow velocities: 0.38 m/s, 0.40 m/s and 0.43 m/s.

For each flow velocity, the channel was fully-filled with water and the turbine rotor was immersed completely. When the turbine is allowed to rotate freely without any external load, the rotational speed increases up to its maximum value where the torque produced is just enough to compensate the mechanical losses. After that, the turbine is gradually loaded by increasing the current supplied to the brake. As the load increases, the rotational speed slows down, and the torque produced rises until reaching the maximum power point. Above that point, if the load is increased any more, the turbine arrives at a condition where it

cannot produce enough torque and stops. The measured vales are: rotational speed (N), water flow rate (Q) (through the calibration of the pumps rotating speed) and mechanical torque (T). These parameters are post processed to obtain the power output (P), the power coefficient ($C_p = P/(0.5 \cdot \rho \cdot A \cdot U^3)$) and the tip speed ratio ($\lambda = \omega \cdot R/U$).

Numerical Methodology

Based on computational fluid dynamics (CFD), a full size three-dimensional simulation has been carried out using the commercial software Fluent/Ansys. The computational domain and the boundary conditions are presented in (Fig. 5). The domain dimensions are based on the hydrodynamic channel size used in the experimental tests, which covers 10 times the turbine diameter in length and a double diameter in width. A velocity inlet boundary condition has been applied to the upstream side of the channel domain, while a zero pressure-outlet boundary condition has been selected to the downstream end of the domain. The interface region includes the simulated turbine (rotational zone) which is located at the center of the channel region (non-rotational zone). The sliding-mesh technique has been used between these two zones for always keeping the meshes connected during the different angular positions for each time-step. The turbine blade surfaces and the channel walls -except the free upper surface- have no-slip wall boundary conditions. The upper surface has a zero-shear stress boundary condition to represent the open-channel free surface.

The whole domain has been discretised using a fully structured shaped mesh (Fig. 6). Three mesh sizes have been used to

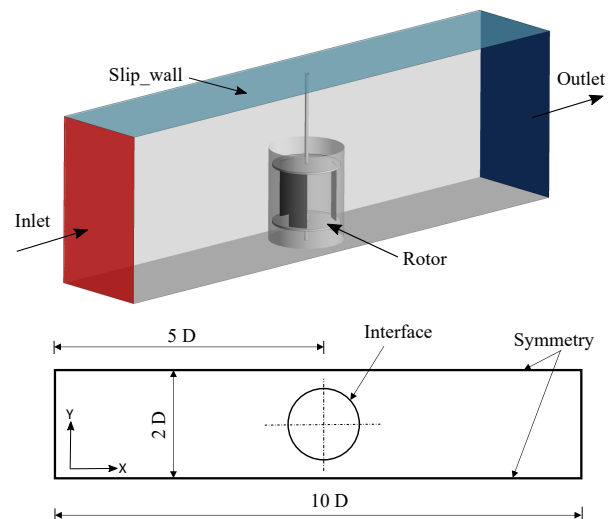


FIGURE 5: Computational domain.

check the mesh quality as shown in Table 1. A refinement factor has been applied around the turbine blades. The first layer height around the blades is kept constant at a value 1.2×10^{-5} m from the blade wall surface, resulting in a non-dimensional wall distance (y^+) with a maximum value of 0.7 as illustrated in (Fig. 7). This value is acceptable to resolve the viscous sub-layer as recommended by the transition turbulence models. In the current numerical study, water is considered as the working fluid, the main equations that govern this turbulent incompressible flow are the continuity ($\nabla \cdot \vec{u} = 0$), and the momentum Reynolds Average Navier Stokes (RANS) equation (1)

$$\rho \frac{\partial \vec{u}}{\partial t} + \rho \cdot \nabla (\vec{u} \cdot \vec{u}) = -\nabla p + \mu \cdot \nabla^2 \vec{u} + \rho \cdot \vec{g} + \Gamma_\sigma \quad (1)$$

where u and p are velocity and pressure field respectively, \vec{g} is the gravitational acceleration vector and Γ_σ is the surface tension force. The Reynolds stress term ($\rho \cdot \nabla (\vec{u} \cdot \vec{u})$) in the RANS equation was solved using the shear stress transport ($k-\omega$ SST) turbulence model developed by Menter [24]. This model combines robust formulations of the near wall ($k-\omega$) Wilcox model [25] and the ($k-\epsilon$) far wall one through a blending function that ensures a smooth transition between the two models without user interaction. The transport equations of the ($k-\omega$ SST) turbulence model are as follow:

$$\rho \frac{\partial (K)}{\partial t} + \rho \nabla (\vec{u} \cdot k) = \nabla \left[\left(\mu + \frac{\mu_t}{\sigma_k} \right) \nabla K \right] + P_K - \rho \epsilon \quad (2)$$

$$\rho \frac{\partial (\omega)}{\partial t} + \rho \nabla (\vec{u} \cdot \omega) = \nabla \left[\left(\mu + \frac{\mu_t}{\sigma_\omega} \right) \nabla \omega \right] + \beta \rho \omega^2 + S_\omega \quad (3)$$

Where k is the turbulent kinetic energy term, ω is the specific dissipation rate, μ_t is the turbulent eddy viscosity, β is empirical coefficient and S_ω is the blending function term. The Grid Conversion Index method (GCI) [26] has been applied to test the mesh refinement. It has been calculated based on the torque coefficient obtained from each mesh, using a safety factor of 1.25 -recommended by Roache [26]- and a calculated order of convergence value of 3.0. The $GCI_{1,2}$ has been found to be 0.172%, while the $GCI_{2,3}$ has a value of 0.018% with the asymptotic convergence value of 0.935. This corresponds to 0.4% change in the torque coefficient value when the mesh has been refined from M2 to M3, indicating that further refinement of the mesh size has a very small influence on the output results. So, the mesh size M2 has been selected for the working simulations. All solution variables have been calculated with the second-order Upwind discretization scheme. The Coupled pressure-based solver

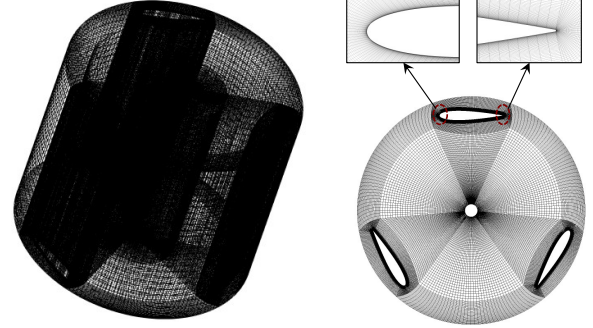


FIGURE 6: Details of the turbine mesh.

TABLE 1: Analysis for mesh selection.

Mesh	No. of volumes (Rotor)	Total volumes	RF
M1	503,622	1,005,372	0.5
M2	889,800	1,391,550	1
M3	1,720,200	2,221,950	2

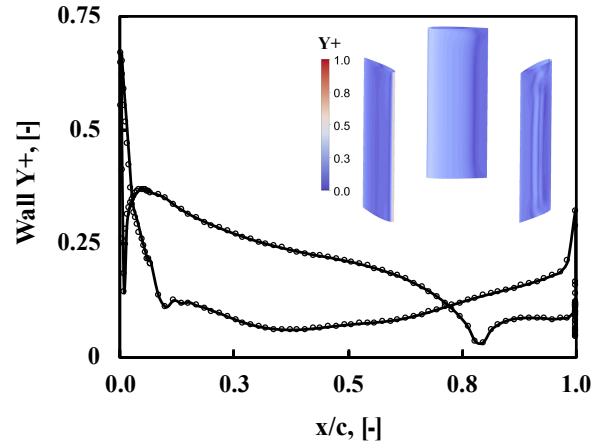


FIGURE 7: The dimensionless wall distance along the blades.

with second order implicit transient formulation has been selected according to a comparison between the Coupled and Simple pressure-velocity coupling as shown in Fig. 8. The Coupled algorithm reaches the converged solution, with a constant power coefficient, faster than the Simple one. Usually three cycles are

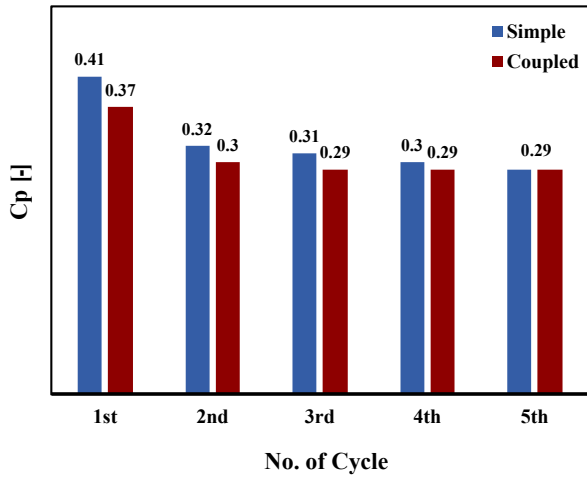


FIGURE 8: Pressure-velocity coupling at 0.43 m/s and $\lambda = 2.5$.

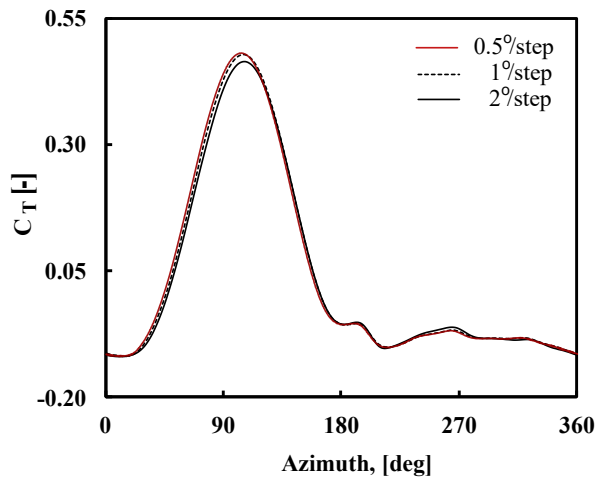


FIGURE 9: The torque coefficient for different time-step values at $\lambda = 2.6$.

enough but typically five revolutions have been completed to obtain smoother results. The selected time step for all runs corresponds to the time needed to rotate 1° ($1^\circ/\text{step}$). Figure. 9, compares between different degrees/time-step values. By decreasing the degrees/time-step values from $1^\circ/\text{step}$ to $0.5^\circ/\text{step}$, only 0.38% increase in the torque coefficient has been observed. A convergence criterion of 10^{-5} has been set for all parameters at each time step.

RESULTS AND DISCUSSION

This section presents the experimental results including the turbine power characteristic curves. Also, a comparison between the numerical and experimental findings are discussed. The pressure contours around the turbine blades for different angular positions and the vorticity field contours are also showed. The experimental measurements are carried out to assess the turbine performance under different flow velocities. As previously mentioned, for each flow velocity, the power produced from the turbine was measured and the characteristic curve was obtained. Upstream water velocity values of 0.38 m/s, 0.40 m/s and 0.43 m/s have been used. Figure. 10, shows the power curves under different upstream flow velocities where power values are plotted against the turbine rotational speeds. By increasing the upstream velocity, the power output increases and the rotational speeds shift to higher values. About the specific values, for the lowest flow velocity (0.38 m/s), the turbine rotational speeds range from 105 rpm to 130 rpm with a maximum power output of 0.25 W. The other flow rates have the same behaviour although with higher values and ranges. For the highest upstream velocity (0.43 m/s), the rotational speed operating range extends from 110 rpm to 150 rpm with a peak power point reaches 0.5 W.

Typically, the vertical-axis turbine characteristics are expressed in terms of tip speed ratio λ and power coefficient C_p . The comparison between experimental and computational characteristic curve obtained for the turbine model is shown in (Fig. 11). A reasonably good match between experiments and numerical results was found for the whole set of tip speed ratios. Both show the same tendencies which confirms that the flow physics has been captured correctly. However, the experimental results are somewhat lower than the computational ones, most likely because the numerical model does not consider the mechanical losses in the rotating equipment of the turbine. For higher tip speed ratios, the difference between numerical and experimental results is very small, for instance, the numerical prediction was found to be 7.6 % higher than the experimental one at $\lambda = 2.6$. This difference increased by decreasing the tip speed ratio value, to reach a maximum value of 9.8 % at $\lambda = 2.1$. It is due to the limitations of the single-phase model, as it cannot predict the change in free surface levels around the rotor while the power is extracted from the turbine. A multiphase numerical modelling is required for more accurate results. For both of numerical and experimental results, the maximum tip speed ratio corresponds to the zero-load condition. Increasing the turbine load increases the power coefficient and decreases the turbine rotational speed and consequently decreases the tip speed ratio value. This behaviour continues until the maximum power coefficient is reached, from that point on-wards, the turbine power coefficient decreases with the decline of the tip speed ratio, which makes this part of the curve unstable. Operation and measurement on this zone would require an active control system. The pressure coefficient fluctuations and pressure distribution contours on the single blade

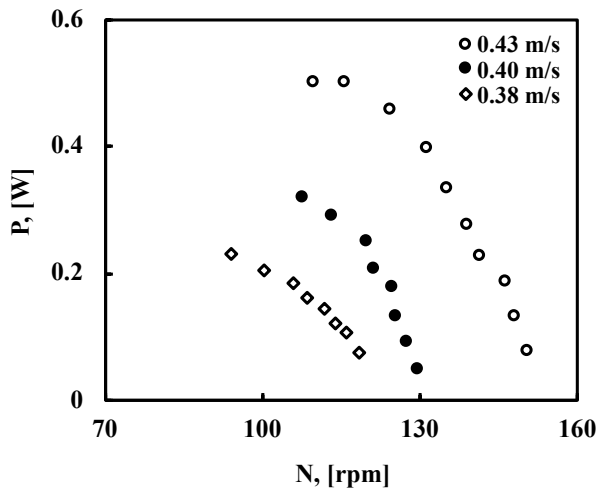


FIGURE 10: Power output for different upstream flow velocities.

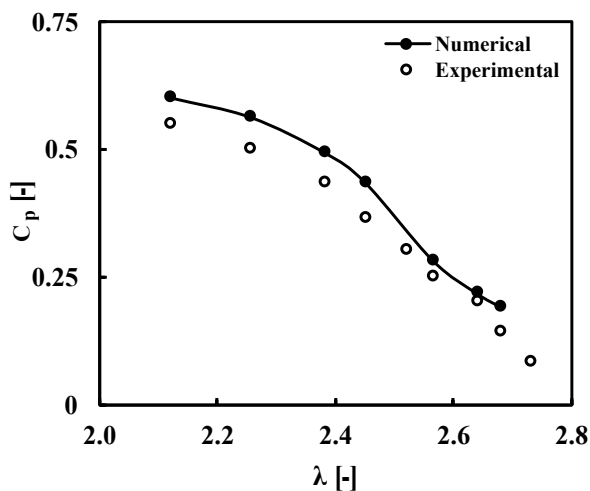


FIGURE 11: Experimental results and numerical model predictions 0.43 m/s.

surface during one complete turn is presented in Fig. 12.

For all azimuth angle positions, the maximum value of the pressure coefficient differences was found near the blade leading edge, these differences tend to zero near the trailing edge, which indicates that, the power coefficient of the turbine model has a high dependency on the blade leading edge design. The maximum values of the pressure difference on the turbine blade surface have been obtained in the upstream region of the turbine rotor (azimuth angles between 0° and 120°). The minimum value

has been observed at the angle of 180° , due to the similarity in the direction between the tangential velocity of the blade and the stream velocity at this position [27]. Conversely, a reduction in the pressure difference has been observed in the downstream side of the turbine compared with the upstream side, this is due to the low value of the angle of attack at this position. Although it was not expected, a cross-over has been observed at azimuth angles of 240° and 300° , where the pressure values on the blade suction side were found to be higher than at the pressure side for the rear part of the blade. This is believed to be caused by the combination of the turbine blockage inside the channel and the high solidity value, which forces the majority of the flow around the turbine instead of crossing through it, resulting in a kind of wake-like secondary flow with a lower pressure field inside the turbine than around the rotor or the downstream zone. This hypothesis is further confirmed by the vorticity distributions around the turbine rotor (Fig. 13). In the downstream region just behind the inner part of the rotor, the vorticity values are very small compared to the top and the bottom of the turbine. The blades move in a circular way generating a path of vortices behind them (Fig. 13 a) and due to the narrow width of the channel, the flow interacts with the shear layers on the channel walls and produces extended counter-rotating vortices streets -linked to each blade passage- at both laterals of the downstream region. Furthermore, the vortices generated from the turbine plates have been illustrated in (Fig. 13 b) where the layers from the upper and lower plates tend to merge and dissipate at a distance of about two times the turbine diameter in the far-downstream.

CONCLUSIONS

A small vertical-axis turbine has been designed, fabricated and tested, both experimentally and numerically, under low flow velocity conditions, looking towards its optimization as a complementary power source for a reverse osmosis water purification unit in the Suez canal waterway.

The NACA-0015 blade profile with a rotor solidity of 2.0 and aspect ratio of 1.0 have been selected to achieve a self-starting and efficient operation under the low flow velocity conditions. Experimentally, the turbine model has been fabricated through additive manufacturing technology. Tests have been carried out in an open channel flume under low flow velocities of 0.38 m/s, 0.40 m/s and 0.43 m/s. Power and non-dimensional curves have been obtained for each operating condition. Also, a reasonably good match has been observed between the experimental and the numerical simulation results which confirm the flow physics description around the turbine rotor. Finally, the good results obtained with low flow velocities indicated that the use of a vertical-axis turbine is a good option for the desalination process in the Suez canal waterway.

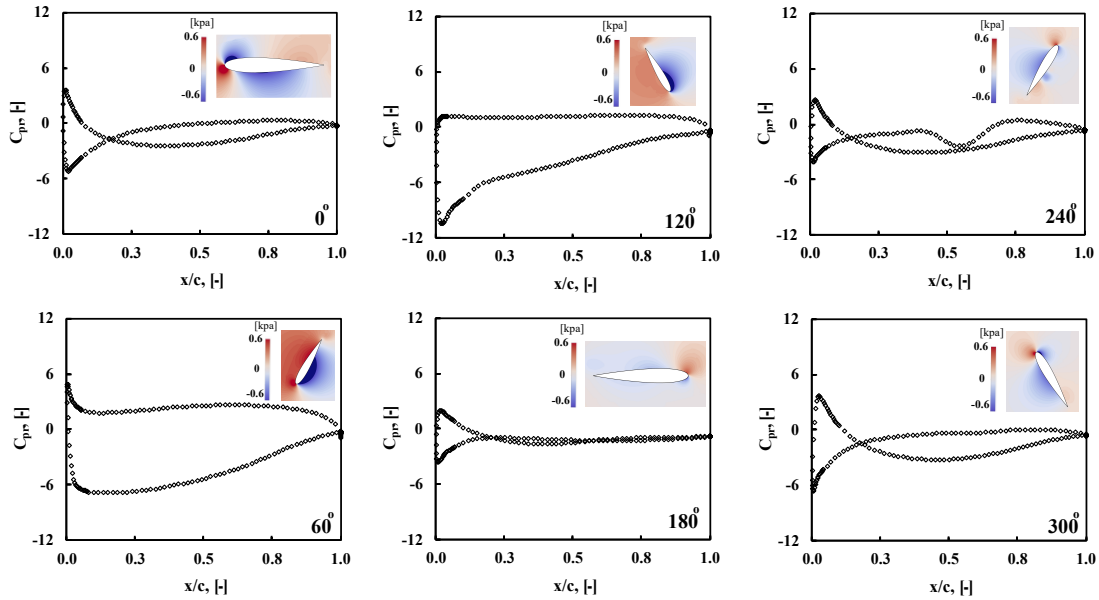


FIGURE 12: Pressure coefficient and pressure contours on a single blade at 0.43 m/s.

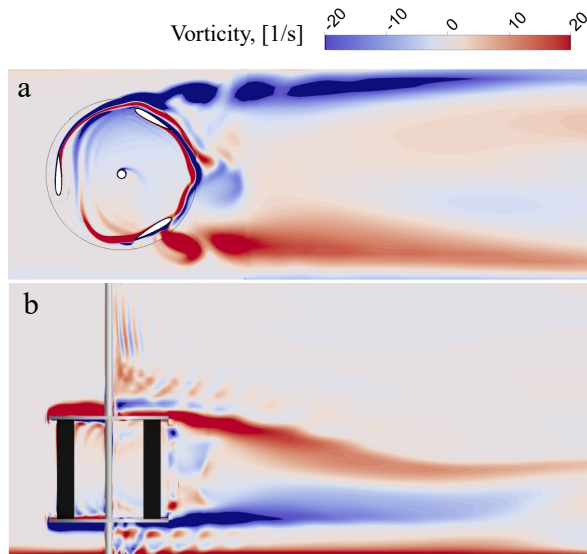


FIGURE 13: Vorticity field distributions at the middle sections; (a) vorticity-K; (b) vorticity-J at 0.43 m/s and $\lambda = 2.3$.

FUTURE WORKS

The total energy required, including the RO and pumping unites, for desalinating $1\text{ m}^3/\text{hr}$ will be estimated. Also, a multi-

phase numerical simulation will be carried out using the Volume of Fluid model (VOF) to track the water free-surface inside an open channel and to study the effect of the free-surface deformations on the overall performance of the turbine. Th numerical results will be validated by the experimental finding that will be achieved using a control gate at the end of the channel, which allows to obtain various free-surface conditions.

ACKNOWLEDGMENT

The author would like to express his gratitude to the Egyptian Cultural Affairs and Missions Sector (the Egyptian Ministry of Higher Education and Scientific Research) along with Port Said University for their financial support.

REFERENCES

- [1] Jones, E., Qadir, M., van Vliet, M. T., Smakhtin, V., and mu Kang, S., 2019. “The state of desalination and brine production: A global outlook”. *Science of The Total Environment*, **657**, pp. 1343–1356.
- [2] Abdelkareem, M. A., El Haj Assad, M., Sayed, E. T., and Soudan, B., 2018. “Recent progress in the use of renewable energy sources to power water desalination plants”. *Desalination*, **435**, pp. 97–113. Desalination using Renewable Energy.

- [3] Nagaraj, R., Thirugnanamurthy, D., Rajput, M. M., and Panigrahi, B., 2016. “Techno-economic analysis of hybrid power system sizing applied to small desalination plants for sustainable operation”. *International Journal of Sustainable Built Environment*, **5**(2), pp. 269–276.
- [4] Gilau, A. M., and Small, M. J., 2008. “Designing cost-effective seawater reverse osmosis system under optimal energy options”. *Renewable Energy*, **33**(4), pp. 617–630.
- [5] Gokcek, M., 2018. “Integration of hybrid power (wind-photovoltaic-diesel-battery) and seawater reverse osmosis systems for small-scale desalination applications”. *Desalination*, **435**, pp. 210–220. Desalination using Renewable Energy.
- [6] Ibrahim, M. M., Mostafa, N. H., Osman, A. H., and Hesham, A., 2020. “Performance analysis of a stand-alone hybrid energy system for desalination unit in egypt”. *Energy Conversion and Management*, **215**, p. 112941.
- [7] Delgado-Torres, A. M., García-Rodríguez, L., and del Moral, M. J., 2020. “Preliminary assessment of innovative seawater reverse osmosis (swro) desalination powered by a hybrid solar photovoltaic (pv)-tidal range energy system”. *Desalination*, **477**, p. 114247.
- [8] Khanjanpour, M. H., and Javadi, A. A., 2021. “Optimization of a horizontal axis tidal (hat) turbine for powering a reverse osmosis (ro) desalination system using computational fluid dynamics (cfd) and taguchi method”. *Energy Conversion and Management*, **231**, p. 113833.
- [9] Zhao, G., Su, X., Cao, Y., Su, J., and Liu, Y., 2016. “Experiments on the hydrodynamic performance of horizontal axis tidal current turbine and desalination of sea water”. *International Journal of Energy Research*, **40**(5), pp. 600–609.
- [10] Golecha, K., Eldho, T., and Prabhu, S., 2011. “Influence of the deflector plate on the performance of modified savonius water turbine”. *Applied Energy*, **88**(9), pp. 3207–3217.
- [11] Yosry, A. G., Fernández-Jiménez, A., Álvarez-Álvarez, E., and Marigorta, E. B., 2021. “Design and characterization of a vertical-axis micro tidal turbine for low velocity scenarios”. *Energy Conversion and Management*, **237**, p. 114144.
- [12] Fernández-Jiménez, A., Álvarez-Álvarez, E., López, M., Fouz, M., López, I., Gharib-Yosry, A., Claus, R., and Carballo, R., 2021. “Power performance assessment of vertical-axis tidal turbines using an experimental test rig”. *Energies*, **14**(20), p. 6686.
- [13] Yagmur, S., Kose, F., and Dogan, S., 2021. “A study on performance and flow characteristics of single and double h-type darrieus turbine for a hydro farm application”. *Energy Conversion and Management*, **245**, p. 114599.
- [14] Guillaud, N., Balarac, G., Goncalves, E., and Zanette, J., 2020. “Large eddy simulations on vertical axis hydrokinetic turbines-power coefficient analysis for various solidities”. *Renewable Energy*, **147**, pp. 473–486.
- [15] Gharib-Yosry, A., Blanco-Marigorta, E., Fernández-Jiménez, A., Espina-Valdés, R., and Álvarez-Álvarez, E., 2021. “Wind–water experimental analysis of small sc-darrieus turbine: An approach for energy production in urban systems”. *Sustainability*, **13**(9), p. 5256.
- [16] Patel, V., Eldho, T., and Prabhu, S., 2019. “Performance enhancement of a darrieus hydrokinetic turbine with the blocking of a specific flow region for optimum use of hydropower”. *Renewable Energy*, **135**, pp. 1144–1156.
- [17] Ouro, P., Runge, S., Luo, Q., and Stoesser, T., 2019. “Three-dimensionality of the wake recovery behind a vertical axis turbine”. *Renewable Energy*, **133**, pp. 1066–1077.
- [18] Gupta, R., Biswas, A., and Sharma, K., 2008. “Comparative study of a three-bucket savonius rotor with a combined three-bucket savonius–three-bladed darrieus rotor”. *Renewable Energy*, **33**(9), pp. 1974–1981.
- [19] Singh, M., Biswas, A., and Misra, R., 2015. “Investigation of self-starting and high rotor solidity on the performance of a three s1210 blade h-type darrieus rotor”. *Renewable Energy*, **76**, pp. 381–387.
- [20] Khanjanpour, M. H., and Javadi, A. A., 2020. “Optimization of the hydrodynamic performance of a vertical axis tidal (vat) turbine using cfd-taguchi approach”. *Energy Conversion and Management*, **222**, p. 113235.
- [21] Kanyako, F., and Janajreh, I., 2014. “Numerical investigation of four commonly used airfoils for vertical axis wind turbine”. *ICREGA14-Renewable Energy: Generation and Applications*, pp. 443–454.
- [22] Jain, S., and Saha, U. K., 2020. “On the influence of blade thickness-to-chord ratio on dynamic stall phenomenon in h-type darrieus wind rotors”. *Energy Conversion and Management*, **218**, p. 113024.
- [23] Sengupta, A., Biswas, A., and Gupta, R., 2016. “Studies of some high solidity symmetrical and unsymmetrical blade h-darrieus rotors with respect to starting characteristics, dynamic performances and flow physics in low wind streams”. *Renewable Energy*, **93**, pp. 536–547.
- [24] Menter, F. R., 1994. “Two-equation eddy-viscosity turbulence models for engineering applications”. *AIAA journal*, **32**(8), pp. 1598–1605.
- [25] Wilcox, D. C., 1988. “Reassessment of the scale-determining equation for advanced turbulence models”. *AIAA journal*, **26**(11), pp. 1299–1310.
- [26] Roache, P. J., 1994. “Perspective: A Method for Uniform Reporting of Grid Refinement Studies”. *Journal of Fluids Engineering*, **116**(3), 09, pp. 405–413.
- [27] Li, Q., Maeda, T., Kamada, Y., Murata, J., Shimizu, K., Ogasawara, T., Nakai, A., and Kasuya, T., 2016. “Effect of solidity on aerodynamic forces around straight-bladed vertical axis wind turbine by wind tunnel experiments (depending on number of blades)”. *Renewable Energy*, **96**, pp. 928–939.

C.2.2 Internet of Energy Applied to Water Hydrokinetic Smart-grids: A Test Rig Example

Proceedings of the ASME 2022 16th International
Conference on Energy Sustainability
ES2022
July 11-13, , Philadelphia, PA, USA

ES2022-85552

INTERNET OF ENERGY APPLIED TO WATER HYDROKINETIC SMART-GRIDS: A TEST RIG EXAMPLE

Ahmed Gharib-Yosry*

Dept. of Mechanical Power Engineering
Port Said University
Port-Said 42526
Egypt
Email: ahmed.gharib@eng.psu.edu.eg

Aitor Fernandez-Jimenez

Dept. of Energy Engineering
University of Oviedo
Mieres 33600
Spain
Email: fernandezaitor@uniovi.es

Victor Manuel Fernandez Pacheco

Dept. of Energy Engineering
University of Oviedo
Mieres 33600
Spain
Email: fernandezpvictor@uniovi.es

Manuel Rico-Secades

Dept. of Electrical and Electronic systems
University of Oviedo
Gijón 33204
Spain
Email: mrico@uniovi.es

ABSTRACT

The internet of things is a novel concept with many applications, one of them is the management of energy in smart power systems, which is known as the Internet of Energy (IoE). This research presents an autonomous system -based on IoE concept- for monitoring and controlling a water supply network using a renewable power generation set formed by a hydrokinetic vertical-axis turbine and a solar panel module. Different sensors that collect water quality and quantity data along with actuator devices are also equipped and interconnected through a low bandwidth Message Queuing Telemetry Transport (MQTT) protocol. Experimental tests have been carried out under laboratory scale conditions to check the working validity of the energy generating system with the proposed IoE structure in a water flume under low flow velocity conditions. An excellent test loop is available for various predictive maintenance and troubleshooting tasks using a novel IoE philosophy. Two communication tests through the MQTT protocol have been carried out successfully,

since all the sensors were able to send the information correctly in real time. The power status of the turbine and batteries have been also monitored. The system was able to send orders to the actuators, which will allow a full control of the operating devices in the remote smart grid locations.

Keywords: Internet of Things, Internet of Energy, Hydrokinetic Turbine, Smart-Grids.

NOMENCLATURE

D	Turbine diameter, m.
f_e	Electrical frequency, Hz.
H	Turbine blade height, m.
h_n	Nominal water height, m.
h_w	Water height, m.
P_e	Electrical power, W.
PP	Pole pairs.
Q_w	Water quality.
V_w	Water velocity, m/s.

*Address all correspondence to this author.

INTRODUCTION

The Internet of energy (IoE) is a leading concept in the field of smart power technology, it is a combination of energy, information and communication systems [1]. Basically, the internet of energy expression was first pioneered by Jeremy Rifkin, an American economic theorist, in his popular book entitled "The Third Industrial Revolution" [2]. In this book, the impact of technological and scientific changes on the economy, including the energy sector have been investigated. Actually, the IoE is categorized as a subcategory of the Internet of Things (IoT) in which all devices are connected to each other through the communication networks and the internet allowing both, the reception and the sending, of information [3]. The IoT technological concept emerged in 1999, being its first application the reception of wireless data from temperature sensors [4].

Many researches have been conducted on the field of smart energy using IoT application, for instance, the implication of the IoT in energy systems including its applications has been reviewed [5]. Also, benefits and initial assessments of emerging different IoT technologies on the current internet-based smart grids have been discussed [6], this can be achieved through the design of a pervasive system using small, inexpensive and compact devices. Furthermore, the IoT emerging researches have been broadened to offer energy forecasting services, which provide a prediction of the energy consumption or production through enormous database that contains historical information, weather prediction and capacities of the system devices [7, 8].

The IoE concept is based on the creation of an IoT architecture within the framework of an intelligent energy network so that both generating and energy-demanding devices are connected and monitored in real time. These systems usually have a user interface so that both smart energy grid and sensor devices are controlled. The utilization of the IoE technology in the renewable energy sector is considered one of the main applications in the smart energy sector, specifically for solar energy harvesting, in which the prediction of energy production was achieved by varying the inclination angle of the panel according to solar radiation during the day [9].

Also, the integration of the IoE in a solar energy harvesting system using smart sensors has been investigated [10]. This gave the end user an absolute control over the solar power production system with the maximum use efficiency. The application of this technology has been extended also to reach the hydraulic sector, especially in the cultivation applications by developing a system with several sensors for monitoring the hydraulic machines employed in the agriculture in order to improve their performance [11]. Actually, the maintenance strategy plays a pivotal role in the energy production systems, more specifically for wind turbines, in which the operational issues arise. Hence, the IoE concept has been integrated with turbines operation to develop a combined strategy for energy production and preventive main-

tenance [12, 13]. This algorithms aims to decrease the total cost and time for problem detection and maintenance in wind turbines by linking both the energy production and the degradation rates.

In fact, the widespread of the IoE has been possible due to the cost reduction of the electronic components, that composed this architecture, and the development in sensors and nano-systems [14], that can store larger amounts of information in smaller spaces and implement fast and reliable cloud-computing systems. Numerous full-scale projects have recently been carried out around the world using the IoE technology in smart grids, for instance, the British electricity company (NationalGrid) started in 2019 an IoE-based project called DynamicDemand (DD). This project is based on an extensive network of sensors that are interconnected between the generation and consumption points of the company using an IoE architecture, through this, the company can offer to its customers a fast response to sudden changes in electrical demands, optimizing the efficiency of the network and freeing up power capacity for other uses such as industrial companies [15]. Moreover, the American company (Lo3Energy) developed in 2020 a Smart-Grid solution based on IoE architecture in Brookling (New York, USA). This system is based on the block chain concept of energy exchange between users, so different buildings through the city are interconnected. Thus, those buildings that have surplus of energy pour their electricity to those that demand it, being a clear application of circular economy concept [16].

The incorporation of IoE strategies in renewable energy generation systems has many potential impacts, among of them, the change of maintenance and operation philosophy, specifically for remote access sites, in which plant operators are avoided and the data analytic to anticipate equipment failures are emerging. Therefore, the current work orients multidisciplinary research towards this type of strategies, as the main objective of this article is to present an autonomous system for monitoring and controlling a water supply network using a renewable and sustainable electric generation set formed by a hydrokinetic vertical-axis turbine and a solar panel module. Different sensors that collect water quality and quantity data of the hydraulic channel are also equipped. The whole system is interconnected using IoE architecture through low bandwidth MQTT communication protocol, so data can be sent in real time through wireless data network. The power status of the turbine and batteries can also be monitored. Additionally, a set of actuator devices are also installed so it can be possible to drive a metal water gate to control the water flow. Experimental tests have been carried out under laboratory scale conditions to check the working validity of the energy generating system, with the proposed IoE structure in a water flume, under low flow velocity conditions. These tests are considered a preliminary step to use the IoE system for operation and control of a power generation unit located in a remote location.

THE IoE COMMUNICATION ARCHITECTURE

Basically, the main vision of the IoT is to connect anything, anywhere and anytime into the main information network [17]. The smart grid goal is to monitor and control the energy generating units by providing bidirectional communication at anytime and anyplace between the grid and energy production system. To achieve this vision, the IoT is used as the infrastructure to support the two-way communication. Hence, the IoT and smart grid visions are combined to be called the internet of energy IoE [18]. The IoE architecture system is made up of different elements including smart sensors, network devices, processing unit, database (DB) and actuators. Smart sensors and actuators can detect and control the physical objects. Also, the data which is captured by sensors can be sent through a communication network applying a certain protocol created by the network devices. All this information is received by the processing unit (computers), which -bidirectionally- sends and receives data from the DB, so that according to the implemented algorithm of the processing unit, commands will be executed by the actuators. Fortunately, specifications and schematics of sensors and actuators are publicly accessible, and in some cases even free [19], these devices usually have a configurable logical unit, which allows the design to be adapted to its use. Some commercial examples stand out such as Arduino or Raspberry Pi [20] which are electronic boards based on open-source hardware philosophy with a central unit, in which expansion boards (shield) can be installed through input and output ports. Some models have a built-in micro-controllers and data network connection elements, so their integration with an IoE architecture is possible.

Due to the fact of that, the micro-grid locations are in remote areas where the wired communication is very expensive and for some cases is impossible, the wireless communication is considered for sending data as a fundamental part of an IoE architecture. The most common wireless ways are Bluetooth, GSM (Global System Mobile) and WiFi. The selection of one way or another will depend on various factors such as the volume of data, the existence of a previous data network or the amount of energy available. The WiFi connection is considered reliable due to its simple connectivity and its wide spreading at home and working centres. For publishing, subscribing and messages transporting, a communication protocols is required. The low bandwidth Message Queuing Telemetry Transport (MQTT) protocol is commonly used. The protocol consists of three main elements: sensors/actuators, broker, and clients (Fig. 1). Each sensor and actuator send all the information to the broker, where the data is published. Subsequently, a series of clients or processing units subscribe to the broker so they can receive, process, and store the information. Internal algorithms use this information to send orders to the actuators. If it is necessary, more devices can be subscribed to MQTT broker, taking the advantage of the MQTT protocol.

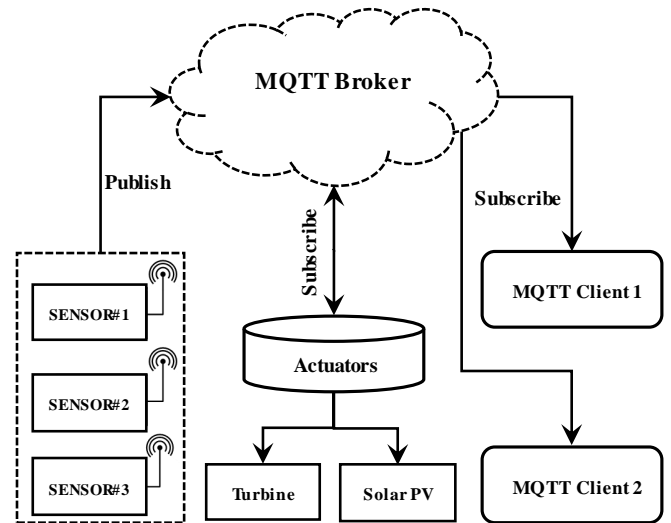


FIGURE 1: The IoE with the MQTT concept.

THE PRACTICAL CASE STUDY

Based on a MQTT communication protocol and an IoE architecture, a test rig has been designed and constructed including a cross-flow hydrokinetic turbine along with a commercial solar panel that will allow an autonomous system to monitor the water quantity and quality of a supply network. This system seeks to efficient operation and cost reduction associated with the management and maintenance of this type of smart grids. A vertical-axis, straight blades, turbine model has been manufactured (Fig. 2) to be tested experimentally in a water flume as a part of Smart-grid energy supply system for remote locations.

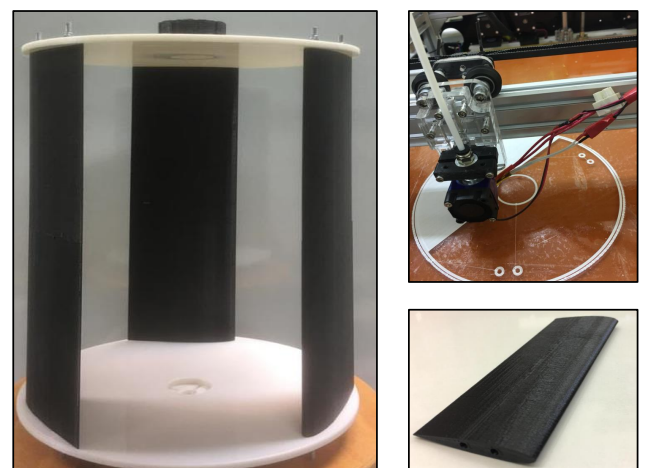


FIGURE 2: Turbine manufacturing details.

The turbine consists of three fixed-pitch NACA-0015 straight blades, that constrained with two ending plates. The model parameters have been selected carefully looking for a self-starting and efficient operation under low flow velocity conditions [21]. The ratio between the turbine height to the diameter (aspect ratio) in the proposed design has been set to 1.0, providing equal diameter (D) and blade height (H) of 0.3 m with a chord length of 0.1 m. The model was designed using 3D-CAD software and fabricated through the additive manufacturing technology (3D printing) using Polylactic acid (PLA) material which offers more flexibility and high strength. The turbine model, with its all components, has been mounted on a steel shaft (Fig. 3) and coupled with a 300 W commercial (Gimbal-GM8112H) permanent magnet generator (PMG) with the characteristics indicated in Table 1. To increase the electrical voltage of the PMG, a mechanical multiplier system of belts and pulleys has been installed. Thus, the rotational speed of the generator is increased 8.0 times. The commercial 40 W solar panel is made of flexible

TABLE 1: PMG characteristics.

Feature	Value
Pair of poles	21
Resistance per phase	7 Ω
Series Inductance per phase	3 mH
Maximum nominal voltage	28 V

mono-crystalline silicon, and is integrated with MPPT (Maximum Power Point Tracking) unit that allows the panel to work always at its maximum capacity. The Energy generated from both the turbine and the solar panel is stored in a 80 Ah capacity Li-ion battery pack which is protected in a waterproof box. Additionally, the system is equipped with DC-AC power inverter that allows the different devices of the system to be powered. Figure. 4 illustrate the solar panel with its power accessories.

METHODOLOGY

The installed sensors are operated through an electronic board composed of two parts: NodeMCU and power supply unit (Fig. 5). The first part sends data through an ESP8266 module, while the second allows the entire board to be powered (at 12 V)

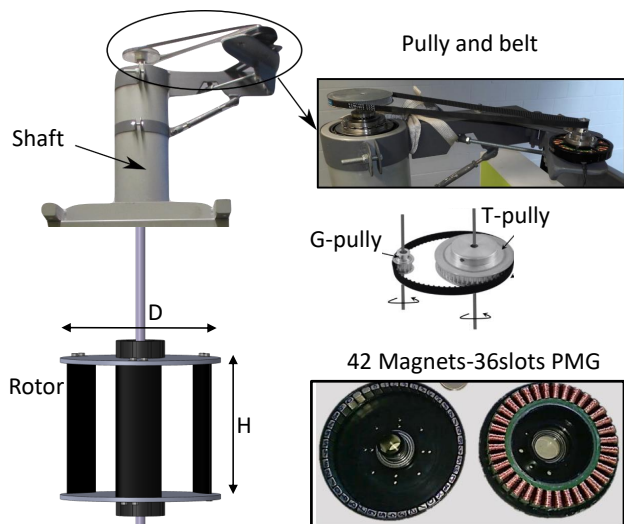


FIGURE 3: Turbine-Generator coupling system.

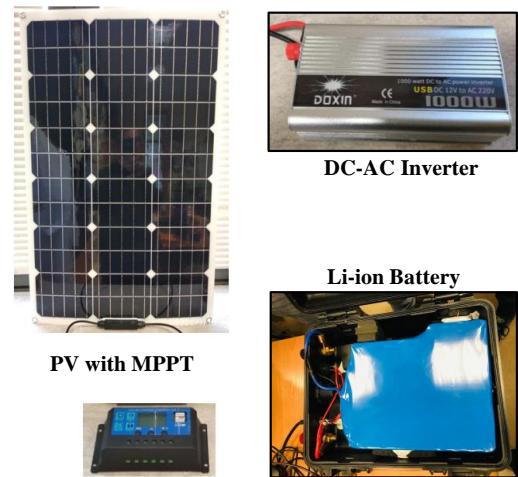


FIGURE 4: PV module and power accessories.

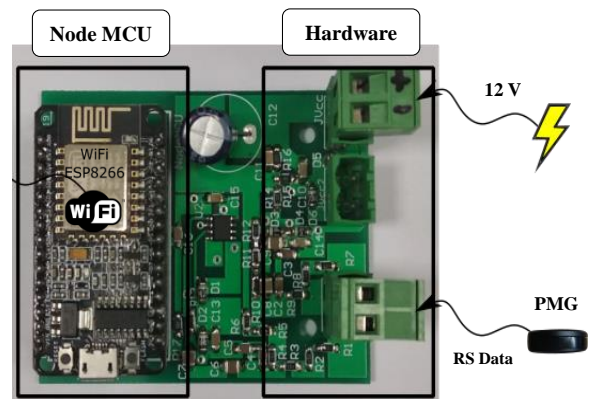


FIGURE 5: Sensors control board details.

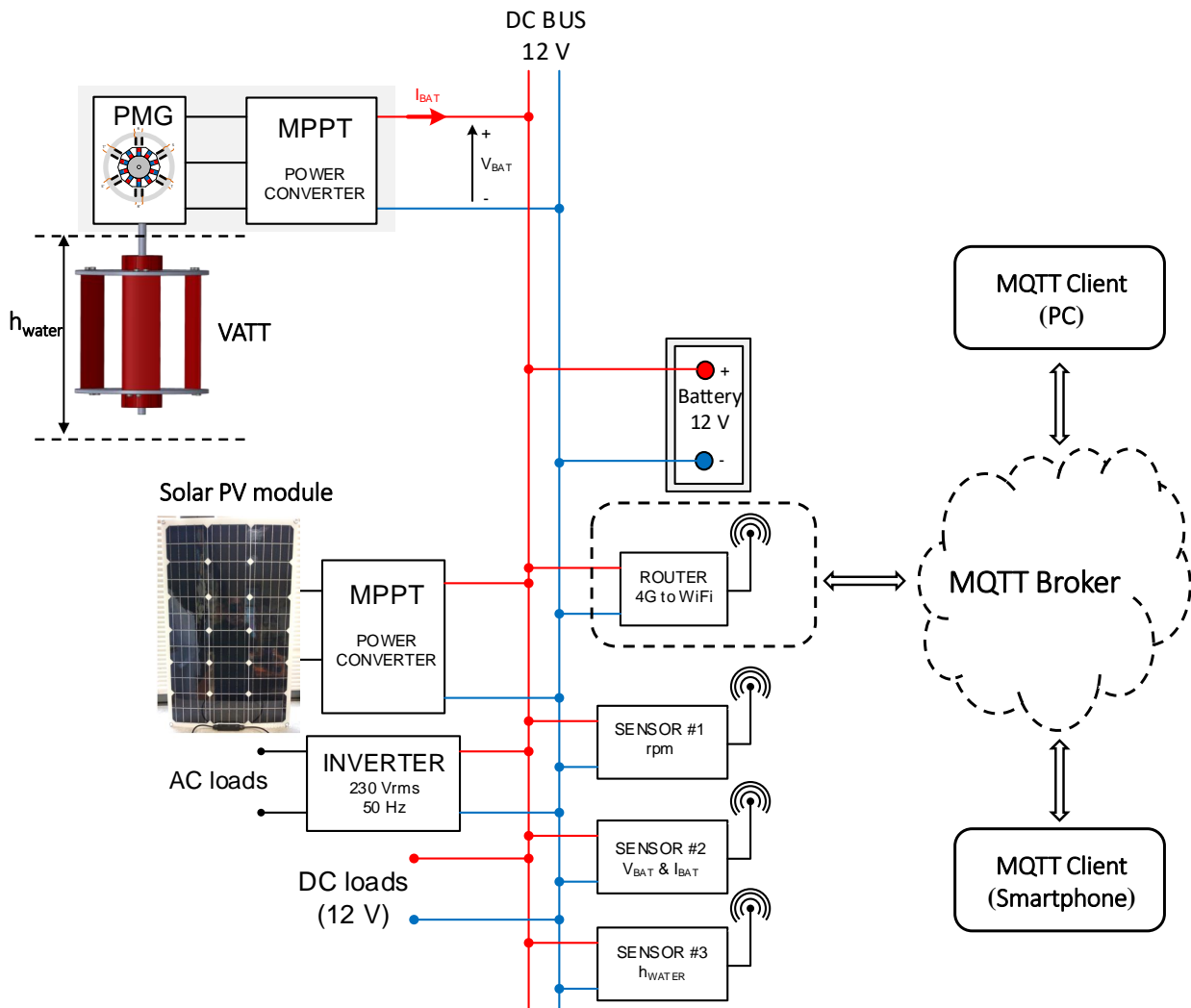


FIGURE 6: The power generation unit integrated with the IoE architecture.

and connected to the two phases of the PMG through RS Data connection, so voltage and electrical frequency are measured. It worth stating that, the NodeMCU module has an emergency storage capacity, so the information is safe in case of connection loss. In addition, an ultrasonic water height sensor (HC-SR04) has been installed, so the flow rate of the water was also calculated. Moreover, a water quality sensor which measures the turbidity and PH of water has been mounted. Finally, two actuators have been used: an electric motor to control the hydraulic water gate - to control the water flow rate- and a LED lighting system. Experimental tests have been carried out under laboratory conditions to check the working validity of the energy generating system with the proposed IoE structure in a water flume under low flow ve-

locity conditions. The vertical axis turbine has been installed in the channel and coupled with the PMG which is connected to the maximum point tracking system (see Fig.6). Through this unit, the power output and the rotational velocity could be characterized using the voltage and frequency output from the generator. The solar PV module with its power converter have been considered in the system but without power measurements in this experimental phase. Also, the water height and quality detection sensors have been installed and integrated with the system. The output data has been collected using the NodeMCU in the electronic board and sent to the MQTT broker -with time intervals related to the electrical frequency from the turbine- using an 4G-WiFi router. Two communication tests using a Smartphone and a

lab PC have been carried out to verify that, the implemented IoE architecture works correctly in the lab scale and ready for the real field installation. Finally, with the help of the collected data, An excellent test loop is available for various predictive maintenance and troubleshooting tasks using a novel IoE philosophy. Allowing a remote maintenance and operation of this energy system in remote areas.

THE IoE TESTING PHASE

One of the main advantages of the current microcontrollers (MCU) is their high computational capacity at a very high speed compared to mechanical systems (much slower). The turbine operation strategy can be implemented with the multi-tasking philosophy. To clearly explain it, the turbine operation is represented by (state machines), where there is a main task -the basic operation of the turbine- and other different tasks for each sensor that are working in parallel with the main one. In this context, the main task represents the basic operation of the turbine

in which the MPPT algorithms are implemented to extract the maximum power from the turbine. Additionally, different tasks work in parallel, one for each sensor (tasks #A, #B, #C and so on) (see Fig. 7). Task (#X) represents a generic task for any sensor, this generic task contains four states: measurement, analysis of the measurement, action when a problem is detected (Alarm-on) and another action when the system is working properly (Alarm-off). The interaction between sensor tasks (#X in general) and the main task will be done by means of flags (alarm f_e , alarm P_e and alarm h_w) that will indicate to the main task the existence of a fault in the system operation. In fact, one of the main advantage of this philosophy is the possibility of adding any other sensors to the system easily and assign to the sensor an independent task to manage its operation.

Technically, the measurement of both the electrical frequency (f_e) at the output of the PMG and the electrical power (P_e) extracted from the rotor (typically involving voltage and current measurements) are the basic requirement for the correct operation of the turbine. It is known that, the PMG with pole pairs (pp) generates pp numbers of electrical cycles for each mechanical one (in our case $pp = 21$). Therefore, by using the MCU system, it is possible to perform electrical frequencies measurements for each mechanical rotation of the turbine with high accuracy. Figure 8 visually indicates this possibility. The more pole pairs (pp) of the PMG, the further measurements could be performed and the more accurate frequencies could be measured.

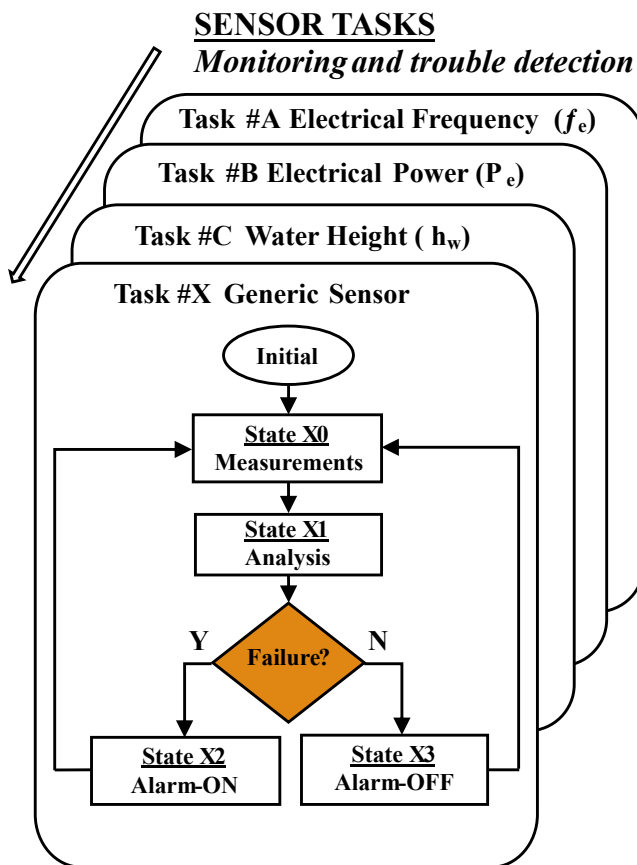


FIGURE 7: MCU task structure (State Machine philosophy).

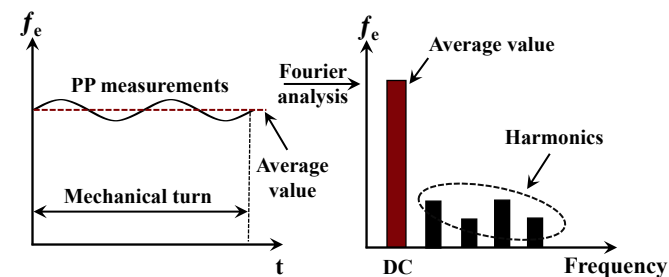


FIGURE 8: Electrical frequency analysis.

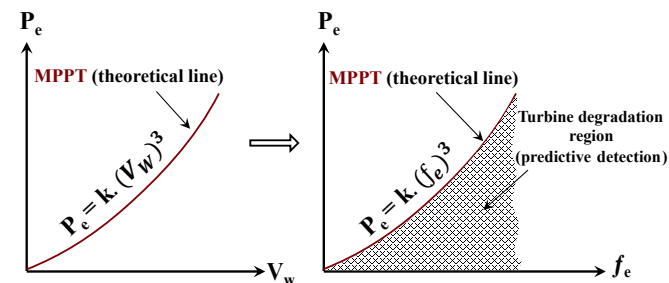


FIGURE 9: MPPT line and predictive degradation region.

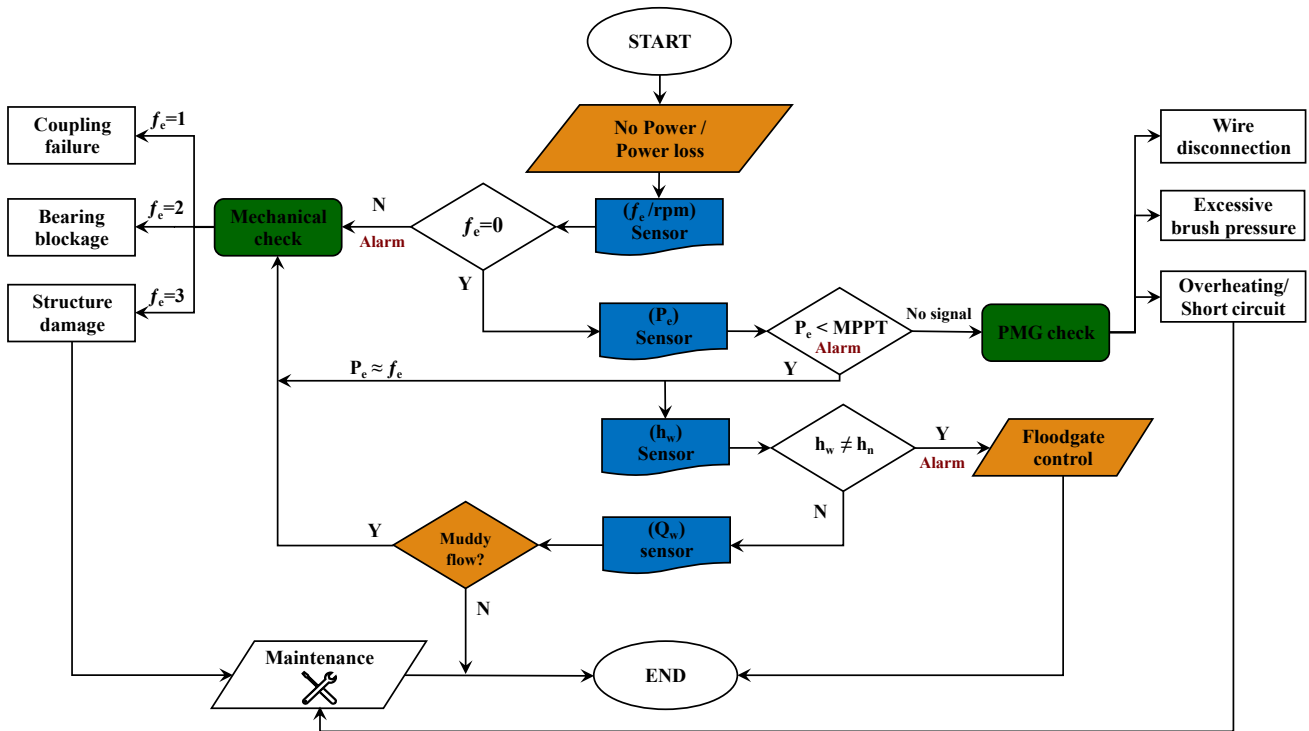


FIGURE 10: The troubleshooting process of the power generation unit in a remote location.

The mechanical and structural problems in the turbine introduce fluctuations in these frequency measurements that can be used as an excellent estimator of mechanical failures in the turbine. The Fourier development of this signal and specifically its harmonics (Fig. 8) are the base of these studies. The (f_c) measurements are the core for implementing simple and efficient MPPT algorithms. As shown in Fig. 9, Each frequency (f_c) value corresponds to a theoretically extracted electrical power (P_e) in MPPT, a more detailed and comprehensive study has been conducted by Alvarez et. al [22]. The relation between the electrical power output and the frequency can be used as an excellent estimator of the turbine degradation (dirt, damage, etc). In Figure. 9, the turbine degradation region has been marked, as the operation is further away from the theoretical MPPT line, the more degradation of the turbine occurs. This is could be used as a predictive indicator for maintenance or rotor cleaning. Based on that, the inclusion of other sensors and other tasks related to maintenance and operation of the turbine can be easily incorporated using this philosophy. A simplified troubleshooting flow chart includes the state machine associated with the measurement of the electrical frequency, the electrical power, the water height and the water quality has been presented in Fig. 10. Obviously, in the IoE context, it is important to send and receive information remotely from each of these state machines. The operation of the MQTT broker

has been also tested using a local WiFi network in the laboratory. The proposed system has been tested experimentally in the laboratory using a water current flume under low flow velocity conditions, simulating the real field environment. Once the turbine rotates and starts to generate electricity, two communication tests have been carried out to verify that the implemented IoE architecture works correctly. Firstly, the system has been tested by sending and receiving information through a smartphone. An open-source application has been configured to connect with the developed MQTT protocol. Through this test, all sensors in the system have been worked correctly and the sent and received information have been displayed including the power output from the turbine rotor and the rotational speed. A small LED has been used to measure the system response to the sent orders. Figure. 11 shows the testing phase that has been carried out with the smartphone. The same tests were carried out as in the previous test, but additionally, the processing unit procedures, DB management, and data storage methods were also adjusted. In the computer-case tests, the reception and sending of information from the sensors and actuators have been also checked by two clients based on Python code. Additionally, it was verified that, the DB stored the data according to the designed form, so that it could be used later by the decision-making algorithm that will be developed for the field application. All tests have been

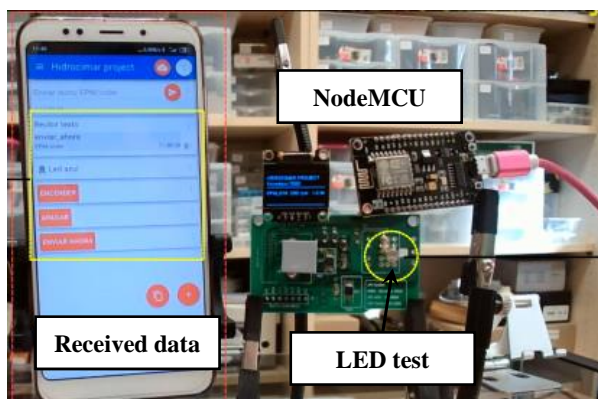


FIGURE 11: Communication test through the MQTT protocol.

carried out successfully since all the sensors were able to send the information correctly. In addition, the smartphone and computer clients could show all the collected data in real time, also the system was able to send orders to the actuators, which will allow a full control of the operating devices in the remote smart grid locations including the hydraulic water gate or other considered devices.

CONCLUSIONS

The accelerated growth in the information and communication technology along with the current trend of sustainable energy development has led to the appearance of a new concept known as the internet of energy (IoE). This article presents an autonomous system -based on the IoE concept- for monitoring and controlling a water supply network using a sustainable power generation set formed by a hydrokinetic vertical-axis turbine and a solar panel module. Also, it aims to change the philosophy of maintenance and operation of hydrokinetic turbines in real field sites with low accessibility. Experimental tests have been carried out under laboratory scale conditions to check the working validity of the energy generating system with the proposed IoE structure in a water flume, under low flow velocity conditions. An excellent test loop is available for various predictive maintenance and troubleshooting tasks using a novel IoE philosophy. Moreover, two communication tests have been carried out through the MQTT broker. All tests have been carried out successfully since all the sensors were able to send the information correctly. The power status of the turbine and batteries have been also monitored. In addition, smartphone and computer communication tests successfully showed all the collected data in real time. The system was also able to send orders to the actuators, which will allow a full control of the operating devices in the remote smart grid locations.

FUTURE WORK

As the proposed system proved a reliability and efficient control and operation in the laboratory scale, the next phase is to install this system in a remote power generation location. A rural site in the mountains with water network supply that is located at the north of Spain (Asturias) has been selected to install the hydrokinetic turbine and the solar panel module with the IoE architecture. The turbine will be mounted in the water channel which passes through a rural house while the solar panel will be installed at the top of the building roof. Figure. 12 shows the selected location.



FIGURE 12: The selected remote location for power generation.

ACKNOWLEDGEMENT

The author would like to express his gratitude to the Egyptian Cultural Affairs and Missions Sector (the Egyptian Ministry of Higher Education and Scientific Research) along with Port Said University for their financial support.

REFERENCES

- [1] Shahinzadeh, H., Moradi, J., Gharehpetian, G. B., Nafisi, H., and Abedi, M., 2019. "Internet of energy (ioe) in smart power systems". In 2019 5th Conference on Knowledge Based Engineering and Innovation (KBEI), IEEE, pp. 627–636.
- [2] Gefter, A., 2010. "Jeremy rifkin and the third industrial revolution". *New Scientist*, **205**(2747), p. 46.
- [3] Miglani, A., Kumar, N., Chamola, V., and Zeadally, S., 2020. "Blockchain for internet of energy management: Review, solutions, and challenges". *Computer Communications*, **151**, pp. 395–418.
- [4] Zanjireh, M. M., and Larijani, H., 2015. "A survey on centralised and distributed clustering routing algorithms for

- wsns”. In 2015 IEEE 81st Vehicular Technology Conference (VTC Spring), IEEE, pp. 1–6.
- [5] Shahinzadeh, H., Moradi, J., Gharehpetian, G. B., Nafisi, H., and Abedi, M., 2019. “Iot architecture for smart grids”. In 2019 International Conference on Protection and Automation of Power System (IPAPS), IEEE, pp. 22–30.
- [6] Bui, N., Castellani, A. P., Casari, P., and Zorzi, M., 2012. “The internet of energy: a web-enabled smart grid system”. *IEEE Network*, **26**(4), pp. 39–45.
- [7] Karnouskos, S., Da Silva, P. G., and Ilic, D., 2012. “Energy services for the smart grid city”. In 2012 6th IEEE International Conference on Digital Ecosystems and Technologies (DEST), IEEE, pp. 1–6.
- [8] Yu, X., Cecati, C., Dillon, T., and Simoes, M. G., 2011. “The new frontier of smart grids”. *IEEE Industrial Electronics Magazine*, **5**(3), pp. 49–63.
- [9] Spanias, A. S., 2017. “Solar energy management as an internet of things (iot) application”. In 2017 8th International Conference on Information, Intelligence, Systems & Applications (IISA), IEEE, pp. 1–4.
- [10] Sahraei, N., Looney, E. E., Watson, S. M., Peters, I. M., and Buonassisi, T., 2018. “Adaptive power consumption improves the reliability of solar-powered devices for internet of things”. *Applied Energy*, **224**, pp. 322–329.
- [11] Coelho, A. D., and de Oliveira Assis, W., 2020. “Internet of things applied to hydraulics”. In 2020 XIV Technologies Applied to Electronics Teaching Conference (TAEE), IEEE, pp. 1–4.
- [12] Hajej, Z., Rezg, N., and Bouzoubaa, M., 2017. “An integrated maintenance strategy for a power generation system under failure rate variation (case of wind turbine)”. In 2017 IEEE 6th International Conference on Renewable Energy Research and Applications (ICRERA), IEEE, pp. 76–79.
- [13] Hajej, Z., Nidhal, R., Anis, C., and Bouzoubaa, M., 2020. “An optimal integrated production and maintenance strategy for a multi-wind turbines system”. *International Journal of Production Research*, **58**(21), pp. 6417–6440.
- [14] Shilpa, A., Muneeswaran, V., Rathinam, D. D. K., Santhiya, G. A., and Sherin, J., 2019. “Exploring the benefits of sensors in internet of everything (ioe)”. In 2019 5th International Conference on Advanced Computing & Communication Systems (ICACCS), IEEE, pp. 510–514.
- [15] The British National Grid Electricity Transmission (NGET), <https://www.nationalgrid.com/uk/electricity-transmission>, Accessed: 2021-11-15.
- [16] Pando - LO3 Energy, 2020, <https://lo3energy.com/pando>, Accessed: 2021-11-21.
- [17] Yun, M., and Yuxin, B., 2010. “Research on the architecture and key technology of internet of things (iot) applied on smart grid”. In 2010 International Conference on Advances in Energy Engineering, IEEE, pp. 69–72.
- [18] Rana, M., 2017. “Architecture of the internet of energy network: An application to smart grid communications”. *IEEE Access*, **5**, pp. 4704–4710.
- [19] Amiri-Kordestani, M., and Bourdoucen, H., 2017. “A survey on embedded open source system software for the internet of things”. In Free and Open Source Software Conference, Vol. 2017.
- [20] Okigbo, C. A., Seeam, A., Guness, S. P., Bellekens, X., Bekaroo, G., and Ramsurrun, V., 2020. “Low cost air quality monitoring: comparing the energy consumption of an arduino against a raspberry pi based system”. In Proceedings of the 2nd International Conference on Intelligent and Innovative Computing Applications, pp. 1–8.
- [21] Yosry, A. G., Fernández-Jiménez, A., Álvarez-Álvarez, E., and Marigorta, E. B., 2021. “Design and characterization of a vertical-axis micro tidal turbine for low velocity scenarios”. *Energy Conversion and Management*, **237**, p. 114144.
- [22] Alvarez, E. A., Rico-Secades, M., Corominas, E., Huerta-Medina, N., and Guitart, J. S., 2018. “Design and control strategies for a modular hydrokinetic smart grid”. *International Journal of Electrical Power & Energy Systems*, **95**, pp. 137–145.

C.2.3 Diagnostic Strategies for Microturbines Operating Status Applied to Predictive Maintenance: Experimental Test Case

Diagnostic Strategies for Microturbines Operating Status Applied to Predictive Maintenance: Experimental Test Case

Eduardo Á. Álvarez¹, Ahmed G. Yosry^{1,2,*}, Aitor F. Jiménez¹, Antonio C. Rodríguez³, Manuel R. Secades³

¹Hydraulic R&D, EP Mieres, University of Oviedo, Mieres, Spain

²Mechanical Power Department, Faculty of Engineering, Port Said University, Egypt

³Electrical and Electronic systems Department, EPI Gijón, University of Oviedo, Gijón, Spain

ABSTRACT

The current study represents a preliminary step towards detecting operating problems in wind microturbines automatically. The electrical frequency signal generated by the turbine allows for the detection of operating issues during its power stage. To conduct a comprehensive study, a vertical-axis microturbine has been tested, under various failure conditions, inside a closed-loop wind tunnel. An electronic data acquisition system has been developed to continuously measure the frequency signal during the experiments. The output data, including the power and the frequency signals, has been analyzed in terms of average frequency and standard deviation. The collected and stored data is accessible through an operation and maintenance system, which uses an AI-based algorithm and a Jupyter Notebook tool that is executed in Python.

Keywords: Predictive maintenance, Wind turbine, Vertical axis turbine, Smart Cities, Internet of Things

NOMENCLATURE

ζ_ω	Rotational speed ratio
$\bar{\omega}_i$	Average rotational speed, [rpm]
ζ_σ	Standard deviation ratio
σ_i	Standard deviation
λ	Tip speed ratio
Ω	Angular velocity, [rad/s]
A	Turbine frontal area, [m ²]
C_p	Power coefficient
F_e	Electrical frequency, [Hz]
F_{mec}	Mechanical frequency, [Hz]
n	Number of blades
P	Power output, [W]
T_{mec}	Mechanical torque, [N.m]
T_e	Electrical torque, [N.m]
u_∞	Wind velocity, [m/s]

*Corresponding author: ahmed.garib@eng.psu.edu.eg

1. INTRODUCTION

1.1 Wind energy potential

Recent geopolitical conflicts in Eastern Europe have highlighted the importance of the European Union's (EU) energy dependence on fossil fuels. The current rise in the price of gas and oil has only served to underline the far-reaching importance of these resources in the European energy market, affecting many sectors such as industry and services. In recent years, the EU has made significant efforts to implement energy sources that reduce energy consumption across the European Union. For instance, it has approved several plans for 2030 and 2050 aimed at reducing energy dependence, combating climate change, and mitigating its effects on the region [1].

Currently, fossil fuels account for 71% of the energy sources used in Europe. Specifically, the main resources are oil (36%), gas (22%) and coal (13%). It should be added that the 14% corresponds to electricity generated by nuclear energy, although the use of this source is very uneven depending on the country. Therefore, although in the EU, renewable energies account for only 15%, this percentage is expected to increase considerably in the coming decades due to the installation of solar photovoltaic plants and wind farms [2].

Wind energy is a renewable source of power that has the potential to play an important role in meeting the world's energy needs [3]. It is abundant and available in many areas around the world, making it a reliable source of power in many regions. Wind energy has been experiencing a steady increase in power since 2019, in both onshore and offshore sectors, with leading countries such as China, the United States, Germany, India, and Spain driving this development. Figure 1 illustrates the growth of wind energy in gigawatts (GW) from 2017 to 2022 [4].

According to the power capacity, wind turbines are classified into three main categories; the first classification is the large-scale turbines. These turbines have a capacity of over 1 MW and are used to generate power for large cities or industrial fa-

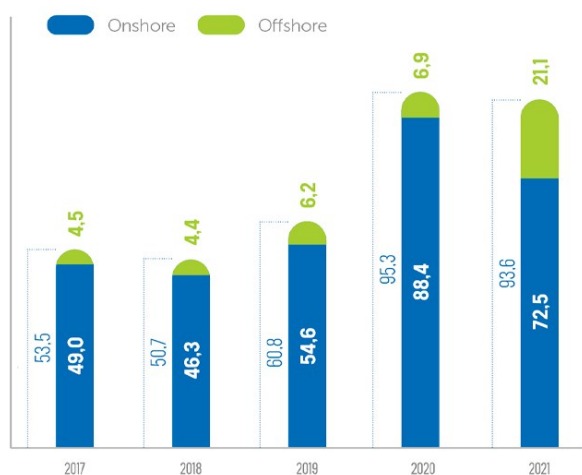


FIGURE 1: Wind power growth rate (2017-2022) [4].

cilities. Large-scale turbines are typically installed in large wind farms and can generate significant amounts of power. The second classification is medium-scale turbines. These turbines have a capacity of between 100 kW and 1 MW and are often used to power small communities or farms. Medium-scale turbines are typically installed in small wind farms and can be used to supplement or replace traditional sources of power. The third classification of wind turbines is small-scale turbines. These turbines have a capacity of up to 100 kW and are typically used to power individual homes or small businesses [5, 6]. Small-scale turbines are usually installed on rooftops or in small wind farms and are designed to be easily integrated into the local power grid. Small-scale turbines are particularly popular in remote areas where there is no access to traditional power sources [7, 8].

As part of the Smart Cities initiative, new wind turbine designs are being developed with smaller and more compact designs to minimize visual and landscape impacts [9]. These inconspicuous wind turbines can be integrated into the urban atmosphere. Though they have small installed power (<1 kW), they can meet the small demands of buildings or industries, as well as supply electricity to off-grid structures. Some of these wind turbines are already in the commercial phase and can be used for urban lighting, urban communication systems (WiFi), or charging points for electric vehicles such as scooters [10].

The emergence of technologies based on small micro-generation wind turbines and the Smart Grid philosophy has led to the commercial installation of vertical axis turbines in some buildings or urban environments. One example is the LS Savonius 3.0 design from the company LuvSide [11], which consists of a 4 m high and 2.2 m diameter rotor with a generating capacity of 300 W (see figure 2a). This turbine is designed to provide electricity to remote industries. In the case of Darrieus-H turbines, one of the most noteworthy projects is the Figeac turbine from Ratier company [12]. This rotor has a diameter of 12 m and a height of 10 m, with a total installed power of 12 kW. Figure 2b shows a photograph of this design.

All the above projects share a common goal of developing commercially viable equipment, which translates into a similar



(a) LUVSide project [11].

(b) Figeac project [12]

FIGURE 2: Savonius and Darrieus wind microturbines

TABLE 1: Real projects of wind microturbines

Project	Turbine type	Power [kW]
LS Savonius [11]	VAT-Savonius	0.3
EVA120 [13]	H-Darrieus	20
Dornier [14]	Savonius	0.55
Ratier [12]	H-Darrieus	12

installed power capacity and physical size. However, in recent times, new designs have emerged that are even smaller and focused on micro-generation applications that are easy to install and use. Some of these designs are equipped with electronic control devices to monitor and manage energy production, increasing their versatility. Table 1 shows the main projects where wind micro-turbines have been employed.

1.2 Predictive maintenance in micro-turbines

A failure in the service of any installation, including those related to energy, can have various consequences. For this reason, energy companies are showing increasing interest in designing and developing systems based on the concept of predictive maintenance. With this approach, it is possible to study the behaviour of micro-turbines and use patterns to anticipate the need for maintenance interventions.

Predictive maintenance involves a series of actions and techniques that aim to anticipate failures and operational problems that may occur in a system [15]. To achieve this goal, different tools and data analysis techniques are utilized to detect anomalies in the operation of specific installations, thereby enabling the prediction of future failures. In this regard, the development of the Internet of Things (IoT) concept has a crucial role to play, as it facilitates the collection of various parameters that can be used for subsequent analysis and the development of accurate failure predictions [16].

The concept of IoT is the interconnection of many devices that allows the exchange of data so that it can be further processed for multiple applications. This methodology allows its capture in real-time so that it is possible to know the operating status of the wind turbine and draw conclusions or risks associated with it. In this sense, it is worth noting that other methodologies such as artificial intelligence or Big Data solutions for processing this

huge amount of data are also good applications for predictive maintenance [16].

Predictive maintenance has found practical applications in the wind energy industry as well. The operating costs of a typical wind turbine can account for 20-30% of its life cycle cost [17], making the implementation of this technique highly cost-effective. Some of the existing systems that have been implemented in this context include the monitoring of the lubrication gap between the shaft and rotor seat, measurement of the displacement of the rotor (clutch disk), continuous auscultation of the wind turbine shaft, and measurement of blade temperatures and vibrations [18]. To accomplish this, various sensors need to be installed on each device to be monitored. Vibration analyzers, thermographic cameras, and ultrasonic meters are among the most widely used types of sensors.

Various studies have been conducted in the field of smart energy that involves the use of IoT applications in the predictive maintenance of wind turbines, either as an isolated turbine [19, 20], or even as a turbine farm [21]. For instance, researchers have utilized the Big Data processing framework to create data-driven predictive models that rely on historical data stored in the cloud. Additionally, an online fault-tolerant monitoring agent has been developed using a Big Data stream processing framework to predict the state of wind turbines at 10-minute intervals. Finally, a front-end has been created that allows for real-time visualization of the status of the wind turbines [22]. Also, A novel integrated approach has been developed for fault diagnosis and prognosis of wind turbines, particularly in cases where degradation data is limited. The approach involves the use of a wavelet transform-based method to analyze incipient defect signatures in the bearings, and the extracted features are then combined using the Health Index algorithm to represent the bearing defect conditions [23]. Another methodology using the vibration signal analysis has been developed for the prediction of the bearing faults in wind turbines [24]. In addition, a new model for predictive maintenance has been introduced, specifically for identifying failures in sub-components of wind turbines. The model combines Machine Learning and statistical process control tools, and utilizes a multivariate approach across all processing levels. It relies on SCADA tags as input. The model has been tested through a large-scale campaign involving 150 wind turbines, and has shown the capability to predict failures in the gearbox, generator, and main bearing components, with a lead time of up to 1-2 months, thereby enabling early detection [25].

The known failure and repair rates of turbine components have been modified to develop predictive and condition-based maintenance strategies, as opposed to a reactive approach. Implementing these strategies can lead to potential cost savings of up to 8 % in the direct operation and maintenance costs and a reduction of up to 11 % in lost production. These estimates assume that advanced monitoring can detect 25% of major generator and gearbox failures, enabling repairs to be carried out before major replacement is needed [26].

However, in the case of small-scale turbines, it is a challenge to house many sensors due to their limited size and the technical and computational complexity of processing the high volume of data they generate. To address this issue, the present article

proposes a simple methodology that uses energy data produced by the turbine's generator to implement predictive maintenance strategies. It should be noted that the generator is the only device common to all turbines, and analyzing its continuous production data and observing patterns in its operation provides insights into operating trends.

2. MATERIALS AND METHODS

2.1 The turbine model

A vertical-axis turbine model has been designed and fabricated (see Fig. 3). It is basically formed by three straight blades with a NACA-0015 profile. The geometrical parameters of the VAWT model are provided in table 2. In order to obtain a self-starting and efficient operation, the design parameters have been selected carefully. Specifically, the symmetrical airfoil NACA-0015 has been chosen due to its good performance under low wind velocity conditions [27, 28]. Also, the VAWT model has two ending plates of 0.15 m in diameter and 0.05 m in thickness to support the turbine blades. The proposed model is designed using 3D-CAD software and manufactured with the FDM (Fused Deposition Modeling) printing technology using Polylactic acid (PLA) material for its flexibility and high strength.



FIGURE 3: The turbine model inside the tunnel.

TABLE 2: Design parameters of the VAWT model

Parameter	Value
Rotor diameter	0.3 m
Rotor height	0.3 m
Blade profile	NACA-0015
Chord length	0.1 m
Number of blades	3
Shaft diameter	0.01 m

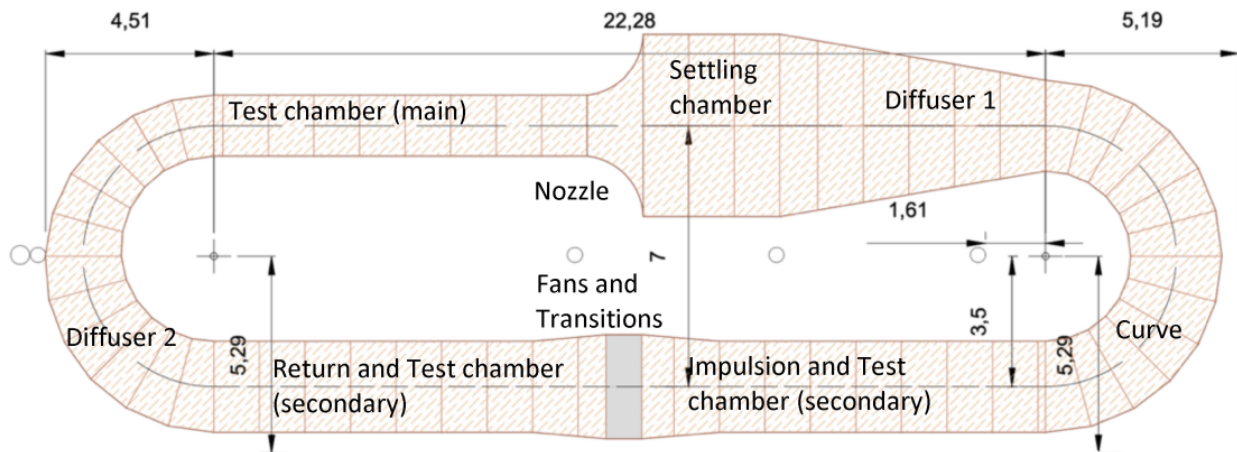


FIGURE 4: Full schematic of the wind tunnel [Dimensions in m].

The rotor is supported using a portable aluminium structure, allowing the turbine to be centered in front of the test section at a distance equal to 6 times the turbine diameter. Also, the rotational axis is supported, above and below, by two radial bearings. The turbine model, with its all components, has been mounted on a steel shaft (Fig. 3) and coupled with a 300 W commercial (Gimbal-GM8112H) permanent magnet generator (PMG) with 21 pairs of poles (pp). This component is connected to the measurement oscilloscope and a data acquisition board for collecting voltage and frequency measurements.

2.2 The wind tunnel

Experimental tests have been carried out in a closed-loop wind tunnel at the Polytechnic School of Mieres (University of Oviedo) in Spain. The tunnel consists of four axial fans with a total power of 180 kW which is controlled by a variable frequency driver, reaching a maximum wind speed of 180 km/h. Also, the tunnel contains several test chambers with different flow conditions. In the current tests, the turbine has been installed in a 2x2 m test chamber upstream of the fans, which limits the turbulence effects and airflow blockage. In addition, the fluid enters the test chamber through flow directors, after passing through a honeycomb panel, which has been designed to ensure the uniformity of the fluid before reaching the prototypes.

A full schematic of the wind tunnel is shown in figure 4. The wind tunnel is equipped with several anemometers to measure wind velocity (with an uncertainty value of ± 0.15), and pressure and temperature sensors (uncertainties of $\pm 0.3\%$ and $\pm 0.75^\circ\text{C}$) are used to correct the wind velocity measurements to the actual test conditions. To prevent any blockage in the airflow, the turbine model has been positioned in the wider zone of the wind tunnel, behind the fan section (in the suction zone). To ensure a steady turbulence flow, the wind is directed across a honeycomb net into the settling chamber after passing through the diffuser section. In the current study, the wind velocity value of 7.0 m/s has been selected to carry out the experimental tests inside the wind tunnel.

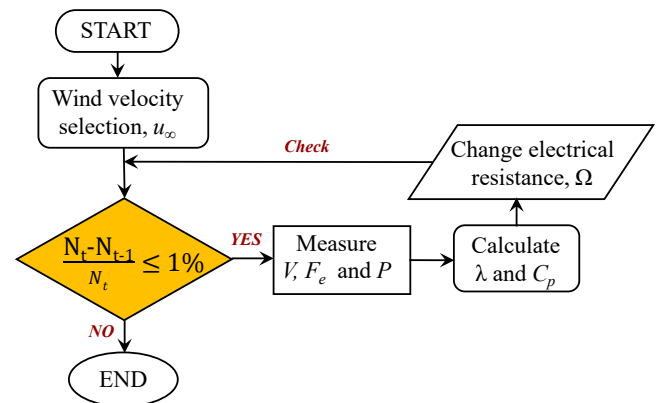


FIGURE 5: Experimental characterization procedures.

2.3 Electrical characterization of the power stage

In order to study the operation of a turbine, first is necessary to characterize it by means of certain parameters that make it possible to determine its performance and behaviour. In this sense, aspects such as its geometry, typology or the number of blades are key to the efficiency of the equipment during its energy production phase. The tip speed ratio (λ) and the power coefficient (C_p) are often the two dimensionless parameters that are used to characterize the turbine. The first one is the ratio of blade tip speed to wind speed (Equation. (1)), while the second is a measure of the equipment performance (Equation. (2)).

$$\lambda = \frac{\Omega \cdot R}{u_\infty} \quad (1)$$

$$C_p = \frac{P}{0.5 \cdot \rho \cdot A \cdot u_\infty^3} \quad (2)$$

Where, Ω is the rotational speed of the turbine [rad/s], R is the radius of the turbine [m], u_∞ is the wind current velocity

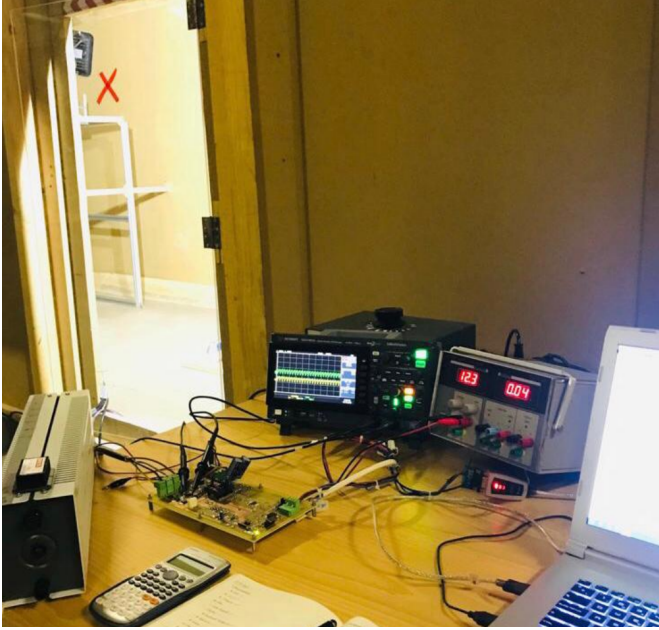


FIGURE 6: A photo of the measuring instruments.

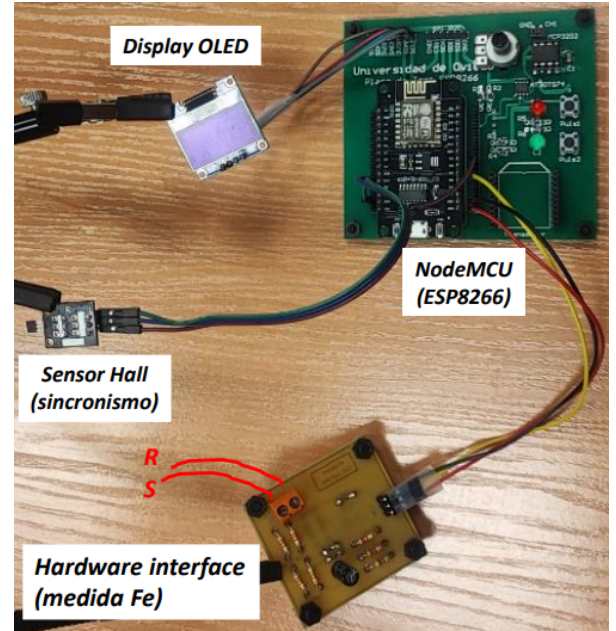


FIGURE 7: The control board and the component details.

[m/s], P is the power extracted from the generator [W], ρ is the air density and A is the turbine cross-section area. For the calculated variables, the uncertainty is about 1.15% for the tip speed ratio, and around 0.12% for the power and power coefficient measurements.

For each wind velocity, the turbine rotates freely without any loading until reaching the steady state condition where the rotational speed is nearly constant. Thereafter, the turbine is gradually loaded by changing the input resistance to brake the turbine through the PMG. Subsequently, the rotational speed decreases and the electrical power produced rises till reaching the maximum power point $MPPT$. From that point onwards, the power output from the turbine decreases with the decline of the rotational speed (the rotational speed at a time-step N_t is not almost equal to the last time-step N_{t-1}) the turbine reaches the deceleration condition and stops. The characterization sequences are summarized in the flow chart in fig. 5. For each mechanical rotation of the turbine, a total of pp (Pair of poles) electrical cycles is produced at the output of the PMG (Equations. (3) and (4)):

$$T_{mec} = pp \cdot T_e \quad (3)$$

Or, in terms of frequency:

$$F_e = pp \cdot F_{mec} \quad (4)$$

Where T_{mec} , F_{mec} and T_e , F_e are the mechanical and electrical torque and frequency respectively in [N.m] and [Hz].

As shown in figure 6, the oscilloscope is used to graphically represent electrical signals that vary over time and observe the waveform of the electrical output produced by the turbine's rotation. The torque produced is then calculated by processing the data using computer programs like Matlab. To supply the electrical energy necessary for the different instrumentation, a power

supply is used which allows regulation and protection against overloads and short circuits.

2.4 Electrical frequency analysis

An MQTT-based printed circuit board has been designed and manufactured to transmit data obtained by an Arduino board (see fig. 7). The basic structure of the hardware is used for the power frequency (F_e) measurement.

As a microprocessor, a NodeMCU system based on the ESP8266 is used, in which the interface circuitry is interconnected to convert the sinusoidal signal between any two phases at the output of the PMG to a square signal with logic levels suitable for the NodeMCU. Figure 8 shows the waveforms obtained for a sinusoidal voltage between phases of 10 V (signal V(R,S)). The V(1) and V(2) signals obtained are overlapped at one-half of the supply voltage.

The D7 port of the NodeMCU is used for the measurement with an accuracy of $\pm 4\mu s$. To simplify the visualisation of the results, an OLED display is interconnected using the I2C bus. An additional Hall effect sensor has been incorporated so that measurements can be carried out in synchronisation with the rotation axis of the turbine. The basic idea of the measurement will be to accurately measure the time elapsing between the high and low edges of the generated square signal, thus obtaining the electrical half-period of the sinusoidal signal (see fig. 9).

In the current study, three software have been developed; the first one is the Arduino program that is loaded in the NodeMCU, which allows the measurement of the electrical periods (maximum, minimum and average values) and all the instantaneous values of a mechanical cycle and sends it by MQTT to the broker as illustrated in fig. 10. The second one is a Python script, which allows measurement requests and saves them in an SQLite-type database. Once the data, including the electrical frequency, has

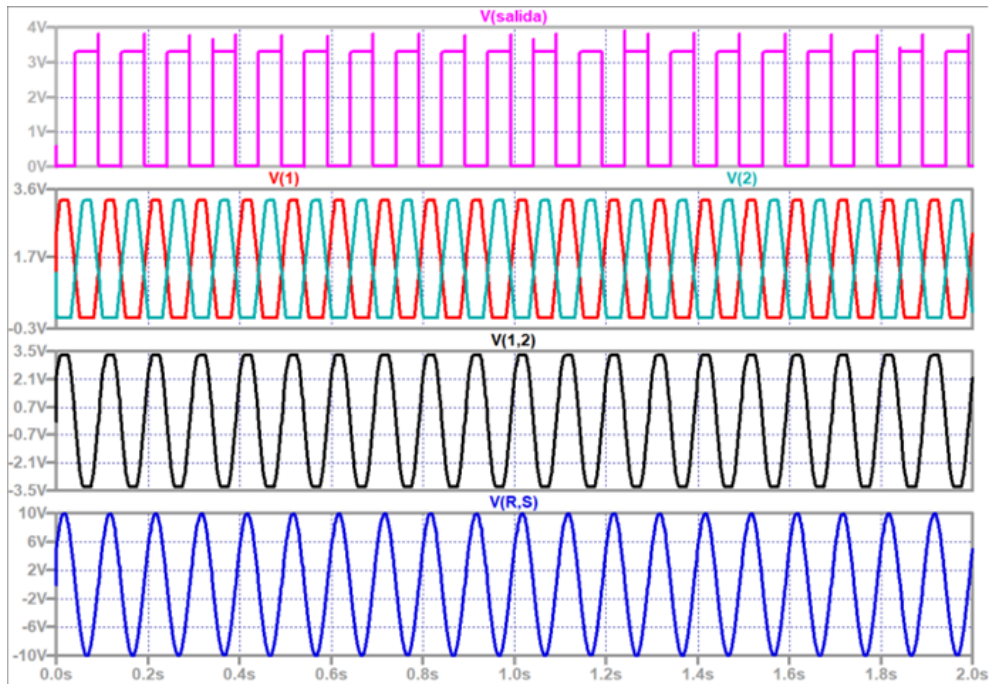


FIGURE 8: The main waveforms: sinusoidal and square signals input to NodeMCU .

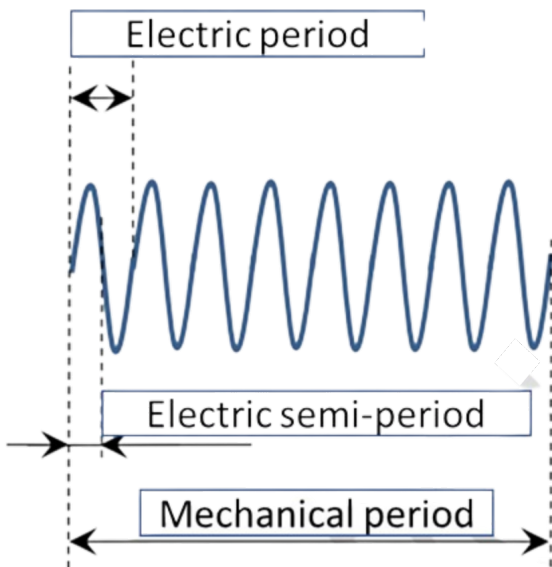


FIGURE 9: Electrical and mechanical periods.

been collected and stored in the database (DB), it is accessed by an operation and maintenance system, which uses an AI-based algorithm executed in Python for easy analysis. A Jupyter Notebook tool has been developed in python to provide a simple and intuitive visualization of the data. Figure 11 shows a part of the routine developed to graphically represent the sample that is stored in the test database.

In this way, the frequency measurement allows us to obtain

de rotational velocity [rpm] of the turbine without implementing any specific sensor. In addition, this measurement will be quite accurate since the number of pp is fixed and known and can be performed with high accuracy due to electronic processors.

The availability of F_e measurements opens the door for analyzing them as a method to detect problems and implement a predictive maintenance strategy for wind turbines. These non-invasive measurements can be performed during normal turbine operation using electronic techniques linked to IoT for simple and inexpensive collection and further processing of information. To this end, the optimal operating frequency has been obtained for the baseline case (A) at a wind speed of 7 m/s to carry out the experimental test. Subsequently, different failure states have been simulated: dirt on the shaft (B), dirt on the blade (C), and breakage of one of the blades (D).

3. Results and discussion

As it has been mentioned before, the characteristics of Vertical axis wind turbines are expressed commonly in terms of power coefficient C_p and tip speed ratio λ . Applying the power stage characterization procedure, the following curve (Fig. 13) has been obtained for a wind speed of 7 m/s. In this case, the tip speed values are above unity, which shows that the rotor design works by lift forces, as predicted. However, these values are considered lower for the current turbine model compared with other similar turbines. This is due to the high solidity value which is selected to avoid the starting issue. In addition, the turbine achieves power coefficient values close to 8%, which corresponds to those obtained in previous investigations in the literature. Thus, it is corroborated that the implemented design works correctly and can be analyzed for the purpose of this investigation.

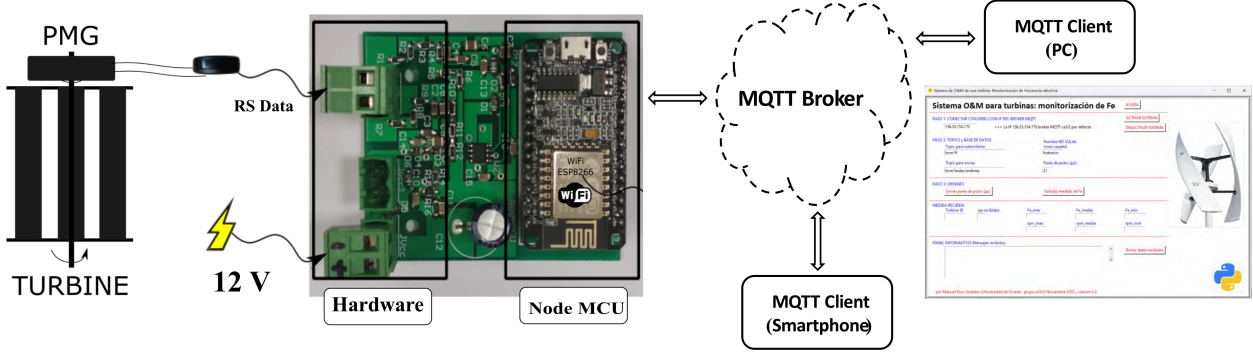


FIGURE 10: A schematic of the PMG power integration with the AI philosophy.

```
def dibujar_datos():
    global nombreDB
    global numero_filas_tabla
    global Fe_max_leida
    global Fe_med_leida
    global Fe_min_leida
    global Fe_leida
    global pp
    global num_fila
    #
    con = sqlite3.connect(BD)
    cursor = con.cursor()
    #
    cursor.execute('SELECT * FROM tabla_medidas;')
    todos=cursor.fetchall()
    numero_filas_tabla=len(todos)
    #
    print("numero de medidas (filas) disponible: ",
          numero_filas_tabla, "(van desde 0 hasta ", numero_filas_tabla-1,")")
    print("cada fila contiene las siguientes columnas: "+
          "Fecha, hora, turbina_ID, pp, Fe_max, Fe_med,Fe_min, Fe(1),...Fe(2*pp)")
    #
    Fe_max_leida=np.zeros(len(todos))
    Fe_med_leida=np.zeros(len(todos))
    Fe_min_leida=np.zeros(len(todos))
    Fe_leida=np.zeros((len(todos),2*pp))
    #
    k=0
    for fila in todos:
        print("Esta es la fila: ", k)
        print(fila)
        print("###")
```

FIGURE 11: A code sample of the Jupyter Notebook in python.

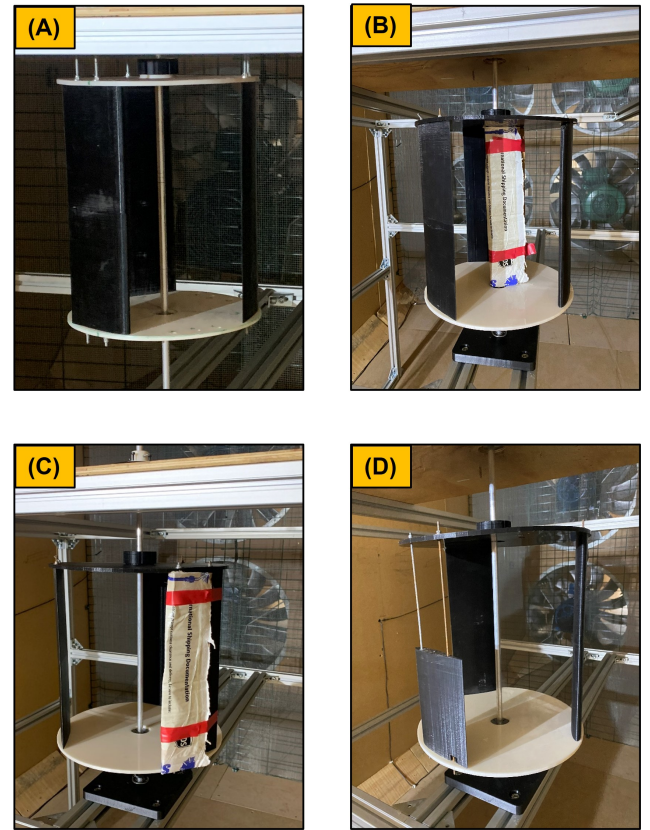


FIGURE 12: The configuration of experimental cases.

For the various scenarios studied, the electrical frequency measurements obtained for each of the operating cases have been analysed. It should be noted that case (A) is the baseline case for comparisons, in which the turbine works properly without any deflections. An analysis has been carried out of the average rotational speeds, defining a rotational speed ratio (ζ_ω) as indicated by equation.(5).

$$\zeta_\omega = \frac{\overline{\omega_i}}{\overline{\omega_A}} \quad (5)$$

Where $\overline{\omega_i}$ is the average rotational speed of each operating case (rpm) and $\overline{\omega_A}$ is the average rotational speed baseline case of the turbine. The rotational speed is calculated by applying equation equation.(6).

$$\omega_L = \frac{2 \cdot \pi \cdot \overline{F_{eL}}}{PP} \quad (6)$$

Where $\overline{F_{eL}}$ is the average electrical frequency of the considered case (Hz) and pp is the pair of poles of the PMG generator.

A variation in the rotational speed has been detected for all three cases as shown in fig. 14. Therefore, the use of the ratio ζ_ω is the first step towards detecting any type of malfunction in the operation of the rotor. However, this analysis is not sufficient to determine the nature of the failure. For this purpose, a ratio related to the standard deviation of each measured electrical frequency data has been defined. This ratio is calculated for each case of failure (ζ_σ), as shown in equation.(7).

$$\zeta_\sigma = \frac{\sigma_i}{\sigma_A} \quad (7)$$

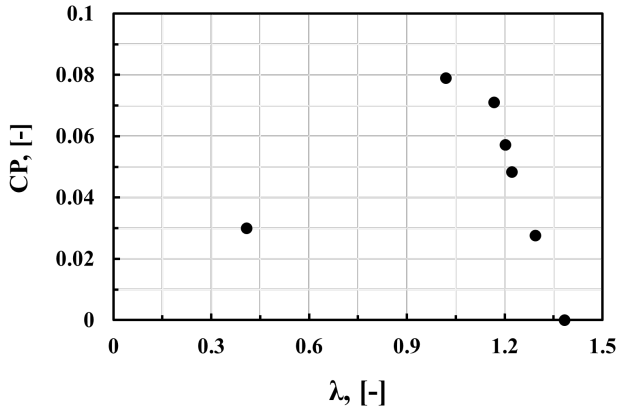


FIGURE 13: Turbine characteristic curve at $u_{\infty}=7$ m/s.

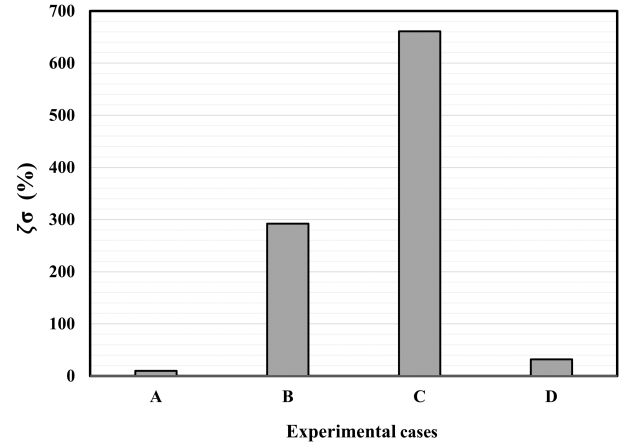


FIGURE 15: The standard deviation ratio for the cases .

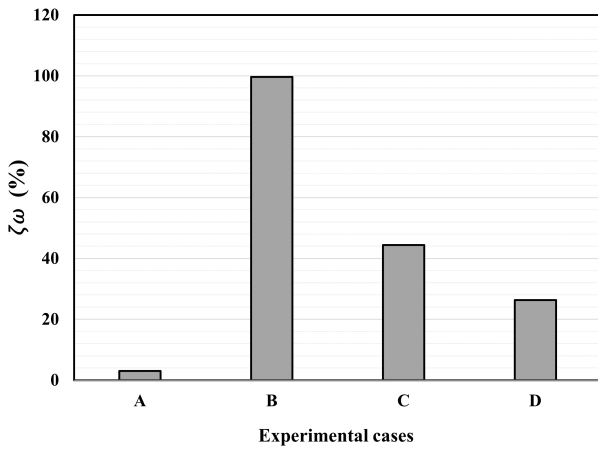


FIGURE 14: Rotational speed ratio for the cases.

Where σ_i is the standard deviation of the observed values in each failure case and σ_A is the standard deviation of the baseline case in the normal operating conditions. The calculation of the standard deviation has been performed according to equation. (8).

$$\sigma = \sqrt{\frac{\sum_{i=1}^N (F e_i - \overline{F e})^2}{N - 1}} \quad (8)$$

Where σ is the standard deviation of the power frequency data corresponding to each case considered, $F e_i$ is the observed power frequency value of each case sample, $\overline{F e}$ is the mean value of these observations and N is the number of observations.

Based on these results, it is evident that each case typology considered has very different values of ζ_{σ} , so it is possible to indicate what type of failure is occurring according to the obtained value. As presented in as shown in figure. 15, when the ζ_{σ} values are higher than 600 % it is because of some kind of failure in the area of the rotating shaft, while when they are around 300 % it is due to the accumulation of some unwanted element on the blade. Finally, when the values of ζ_{σ} are very low (< 100%), it indicates that one of the blades has been broken.

4. CONCLUSIONS

This investigation based on the predictive maintenance of micro wind turbines has shown consistent results in this first experimental wind tunnel approach. On the one hand, the analysis of the electrical frequency data has shown that in all cases in which the turbine presents some anomaly, a considerable reduction of the rotational speed is observed. On the other hand, with the analysis of the standard deviation it can be observed how there is also a considerable increase that is associated with the bad condition of the turbine.

5. FUTURE WORK

In the future, a new electronic board will be built to group all the components that make up the frequency measurement system, as well as to implement data analysis technologies that will allow the system to measure the frequency with more accuracy. This will make it possible to detect phenomena of rotor erosion and anticipate its failure, even indicating the component that has suffered this degradation. Also, the study will be widened to include other designs of wind turbines.

ACKNOWLEDGMENTS

The author would like to express his gratitude to the Instituto Universitario Tecnológico de Asturias (IUTA) for the funding and support received to carry out this research. Project title: "Estrategias de diagnóstico del estado de funcionamiento de turbinas hidrocínicas aplicadas al mantenimiento predictivo".

REFERENCES

- [1] Mišík, Matúš. "The EU needs to improve its external energy security." *Energy Policy* Vol. 165 (2022): p. 112930.
- [2] "EOM, "El mapa de la energía fósil en Europa - Mapas de El Orden Mundial- EOM." <https://elordenmundial.com/mapas-y-graficos/mapa-energia-fosil-europa/>. Accessed: 2022-10-17.
- [3] Elsakka, Mohamed Mohamed, Ingham, Derek B, Ma, Lin and Pourkashanian, Mohamed. "Comparison of the computational fluid dynamics predictions of vertical axis wind

- turbine performance against detailed pressure measurements.” *International Journal of Renewable Energy Research* Vol. 11 No. 1 (2021): pp. 276–293.
- [4] “AEE, “La eólica en el mundo - Asociación Empresarial Eólica.” <https://aeolica.org/sobre-la-eolica/la-eolica-en-el-mundo>. Accessed: 2022-10-18.
- [5] Tummala, Abhishiktha, Velamati, Ratna Kishore, Sinha, Dipankur Kumar, Indraj, V and Krishna, V Hari. “A review on small scale wind turbines.” *Renewable and Sustainable Energy Reviews* Vol. 56 (2016): pp. 1351–1371.
- [6] Porté-Agel, Fernando, Bastankhah, Majid and Shamsoddin, Sina. “Wind-turbine and wind-farm flows: A review.” *Boundary-layer meteorology* Vol. 174 (2020): pp. 1–59.
- [7] Gharib-Yosry, Ahmed, Blanco-Marigorta, Eduardo, Fernández-Jiménez, Aitor, Espina-Valdés, Rodolfo and Álvarez-Álvarez, Eduardo. “Wind–water experimental analysis of small sc-darrieus turbine: an approach for energy production in urban systems.” *Sustainability* Vol. 13 No. 9 (2021): p. 5256.
- [8] Ferraiuolo, Roberta, Gharib-Yosry, Ahmed, Fernández-Jiménez, Aitor, Espina-Valdés, Rodolfo, Álvarez-Álvarez, Eduardo, Del Giudice, Giuseppe and Giugni, Maurizio. “Design and Experimental Performance Characterization of a Three-Blade Horizontal-Axis Hydrokinetic Water Turbine in a Low-Velocity Channel.” *Environmental Sciences Proceedings* Vol. 21 No. 1 (2022): p. 62.
- [9] Farmanbar, Mina, Parham, Kiyam, Arild, Øystein and Rong, Chunming. “A widespread review of smart grids towards smart cities.” *Energies* Vol. 12 No. 23 (2019): p. 4484.
- [10] Gharib-Yosry, Ahmed, Fernandez-Jimenez, Aitor, Manuel Fernandez Pacheco, Víctor and Rico-Secades, Manuel. “Internet of Energy Applied to Water Hydrokinetic Smart-Grids: A Test Rig Example.” *Energy Sustainability*, Vol. 85772: p. V001T01A005. 2022. American Society of Mechanical Engineers.
- [11] “LuvSide, “LuvSide: The Powerful Turn, Savonius vertical axis wind turbines operate with low start-off wind speeds.” <https://www.luvside.de/en/>. Accessed: 2022-10-18.
- [12] “LuvSide, “LuvSide: Small-scale turbines to private communities.” <https://es.wind-turbine-models.com/turbines/1569-ratier-figeac-darrieus>. Accessed: 2022-10-18.
- [13] “Eovent, “Wind turbine models: EVA120 H-Darrieus-20,00 kW-Aerogenerator.” <https://es.wind-turbine-models.com/turbines/1691-eovent-eva120-h-darrieus>. Accessed: 2022-06-30.
- [14] “Dornier, “Small-scale turbines: Turbinas eólicas de Dornier.” <https://es.wind-turbine-models.com/turbines?manufacturer=102>. Accessed: 2022-06-30.
- [15] Garan, Maryna, Tidriri, Khaoula and Kovalenko, Iaroslav. “A data-centric machine learning methodology: application on predictive maintenance of wind turbines.” *Energies* Vol. 15 No. 3 (2022): p. 826.
- [16] Adekanbi, Michael Lanre. “Optimization and digitization of wind farms using internet of things: A review.” *International Journal of Energy Research* Vol. 45 No. 11 (2021): pp. 15832–15838.
- [17] Yildirim, Murat, Gebraeel, Nagi Z and Sun, Xu Andy. “Integrated predictive analytics and optimization for opportunistic maintenance and operations in wind farms.” *IEEE Transactions on power systems* Vol. 32 No. 6 (2017): pp. 4319–4328.
- [18] Lacey, Steve. “The role of vibration monitoring in predictive maintenance.” *Asset Management & Maintenance Journal* Vol. 24 No. 1 (2011): pp. 42–51.
- [19] Udo, Wisdom and Muhammad, Yar. “Data-driven predictive maintenance of wind turbine based on SCADA data.” *IEEE Access* Vol. 9 (2021): pp. 162370–162388.
- [20] Maron, Janine, Anagnostos, Dimitrios, Brodbeck, Bernhard and Meyer, Angela. “Artificial intelligence-based condition monitoring and predictive maintenance framework for wind turbines.” *Journal of Physics: Conference Series*, Vol. 2151. 1: p. 012007. 2022. IOP Publishing.
- [21] Tian, Zhigang and Zhang, Han. “Wind farm predictive maintenance considering component level repairs and economic dependency.” *Renewable Energy* Vol. 192 (2022): pp. 495–506.
- [22] Canizo, Mikel, Onieva, Enrique, Conde, Angel, Charra-mendieta, Santiago and Trujillo, Salvador. “Real-time predictive maintenance for wind turbines using Big Data frameworks.” *2017 IEEE international conference on prognostics and health management (icphm)*: pp. 70–77. 2017. IEEE.
- [23] Wang, Jinjiang, Liang, Yuanyuan, Zheng, Yinghao, Gao, Robert X and Zhang, Fengli. “An integrated fault diagnosis and prognosis approach for predictive maintenance of wind turbine bearing with limited samples.” *Renewable energy* Vol. 145 (2020): pp. 642–650.
- [24] Durbhaka, Gopi Krishna and Selvaraj, Barani. “Predictive maintenance for wind turbine diagnostics using vibration signal analysis based on collaborative recommendation approach.” *2016 International conference on advances in computing, communications and informatics (ICACCI)*: pp. 1839–1842. 2016. IEEE.
- [25] Gigoni, Lorenzo, Betti, Alessandro, Tucci, Mauro and Crisostomi, Emanuele. “A scalable predictive maintenance model for detecting wind turbine component failures based on SCADA data.” *2019 IEEE Power & Energy Society General Meeting (PESGM)*: pp. 1–5. 2019. IEEE.
- [26] Turnbull, Alan and Carroll, James. “Cost benefit of implementing advanced monitoring and predictive maintenance strategies for offshore wind farms.” *Energies* Vol. 14 No. 16 (2021): p. 4922.
- [27] Roh, Sung-Cheoul and Kang, Seung-Hee. “Effects of a blade profile, the Reynolds number, and the solidity on the performance of a straight bladed vertical axis wind turbine.” *Journal of Mechanical Science and Technology* Vol. 27 No. 11 (2013): pp. 3299–3307.
- [28] Gharib-Yosry, Ahmed, Espina Valdes, Rodolfo, Blanco-Marigorta, Eduardo and Alvarez-Alvarez, Eduardo. “An Approximation of Using Vertical-Axis Tidal Turbine for Water Desalination in the Suez Canal Waterway.” *Energy Sustainability*, Vol. 85772: p. V001T14A001. 2022. American Society of Mechanical Engineers.